The Road to Colloidal Self-Replication

by

Kun-Ta Wu

A dissertation submitted in partial fulfillment

of the requirements for the degree of

Doctor of Philosophy

Department of Physics

New York University

January, 2014

Paul M. Chaikin

ProQuest LLC.
789 East Eisenhower Parkway
P.O. Box 1346
Ann Arbor, MI 48106 - 1346

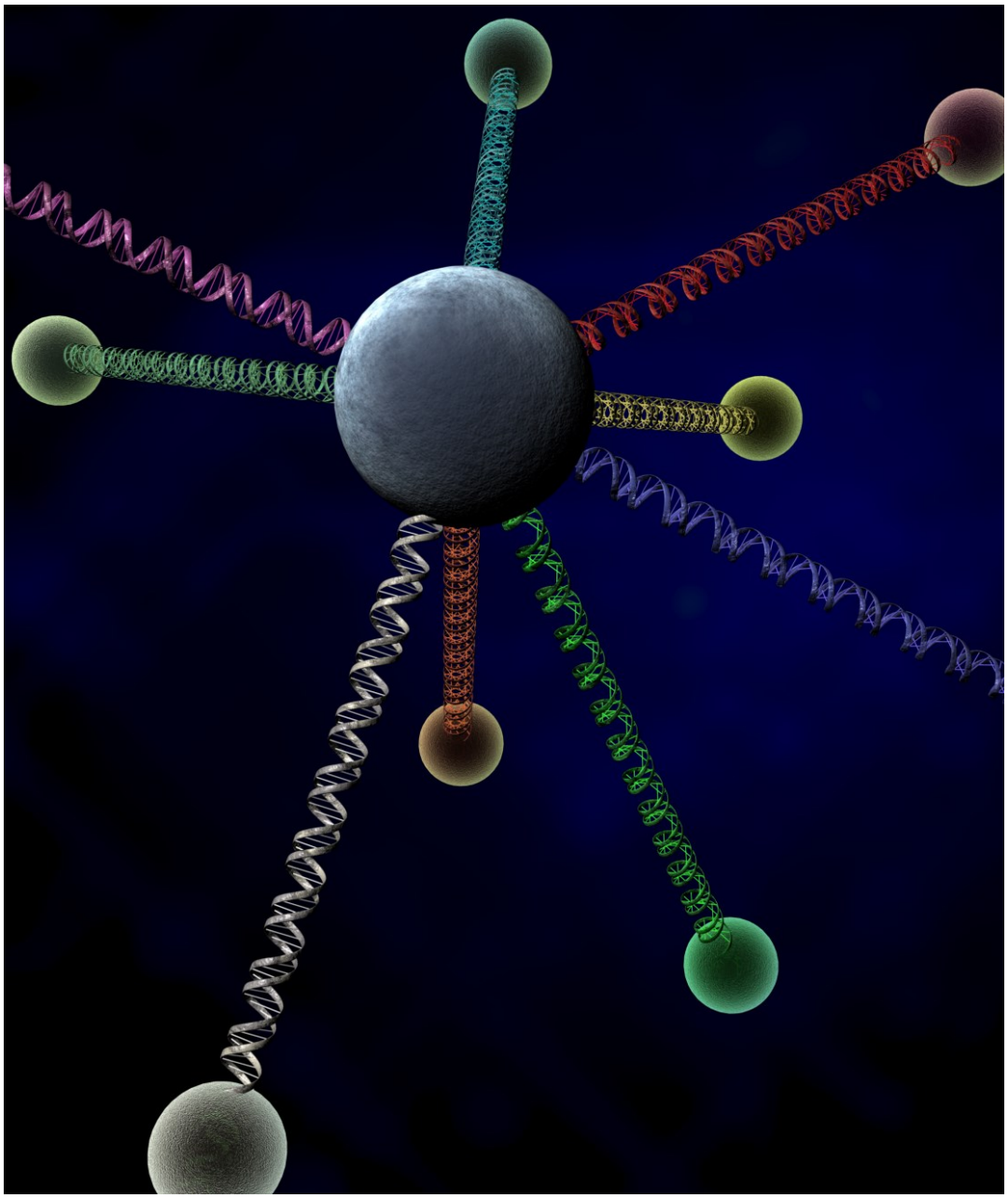

Art Created by Min-Wan Chiu

DEDICATION

To Yih-Chyi Wu, Pao-Chi Chang, and Min-Wan Chiu

ACKNOWLEDGEMENTS

I would like to thank my advisor, Professor Paul M. Chaikin, a very dedicated mentor. Whenever I felt frustrated or my experiment reached a dead end, he would show me a new path and new direction and would open a new window and bring in fresh air and new thinking. His creativity is far beyond my imagination. Whenever I spoke to him, I got inspired and had a new way to look at my research. If I do not understand the background, he would enlighten me in simple terms and in an intuitive way. I keep wondering where-from he would find all those countless hours helping me through many of my presentations. As a non-native English speaker, presenting my research in an easy-to-understand way is a challenge for me. Fortunately, I found in Professor Chaikin a kind and generous person who taught me how to give impressive and effective presentations to the audience and infused in me rare courage and helped me build confidence to successfully present my research to an audience that consisted of many experts at international meetings. Professor Chaikin is not only a mentor but also a great leader and I am extremely fortunate to have worked with him and fallen under his

spell. I wish to thank Professor Chaikin for guiding me through every challenge in my graduate study at New York University.

Secondly, I wish to thank Professor Nadrian Seeman. DNA is the very delicate molecule and Professor Seeman showed me how we can use it as a tool for complicated self-assembly. More importantly, whenever my research got stuck or I was confused about DNA, he enlightened me the right way of looking at DNA strands and guided how to correctly use them as the tool for self-assembly of colloids. Hence, my grateful thanks are due to Professor Seeman for solving my DNA-related problems.

Thirdly, I wish to thank Professor Alexander Grosberg. DNA hybridization is a complicated process, and Professor Grosberg gave me a great amount of help in model building, especially the kinetics of self-assembly of DNA-coated particles. Thanks to Professor Grosberg's help, I have understood the aggregation behavior of DNA-coated colloids in a reasonable and intuitive way. I therefore wish to convey my heartfelt thanks to Professor Grosberg for his dedicated teaching and guidance.

I now wish to thank Doctor Ruojie Sha. Since my research is deeply related to DNA, running polyacrylamide gel electrophoresis and radioactively labeling DNA strands is unavoidable. These experiments are very chemistry-oriented and are not straightforward for physicists. Doctor Sha showed me how to use the facilities in Professor Seeman's laboratory. Whenever I had technical issues, he always knew how to solve them. My DNA-related experiments could not have been done without his kind help. Thank you Doctor Sha for all your kind help!

I now wish to thank Doctor Lang Feng who gave me many simple and clever clues while performing experiments. He has the rare gift of building effective models. He has eyes to decipher the most complicated systems and reorganize and present data in an easy-to-understand and comprehensible manner. Most of the models presented here would not have been possible without Doctor Feng's support. I, therefore, wish to thank him for his dedication and contribution to my research at New York University.

I now wish to thank Doctor Remi Dreyfus. The thermodynamics study of self-assembly of DNA-coated particles presented here is based on his work. Doctor Dreyfus gave important and timely advise on both the experiments and models. With his help, our thermodynamics study progressed efficiently. My thanks therefore are due to Doctor Dreyfus for helping me through the thermodynamic study of self-assembly of DNA-functionalized colloids.

I now wish to thank Professor Andrew Hollingsworth who knew how to fix the experimental instrumentation in the laboratory in a simple and elegant way. I am immensely grateful to him for his care of the equipment which has smoothened my work and I could work without interruptions.

I now wish to thank Doctor Emily Chan, who cared for my health during my stay here at New York. With her professional knowledge she helped me fight whenever I fell sick and could recover myself well and go back to focus on my research in a short period of time. Therefore, I wish to thank Doctor Chan for guarding my health and for guiding to keep me fit and healthy.

I will be failing in my duty if I fail to thank my teammates of New York University Badminton Team, Dr. Ken Ho, Mr. Fabrice Jaumount, Mr. Chi-Lin Tsai, and colleagues at Center for Soft Matter Research, Mr. Colm Kelleher, Doctors John Royer, Corinna Maass, and Jeremie Palacci. My graduate study would have been different and tedious if these people had not been part of my life at New York. I wish to thank all of them for their friendship and for making my life both fruitful and colorful.

I wish now to thank my parents, Mr. Yih-Chyi Wu and Ms. Pao-Chi Chang. They have been pillars of strength and support to me all through my life, and encouraged me to aim high. I would not have been where I am now without their concern, love, affection, motivation and moral support. I wish to thank them wholeheartedly for inspiring, nurturing me and for molding my character.

Finally, I wish to thank my loving wife, Ms. Min-Wan Chiu. She stood by me through thick and thin, and shared happy and sad times. She comforted me whenever I felt frustrated or could not get sleep in the middle of cold snowy night in New York City. She gave me the mental strength and new energy to face every challenge in my life. I want to thank her for protecting my soul and for mentally and physically supporting me all through my life.

PREFACE

In recent times, science and technology have progressed rapidly. More and more impossible things have turned out to be real. Just about 100 years ago, man could not think of flying in the sky. It has now become a commonplace event. These days even mail is carried on planes. Similarly, science fiction today might turn into reality tomorrow. Many movies presented themes on self-replicating human beings or creating artificial life. Although they sound far from real, in 2008, I joined Chaikin's research group and learnt that he wanted to gift the ability to self-replicate to lifeless materials. I was surprised and taken aback when I heard of such a project. After five years of working with Professor Chaikin I realize that the fantasy of creating artificial life, which I saw in movies, might actually come true. This is an unprecedented project. Although Wilnut and Campbell's research team successfully replicated and produced a sheep, Dolly, the method relied on the existing somatic cell. The ambition of Chaikin's research team is to develop such self-replication ability from the ground level: self-replicating a lifeless object. Such research, if it succeeds, will be the first evidence of creating an artificial life and help researchers understand the origins of life and natural

evolution. However, to implement such a sacred project, we need to be able to synthesize and control the ingredients needed. The materials we use are DNA-functionalized colloids. Although DNA already exists in nature, human beings are already able to synthesize it with a specific sequence from basic lifeless chemicals. Therefore, the DNA we used in our research is treated as a lifeless molecule and does not have any sign of life. Our goal is to find a way to gift DNA-functionalized colloids the ability to self-replicate. The success of this project will bring human technology, especially biotechnology, to a whole new level. In this dissertation, I will show you how we prepare the ingredient needed for colloidal self-replication and pave the path to the realization of self-replicating lifeless materials. Hopefully, after reading this dissertation, you will feel as excited and obsessed as me about such an upcoming historical development.

Kun-Ta Wu

August 31, 2013.

ABSTRACT

Self-replication exists everywhere in nature from bacteria to human beings. Several generations of scientists have worked on self-replication in nature. However, a more challenging breakthrough is to self-replicate through lifeless matter, such as colloids. To accomplish this paradigm shift, technically, we need to investigate thermodynamics, kinetics, multi-functionality, mobility, and the formation of specific covalent bonds of DNA-coated colloids. These are the essential studies for realizing colloidal self-replication.

We present and experimentally test a mean field thermodynamic model for DNA-functionalized colloidal aggregation and find excellent agreement when accounting for the binding configurations between a pair of particles and adding an additional entropic term due to restricted configurations for DNA bound to both surfaces. We study the kinetics of aggregation as a function of DNA coverage and salt concentration over the range: 4 minutes $-$ 79 hours. The fundamental factor is an intrinsic hybridization time for a pair of complementary DNA in solution retarded by Coulomb repulsion, and

the entropic search for inter-particle binding configurations. We investigate the flexibility of the DNA colloid system for colloidal architecture by evaluating theoretically and experimentally the number of specific associations each of our colloids can have with its neighbors. In theory, we find that our particles can recognize up to 76 different particles due to intrinsic properties of DNA hybridization and sequence combination while in experiment we confine that up to 40 different particles can be bound. A practical limit is ~ 100. To demonstrate the utility of our "polygamous particles," we synthesize a dual-phase material, which by control process forms either gels or liquids at the same temperature.

"Sticky" particles typically have low mobility. We demonstrate a novel solution to this problem by combining depletion and DNA interactions, and we successfully synthesize crystals and designed hexagon clusters. Finally, we use cinnamate-modified DNA to control formation of specific covalent bonds and develop a new DNA photolithography. We functionalize a patterned area on a gold surface by a controlled UV light pattern.

TABLE OF CONTENTS

LIST OF FIGURES

LIST OF TABLES

LIST OF APPENDICES

CHAPTER 1 INTRODUCTION

Earth is the only known planet that harbors life despite scientists' efforts at finding extraterrestrial life for years. In the Solar System, the subsurface of Mars, the atmosphere of Venus, and subsurface oceans on Europa, one of Jupiter's moons, may have all it takes to host life [1, 2]. Scientists are trying to find evidence for life outside of the Earth. It is believed that life and water are deeply connected. The National Aeronautics and Space Administration (NASA) recently sent a rover, Curiosity, to Mars [3] to find evidence of water and life on the red planet and prove the existence of extraterrestrial life.

The earliest evidence of life on Earth is the traces of life found in fossils dating back to 3.4 billion years [4]. Through the years, the formation of life became more and more complicated, from single-celled organisms to multicellular bodies. Eventually, the organisms have grown the intelligence complicated enough to doubt the existence of their own intelligence [5]. The question of "What is Life?" has been discussed for thousands of years. In about 430 BC, Empedocles proposed that the universe is made up of four ele-

ments: earth, water, air, and fire [6]. Life is caused by an appropriate mixture of these elements. In about 460 BC, Democritus believed that the main characterization of life is the possession of soul, which is made by fiery atoms [6]. Through many years, the definition of life is still a challenge for scientists and philosophers since life is rather a process than a material [7]. Life has to be carefully defined, so the definition covers not only the life on Earth but the extraterrestrial life as well [8-10]. Therefore, in our definition, the most essential elements a life must possess are:

1. Metabolism,
2. Mobility, and
3. Self-replication.

The organisms possessing these three elements can be considered simple life. In colloidal research, creating colloids that can perform these three characteristics will be the evidence of creating colloidal artificial life. Fortunately, colloids with both metabolism and mobility can be created using a Pacman particle encapsulating a canted antiferromagnetic hematite cube in hydrogen peroxide solution [11]. When such colloids are exposed to blue light, they will consume hydrogen peroxide (metabolism) and create a concentration gradient in which they are driven to move (mobility). However,

such colloids still lack the ability to self-replicate. Therefore, colloidal self-replication is the last key element to give colloids life and is also the essence of life.

1.1. SELF-REPLICATION

To give life to colloids, we have to realize self-replication of colloidal particles. It can be done in many complicated ways [12]. To illustrate the idea, we choose the simplest example described in the following. As shown in Figure 1-1, we consider two species of particles: blue and red. They can bind together with a melting temperature, T_M. Blue particles can bind to themselves with a melting temperature, T_m and red ones with T_m. T_M is designed to be higher than T_m. Additionally, the bonds formed between pairs of particles with the same color (blue–blue or red–red) become permanent/unbreakable bonds when exposed to specific ultraviolet light. Our simplest colloidal self-replication scheme is done in the following way:

(a) Use blue particles to make a seed as shown in Figure 1-2 (a).

(b) Immerse the seed into the system containing blue and red particles at the system temperature, T higher than both T_M and T_m, namely,

$T > T_M > T_m$. At this stage, no bonds should be formed, so the system contains only single blue and single red particles, and the seed as shown in Figure 1-2 (b).

(c) Set the temperature between T_M and T_m, namely $T_M > T > T_m$. Then, pairs of particles with different colors (blue and red) bind together, but those with the same color (blue–blue or red–red) do not bind together. At this stage, red particles in the solution will bind to the seed as shown in Figure 1-2 (c).

(d) Set the temperature below both T_M and T_m, namely $T_M > T_m > T$. At this stage, the red particles bound to the seed will bind together as shown in Figure 1-2 (d).

(e) Expose the ultraviolet light to activate the permanent binding between pairs of particles with the same color. At this stage, red particles bound to the seed are bound together permanently.

(f) Increase the temperature beyond both T_M and T_m, namely $T > T_M > T_m$ when the bonds between blue and red particles break. However, the permanent bonds between red particles formed at Step (e) do not break. As a result, the system contains a complete copy of the seed from Figure 1-2 (a) as shown in Figure 1-2 (f).

(g) Repeat Steps (b)-(f).

The above protocol is the scheme of our colloidal self-replication. Since blue and red particles are symmetric in this self-replication, after following the same cycle, both blue and red seeds should give birth to their children, and the overall population should grow exponentially, doubling with each cycle. Therefore, our self-replication scheme provides the guide to give colloids the ability to self-replicate and therefore satisfies the third characteristic of life in our definition.

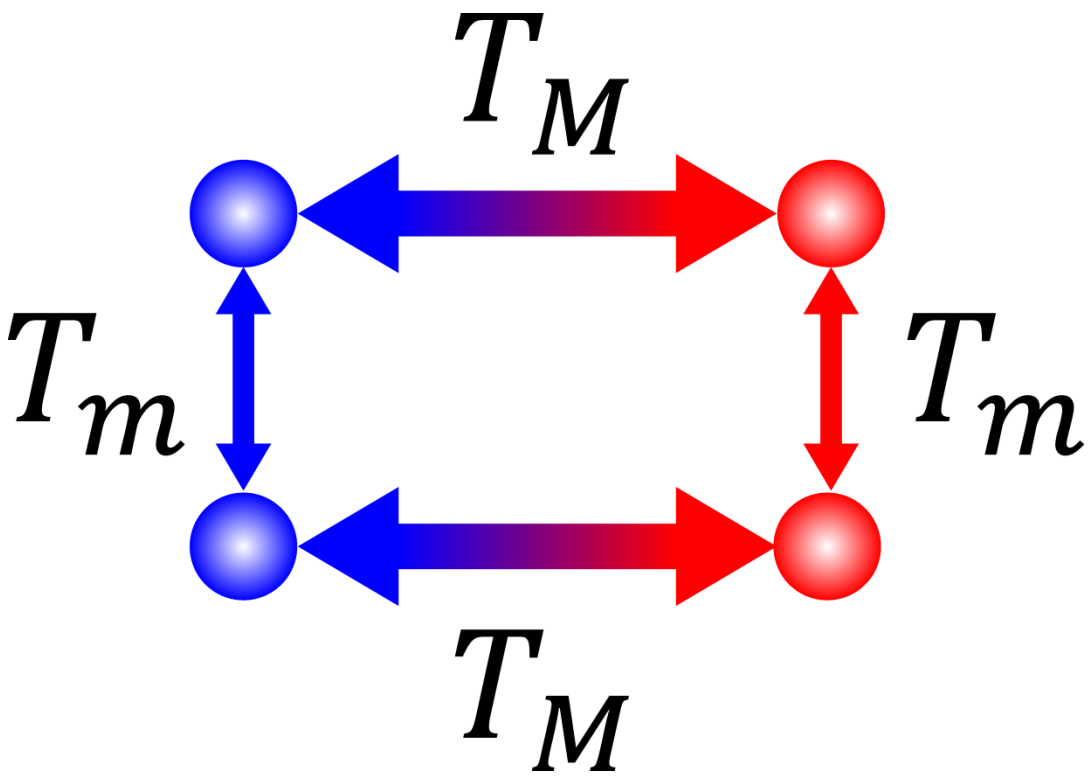

Figure 1-1: Interaction diagram of blue and red particles. The melting temperature of a blue and a red particle is T_M. The melting temperature of one blue particle and another is T_m, and of one red particle and another is also T_m. In the self-replication system, T_M is designed to be higher than T_m.

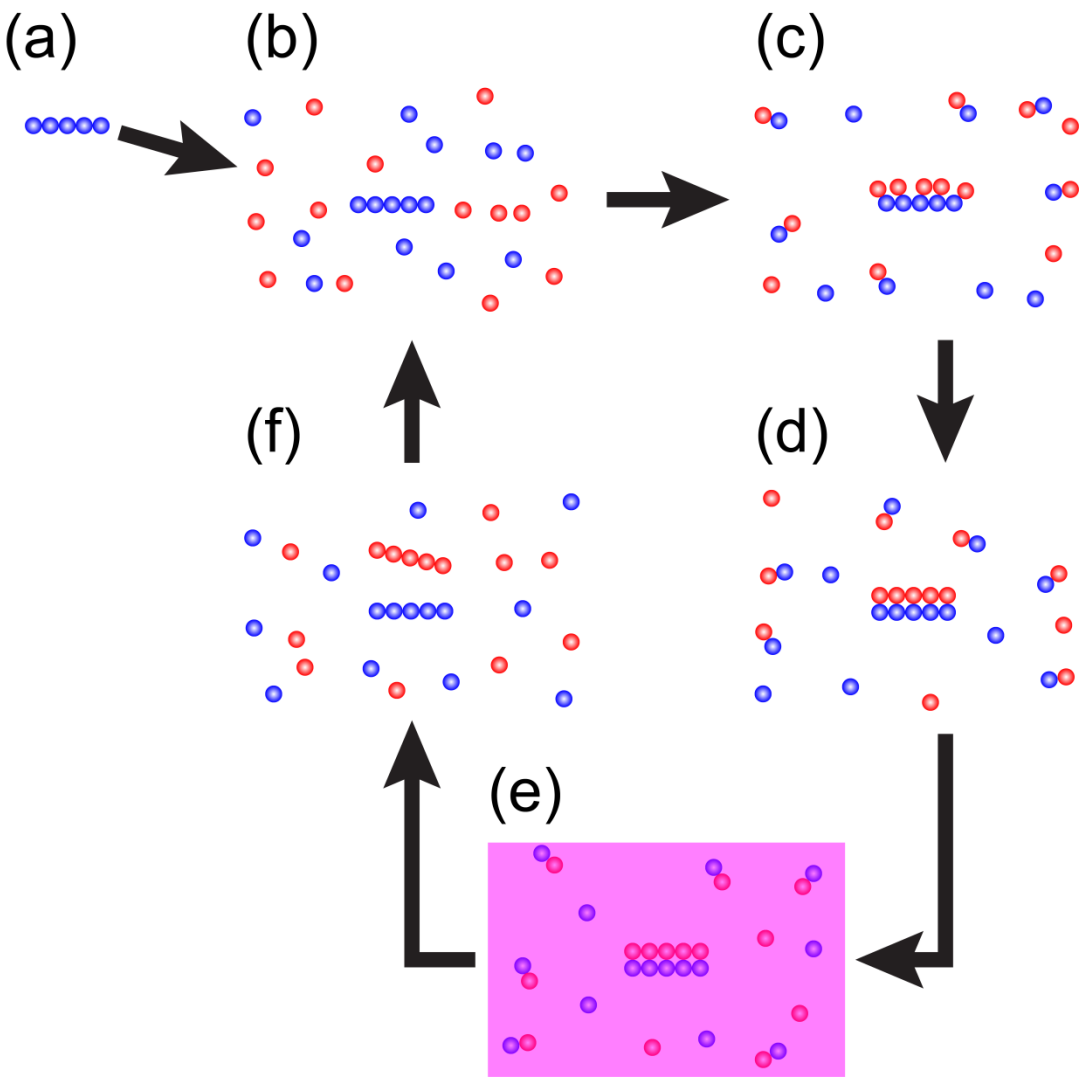

Figure 1-2: Colloidal self-replication scheme. (a) A seed. (b)–(f) A cycle of colloidal self-replication.

1.2. DNA MOLECULES

To perform self-replication discussed in Section 1.1, we have to synthesize particles that satisfy the colloidal interaction (Figure 1-1). However, these interactions are specific. Blue particles recognize and bind to red particles with a melting temperature, T_M. At the same time, blue particles can recognize other blue particles and bind together with another melting temperature, T_m. Conventional colloidal interactions, such as depletion and electrostatics [13], do not have the specificity. Fortunately, deoxyribonucleic acid (DNA) molecules have very specific binding. Hybridization between a pair of DNA strands highly depends on the base sequence. Therefore, by introducing DNA interactions into our colloidal system, we are able to synthesize colloids that satisfy the interactions shown in Figure 1-1.

1.2.1. SPECIFICITY OF DNA HYBRIDIZATION

DNA hybridization is highly specific due to DNA's special structure. The discovery of DNA structures is one of the most important scientific discoveries of the 20th century. James Watson and Francis Crick found the structure of

DNA to be a double helix [14]. DNA is composed of nucleotides (Figure 1-3). A nucleotide contains three components: a sugar group, a phosphate group, and a base [15]. The base is attached to the sugar group at the first carbon. The phosphate group is attached to the sugar group at the fifth carbon. There are four kinds of bases: Thymine (T), Adenine (A), Guanine (G), and Cytosine (C). As shown in Figure 1-4, thymine and adenine are complementary to each other and form two hydrogen bonds, and guanine and cytosine are complementary to each other and form three hydrogen bonds. Nucleotides are linked together to become a polynucleotide chain or a single-stranded DNA (ssDNA). The phosphate group links a pair of sugar groups by attaching one sugar group at the fifth carbon and the other at the third (Figure 1-5). At the ends, the ssDNA has a free $5'$ end and a free $3'$ end. Therefore, the ssDNA strand is given a direction from the 5' end to the 3' end, and a pair of them will hybridize into a duplex helix or a double-stranded DNA (dsDNA) not only if the sequences are complementary to each other but also if the strands are anti-parallel (Figure 1-6). For example, a DNA strand with the sequence 5'–GTA GAA GTA GG–3' hybridizes to one with the sequence 5'–CCT ACT TCT AC–3' but does not hybridize to the strand with the sequence 5'–TTT TTT TTT TT–3' or with the sequence

5'–CAT CTT CAT CC–3', which has the complementary sequence but has the wrong polarity. Both complementary sequences and anti-polarity are required for a pair of DNA strands to hybridize. As a result, DNA hybridization is highly specific and sequence-sensitive. By carefully designing DNA sequences, we can specify whether or not a pair of ssDNA strands will hybridize.

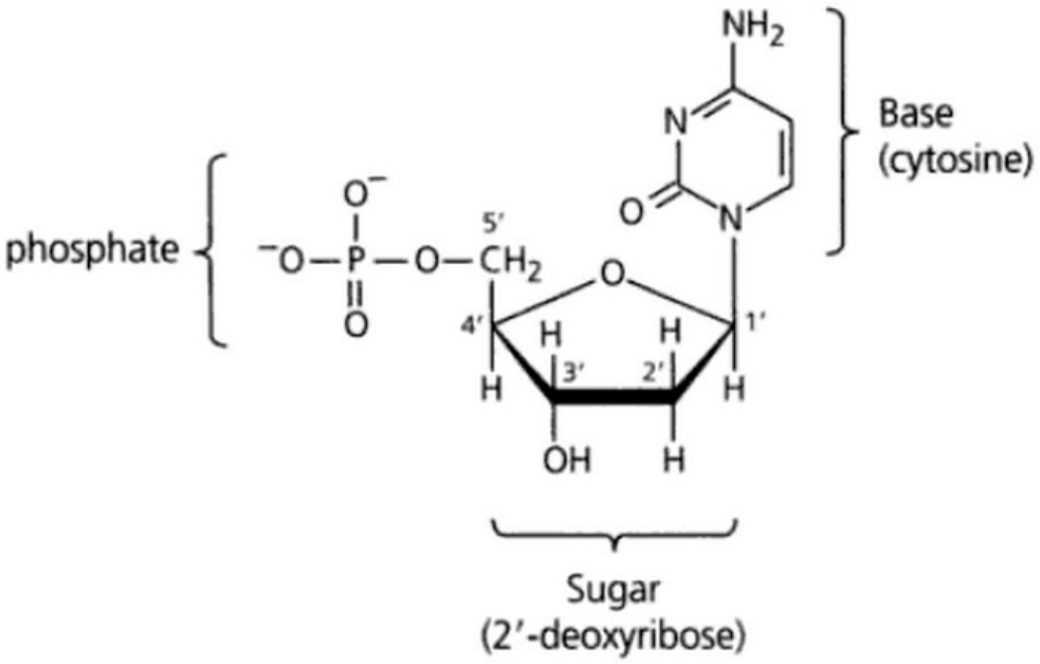

Figure 1-3: (Adopted from Bates and Maxwell, *DNA topology*, 2005) A nucleotide.

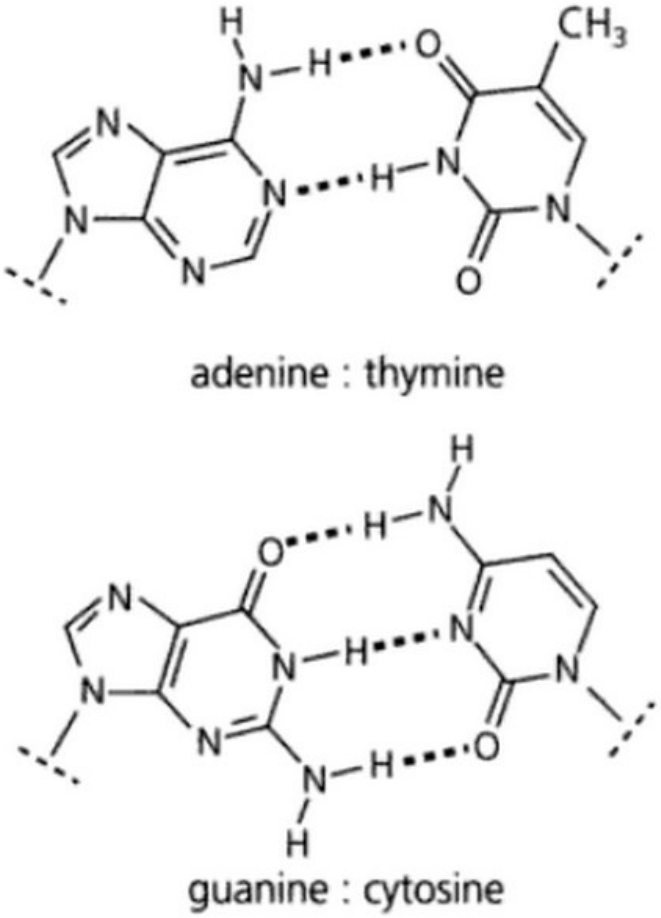

Figure 1-4: (Adopted from Bates and Maxwell, *DNA topology*, 2005) Base pairing. Top: Adenine-thymine pairing. Bottom: Guanine-cytosine pairing.

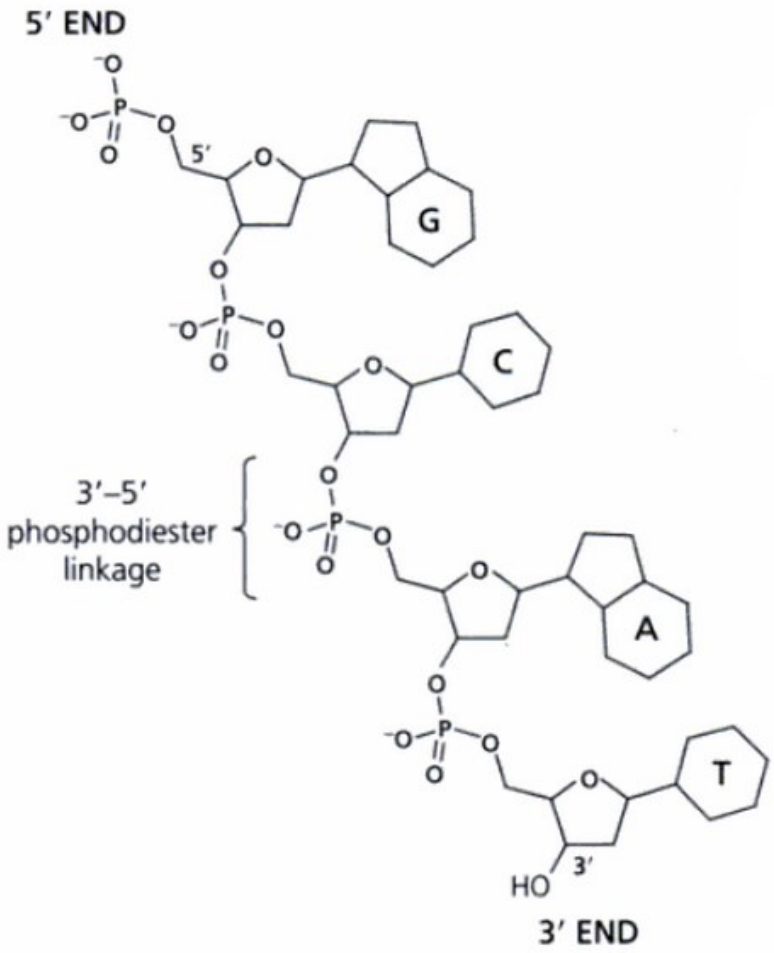

Figure 1-5: (Adopted from Bates and Maxwell, *DNA topology*, 2005) A polynucleotide chain.

Figure 1-6: (Adopted from Lodish and Darnell, *Molecular cell biology*, 2000) A schematic diagram of a double helix.

1.2.2. HYBRIDIZATION FREE ENERGY

The advantage of using DNA as the tool in our self-replication system is that the hybridization free energy is highly predicable and programmable. From Section 1.2.1, we learn that the DNA structures consist of sugar and phosphate groups, and bases. Sugar and phosphate groups are hydrophilic, and bases hydrophobic. Therefore, in a dsDNA strand, the hydrophilic sug-

ar–phosphate backbones stay on the outside of the duplex helix, while the hydrophobic bases face each other and stay inside the helix. Energy costs due to such hydrophobic and hydrophilic interactions along with hydrogen bonds formed between base pairs determine the enthalpy $\Delta H°$ for hybridization. Additionally, since ssDNA strands are flexible and dsDNA strands are rigid with a persistence length $\sim 50\ \mathrm{nm}$ [16], DNA hybridization, which goes from flexible ssDNA to dsDNA, costs entropy, $\Delta S°$. Therefore, hybridization free energy for a pair of complementary DNA strands can be determined as

$$\Delta F° = \Delta H° - T\Delta S°. \tag{1-1}$$

In 1998, SantaLucia Jr. proposed a unified nearest neighbor (NN) model that provided the prediction of the hybridization enthalpy $\Delta H°$ and entropy $\Delta S°$ of a pair of complementary strands [17]. The NN model assumes that the stability of a given base pair depends on its neighboring base pairs. The four different bases (T, A, G, and C) assemble 10 unique NN dimer duplexes as shown in Table 1-1. For simplicity of notation, the NN dimer, such as 5'–T A–3' paired with 3'–A T–5', is written as TA/AT. For a dsDNA strand, the hybridization enthalpy and entropy at $1\ \mathrm{M}\ \mathrm{Na}^+$ can be determined as

$$\begin{cases} \Delta H°(1\ \mathrm{M\ Na^+}) = \sum_{i=1}^{10} n_i \Delta H°_i + \Delta H°_{end,1} + \Delta H°_{end,2} \\ \Delta S°(1\ \mathrm{M\ Na^+}) = \sum_{i=1}^{10} n_i \Delta S°_i + \Delta S°_{end,1} + \Delta S°_{end,2} + \Delta S°_{sym} \end{cases}, \quad (1\text{-}2)$$

where $\Delta H°_i$ and $\Delta S°_i$ are the enthalpic and entropic contributions of the 10 possible NN dimers in Table 1-1, n_i, the number of occurrences of the corresponding NN dimers in the dsDNA, $\Delta H°_{end}$'s and $\Delta S°_{end}$'s are respectively the enthalpic and entropic contributions depending on the base pairs at the two ends, and $\Delta S°_{sym}$ is $-5.86\ \mathrm{J/K \cdot mol}$ if the sequence is self-complementary and zero if not. All the values of $\Delta H°$'s and $\Delta S°$'s can be found in Table 1-1 and Table 1-2. Then, according to equation (1-2), hybridization enthalpy and entropy in the solution containing $1\ \mathrm{M\ Na^+}$ can be predicted. Since enthalpy depends on hydrophobic and hydrophilic interactions and the hydrogen bonds are formed between base pairs, enthalpy does not strongly depend on sodium concentration. However, the persistence length of dsDNA strand strongly depends on sodium concentration, so the hybridization entropy caused due to the difference of persistence length between ssDNA and dsDNA changes with sodium concentration [16]. From Santa-

Lucia's model, the hybridization enthalpy and entropy at the given sodium concentration $[\mathrm{Na^+}]$ can be determined as

$$\begin{cases} \Delta H°([\mathrm{Na^+}]) = \Delta H°(1\ \mathrm{M\ Na^+}) \\ \Delta S°([\mathrm{Na^+}]) = \Delta S°(1\ \mathrm{M\ Na^+}) + \left[1.54 \times N \times \ln\left(\frac{[\mathrm{Na^+}]}{C°}\right)\right]\ \mathrm{J/K \cdot mol} \end{cases}, \tag{1-3}$$

where $C° = 1\ \mathrm{M}$ and N, the number of base pairs of the dsDNA strand. According to equation (1-3), hybridization enthalpy and entropy at an arbitrary sodium concentration can be determined, and the hybridization free energy can be determined from equation (1-1). Additionally, the melting temperature of hybridization of self-complementary strands can be determined as

$$T_m = \frac{\Delta H°}{\Delta S° + R_g \ln\left(\frac{C_{DNA}}{C°}\right)}, \tag{1-4}$$

where R_g is the gas constant and C_{DNA}, the strand concentration for self-complementary strands. For non-self-complementary strands, the melting temperature can be determined as

$$T_m = \frac{\Delta H°}{\Delta S° + R_g \ln\left(\frac{C_\mathrm{A} - C_\mathrm{B}/2}{C°}\right)}, \tag{1-5}$$

where C_{A} and C_{B} are the concentrations of more concentrated and less concentrated complementary DNA strands, respectively. Therefore, from SantaLucia's unified nearest neighboring model, equations (1-2) and (1-3), Table 1-1 and Table 1-2, along with equations (1-4) and (1-5), we can predict and program the melting temperature of a pair of complementary DNA strands.

To demonstrate the use of SantaLucia's model, we consider a pair of complementary strands and calculate the melting temperature at the specific strand and sodium concentrations. As shown in Figure 1-7, a strand with the sequence: 5'–GTA GAA GTA GG–3' is complementary to another strand with the sequence: 5'–CCT ACT TCT AC–3'. Since these strands are not self-complementary, $\Delta S°_{sym} = 0$. Also, since the first base pair and the last base pair are both G-C, $\Delta H°_{end,1} = \Delta H°_{end,2} = 418\,\mathrm{J/mol}$ and $\Delta S°_{end,1} = \Delta S°_{end,2} = -11.7\,\mathrm{J/K \cdot mol}$. From Figure 1-7, we can recognize the NN dimers in the dsDNA strand from left to right as GT/CA, TA/AT, AG/TC, GA/CT, AA/TT, AG/TC, GT/CA, TA/AT, AG/TC, and GG/CC. Ac-

cording to equation (1-2), the hybridization enthalpy and entropy at $1\ \mathrm{M\ Na^+}$ can be determined as

$$\begin{cases} \Delta H°(1\ \mathrm{M\ Na^+}) = -328{,}000\ \mathrm{J/mol} \\ \Delta S°(1\ \mathrm{M\ Na^+}) = -922\ \mathrm{J/K \cdot mol} \end{cases}.$$

Then, we consider that the strands are dissolved in the solution containing $10\ \mathrm{mM}$ phosphate-buffered saline (PBS) and $50\ \mathrm{mM\ NaCl}$. Since PBS contains $\sim 18\ \mathrm{mM\ Na^+}$, the overall sodium concentration is $68\ \mathrm{mM}$. Then, we can determine the hybridization enthalpy and entropy at $68\ \mathrm{mM}$ sodium concentration as

$$\begin{cases} \Delta H° = -328{,}000\ \mathrm{J/mol} \\ \Delta S° = \Delta S°(1\ \mathrm{M\ Na^+}) + [1.54 \times 11 \times \ln(0.068)]\ \mathrm{J/K \cdot mol} = -968\ \mathrm{J/K \cdot mol} \end{cases}.$$

Suppose that the concentration of each ssDNA strand is $3\ \mu\mathrm{M}$. Then, the melting temperature of the hybridization in Figure 1-7 in the solution containing $68\ \mathrm{mM\ Na^+}$ can be determined from equation (1-5) as

$$T_m = \frac{-328{,}000\ \mathrm{J/mol}}{-968\ \mathrm{J/K \cdot mol} + R_g \ln\left(\frac{3\ \mu\mathrm{M} - 3\ \mu\mathrm{M}/2}{1\ \mathrm{M}}\right)} = 31\ ℃. \quad (1\text{-}6)$$

Therefore, from SantaLucia's NN model, we can predict the melting temperature of a specific dsDNA at a given sodium concentration.

To verify that SantaLucia's unified nearest neighboring model provides reliable prediction, we compare it with a measurement of the melting temperature of complementary strands. We dissolve $\sim 3\ \mu\mathrm{M}$ of the dsDNA strands in Figure 1-7 in the buffer: $10\ \mathrm{mM\ PBS}, 50\ \mathrm{mM\ NaCl}$. Then, we use a Cary 100 bio-visible spectrophometer (Figure 1-8) to measure the absorbance of $260\ \mathrm{nm}$ wavelength light of the DNA sample as a function of temperature. The measurements are done by sweeping the temperature from 10 to $60\ ℃$ with the rate $0.5\ ℃/\mathrm{min}$ and then sweeping the temperature from 60 to $10\ ℃$ at the rate of $-0.5\ ℃/\mathrm{min}$. The measured experimental data are the blue dots shown in Figure 1-9 (a) and Figure 1-9 (b), respectively. The blue curves in Figure 1-9 are the polynomial fitting curves of the blue dots. Since the denaturation of dsDNA leads to a hyperchromism, the absorbance increases with the de-hybridization of dsDNA [18]. In Figure 1-9, the absorbances increases from $\sim 0.56\ \mathrm{O.D.}$ to $\sim 0.64\ \mathrm{O.D.}$ at $T \approx 35\ ℃$. Such changes are the result of DNA melting. To find the melting temperatures, we take the

derivative of the blue curve with respect to temperature and plot the red curves in Figure 1-9. The central peaks of the red curves indicate the melting temperatures of DNA hybridization from both measurements. The measured melting temperatures in Figure 1-9 (a) and Figure 1-9 (b) are $35.1\ ℃$ and $34.1\ ℃$, respectively. Therefore, our measured melting temperature of hybridization of the dsDNA in Figure 1-7 is:

$$T_m = (34.6 \pm 0.7)\ ℃. \tag{1-7}$$

Comparing equations (1-6) and (1-7), we note that SantaLucia's prediction is basically consistent with the actual measurement of DNA hybridization. Therefore, SantaLucia's unified nearest neighboring model provides guide to the design of complex DNA self-assembly. A typical example is DNA origami [19]. As shown in Figure 1-10, the black strand is a long ssDNA from the virus M13mp18. The colored strands are staple strands. The staple strands and parts of the black strand hybridize. As a result, the black strand is folded into a designed structure. Figure 1-11 shows the results of using such method of DNA origami. The success of DNA origami proves that DNA is not only the biological storage containing the information of life which characterizes each species but also a useful and convenient tool for specific and designed self-assembly. This is not only because hybridization

is highly specific but also because its strength is programmable through SantaLucia's unified nearest neighboring model.

Sequence	ΔH°_i (J/mol)	ΔS°_i (J/K · mol)
AA/TT	$-33{,}100$	-92.9
AT/TA	$-30{,}100$	-85.4
TA/AT	$-30{,}100$	-89.1
CA/GT	$-35{,}600$	-95.0
GT/CA	$-35{,}100$	-93.7
CT/GA	$-32{,}600$	-87.9
GA/CT	$-34{,}300$	-92.9
CG/GC	$-44{,}400$	-114
GC/CG	$-41{,}000$	-102
GG/CC	$-33{,}500$	-83.3

Table 1-1: ΔH° and ΔS° in unified nearest neighbor model in 1 M NaCl. The data is taken from Ref. [17].

Ending sequence pairs	ΔH°_{end} (J/mol)	ΔS°_{end} (J/K · mol)
G-C	418	−11.7
A-T	9,620	17.2

Table 1-2: Enthalpic and entropic contributions due to different base pairs at the ends of a dsDNA strand. The data is taken from Ref. [17].

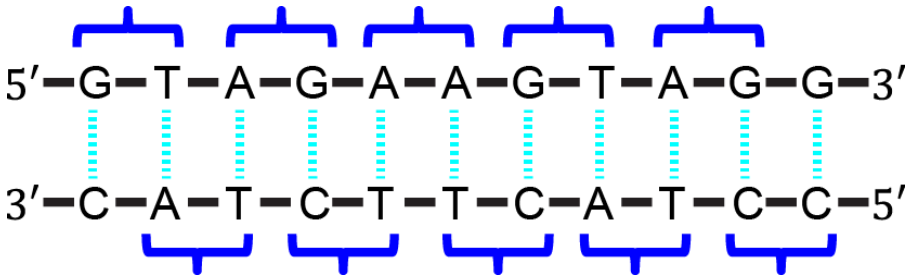

Figure 1-7: Demonstration of unified nearest neighbor model.

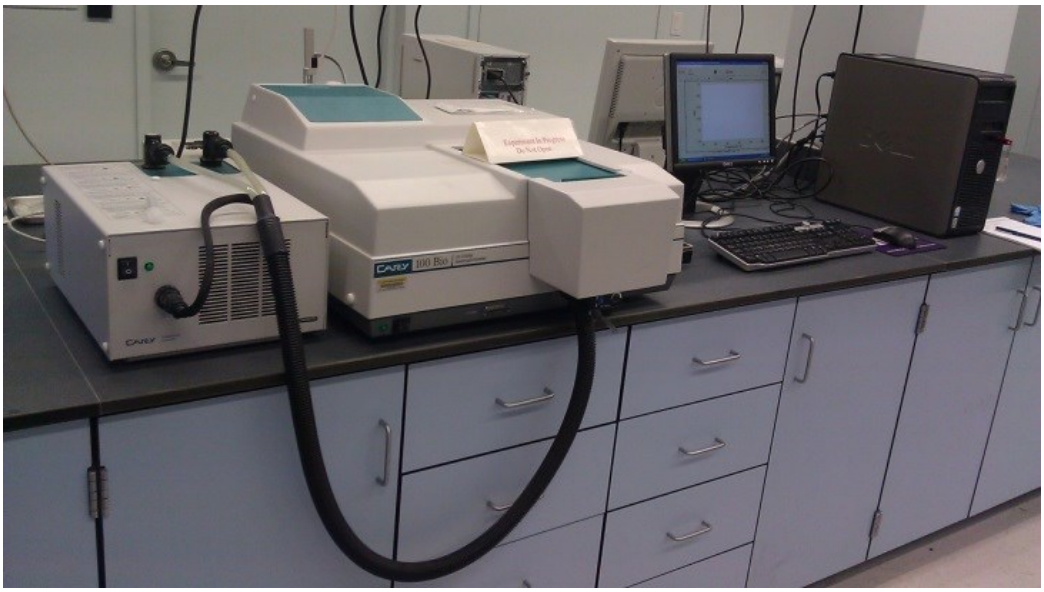

Figure 1-8: Cary 100 bio UV-visible spectrophometer.

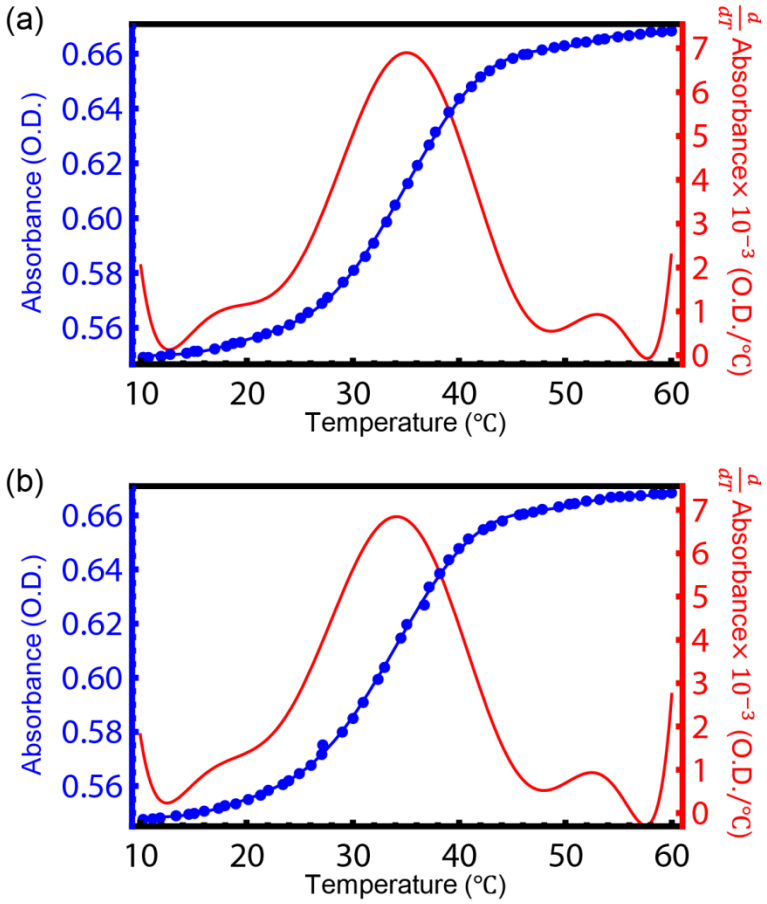

Figure 1-9: Measurements of DNA melting. Blue dots represent the experimental data for the measurement of DNA absorbance with respect to temperature. The blue curves represent the polynomial fit of blue dots and red curves are the derivative of blue curves with respect to temperature. (a) Measurement of sweeping temperature from 10 ℃ to 60 ℃. (b) Measurement of sweeping temperature from 60 ℃ to 10 ℃.

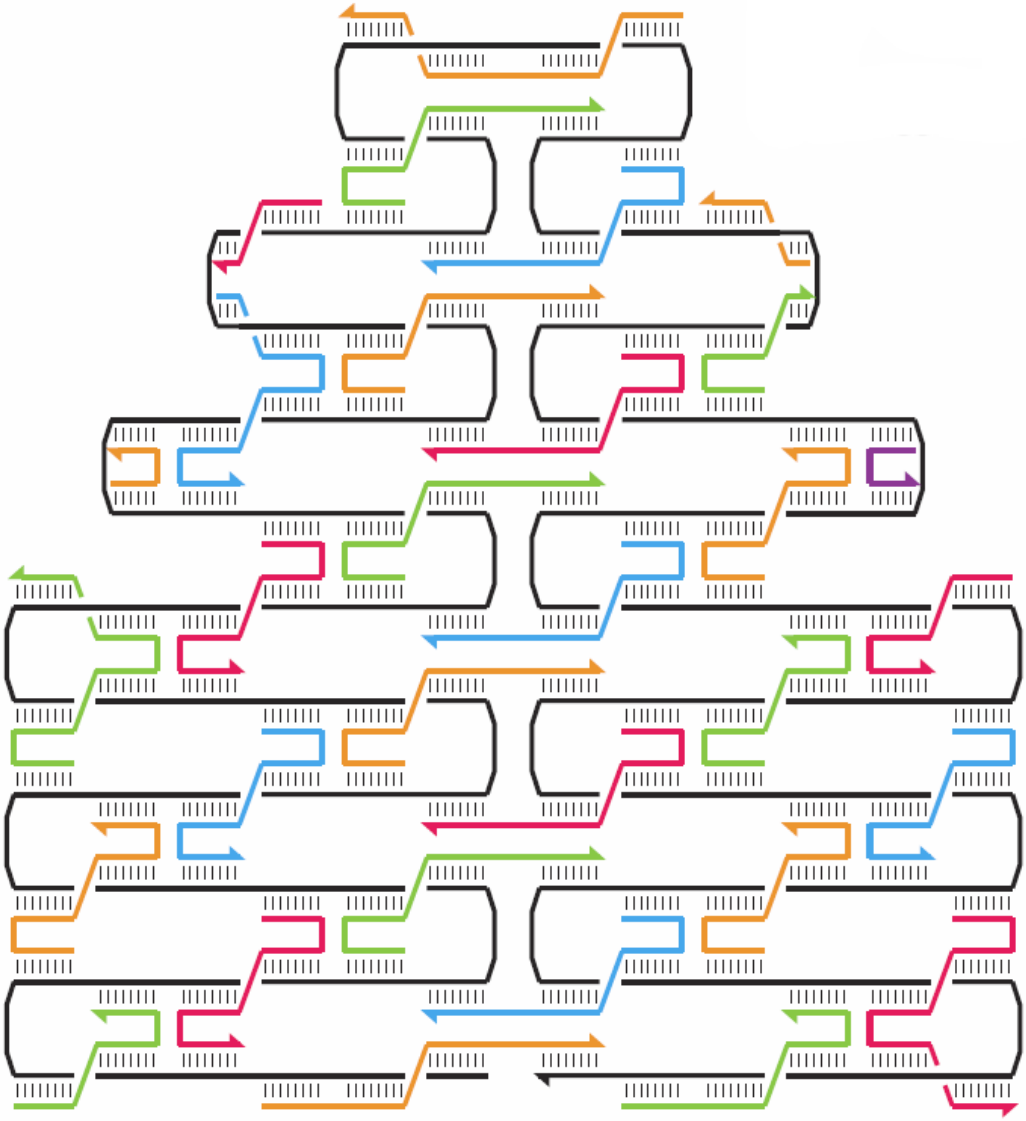

Figure 1-10: (Adopted from Rothemund, *Nature*, 2006. 440: p. 297) Design of DNA origami. The black strand is a long ssDNA from the virus M13mp18. The colored strands are staple strands.

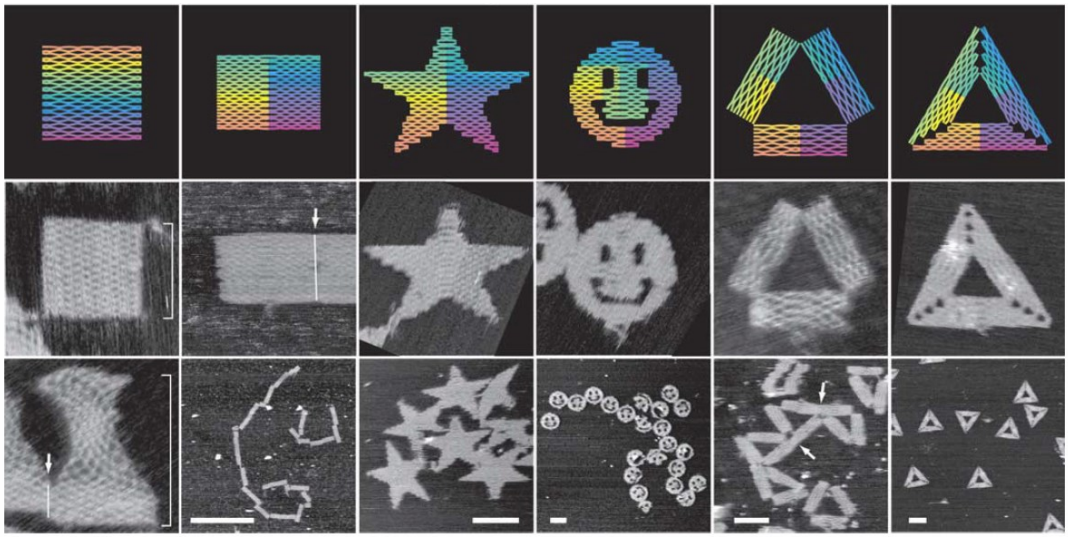

Figure 1-11: (Adopted from Rothemund, *Nature*, 2006. 440: p. 297) AFM images of DNA origami. From left to right, the designed structures are square, rectangle, star, disk with three holes, triangle with rectangular domains, and sharp triangle with trapezoidal domains and bridges between them.

1.3. DNA-FUNCTIONALIZED COLLOIDS

To perform colloidal self-replication discussed in Section 1.1, we need colloids that can bind specifically and reversibly. Since DNA hybridization is highly specific and thermo-reversible, functionalizing colloids with DNA

strands gives colloids specific and thermo-reversible binding. Recently, DNA-functionalized colloids have been widely and intensely studied [20-37]. Introducing DNA interaction into colloidal systems opens the door to many new colloidal self-assemblies. Therefore, in this section, we will see how DNA-functionalized colloids self-assemble and how they can be good candidates for performing colloidal self-replication.

1.3.1. WATSON-CRICK-LIKE MICROSPHERES

The most commonly used system of DNA-coated microspheres is the Watson-Crick-like system. Valignat *et al.* performed the experiment of self-assembly of fluorescently labeled particles coated with complementary strands [26]. As shown in Figure 1-12 (A), red and green particles are coated with complementary strands. To stabilize particles and avoid non-specific binding, the surface of each particle is coated with pluronic F108. Since the DNA strands on the red and green particles are complementary to each other, the complementary DNA strands between particles hybridize and become DNA bonds that hold red and green particles together. As shown in Figure 1-12 (B), we can see that green and red particles are bound together. However, binding between two green or two red particles is

not found. Therefore, Figure 1-12 (B) proves that by coating particles with DNA strands, particles have specific bindings. Only particles coated with complementary DNA strands will bind together. Therefore, we can use DNA-coated particles to direct colloidal self-assembly.

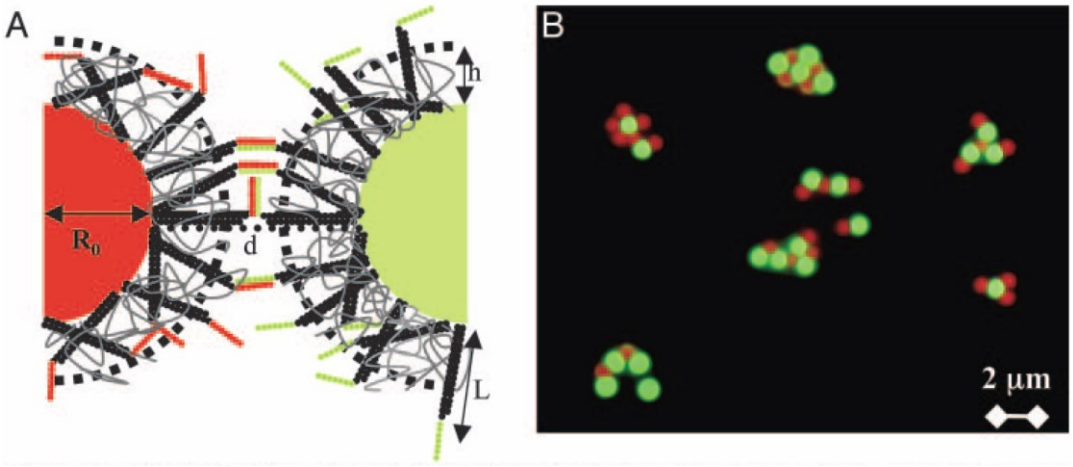

Figure 1-12: (Adopted from Valignat, *et al.*, *PNAS*, 2005. 102: p. 4225) Particles coated with complementary DNA strands. (A) Schematic diagram of DNA-coated particles. Particles coated with complementary strands are bound together through DNA bonds formed between particles. To stabilize particles, their surfaces are coated with a polymer bush. (B) Images of aggregation of fluorescently labeled DNA-coated particles.

1.3.2. ANISOTROPIC BUILDING BLOCKS

In addition to directing self-assembly by the specific binding of DNA-coated particles, the shape of colloids also plays an important role in the final assembly structure. Jones *et al.* used DNA-coated nanoparticles with various shapes and demonstrated how particle shape influences crystal formation [38]. The particle shapes investigated are rods, triangular prisms, rhombic dodecahedra, and octahedra (Figure 1-13). The surface of each particle is also functionalized by DNA strands as shown in Figure 1-14. From Figure 1-15, we can see that the rods favor interactions perpendicular to their long axis and self-assemble into a 2D lattice. Figure 1-16 shows that the triangular sides of the prisms prefer to face each other since most DNA bonds can be formed in this configuration. As a result, the prisms self-assemble into 1D pillars. Figure 1-17 shows that the rhombic dodecahedra self-assemble into face-centered crystals (FCC) and Figure 1-18 that the octahedra self-assemble into body-centered crystals (BCC). Therefore, putting together Figure 1-15, Figure 1-16, Figure 1-17, and Figure 1-18, we can see that the shape of particles also controls the final structure, the periodicity, and orientation of self-assembly of DNA-coated particles. Combining the specific

binding of DNA-coated particles with shape dependence self-assembly creates a more sophisticated and fruitful self-assembly of colloids.

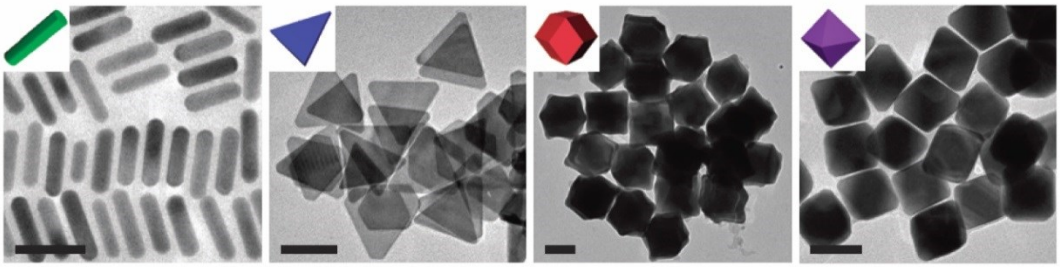

Figure 1-13: (Adopted from Jones, *et al.*, *Nature Materials*, 2010. 9: p. 913) Anisotropic nanoparticles. From left to right, the shapes of nanoparticles are rods, triangular prisms, rhombic dodecahedra, and octahedra.

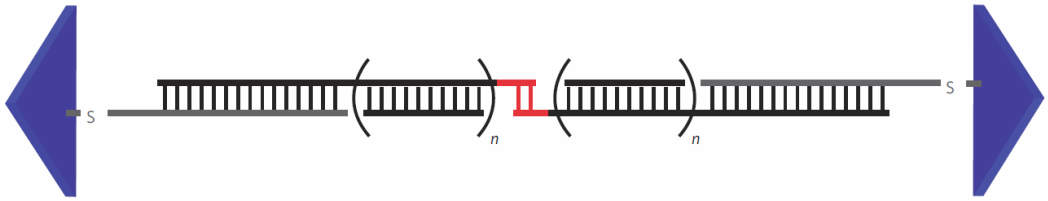

Figure 1-14: (Adopted from Jones, *et al.*, *Nature Materials*, 2010. 9: p. 913) Schematic diagram of a DNA link between nanoparticles.

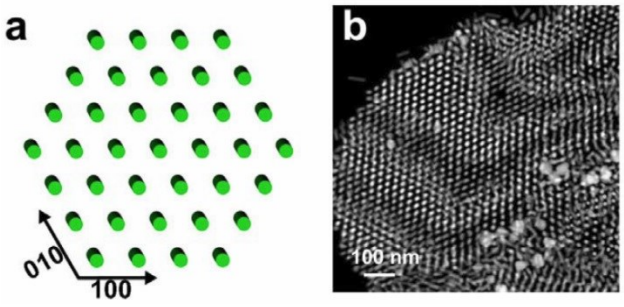

Figure 1-15: (Adopted from Jones, *et al.*, *Nature Materials*, 2010. 9: p. 913) Self-assembly of rods. (a) Schematic diagram of crystallized rods, and (b) Transmission electron microscopy of the crystallized rods.

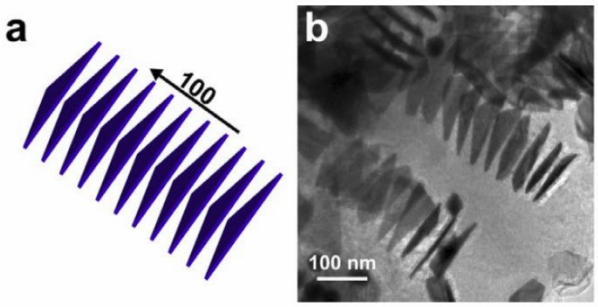

Figure 1-16: (Adopted from Jones, *et al.*, *Nature Materials*, 2010. 9: p. 913) Self-assembly of triangular prisms. (a) Schematic diagram of crystallized prisms, and (b) Transmission electron microscopy of the crystallized prisms.

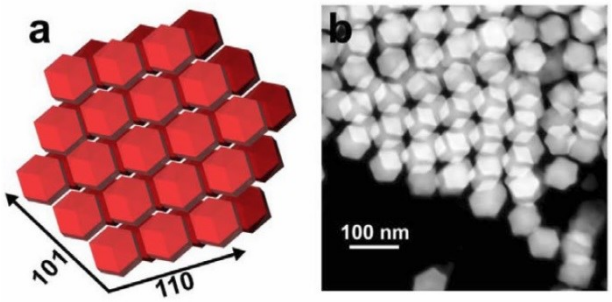

Figure 1-17: (Adopted from Jones, *et al.*, *Nature Materials*, 2010. 9: p. 913) Self-assembly of rhombic dodecahedra. (a) Schematic diagram of crystallized rhombic dodecahedra. The crystals are FCC, and (b) Transmission electron microscopy of the crystallized rhombic dodecahedra.

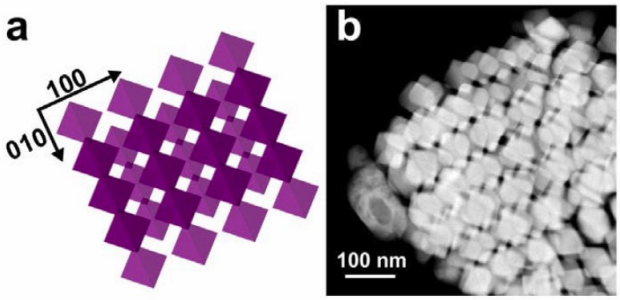

Figure 1-18: (Adopted from Jones, *et al.*, *Nature Materials*, 2010. 9: p. 913) Self-assembly of octahedra. (a) Schematic diagram of crystallized octahedra. The crystals are BCC, and (b) Transmission electron microscopy of the crystallized octahedra.

1.3.3. PATCHY PARTICLES

In addition to the specific binding of DNA-induced interaction between particles and the influence of particle shapes on self-assembly, locally functionalizing particles with DNA strands also enriches the self-assembly of DNA-coated particles. Feng *et al.* synthesized colloidal particles with only one functionalized patch [23]. As shown in Figure 1-19, the DNA-functionalized patch of the colloidal particles is hybridized to fluorescently labeled DNA strands. Therefore, with confocal images, we can see that the particles look

like dim green eye balls with bright green corneas. The non-specific binding of the fluorescently labeled DNA strands form the shape of eye balls. The bright green corneas are due to specific hybridization of the fluorescently labeled DNA strands and functionalized patch of particles. As shown in Figure 1-20, pairs of complementary DNA patchy particles form dimers. Such result shows that synthesizing DNA patchy particles provides colloidal self-assembly in a more controllable way. Wang *et al.* synthesized colloidal particles functionalized with many directionally symmetric patches and demonstrated the advantage of using DNA patchy particles [39]. As shown in Figure 1-21, particles functionalized with a specific number of patches were synthesized. The DNA strands at the green and red patches are complementary to each other. As a result, the valence and structure of self-assembly of these particles are well controlled and programmed. Therefore, locally functionalizing particles creates more directionally controlled self-assembly and opens the door to better-programmed colloidal self-assembly.

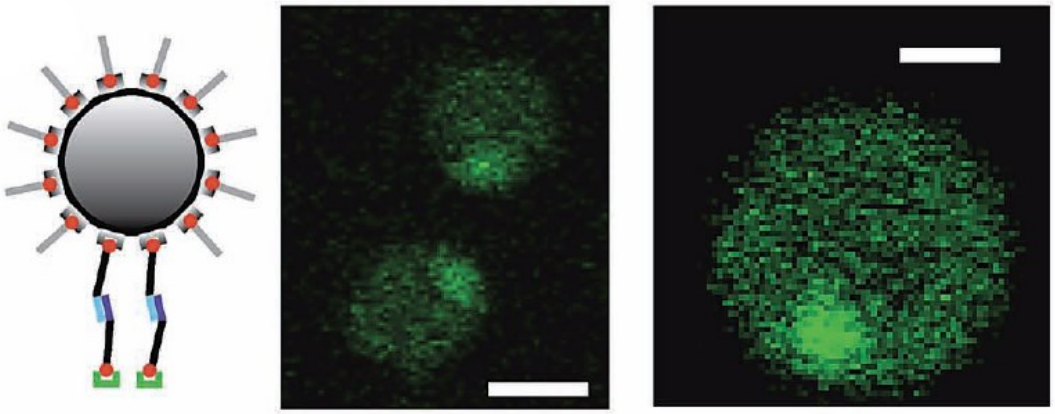

Figure 1-19: (Adopted from Feng, *et al.*, *Advanced Materials*, 2013. 25: p. 2779) DNA patchy particles. Left: The schematic diagram of the particle. The functionalized patch is hybridized to fluorescently labeled DNA. Middle and Right: Confocal images of DNA patchy particles. The scale bar is 1 μm.

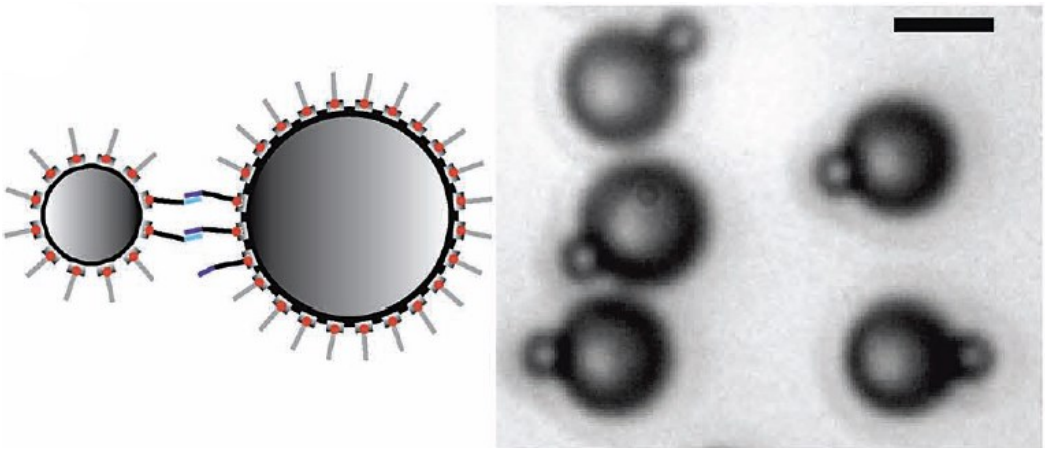

Figure 1-20: (Adopted from Feng, *et al.*, *Advanced Materials*, 2013. 25: p. 2779) Self-assembly of complementary DNA patchy particles. Left: Schematic diagram of self-assembly of two patchy particles. Right: Micrograph of self-assembly of two patchy particles. The scale bar is 3 μm.

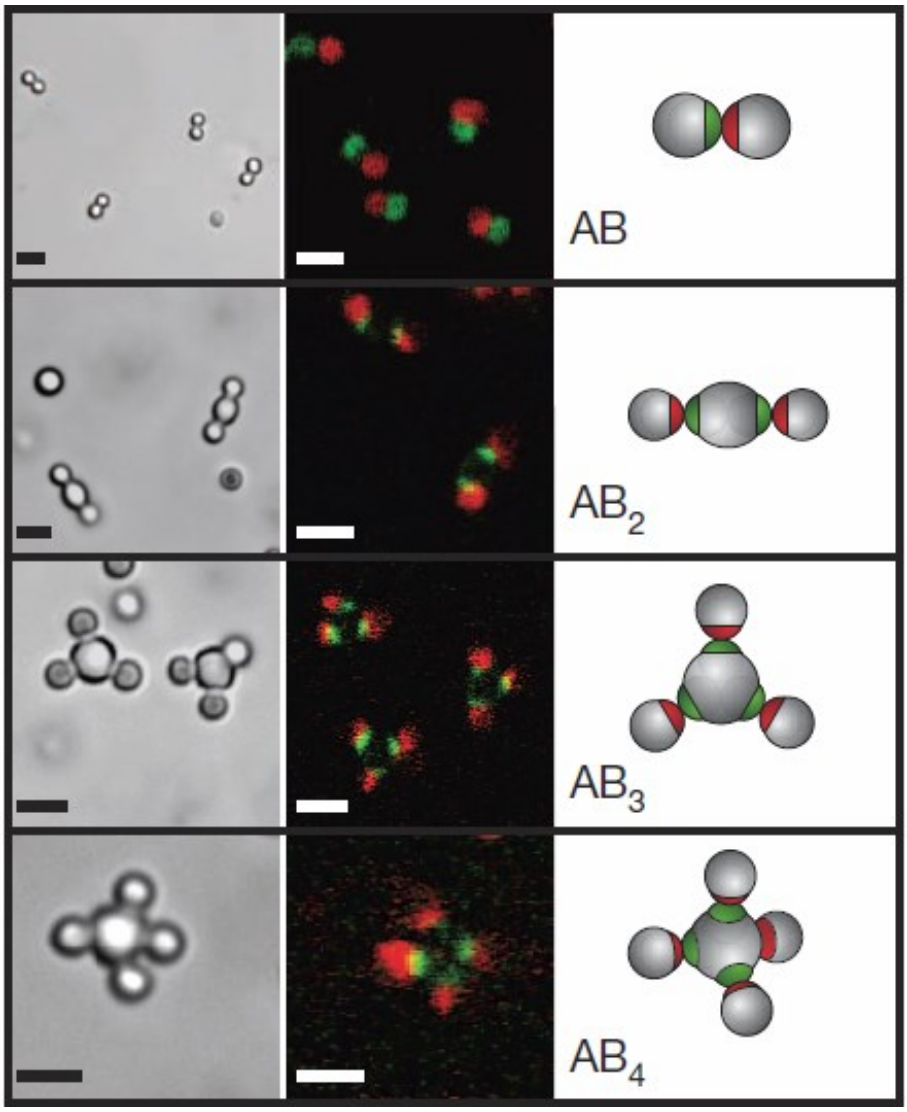

Figure 1-21: (Adopted from Wang, *et al.*, *Nature*, 2012. 491: p. 51) Particles functionalized with various patches. The DNA strands at the green and red patches are complementary to each other.

1.3.4. COLLOIDAL ARCHITECTURE

The advantage of binding specificity of DNA-coated particles is that it enables the synthesis of colloidal clusters with a designed structure. Arkus, Manoharan, and Brenner proposed the possibility of performing colloidal architecture [40, 41]. By carefully designing the interactions between many different particles, when the system reaches thermal equilibrium, particles can self-assemble into the lowest energy state which is the designed structure. Halverson and Tkachenko performed simulations to illustrate mesoscopic architecture [42]. As shown in Figure 1-22, the designed structure is an Empire State Building. The interactions between different color particles are carefully programmed. As a result, when the system reaches thermal equilibrium, particles form the mesoscopic Empire State Buildings as shown in Figure 1-23. Therefore, the self-assembly of DNA-coated particles is highly programmable, and by means of carefully designed particle interactions, one can force particles to self-assemble into a designed structure and realize colloidal architecture.

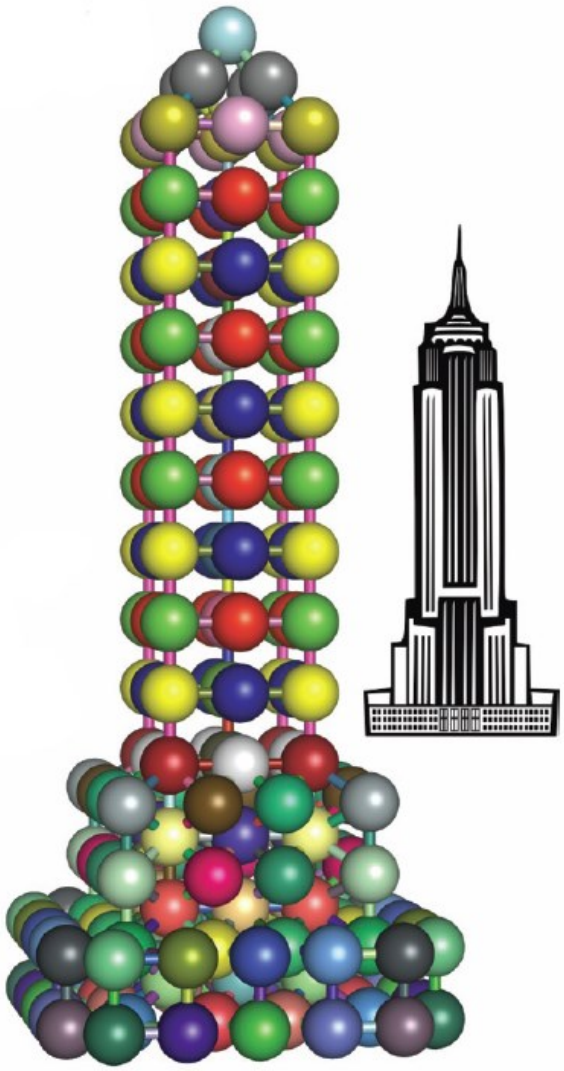

Figure 1-22: (Adopted from Halverson and Tkachenko, *Physical Review E*, 2013. 87: p. 062310) Design of mesoscopic architecture. The design structure is Empire State Building.

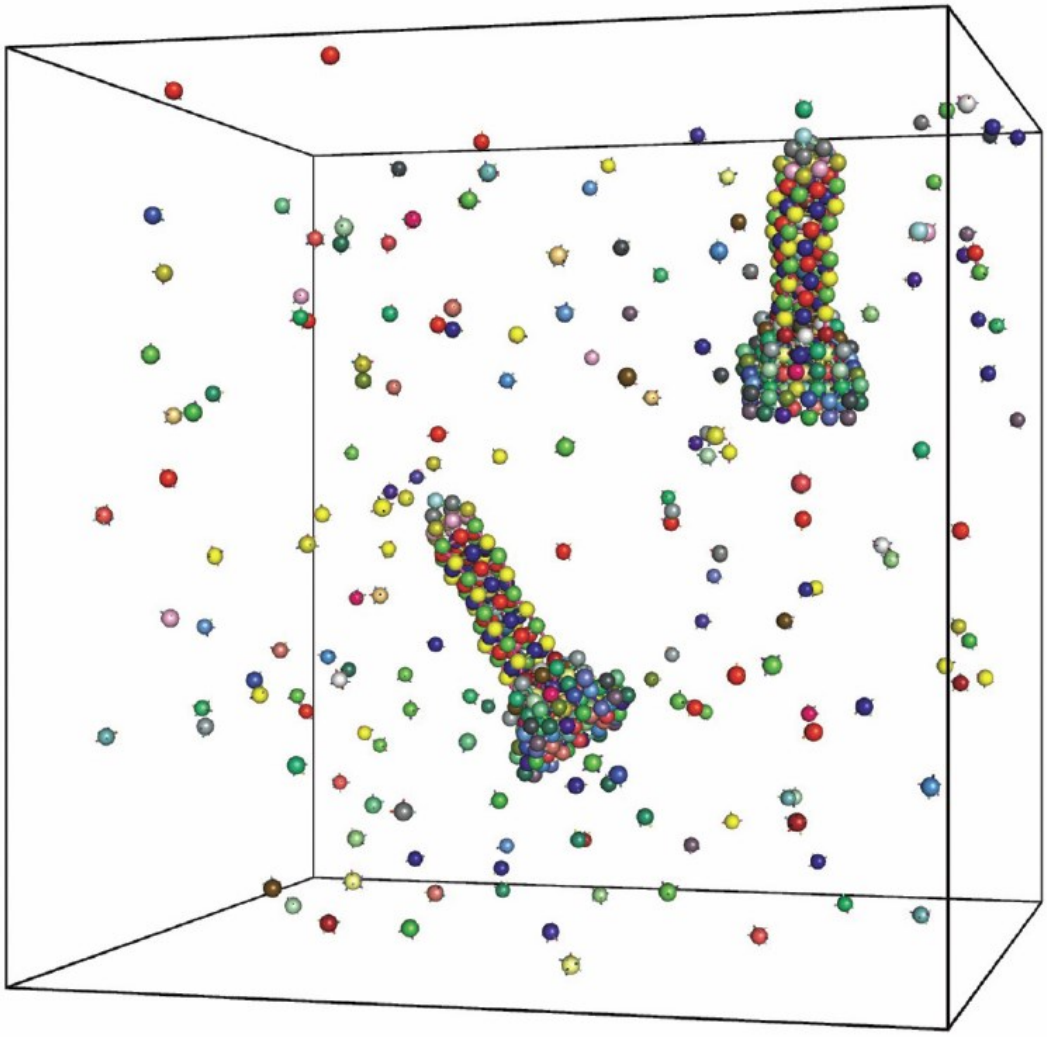

Figure 1-23: (Adopted from Halverson and Tkachenko, *Physical Review E*, 2013. 87: p. 062310) Implementation of mesoscopic architecture.

DNA-coated particles open the door to fruitful, controllable, and programmable self-assembly. Coating carefully designed DNA sequences on many different colloids gives the colloids specific and thermo-reversible interactions. The binding is predictable and versatile. Most importantly, the interactions needed for self-replication as shown in Figure 1-1 are achievable through the use of DNA-coated particles. We will use DNA-coated particles as the tool for implementing colloidal self-replication to fulfill the third requirement of creating the colloidal artificial life.

1.4. THE ROAD TO COLLOIDAL SELF-REPLICATION

To use DNA-coated particles to perform colloidal self-replication, several issues regarding the use of DNA and DNA-coated particles need attention. DNA hybridization is highly specific and thermo-reversible. According to SantaLucia's model, we can predict and control the DNA interaction induced between DNA-coated particles. Ideally, by means of coating DNA on colloids, the interactions needed for self-replication (Figure 1-1) should be straightforward, and therefore, our scheme of colloidal self-replication as shown in Figure 1-2 is doable. However, practically, to create the actual

system proposed in Figure 1-1 and Figure 1-2, we need to face several fundamental problems:

1. **Thermodynamics of self-assembly:** From Figure 1-1, we know that the system has two melting temperatures: T_M and T_m. The mechanism of controlling the melting temperatures of DNA-coated "particles" needs to be understood. More importantly, both interactions need to be independent. Therefore, at each step of self-replication, we can decide which interaction to turn on. For example, in Step (c) in Figure 1-2, we need blue and red particles to bind together. At the same time, we do not wish blue and blue particles or red and red particles to bind and mess up the process. Even though DNA melting behaviors are predictable and well known, the melting behavior of DNA-coated particles can not be straightforwardly predicted from the melting of DNA. Therefore, to ensure that particle binding is well controlled at each step of self-replication, we need to understand the DNA hybridization process between DNA-coated particles. Additionally, whether or not the melting transition of DNA-coated particles is sharp enough that we can independently control each interaction needs to be investigated. In Chapter 2, we will discuss how we can

control the melting temperature and melting transition of DNA-coated particles.

2. **Kinetics of self-assembly:** At Step (c) in Figure 1-2, we turn on the binding between blue and red particles and allow the red particles bind to the seed. However, the question of how much time the seed will need to collect enough red particles is unclear. The process depends on the reaction rate of the binding between blue and red particles. The reaction can be either diffusion- or reaction-limited and should directly depend on the DNA hybridization rates between particles. In Chapter 3, we will discuss how to relate DNA hybridization rate to colloidal aggregation rate. Additionally, we will see how we can control the DNA hybridization rate, and as a result, control how fast DNA-coated particles bind together.
3. **Polygamy:** Figure 1-1 shows that we need each particle to recognize different species at the same time. For example, the blue particle needs to recognize the red and blue particles at the same time. Making particles multi-functional is necessary to fulfill the interaction diagram shown in Figure 1-1. Coating particles with many different DNA strands should give colloids multi-functionality. However, how

to design DNA sequences that can be used for multi-functionalizing colloids is still vague. Additionally, the upper limit of functions of a colloidal particle was not known. In Chapter 4, we will outline the design rules and show that the upper limit of multifunction of a colloidal particle depends on the intrinsic properties of DNA hybridization and sequence combination rather than on the number of DNA strands a colloidal particle can accommodate. We will also demonstrate the application of multifunctional particles by synthesizing dual-phase materials, which behave like gels if quenched and like fluids if cooled slowly.

4. **Mobile bonds:** In Figure 1-2 (d), we turn on the interaction between the same color particles. As a result, the red particles attached to the seed should link together. However, to link these red particles, we need to allow the red particles to be able to roll along the surface of blue particles while they are bound. Therefore, when we turn on the same color interaction, the red particles will reach the lowest energy state and bind together while bound to the seed. However, in our DNA-coated particles such rolling does not occur and therefore the particles are prohibited from self-assembling into the lowest energy

state. In Chapter 5, we will show how we can combine the DNA interaction and depletion to create a more flexible binding while specificity and thermo-reversibility of the binding still remain. To demonstrate the use of such a technique, we created a binary system and controlled the ratio between the two species to synthesize hexagon clusters. This result proves that by carefully controlling the DNA interaction and depletion in the system, we can make DNA-coated particles self-assemble into the desired lowest energy state.

5. **Specific photo-crosslinking:** Figure 1-2 (e) shows that we need to permanently crosslink the same color particles with exposure to ultraviolet light. Then, when we melt all the reversible bonds as shown in Figure 1-2 (f), the system produces an autonomous copy of the seed. In Chapter 6, we will use cinnamate as the crosslinking agent and show how to use cinnamate-modified DNA strands to perform specific photo-crosslinking. Furthermore, we demonstrate a new photolithographic technique. We functionalize a surface with a specific pattern determined by the pattern of ultraviolet light exposure. This result demonstrates that using a cinnamate-modified DNA

strand, we can locally and specifically crosslink the particles we want as needed for implementing our colloidal self-replication scheme.

All the above problems are needed to be understood and solved for implementing colloidal self-replication through DNA-coated particles. In this dissertation, we will show the potential and power of using DNA-coated particles and how we made contributions to each of these problems. As a result, realizing colloidal self-replication is doable. Once we realize colloidal self-replication, along with the ability of making colloids to perform metabolism and mobility, we can synthesize the colloids with the three fundamental requirements of life (metabolism, mobility, and self-replication) and demonstrate the creation of colloidal artificial life.

CHAPTER 2 THERMODYNAMICS

A defining feature of DNA nanotechnology is the ability of DNA single strands to bind selectively only with complementary strands [43-50]. Identical particles coated with identical DNA strands can be joined together by adding to the suspension a linker strand that attaches to the two coatings [38, 51]. Such structures have been used for immunoassays [52], particle aggregation, and formation of crystalline structures, typically FCC [53]. Use has also been made of different particles, A and B, functionalized with complementary DNA strands [32]. This configuration, where A-A and B-B bonds do not occur but A-B bonds do [26, 35, 36], has been exploited to form more complex crystals, such as BCC or CsCl structures [33, 53]. Over the past several years, there has been a great deal of progress in modeling DNA-mediated inter-particle interaction making quantitative comparisons with experiments [21, 26, 27, 34, 37, 54, 55]. In this chapter, I am going to show how we can quantitatively control the melting temperatures and melting behaviors of DNA-coated particles from 10 to 50 ℃ by controlling the DNA coverage on particles. Three particles which can form a closed, trian-

gle structure will have a higher melting temperature than the same particles which can form only open structures.

2.1. PARTICLE AND DNA STRUCTURES

To quantitatively study DNA binding between a pair of colloidal particles coated with complementary DNA strands, we choose 2-μm streptavidin-coated polystyrene particles (Polysciences, Inc., 1.25% polydispersity, batch #: 610816) [21, 22, 25, 27, 28]. The radius of the particles is $R_p \approx 980$ nm. The scanning electron microscopy (SEM) images are shown in Figure 2-1. To grow DNA strands on the surface of particles, a DNA double strand is functionalized with a biotin molecule as shown in Figure 2-2 (Integrated DNA Technologies, Coralville, IA). The 5' end of a DNA single strand, 61-mer long, is connected to the biotin group by a flexible polymer PEG spacer. On the other end, the single strand is terminated by an 11-base "sticky end," S, S', or T, the DNA sequences of which are listed in Table 2-1. A 49-base complementary strand makes a rigid double helix, the length of which is $L \approx 15$ nm, between the PEG spacer and the sticky end. To coat our strep-

tavidin-coated particles with biotinylated DNA strands, we follow the protocol listed below:

1. Incubate particles in the biotinylated DNA solution for 90 minutes in the buffer containing 10 mM phosphate buffered saline (PBS), 50 mM NaCl, 0.15% w/w sodium lauryl sulfate (SDS), and 0.5% w/w pluronic F127. The buffer contains surfactants SDS and F127 to stabilize the particles.
2. After 90 minutes, centrifuge the sample to separate particles and solution, which contains extra unbound DNA strands.
3. Remove the solution and re-suspend particles in the same buffer.
4. Repeat Step 2 to Step 3 at least three times.

Since our particles are coated with streptavidin, which can bind irreversibly below 60 ℃ to biotinylated DNA [56, 57], after following the above protocol, we can successfully synthesize DNA-coated particles stabilized by surfactants SDS and F127 for a long period of time [21, 22, 25].

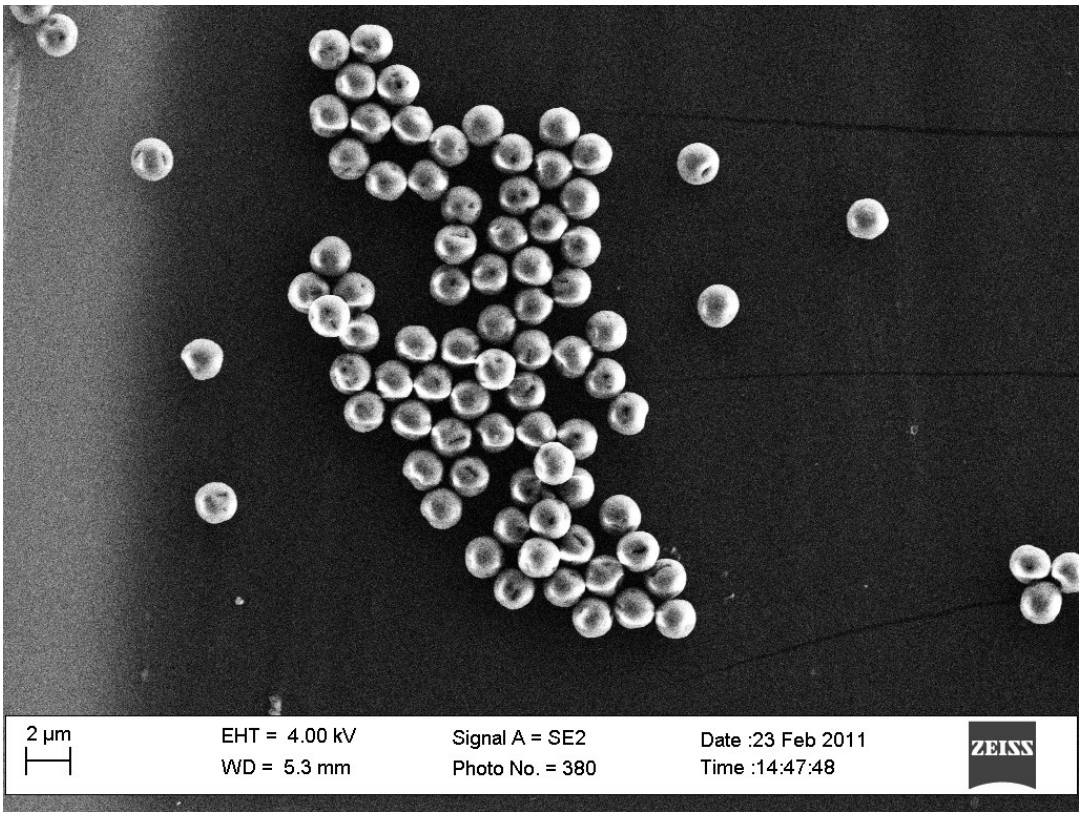

Figure 2-1: A scanning electron microscopy of 2-µm polystyrene microspheres.

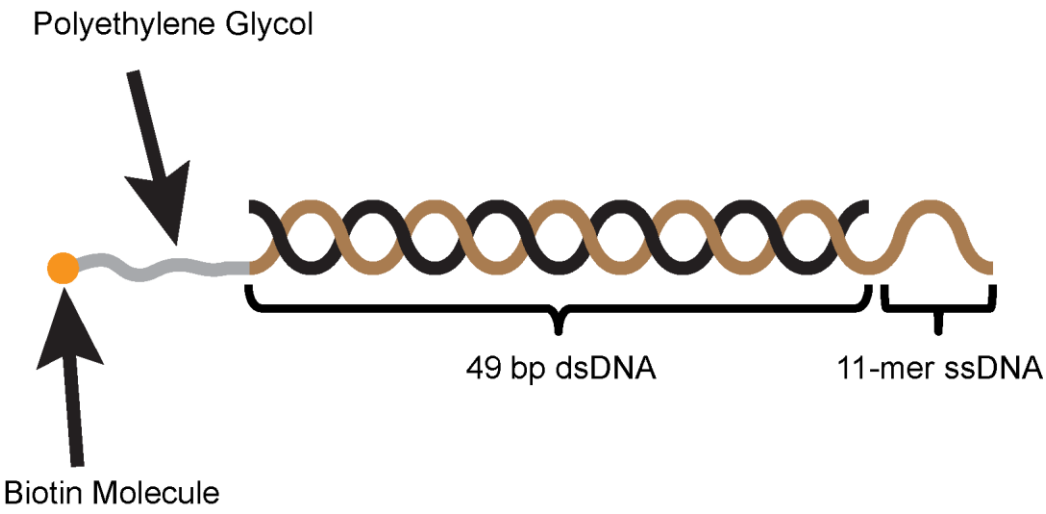

Figure 2-2: Our DNA construct. Our DNA consists of an 11-mer ssDNA as a sticky end, a 49 bp dsDNA as a backbone, a polyethylene glycol as a spacer, and a biotin molecule, which can be bound irreversibly to streptavidin below 60 ℃.

DNA Symbols	Sequences
S	5' – GTA GAA GTA GG – 3'
S′	5' – CCT ACT TCT AC – 3'
T	5' – TTT TTT TTT TT – 3'

Table 2-1: DNA Sequences of our sticky ends.

2.2. DNA COVERAGE MEASUREMENT

To quantify the DNA coating quality of our DNA-coated particles, we measure the surface DNA coverage of our particles. Since our DNA strands are not visible through Scanning Electron Microscopy, we measure the DNA coverage by radioactively labeling our DNA strands with phosphorus 32 [21], the nucleus of which contains 15 protons and 17 neutrons. Phosphorus 32 has a short half-life of 14.29 days and decays into sulfur 32 by β decay as shown in the following nuclear equation:

$$^{32}_{15}P \rightarrow {}^{32}_{16}S^{1+} + e^{-} + \bar{\nu}_e.$$

In our DNA construct, we label the complementary strand at its 5' end by phosphorus 32 as shown in Figure 2-3. The method of labeling DNA is in APPENDIX C. Labeled DNA strands are mixed with unlabeled DNA strands, SCS with a ratio $1{:}\,200$ as shown in Figure 2-4. The overall fractionally labeled DNA strands are called SCS^{*}. Then, we follow the same protocol in Section 2.1 to coat particles with SCS^{*}.

To quantify the amount of β decay, we use a Intertechnique SL30 Scintillation Counter (Figure 2-5) to measure the number of electrons (β rays) radiated from samples. Since the strength of measured β radiation is sensitive to the size and geometry of the samples, the total volume of each sample is controlled to be 5 mL in glass containers with the same shape. A sample of 200 pm fractionally labeled $(1{:}\,200)$ strands SCS^* emits $(89{,}000 \pm 500)$ electrons per minute. A sample of DNA-coated particles emits (805 ± 24) electrons per minute.

To further check that the measured emitted electrons from the sample of DNA-coated particles are actually radiated from labeled DNA strands attached to the surface of particles, we dilute the coated fraction of SCS^* by unlabeled DNA strands TCS, the sticky end of which is replaced by T [see Table 2-1]. Then, similar measurements were made except that the surface fraction of SCS^*, χ, varied from 0.8 to 0.2. The number of electrons per minute emitted from the particle sample based on different χ is listed in Table 2-2. The number of electrons per minute from the particle sample vs. the surface covered fraction of SCS^* is plotted in Figure 2-6. From the linear fit

of our data, we notice that the amount of decay events per minute approaches almost zero as the fraction of SCS^* goes to zero. This result shows that the measured number of electrons from the sample of DNA coated particles mainly came from the labeled DNA strands on the surface of the particles.

To measure how many SCS^* are on each particle, we measure how many electrons radiated from particle sample and compare to the number of electrons radiated from a 200 pm SCS^* sample. Since the slope of the linear fit in Figure 2-6 is (770 ± 36) electrons per minute, the total number of SCS^* in our particle sample can be determined as

$$\frac{x \text{ pm } \mathrm{SCS}^*}{(700 \pm 36) \text{ electrons/min}} = \frac{200 \text{ pm } \mathrm{SCS}^*}{(89{,}000 \pm 500) \text{ electrons/min}}$$

as shown in Figure 2-7. We find that the total number of SCS^* in our particle sample is $x = 1.73 \pm 0.08$ pm. Along with the fact that our particle sample contains $14{,}920{,}000 \pm 746{,}000$ particles, we can determine that each of the particles is coated with

$$N_t \approx 69{,}800 \pm 4{,}800 \tag{2-1}$$

DNA strands. Since the radius of particles is 980 nm, the surface density of DNA coverage is

$$\rho = 5800 \pm 400\ \mu\text{m}^{-2}. \tag{2-2}$$

The spacing between DNA strands is about 13.3 ± 0.5 nm.

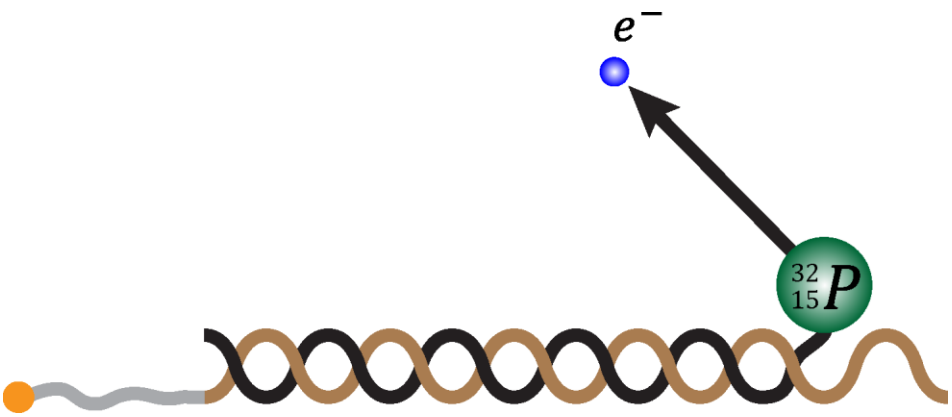

Figure 2-3: Schematic diagram of our labeled DNA strands. The 5' end of the complementary strand is labeled by phosphorus 32, which decays into sulfur and emits an electron.

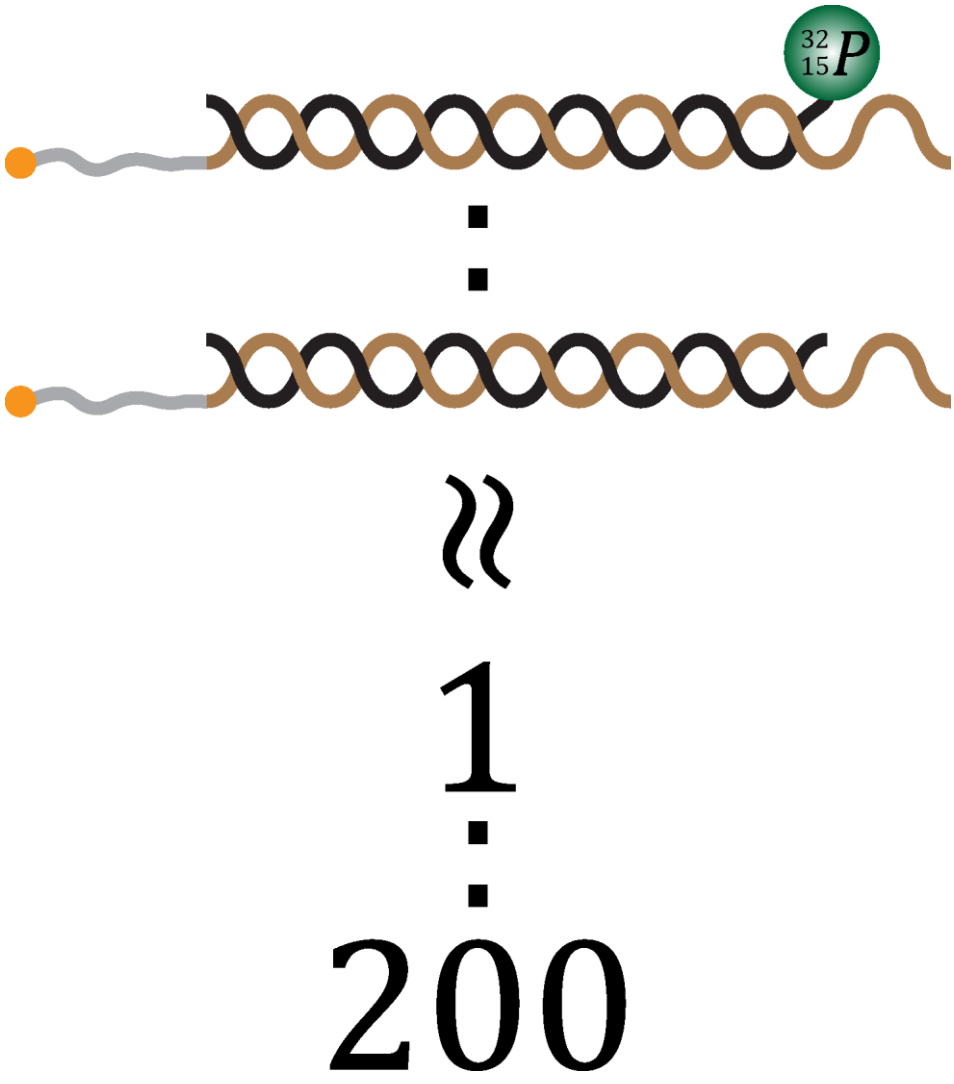

Figure 2-4: Labeled DNA and unlabeled DNA are mixed with a ratio ≈ 1: 200.

Figure 2-5: Intertechnique SL30 scintillation counter.

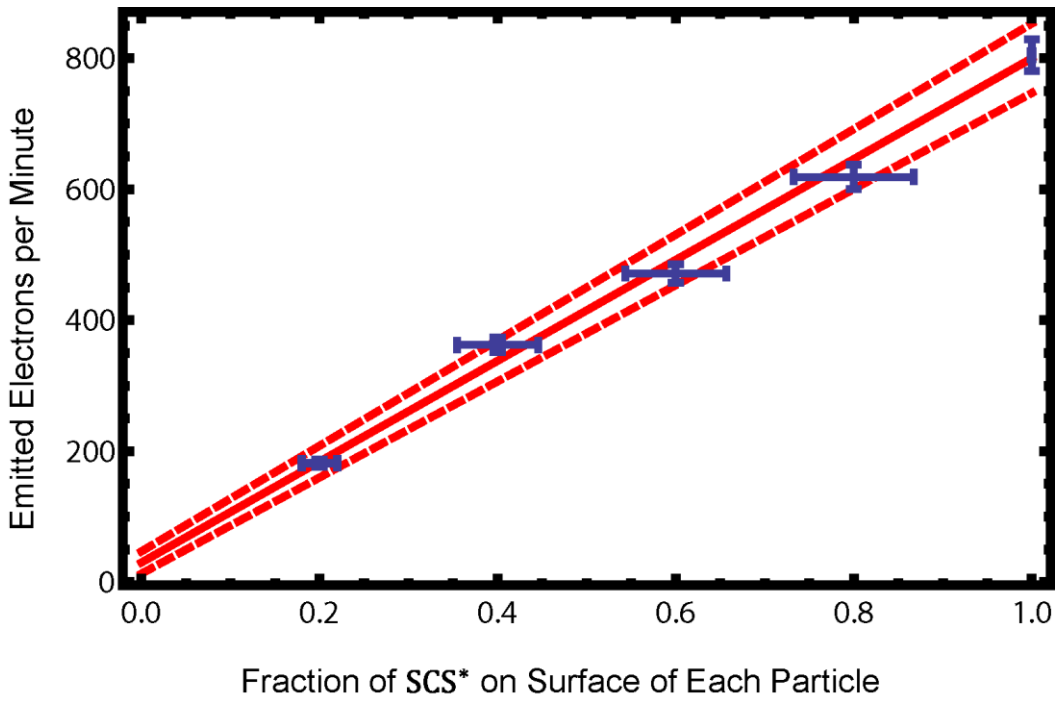

Figure 2-6: Number of emitted electrons per minute vs. fraction of SCS* on surface of each particle. A linear fit is plotted as the red solid line. Dashed red lines are plotted based on fitting errors.

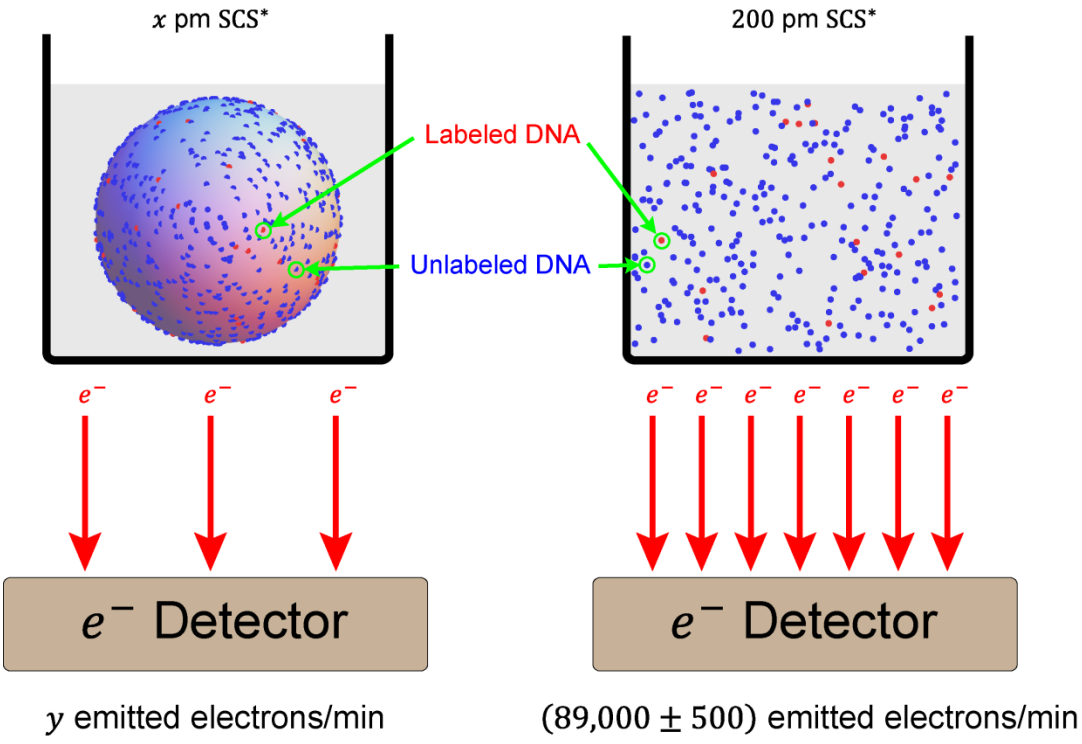

Figure 2-7: Particles coated with fractionally labeled DNA (left) and fractionally labeled DNA in solution (right). The fractions of labeled DNA on surface of particles (left) and in solution (right) are the same.

Surface Fraction of SCS^*, χ	Emitted Electrons per Minute
1	805 ± 24
0.8	619 ± 19
0.6	471 ± 14
0.4	362 ± 11
0.2	182 ± 5

Table 2-2: Data of measured emitted electrons per minute at various surface fractions of SCS^*, χ.

2.3. EXPERIMENT

Many factors change the binding or aggregation of DNA-coated colloids, such as salt concentration, DNA surface coverage, and DNA melting temperature. Here, we choose to study the effect of reducing the DNA coverage.

2.3.1. SYSTEM DESCRIPTION

To study the effect of DNA coverage on the aggregation of DNA-coated particles, we have coated our particles with complementary S and S' strands (Table 2-1) to form a Watson-Crick-like paired system. We mix Watson, coated with S, and Crick, coated with S', homogeneously in equal amounts. To change the coverage of S (S'), at Step 1 in Section 2.1, we incubate particles in the DNA solution with a ratio $\chi \equiv \frac{n_{\mathrm{S(S')}}}{n_{\mathrm{S(S')}}+n_{\mathrm{T}}}$, where $n_{\mathrm{S(S')}}$and n_{T} are the numbers of $\mathrm{S(S')}$ and T in the DNA solution [21, 22, 27]. For example, for synthesizing S-coated particles with $\chi = 0.5$, we incubate particles in the DNA solution with 30 pm S and 30 pm T. In our experiments, we made samples with $\chi = 1, 0.75, 0.5, 0.4, 0.3, 0.2, 0.1, 0.05,$ and 0.025.

2.3.2. TEMPERATURE GRADIENT SETUP

To conveniently study the temperature dependence of the aggregation of DNA-coated particles, we place samples on a temperature gradient stage [21, 22, 27, 28] (Figure 2-8). Our sample is placed on a copper plate, the ends of each of which are connected to a peltier, which is attached to the

microscope stage. The microscope stage is specially made of metal with an internal liquid circulation system through which we flow water from a temperature-controlled water bath. The two ends of the sample are attached to thermal sensors, which are connected to a temperature controller. One peltier is controlled by the temperature controller and the other is connected to a DC power supply. The power supply and the temperature controller are both computer-controlled. We use a proportional-integral-derivative algorithm (PID) [58-60] to control cooling/heating of the left peltier through the DC power supply. The computer monitors temperatures throughout the experiment (Figure 2-9). Typically, the fluctuation in temperatures measured by either the left or the right sensor is about $0.1\ ℃$. In Figure 2-9, the average of the higher (red) and lower (blue) temperatures measured through a 27-day experiment are $(10.1 \pm 0.1)\ ℃$ and $(25 \pm 0.01)\ ℃$, respectively. Using the PID algorithm on one side and the temperature controller on the other, we are able to create a temperature gradient which lasts months and is stable.

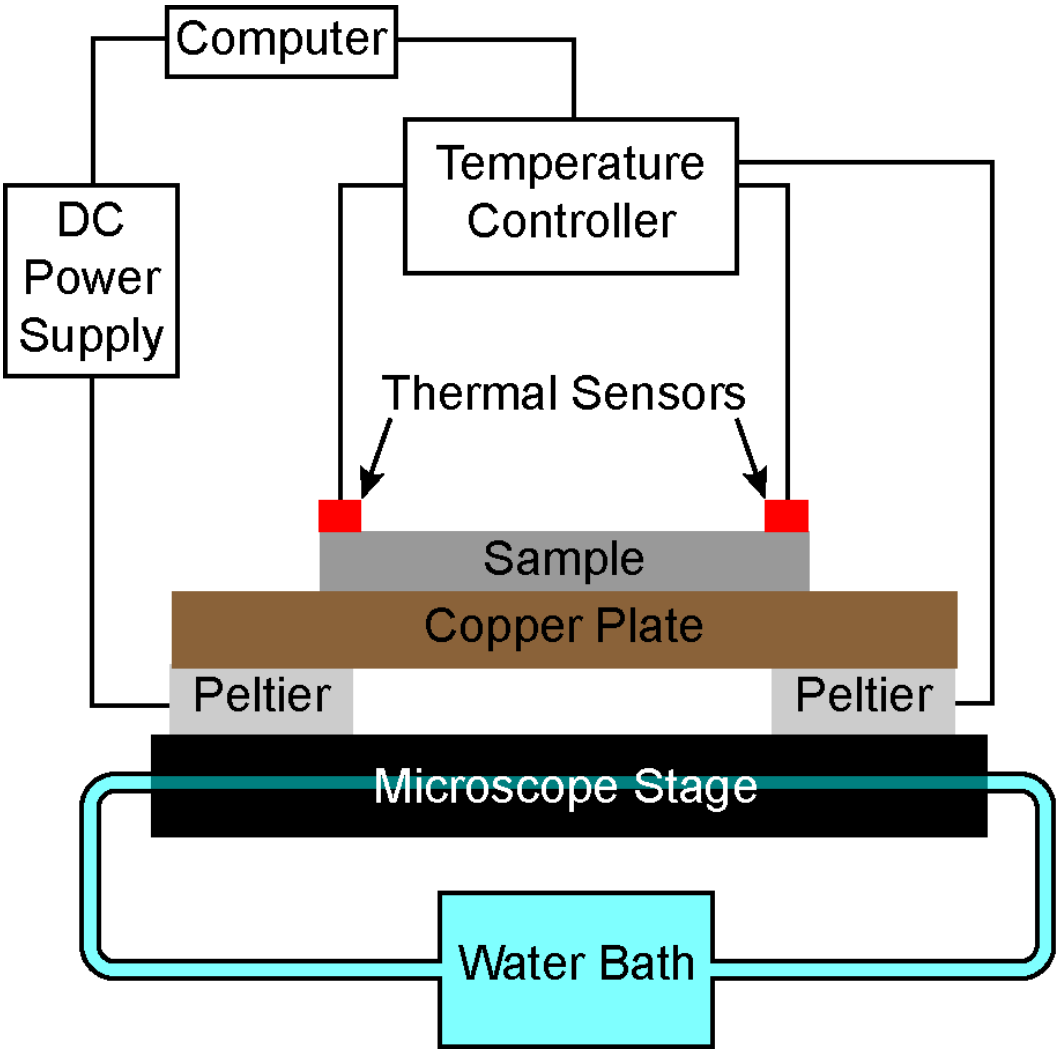

Figure 2-8: A schematic diagram of our temperature gradient set-up.

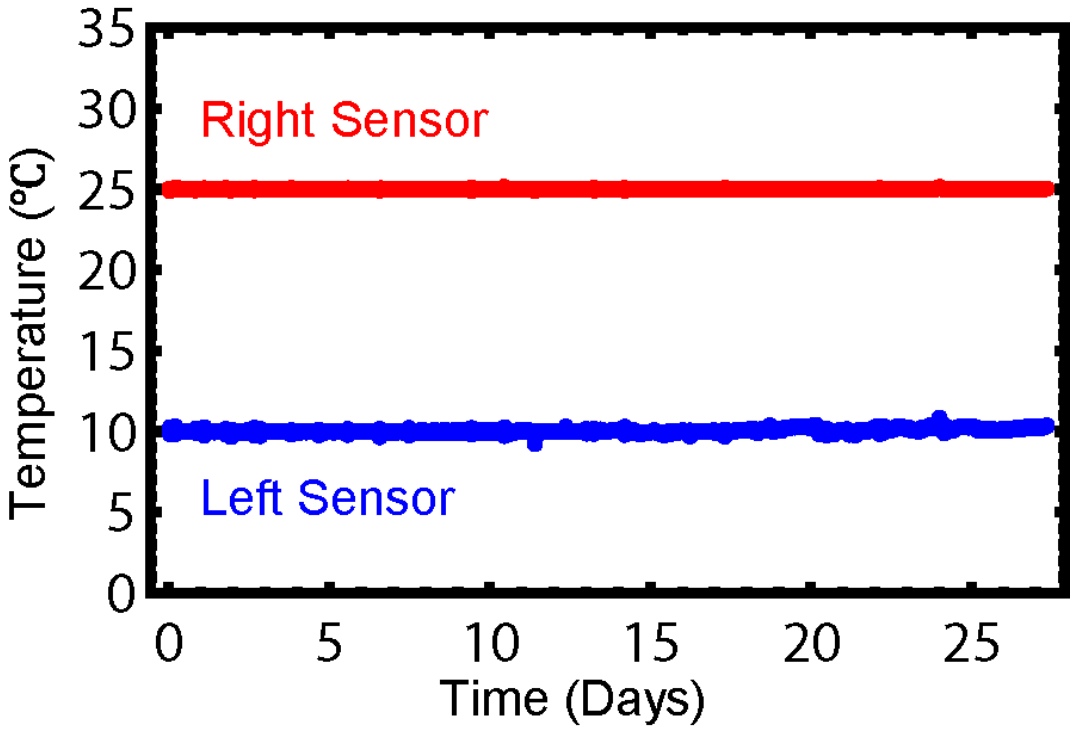

Figure 2-9: Monitored temperature through a 27-day experiment. The upper (red) dots and lower (blue) dots are the temperature measured through the right and left sensors as a function of time, respectively, and their averages over a period of 27 days were $(\mathbf{10.1 \pm 0.1})$ ℃ **and** $(\mathbf{25 \pm 0.01})$ ℃, **respectively.**

2.3.3. SINGLET FRACTION

To quantify the aggregation of DNA-coated particles, we measure the fraction of un-aggregated particles, called singlet fraction f, of the system [12, 21, 22, 25, 27, 28]. In a three-dimensional system, singlet fraction is hard to measure through an optical microscope since it can capture only a two dimensional image, which does not provide sufficient information on the coordinates along the third axis of all particles. Fortunately, our polystyrene particles have a density of $\rho_p = 1.05\ \mathrm{g/cm^3}$. Since their size is $2\mu\mathrm{m}$, the gravitational height of our $2\mu\mathrm{m}$ polystyrene particles is $\frac{k_B T}{mg} = 2.2\ \mu\mathrm{m}$, where $k_B T$ is the thermal energy, $= 9.8\ m/s^2$, the gravitational acceleration, and $m \equiv \left(\rho_p - \rho_w\right)\frac{4}{3}\pi R_p^3$, in which ρ_w is the density of water and R_p, the radius of our particles. Since the gravitational height is about the size of our particle, our system is basically a two-dimensional one. We can easily locate each particle along an x-y plane, identify whether or not a particle is bound, and therefore, determine the fraction of single particle of the system.

To determine the singlet fraction of the system, we identify if an object is a single particle or a cluster by its area observed with an optical microscope image. Although there are many ways, such as particle tracking, to identify if an object is a single particle, identifying a cluster and a single particle by its size is the most efficient and easiest method to measure singlet fractions. Our protocol to measure the singlet fraction of an image is the following.

1. Take an image through an optical microscope (Figure 2-10 (a)).
2. Calculate the areas of each object in the image. Here, an object is defined to be a set of pixels that are connected together.
3. If the area of an object is the area of one single particle, we consider it a single particle and color it red, and if otherwise it is a cluster and color it green. Here, the area of an object is determined by the number of pixels in an object. An example of coloring objects of Figure 2-10 (a) is shown in Figure 2-10 (b).
4. Singlet fraction f of this image can be determined as the total red / (red area + green area).

Practically, we write a C++ program to perform such image analysis. By following the above protocol, we can conveniently measure the fraction of sin-

gle particles we take through an optical microscope and therefore quantify the aggregation of DNA-coated particles.

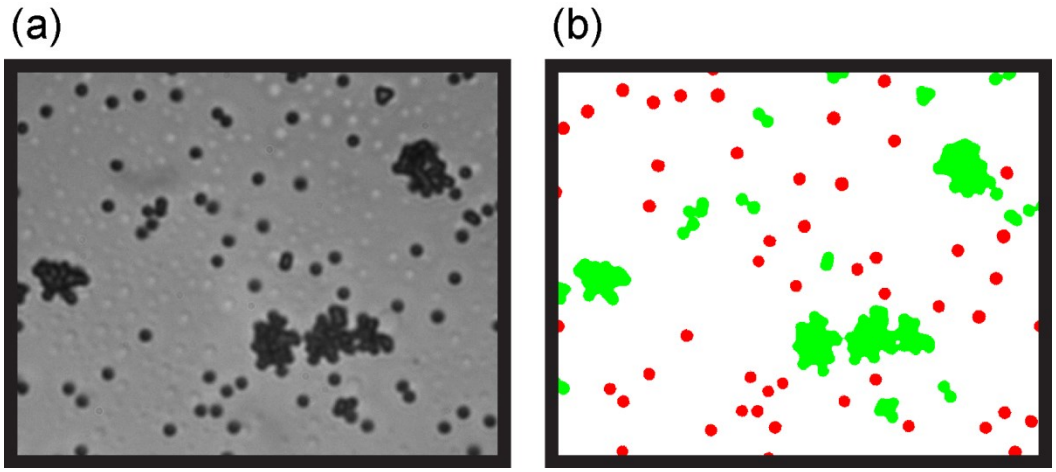

Figure 2-10: Image analysis for singlet fraction measurement. (a) An image taken from an optical microscope. (b) Categorization of single particles and clusters. Single particles are colored red, and clusters green.

2.3.4. MEASUREMENT OF MELTING CURVES

Aggregation of DNA-coated particles depends on temperature because DNA hybridization is temperature dependent. When a pair of particles coat-

ed with complementary DNA strands are close enough and the strands on their surface can reach each other, the DNA strands can hybridize and hold the particles together. A pair of complementary DNA strands hybridizes if the temperature is below and de-hybridizes if it is above the hybridization melting temperature. Similarly, the aggregation behavior of DNA-coated particles also depends on temperature. If the temperature is below the melting temperature, T_m of DNA-coated particles, particles flocculate, otherwise they dissociate.

To analyze how the aggregation of DNA-coated particles depends on temperatures, we measure the singlet fraction f vs. temperature when the sample reaches thermal equilibrium [21, 22, 27, 28]. We place the sample in Section 2.3.1 on the temperature gradient described in Section 2.3.2. The schematic diagram of our experimental set-up is shown in Figure 2-11. The particles aggregate at low temperature (left), ($f = 0$), and not at high temperature end (right), ($f = 1$). At the melting temperature, half of particles aggregate ($f = 0.5$). We measure the singlet fraction, $f(T)$, by measuring at different positions along the temperature gradient after sample equilibration.

We monitor the time evolution of $f(T)$ until it does not change anymore with time. An example of such measurement with $\chi = 0.05$ is shown in Figure 2-12, wherein the singlet fraction did not change with time after 23 hours. This means that the system reaches a thermal equilibrium state after 23 hours. We take $f(T)$ measured after 23 hours as the melting curve of the system. In the same way, we measure the melting curves of our DNA-coated particles in which $\chi = 1, 0.75, 0.5, 0.4, 0.3, 0.2, 0.1, 0.05,$ and 0.025, respectively (Figure 2-13).

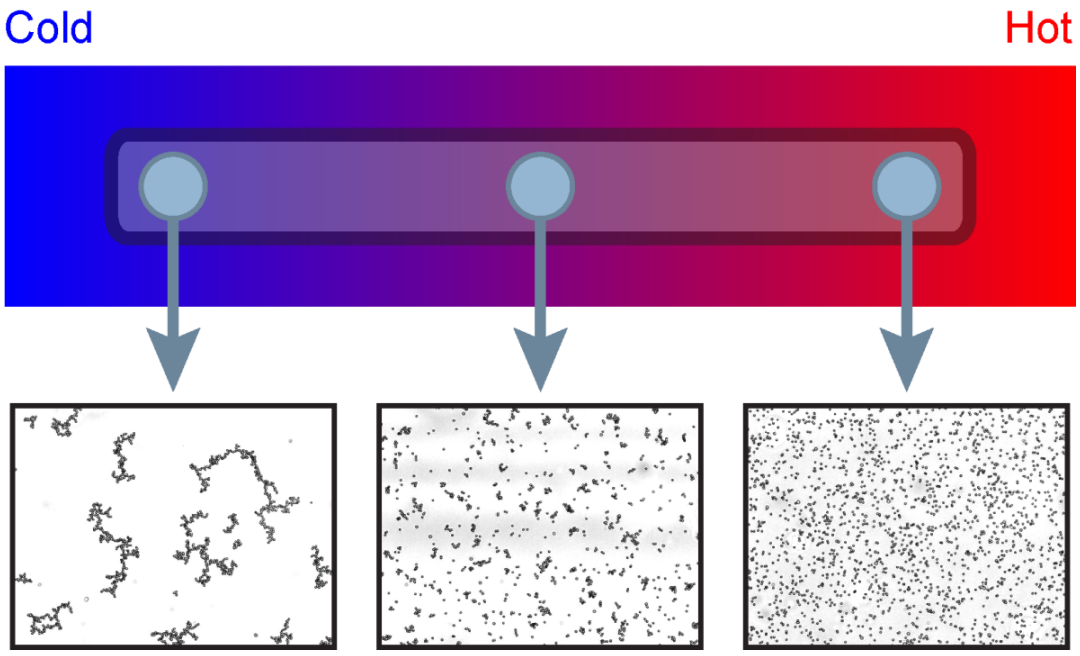

Figure 2-11: A schematic diagram of our experimental set-up. Our sample is placed on a temperature gradient. At cold end (left), particles flocculate, and dissociate at hot end (right). At about melting temperature (middle), half of the particles aggregate.

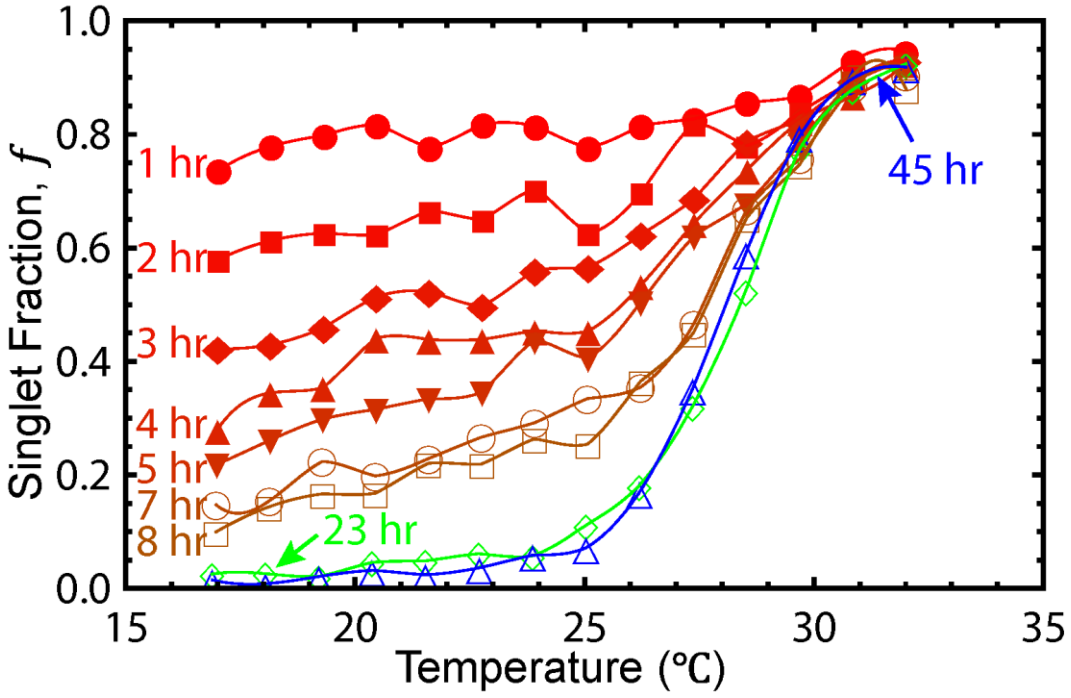

Figure 2-12: Time evolution of singlet fraction vs. temperature, $f(T)$ for $\chi = 0.05$. After 23 hours, $f(T)$ barely changes with time. This means that the system reaches thermal equilibrium, and any $f(T)$ measured after 23 hours is the melting curve of the system.

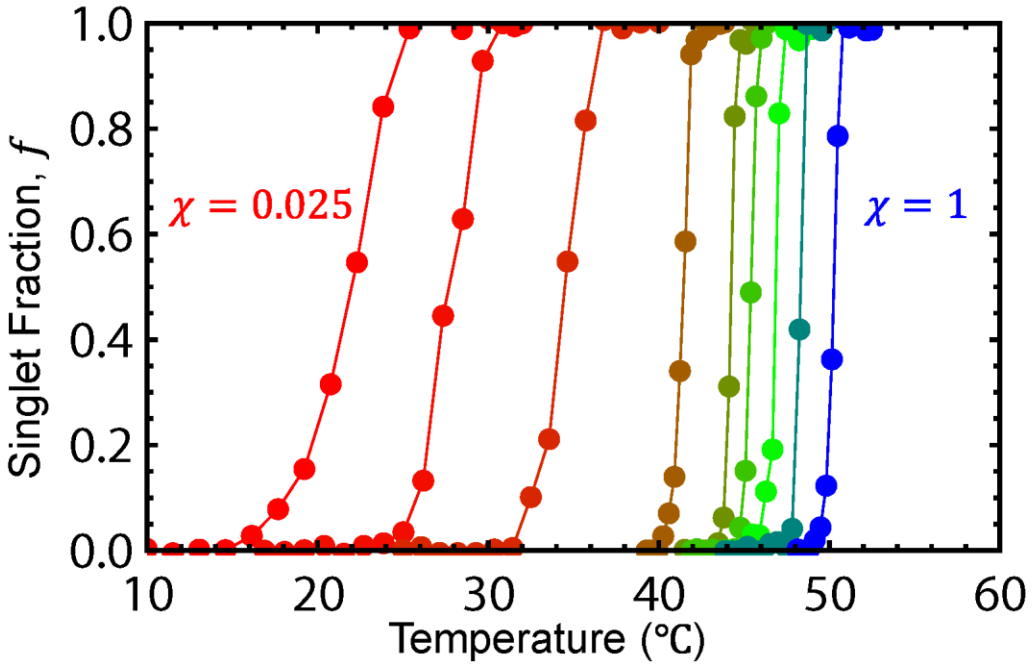

Figure 2-13: Measured melting curves of DNA-coated particles with different DNA coverages, χ. From left (red) to right end (blue), $\chi = 0.025, 0.05, 0.1, 0.2, 0.3, 0.4, 0.5, 0.75,$ and 1.

2.4. MODEL

To quantitatively understand the aggregation of DNA-coated particles, we first study a binding energy, ΔF_p, between a pair of particles as a function of DNA coverage, χ [21, 22, 27].

To describe how particles with a binding energy, ΔF_p, aggregate, we categorize the structures of particle aggregation into closed structures in which three particles can form a triangle, and open structures with no three particle rings with three bonds.

2.4.1. CLOSED STRUCTURES

Closed structures with triangles are found in one-component systems where each particle can stick to every other particle and in three or more component systems in which each species can stick to the other species [27]. To quantify the aggregation in such systems, we first consider the possible clusters shown in Figure 2-14 in which i represents the number of particles in a cluster and α, the number of subclusters with three particle triangles. We now wish to calculate the partition function of the overall system.

For a group of i-particle clusters with α triangles, $O_{i,\alpha}$'s, the partition function $Z_{i,\alpha}$ can be written as

$$Z_{i,\alpha} = \frac{1}{N_{i,\alpha}!}\left[\frac{S}{\Lambda^2} g_{i,\alpha} e^{-\beta \Delta \epsilon_{i,\alpha}}\right]^{N_{i,\alpha}}, \tag{2-3}$$

where $N_{i,\alpha}$ is the number of clusters $O_{i,\alpha}$'s in the system, S, the surface area of the system, and Λ, a unit length that will cancel out in taking ratios [27]. $\Delta\epsilon_{i,\alpha}$ is the energy of a cluster $O_{i,\alpha}$. Consider ΔF_p the binding free energy of a pair of particles. For a cluster with i particles in which no three particles form a triangle ($\alpha = 0$), $\Delta\epsilon_{i,0}$ can be determined as $\Delta\epsilon_{i,0} = (i-1)\Delta F_p$. However, if the cluster has α triangles, each triangle contributes an extra binding free energy, ΔF_p. Hence, $\Delta\epsilon_{i,\alpha}$, the binding free energy of an $O_{i,\alpha}$, can be determined as $\Delta\epsilon_{i,\alpha} = (i-1)\Delta F_p + \alpha\Delta F_p$. $g_{i,\alpha}$ relates the phase space of configurations for a particular cluster which we describe in terms of a wiggling area and wiggling angle:

- **Wiggling area, A_w:** The wiggling area of a particle when bound can be written as $A_w = \left[2\pi\left(2R_p\right)\right]t_r$, where t_r is the wiggling of a particle along the radial direction when bound [27]. In our case, since the construct of our DNA bridges is a 49bp dsDNA + 1 base ssDNA +

11bp dsDNA + 1 base ssDNA + 49bp dsDNA (Figure 2-15), a DNA bridge can expand or shrink with a magnitude of two bases of ssDNA. Since the spacing of bases along a dsDNA is $b \approx 0.34\ \mathrm{nm}$ [14, 15], in our case, the wiggling amplitude along the radial direction is $t_r \approx 2b$. Then, the wiggling area is $A_w = \left[2\pi\left(2R_p\right)\right](2b)$.

- **Wiggling angle, Ω:** The wiggling angle is defined as the angle a particle can wiggle along the surface of another particle when bound [27]. As shown in Figure 2-16 (a), if particle 3 is bound to particle 2 and does not interact with particle 1, the wiggling angle of particle 3 can be written as $\Omega_1 \approx 2\pi(5/6)$. As shown in Figure 2-16 (b), if particle 3 is bound to both particle 1 and particle 2 simultaneously, the wiggling angle of particle 3 is defined as Ω_w. In our system, since the length of DNA sticky end is $l \approx 3.6\ \mathrm{nm}$, $\Omega_w \approx l/R_p$.

Putting together, we can determine that $g_{i,\alpha} = \left(\frac{A_w}{\Lambda^2}\right)^{i-1}\left(\frac{\Omega_w}{\Omega_1}\right)^{\alpha}$. The first term, $\left(\frac{A_w}{\Lambda^2}\right)^{i-1}$, is referred to as the entropy cost when i particles are bound to-

gether without forming triangles. The second term, $\left(\frac{\Omega_w}{\Omega_1}\right)^{\alpha}$, is referred to as the entropy cost when an i-particle cluster form α triangles compared to another i-particle cluster which does not form any triangles. Hence, the physical meaning of $\ln(g_{i,\alpha})$ is the overall entropy cost of a cluster due to inner cluster configurations. Therefore, after considering inner particle structures of an i-particle cluster with α triangles, $O_{i,\alpha}$, we can determine the overall partition function of all the clusters, $O_{i,\alpha}$'s from equation (2-3).

Once we know the partition of the group of clusters, $O_{i,\alpha}$'s, the free energy of the clusters, $\Delta F_{i,\alpha}$, is straightforward and can be determined as

$$\Delta F_{i,\alpha} = -k_B T \ln Z_{i,\alpha} = -k_B T \left\{ -\ln(N_{i,\alpha}!) + N_{i,\alpha} \ln \left[\frac{S}{\Lambda^2} \left(\frac{A_w}{\Lambda^2} \right)^{i-1} \left(\frac{\Omega_w}{\Omega_1} \right)^{\alpha} e^{-\beta \Delta \epsilon_{i,\alpha}} \right] \right\}$$

[21, 22, 27, 61]. Here, we adopt Stirling's approximation: $\ln(n!) \approx n \ln(n) - n$ for $n \gg 1$. Then, $\Delta F_{i,\alpha}$ can be written as:

$$\Delta F_{i,\alpha} = k_B T N_{i,\alpha} \ln N_{i,\alpha} - k_B T N_{i,\alpha}$$
$$- k_B T N_{i,\alpha} \left\{ \ln\left(N_{i,\alpha} \frac{S}{N_{i,\alpha}} \frac{1}{\Lambda^2} \right) + \ln\left[\left(\frac{A_w}{\Lambda^2} \right)^{i-1} \left(\frac{\Omega_w}{\Omega_1} \right)^{\alpha} \right] \right.$$
$$\left. - \frac{1}{k_B T} (i + \alpha - 1) \Delta F_p \right\}.$$

If we define $C_{i,\alpha} \equiv \frac{N_{i,\alpha}}{S}$, the concentration of clusters, $O_{i,\alpha}$, we can rewrite $\Delta F_{i,\alpha}$ as

$$\Delta F_{i,\alpha} = -k_B T N_{i,\alpha} + N_{i,\alpha}(i + \alpha - 1)\Delta F_p + k_B T N_{i,\alpha} \ln\left(C_{i,\alpha} \Lambda^2\right)$$
$$- k_B T N_{i,\alpha} \ln\left[\left(\frac{A_w}{\Lambda^2} \right)^{i-1} \left(\frac{\Omega_w}{\Omega_1} \right)^{\alpha} \right].$$

Then, the chemical potential of the clusters $O_{i,\alpha}$ can be determined as [61]

$$\mu_{i,\alpha} = \frac{\Delta F_{i,\alpha} + N_{i,\alpha} k_B T}{N_{i,\alpha}}$$
$$= (i + \alpha - 1)\Delta F_p + k_B T \ln\left(C_{i,\alpha} \Lambda^2\right) - k_B T \ln\left[\left(\frac{A_w}{\Lambda^2} \right)^{i-1} \left(\frac{\Omega_w}{\Omega_1} \right)^{\alpha} \right]. \quad (2\text{-}4)$$

When the system reaches thermal equilibrium,

$$\begin{cases} O_{1,0} + O_{i,0} \rightleftharpoons O_{i+1,0} \\ O_{i,\alpha} \rightleftharpoons O_{i,\alpha'} \end{cases}$$

or equivalently,

$$\begin{cases} \mu_{1,0} + \mu_{i,0} = \mu_{i+1,0} \\ \mu_{i,\alpha} = \mu_{i,\alpha'} \end{cases} \tag{2-5}$$

[21, 22, 27]. Introducing equation (2-4) into equation (2-5), after some algebra, we get that

$$\begin{cases} \dfrac{C_{i+1,0}}{C_1 C_{i,0}} = A_w e^{-\beta \Delta F_p} \equiv K \\ \\ \dfrac{C_{i,\alpha}}{C_{i,\alpha'}} = \gamma^{\alpha-\alpha'} e^{-(\alpha-\alpha')\beta\Delta F_p} \equiv \Gamma^{\alpha-\alpha'} \end{cases},$$

where $C_1 \equiv C_{i,0}$, $\gamma \equiv \frac{\Omega_w}{\Omega_1}$, $K \equiv A_w e^{-\beta \Delta F_p}$, and $\Gamma \equiv \gamma e^{-\beta \Delta F_p}$. Then, $C_{i,\alpha}$ can be written in terms of C_1 as

$$C_{i,\alpha} = \Gamma^{\alpha} C_{i,0} = \Gamma^{\alpha} K^{i-1} C_1. \tag{2-6}$$

Define C_p as the total particle density. According to the conservation of total number of particles, we have that

$$C_p = \sum_{i=1}^{\infty} \sum_{\alpha=0}^{i-2} i \, C_{i,\alpha} = C_1 - \frac{C_1^2 K [C_1 K(\Gamma + 1) - 2]}{(C_1 K - 1)^2 (C_1 K \Gamma - 1)^2} \tag{2-7}$$

Note that the upper limit of α is $(i-2)$ because an i-particle cluster can only have up to $(i-2)$ sub-clusters with three particles touching each other. Since singlet fraction $f \equiv C_1/C_p$, equation (2-7) can be rewritten as

$$\frac{1}{f} = 1 - \frac{C_p f K\left[C_p f K(\Gamma+1) - 2\right]}{\left(C_p f K - 1\right)^2 \left(C_p f K \Gamma - 1\right)^2}. \tag{2-8}$$

Unfortunately, equation (2-8) does not have an analytic solution for f, but we can solve equation (2-8) numerically and find the singlet fraction f. Hence, for systems with closed structures, we can quantify the aggregation behaviors of particles by numerically solving the singlet fraction f in equation (2-8).

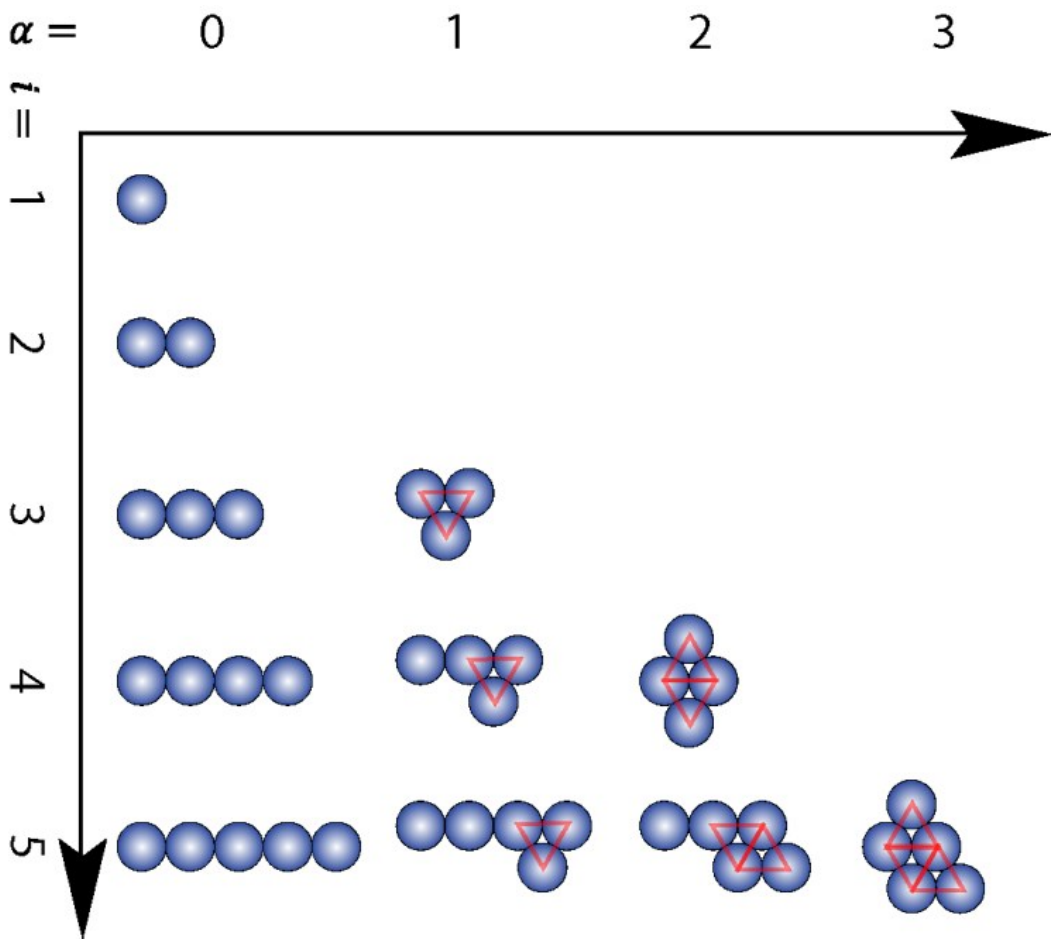

Figure 2-14: Cluster identification in terms of size or number of particles, i, and the number of subclusters with triangles (three particles bound to each other), α.

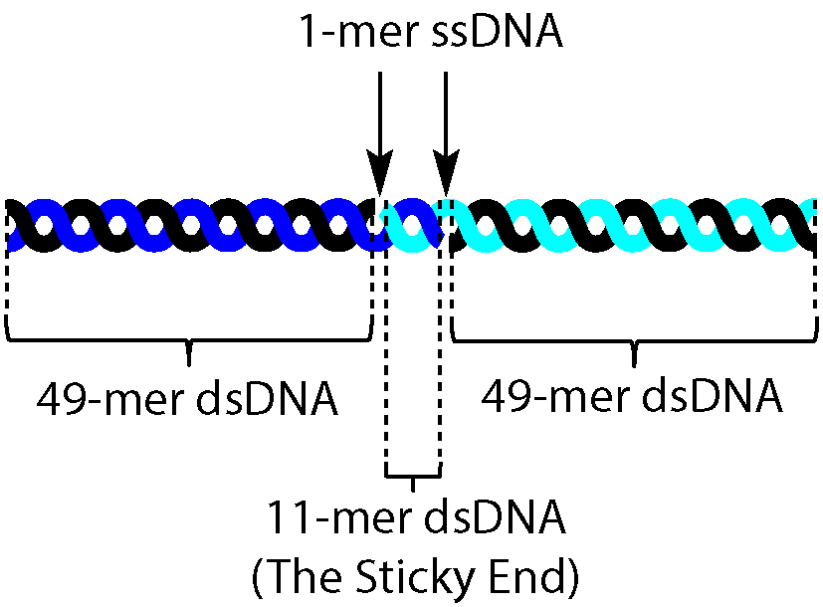

Figure 2-15: The construct of a DNA link in our system.

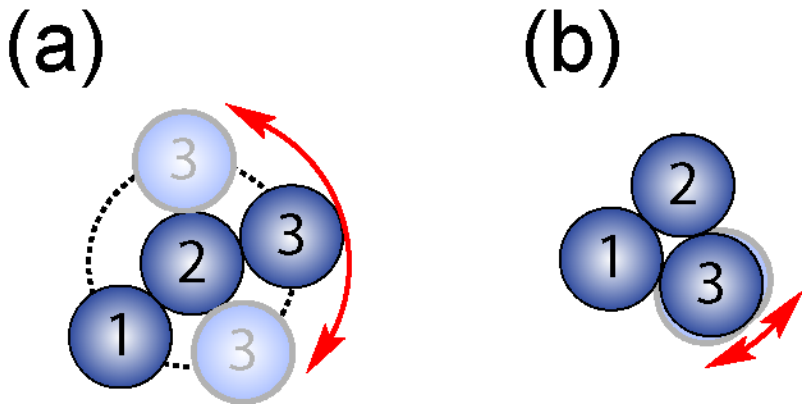

Figure 2-16: Wiggling angle of a particle bound to (a) only one particle, and (b) two particles simultaneously.

2.4.2. OPEN STRUCTURES

Open structures are typically found in a Watson–Crick-like system, in which two species, A and B, can bind to each other but A+A or B+B do not bind [21, 22, 27]. In such a system, three particles can not form a closed triangle structure.

To quantify the aggregation behavior of such a system, we follow the derivation in Section 2.4.1 except $\alpha = 0$ since no triangles can be formed in the system of open structures. Therefore, equation (2-6) can be reduced to

$$C_i \equiv C_{i,0} = K^{i-1} C_1$$

and equation (2-7) to

$$C_p = \sum_{i=1}^{\infty} i\, C_i = \frac{C_1}{(KC_1 - 1)^2}.$$

Similarly, we have

$$f = \left(KC_p f - 1\right)^2.$$

Then, we can analytically solve for the singlet fraction f as

$$f = \frac{1 + 2KC_p - \sqrt{1 + 4KC_p}}{2K^2C_p^2} \tag{2-9}$$

[21, 22, 27]. From equation (2-9), we can quantify the aggregation behaviors of the system of open structures.

2.4.3. BINDING FREE ENERGY OF A PAIR OF COMPLMENTARY DNA-COATED PARTICLES, ΔF_p

In equation (2-8) or (2-9), we can solve the singlet fraction based on the value of K and C_p. C_p is a measurable quantity. $K \equiv A_w e^{-\beta \Delta F_p}$ can be determined only if the binding free energy ΔF_p is determined. Hence, in this section, we will calculate the binding free energy ΔF_p for a pair of particles coated with complementary DNA strands.

To calculate ΔF_p, we must consider the hybridization free energy for a pair of complementary sticky-end DNA strands between a pair of particles as shown in Figure 2-17. In Figure 2-2, the construct of our DNA strands is an

ssDNA (sticky end), a dsDNA (backbone), a PEG, and a biotin molecule. Biotin is bound to streptavidin coated on the surface of a particle (Figure 2-17). Since PEG is floppy, and dsDNA backbone is rigid, we expect the ssDNA sticky end to perform free rotational diffusion along the surface of a hemisphere as shown in Figure 2-17. When a pair of such complementary DNA sticky end hybridizes in solution, the binding free energy, $\Delta F°$, is well known [17, 62-66]: $\Delta F° = \Delta H° - T\Delta S°$, where $\Delta H°$ is the enthalpy due to hydrogen bonds of DNA bases and their hydrophobic interactions, and $\Delta S°$, the entropy loss in going from flexible to rigid dsDNA as shown in Figure 2-18 (a). However, when DNA strands are attached to the surface of a particle, before they hybridize, each of them can explore the surface of a hemisphere as shown in Figure 2-18 (b). However, after they hybridize, they are restricted to diffuse in a ring. Therefore, such change in configurational space must be taken into account. Define ΔS_p as the extra configurational entropy cost. The hybridization free energy for a pair of complementary particles each of which is attached to the surface of a particle can be written as:

$$\Delta F° = \Delta H° - T\left(\Delta S° + \Delta S_p\right). \tag{2-10}$$

To quantify the binding free energy for a pair of complementary particles due to inter-particle DNA hybridization, $\Delta F_{p,DNA}$, we quantify the statistics of DNA hybridization between a pair of particles as shown in Figure 2-17 by calculating the overall partition function, Z_s. Generally, a partition function of a system can be written as:

$$Z_s = \sum_i e^{-\beta \epsilon_i}, \tag{2-11}$$

where ϵ_i is the energy state i [61]. In our case, we treat the partition function in a mean-field approximation [21, 22, 27]. First, we consider the partition function of just one DNA strand $Z_{s,1}$, such as the left cyan DNA in Figure 2-17. Such DNA strand can have three DNA energy states: 1) Unbound, in which $\epsilon_1 = 0$, 2) Bound to the left blue DNA strand, in which $\epsilon_2 = \Delta F°$, and 3) Bound to the right blue DNA strand, in which $\epsilon_3 = \Delta F°$. Therefore, from equation (2-11), the partition function of the cyan DNA strand can be written as:

$$Z_{S,1} = e^{-\beta \epsilon_1} + e^{-\beta \epsilon_2} + e^{-\beta \epsilon_3} = 1 + 2e^{-\beta \Delta F°}$$

or more generally,

$$Z_{S,1} = 1 + g_b e^{-\beta \Delta F^\circ}, \tag{2-12}$$

where g_b is the number of sticky ends on one particle that an opposing sticky end can reach. For the cyan DNA strand, $g_b = 2$. From the single DNA strand partition function, equation (2-12), within the mean-field approximation (uncorrelated bonds), the partition function for the total DNA strands between a pair of complementary particles is

$$Z_S \approx \left(Z_{s,1}\right)^{N_b} = \left(1 + g_b e^{-\beta \Delta F^\circ}\right)^{N_b}, \tag{2-13}$$

where N_b is the number of DNA strands that have the potential to form inter-particle DNA bonds. After knowing the overall partition function, the binding free energy of a pair of complementary particles due to the inter-particle DNA hybridization can be determined as:

$$\begin{aligned} \Delta F_{p,DNA} &= -k_B T \ln(Z_s - 1) \\ &\approx -k_b T \ln\left[\left(1 + g_b e^{-\beta \Delta F^\circ}\right)^{N_b} - 1\right]. \end{aligned} \tag{2-14}$$

In addition to the binding free energy due to the inter-particle DNA hybridization, we also need to determine the contribution of entropy loss if the particle surface is not fully covered by DNA strands [27]. The extra entropic cost will be significant when DNA coverage of particle is low. Consider a

pair of complementary particles, the surface of each of which is only partially coated with DNA strands. Before they are bound, the allowed orientation of each particle is 4π, and after they are bound together, it is Ω. Define ΔS_r as the entropic cost due to the loss of orientation. $\Delta S_r = k_B \ln \frac{\Omega}{4\pi}$. The rotational entropy cost contributes

$$\Delta F_{p,r} = -T\Delta S_r \tag{2-15}$$

to the binding free energy of a pair of complementary particles.

Combining equations (2-14) and (2-15), the overall binding free energy for a pair of complementary particles can be determined as

$$\begin{aligned} \Delta F_p &= \Delta F_{p,DNA} + \Delta F_{p,r} \\ &\approx -k_b T \ln\left[\left(1 + g_b e^{-\beta \Delta F^\circ}\right)^{N_b} - 1\right] - T\Delta S_r. \end{aligned} \tag{2-16}$$

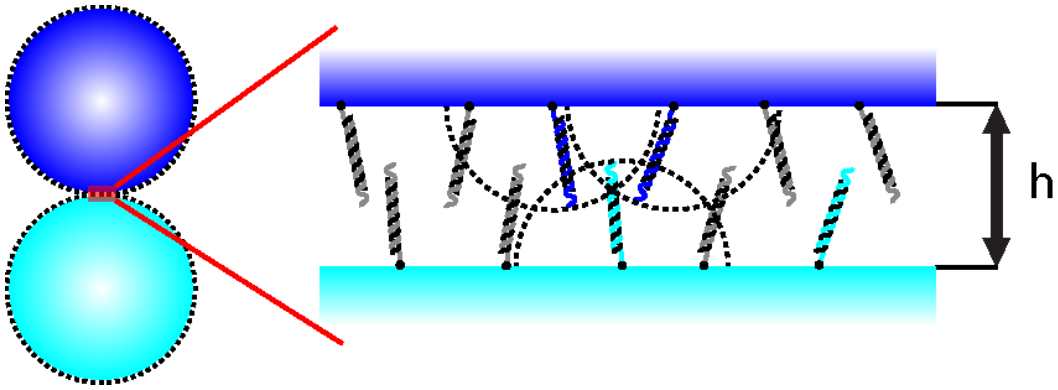

Figure 2-17: Blow-up of binding region between two DNA-coated colloidal particles. We can change coverage with active and neutral DNA strands. Here, blue and cyan sticky ends are complementary to each other and are active, whereas the gray strands are neutral DNA and are inactive.

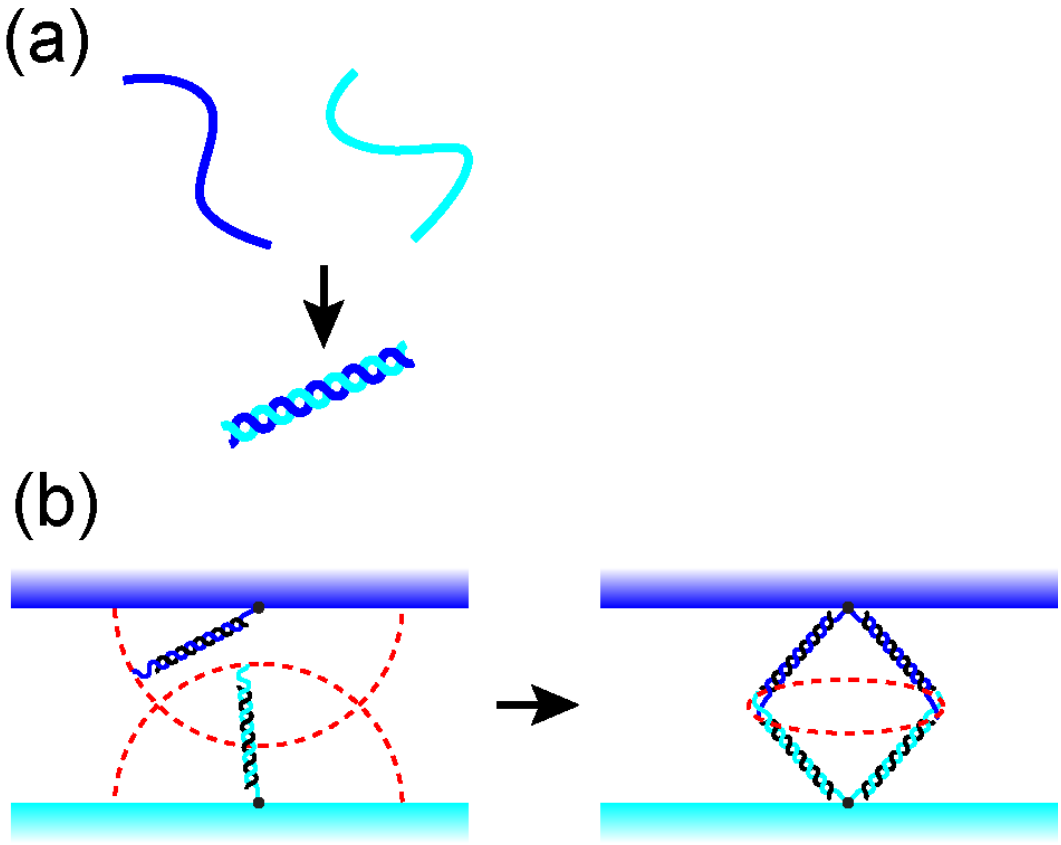

Figure 2-18: DNA entropy losses from hybridization. (a) Entropy loss in going from two flexible single strands to one rigid double strand. (b) dsDNA with one end freely joined on a surface entropy can have a hemisphere of configurations. When bound, the configurations are reduced to a ring.

2.4.4. CONFIGURATIONAL ENTROPY, ΔS_p

The configurational entropy ΔS_p needs to be determined for calculating the hybridization energy $\Delta F°$ in equation (2-10) and the binding free energy ΔF_p in equation (2-16). As shown in Figure 2-18 (a), in solution, the hybridization of DNA is governed by: 1) hydrogen bonds, 2) the hydrophobic effect of bases, and 3) the loss of configurational entropy in two flexible DNA single strands joining to form a rigid DNA double strand. The first two terms result in the enthalpy change $\Delta H°$, and the last term in $\Delta S°$. In addition, when the DNA strands are attached to a particle surface, the entropic cost of DNA hybridization involves a configurational entropy penalty as shown in Figure 2-18 (b) [21, 22, 27]. Each dsDNA strand freely linked to a surface explores a hemisphere of area $2\pi(L + l/2)^2$, where L is the length of the dsDNA backbone, and l, the length of the sticky end. The entropy before hybridization can be determined as $S_{p,i} = 2k_B \ln\left[\frac{2\pi(L+l/2)^2}{\Lambda^2}\right]$, where Λ is the unit length, and k_B, is Boltzmann's constant. However, once the sticky ends are hybridized, the configurational freedom is reduced to a ring, which has a circumference of $2\pi\sqrt{(L + l/2)^2 - (h/2)^2}$, where h is the surface separation of the pair of particles. Then, the entropy after hybridization can be deter-

mined as $S_{p,f} = k_B \ln\left(\frac{2\pi\sqrt{(L+l/2)^2-(h/2)^2}}{\Lambda}\right)$. Therefore, the overall configurational entropy cost can be determined as

$$\Delta S_p = S_{p,f} - S_{p,i} = k_B \ln\left\{\frac{2\pi\sqrt{\left(L+\frac{l}{2}\right)^2-\left(\frac{h}{2}\right)^2}}{C^\circ\left[2\pi\left(L+\frac{l}{2}\right)^2\right]^2}\right\}, \tag{2-17}$$

where $C^\circ \equiv 1/\Lambda^3 = 1\,\mathrm{M}$. In our case, $L \approx 15\,\mathrm{nm}$, $l \approx 3.6\,\mathrm{nm}$, and $h \approx L + l/2 \approx 16.8\,\mathrm{nm}$, so $\Delta S_p \approx -10k_B$.

2.4.5. ROTATIONAL ENTROPY, ΔS_r

To determine the binding free energy ΔF_p in equation (2-16), the rotational entropy ΔS_r must also be determined. Consider a pair of spherical particles fully covered by active DNA strands as shown in Figure 2-19 (a). The binding can happen in any orientation. However, for a pair of particles only partially covered by active DNA strands as shown in Figure 2-19 (b), the binding is limited to a certain orientation between particles [27]. An active patch on each particle has to face another on another particle to allow binding. The ratio of orientations that allow binding compared with all orientations determines the rotational entropy cost ΔS_r.

To calculate the rotational entropy cost of a pair of particles each of which has only one DNA strand, as shown in Figure 2-19 (c), we calculate the orientation change before and after bonding [27]. As shown in Figure 2-19 (c), each particle has only one DNA strand and is held together with a surface separation h as shown in Figure 2-19 (c). For this pair of particles, before bonding, each particle can have any orientation, a solid angle of 4π. The entropy before bonding is $S_{r,i} = 2k_B \ln\left(\frac{4\pi}{\Omega}\right)$, where Ω is the unit angle. After bonding, the orientation of these particles allowed relatively is $4\pi\left(A_{DNA}/A_{surface}\right)$, where $A_{DNA} \approx \pi[(L + l/2)^2 - (h/2)^2]$ is the "active" area for a single DNA on the surface of the dashed virtual sphere shown in Figure 2-19 (c), and $A_{surface} = 4\pi\left(R_p + h/2\right)^2$ is the surface area of the dashed virtual sphere. Then, we can determine that the entropy after bonding is $S_{r,f,1} = 2k_B \ln\left(4\pi \frac{A_{DNA}}{A_{surface}}/\Omega\right)$. Therefore, the rotational entropy cost of a pair of particles each of which has only one DNA strand is $S_{r,f,1} - S_{r,i} = 2k_B \ln\left(\frac{A_{DNA}}{A_{surface}}\right)$.

To calculate the rotational entropy cost of a pair of particles each of which has N_{tot} DNA strands randomly distributed on the surface, we follow a similar calculation. We calculate the fraction of area covered by the active patches associated with DNA strands, ϕ. The fraction of area not covered by one DNA strand is $1 - A_{DNA}/A_{surface}$. The average fraction of area not covered by N_{tot} DNA strands is $\left(1 - A_{DNA}/A_{surface}\right)^{N_{tot}}$. Therefore, the fraction of area covered by N_{tot} DNA strands can be written as

$$\phi \approx 1 - \left(1 - \frac{A_{DNA}}{A_{surface}}\right)^{N_{tot}},$$

which means that the allowed orientation is $4\pi\phi = 4\pi\left[1 - \left(1 - \frac{A_{DNA}}{A_{surface}}\right)^{N_{tot}}\right]$. We can determine the entropy after bonding. It is $S_{r,f} = 2k_B \ln\left\{\frac{4\pi}{\Omega}\left[1 - \left(1 - \frac{A_{DNA}}{A_{surface}}\right)^{N_{tot}}\right]\right\}$. Therefore, we can determine the rotational entropy cost of a pair of particles each of which has N_{tot} DNA strands randomly distributed on the surface as

$$\Delta S_r = S_{r,f} - S_{r,i}$$

$$= 2k_B \ln\left[1 - \left(1 - \frac{\pi\left[\left(L + \frac{l}{2}\right)^2 - \left(\frac{h}{2}\right)^2\right]}{4\pi\left(R_p + \frac{h}{2}\right)^2}\right)^{N_{tot}}\right]. \quad \text{(2-18)}$$

In our case, from Section 2.2 and equation (2-1), we know that a fully covered particle has $N_t = 69{,}800 \pm 4{,}800$ DNA strands. For a particle with a surface coverage χ, $N_{tot} = N_t\chi$.

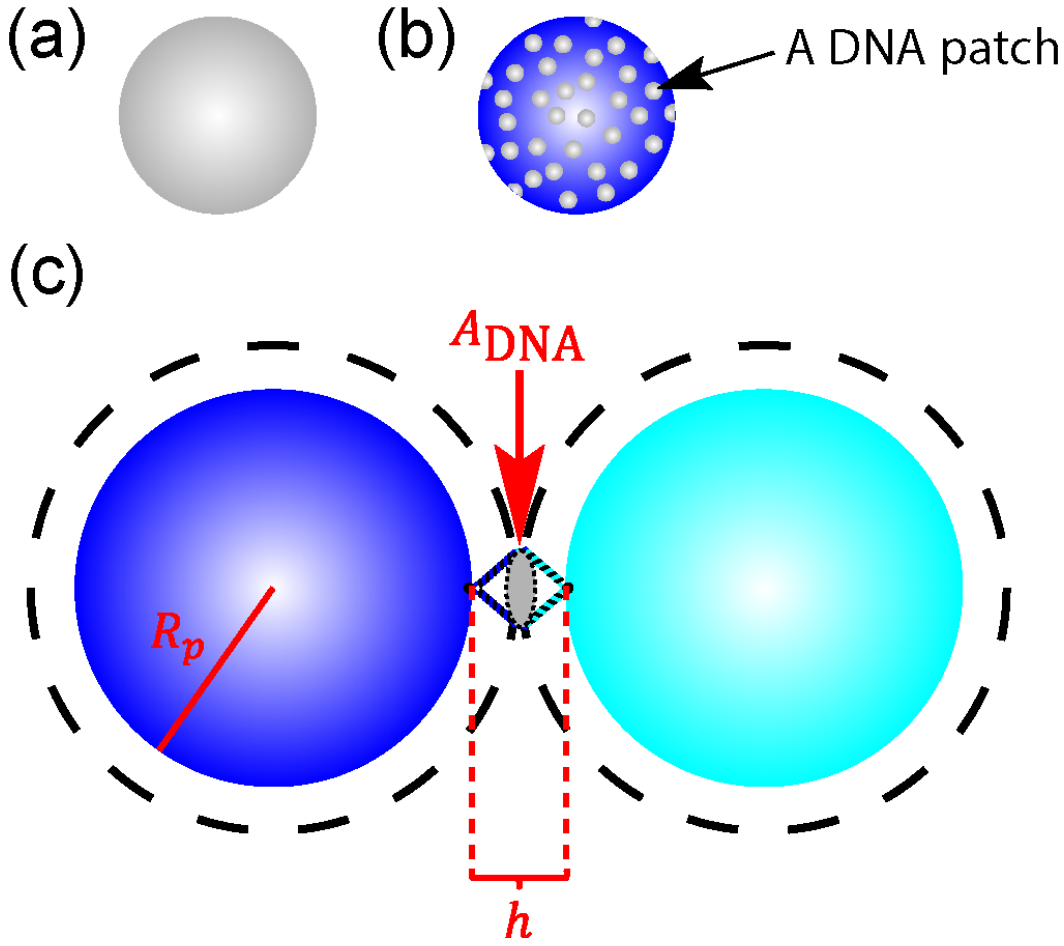

Figure 2-19: Rotational entropy of spherical particles. (a) Particle fully covered by DNA. (b) Particle partially covered by DNA. Gray areas are "active" patches of area $\sim \pi(L + l/2)^2$. (c) Particles each with a single DNA strand. The allowed configurations for binding require the overlap of two active patches, greatly reducing the configurations allowed without binding.

2.4.6. CALCULATION AND COMPUTATION OF g_b AND N_b

To fully calculate ΔF_p in equation (2-16), we need to determine g_b and N_b for a pair of complementary particles each of which has surface DNA coverage χ. For high coverage particles, g_b and N_b can be calculated via geometry [21, 22, 27, 28]. For low-coverage particle, g_b and N_b can be determined by computation [27].

To calculate N_b for high coverage particles, we consider the geometry in Figure 2-20 [21, 22, 27, 28]. For any pair of hybridized complementary DNA strands between particles, the distance between their biotin–streptavidin binding sites should be less than $2L + l$. Therefore, the DNA strands in the red area can find complementary DNA strands on the opposing particles. From the geometry, we can determine that

$$\theta_{patch} = \arccos\left\{\frac{2R_p + h - (2L + l)}{2} / R_p\right\}.$$

Then, we can calculate the red area as

$$A_{patch} = \int_{0}^{\theta_{patch}} d\theta \, 2\pi R_p^2 \sin\theta$$

$$= 2\pi R_p^2 \cos\theta \Big|_{\theta_{patch}}^{0}$$

$$= 2\pi R_p \left(L + \frac{l}{2} - \frac{h}{2}\right).$$

N_b can be determined as

$$N_b = A_{patch}\rho\chi = 2\pi\rho\chi R_p \left(L + \frac{l}{2} - \frac{h}{2}\right), \quad (2\text{-}19)$$

where ρ is the DNA coverage density [see equation (2-2)],and χ, the ratio of active DNA strands on the surface of particles [see Section 2.3.1].

To calculate g_b for high-coverage particles, we consider the geometry in Figure 2-21 [21, 22, 27, 28]. Because of the geometry constraint, all the cyan DNA strands in the red area on the top can be reached by the blue DNA strand at the bottom. The red area is $\pi[(2L + l)^2 - h^2]$. Therefore, g_b is the number of DNA strands in the red area and can be determined as

$$g_b = \rho\chi\pi[(2L + l)^2 - h^2]. \quad (2\text{-}20)$$

From equations (2-19) and (2-20), we can calculate N_b and g_b for high-coverage particles. We know that both N_b and g_b are proportional to the fraction of active DNA on the surface of particle χ. However, particles coated with low DNA coverage need computation to get a more accurate N_b and g_b.

To determine the value of g_b and N_b for a pair of particles with a specific χ, we perform a simple computation [27]. Figure 2-22 is the schematic diagram of our computation. We randomly place χN_t points on the surface of each of sphere $\mathrm{P1}$ and $\mathrm{P2}$. The radius of each sphere is $R_p = 980\ \mathrm{nm}$. We hold these two spheres together with a surface separation $h = \frac{1}{2}(2L + l)$. Then, we determine g_b and N_b of this configuration by counting all the possible binding pairs between $\mathrm{P1}$ and $\mathrm{P2}$. We average over $1{,}000$ configurations to determine $\langle g_b \rangle$ and $\langle N_b \rangle$. The algorithm of our computation is as follows:

1. Randomly place χN_t points on the surface of each of $\mathrm{P1}$ and $\mathrm{P2}$ [67].
2. Place $\mathrm{P1}$ and $\mathrm{P2}$ with a surface separation h.
3. Pick a point i on $\mathrm{P1}$, and calculate the distances, r_{ij}'s, between the point i on $\mathrm{P1}$ and all the points j on $\mathrm{P2}$.
4. If r_{ij}'s $\leq (2L + l)$, add 1 to $g_{b,i}$, the binding degeneracy for the point i on $\mathrm{P1}$.
5. Repeat steps 3 and 4 for all the points i on $\mathrm{P1}$.
6. Assign the average of nonzero $g_{b,i}$'s to g_b, the binding degeneracy for this configuration.
7. Assign the number of nonzero $g_{b,i}$'s to N_b, the number of DNA bonds for this configuration.

The computation results for $N_t = 69{,}800 \pm 4{,}800$ and $h = 16.8\ \mathrm{nm}$ at various χ are shown in Figure 2-23. For high DNA coverage, $\chi \gtrsim 0.2$, there are many overlapping DNA strands between a pair of particles. Hence, g_b and N_b are proportional to χ. These are consistent with equations (2-19) and (2-20). However, when $\chi < 0.2$, g_b and N_b are proportional to χ^2 rather than χ. By following the above algorithm, we can determine g_b and N_b for any pair

of complementary particles coated with χN_t DNA strands and separated by a surface separation h.

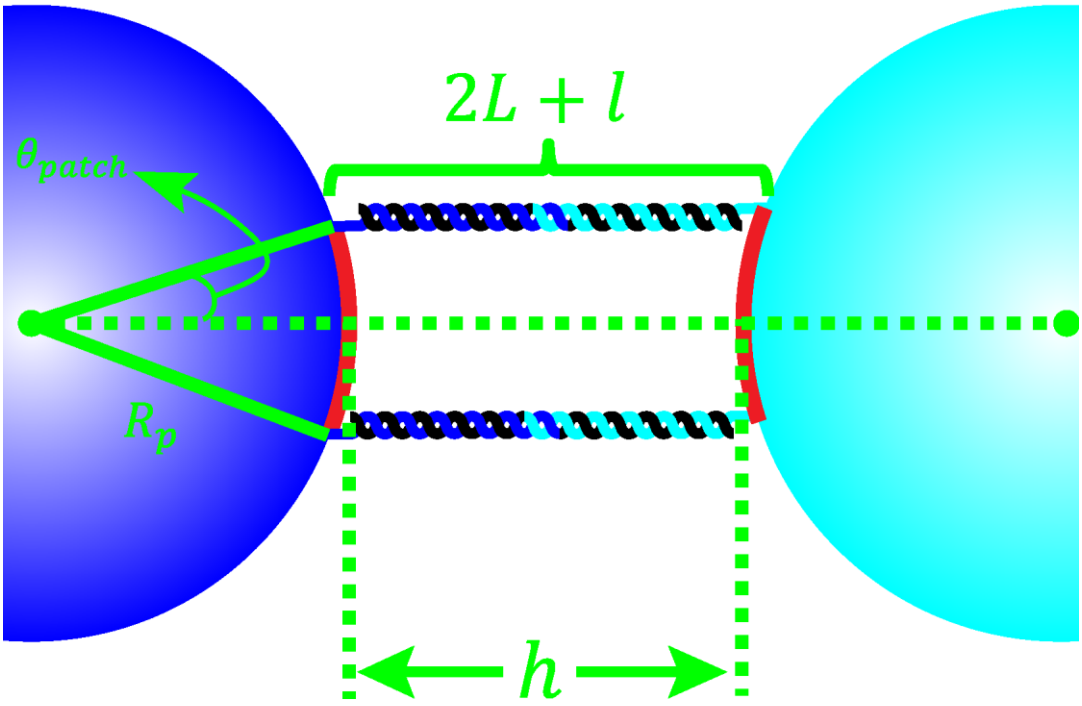

Figure 2-20: A schematic diagram of calculating N_b. The DNA strands in the red area can reach those on the opposing particles.

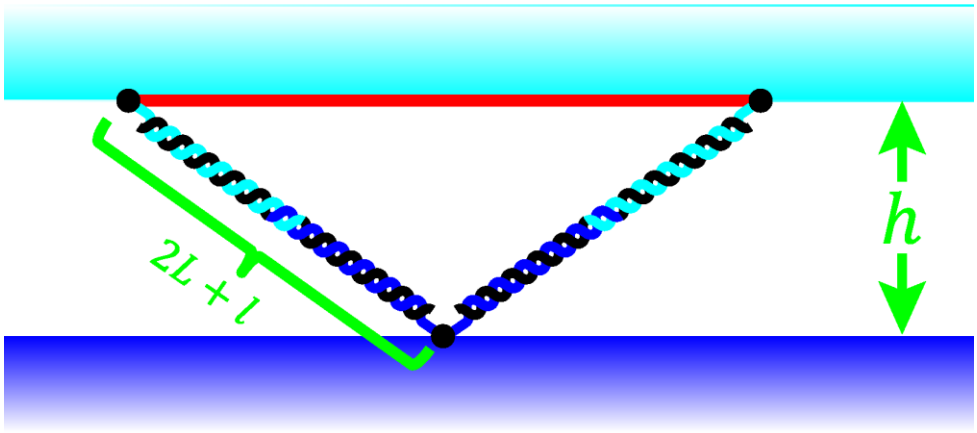

Figure 2-21: A schematic diagram of calculating g_b. All the top DNA strands in the red area can be reached by the DNA strand at the bottom.

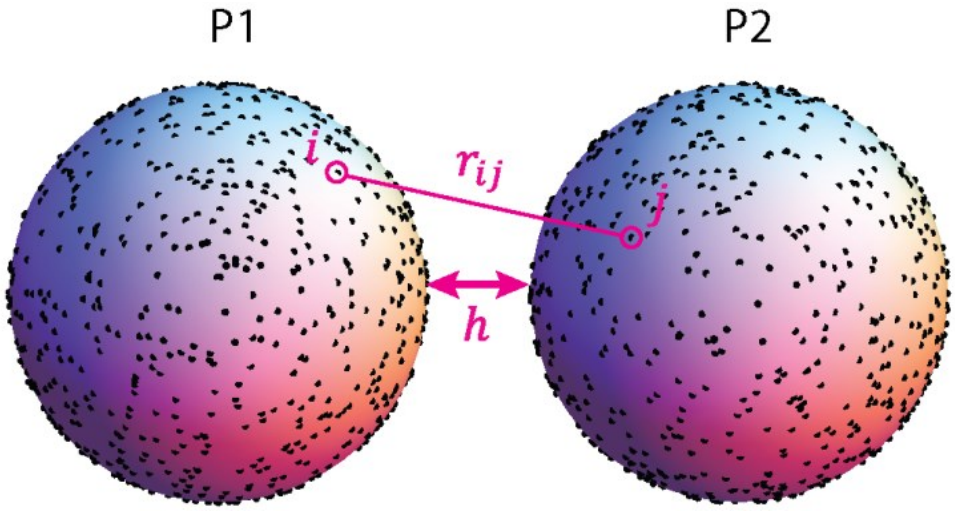

Figure 2-22: The schematic diagram of computation of g_b and N_b.

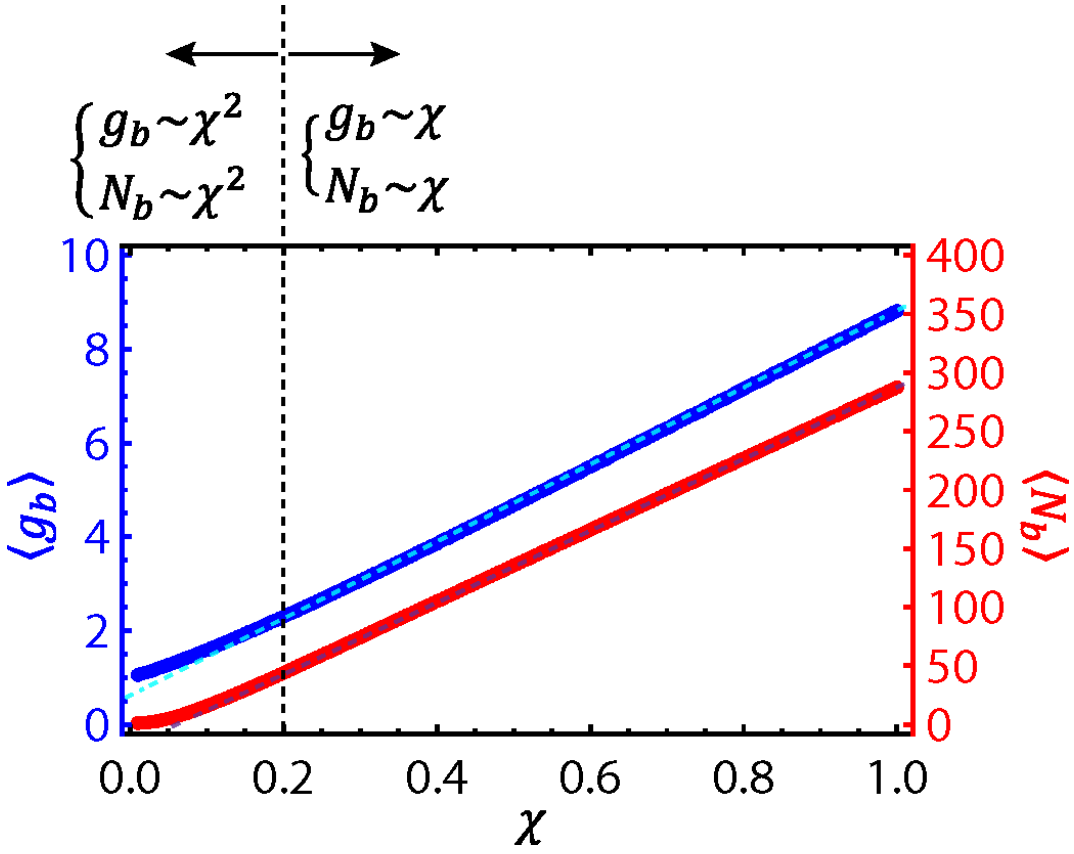

Figure 2-23: $\langle g_b \rangle$ (blue) and $\langle N_b \rangle$ (red) as a function of χ. Both $\langle g_b \rangle$ and $\langle N_b \rangle$ are proportional to χ at high DNA coverage, and are proportional to χ^2 at low coverage. The dashed lines indicate $g_b \sim \chi$ and $N_b \sim \chi$.

2.4.7. CONCLUSIONS

To quantitatively measure the aggregation behavior of DNA-coated particles, we first categorize the systems as open and closed structures.

For the system of open structures, the singlet fraction can be determined by equation (2-9):

$$f = \frac{1 + 2KC_p - \sqrt{1 + 4KC_p}}{2K^2C_p^2}, \tag{2-9}$$

where $K \equiv A_w e^{-\beta \Delta F_p}$, in which A_w is the wiggling area when a particle is bound to another particle, ΔF_p, the binding free energy for a pair of complementary particle, and C_p, the total particle density [21, 22, 27]. By knowing the extra configurational entropy cost ΔS_p [see Section 2.4.4], the rotational entropy cost ΔS_r [see Section 2.4.5], g_b, and N_b [see Section 2.4.6], we can determine the binding free energy of a pair of complementary particles, ΔF_p from equation (2-16). Then, K is determined. Along with a measurable particle density, C_p, we can calculate the singlet fraction f of the system of open structures.

For the system of closed structures, we determine the singlet fraction, f by using equation (2-8):

$$\frac{1}{f} = 1 - \frac{C_p f K\left[C_p f K(\Gamma + 1) - 2\right]}{\left(C_p f K - 1\right)^2 \left(C_p f K \Gamma - 1\right)^2}, \tag{2-8}$$

where $\Gamma \equiv \frac{\Omega_w}{\Omega_1} e^{-\beta \Delta F_p}$ in which Ω_1 and Ω_w are, respectively, the wiggling angles if a particle is bound only to one particle (Figure 2-16 (a)), and if bound to two particles simultaneously (Figure 2-16 (b)) [27]. By numerically solving f in equation (2-8), we can determine the value of singlet fraction f and quantify the aggregation of the system of closed structures.

From equations (2-8) and (2-9), we can quantify the general aggregation of a system of closed and open structures, respectively [27]. For system of DNA-coated particles, the binding free energy ΔF_p can be determined by equation (2-16). Putting equations (2-8), (2-9), and (2-16) together, we can describe the aggregation behaviors of DNA-coated particles for the system of either closed or open structures.

2.5. COMPARISONS BETWEEN MODEL AND DATA

In Section 2.4, we built a model to describe the aggregation behaviors of DNA-coated particles for the system of either closed or open structures. In this section, we test if the model is consistent with experiment.

In Section 2.3, we measured the melting curves of DNA-coated particles for various DNA coverages, χ's. Since the system is a Watson-Crick-like system, aggregation of three particles forming a triangle as shown in Figure 2-16 (b) is not allowed. The aggregates in such a system are open. Therefore, we can apply equation (2-9):

$$f = \frac{1 + 2KC_p - \sqrt{1 + 4KC_p}}{2K^2C_p^2} \tag{2-9}$$

to calculate the singlet fraction. By direct measurement, our particle density is $C_p \approx 0.01\ \mu\text{m}^{-2}$. To determine $K = A_w e^{-\beta \Delta F_p}$, we need to calculate the wiggling area A_w and the binding free energy of a pair of complementary particles, ΔF_p. In Section 2.4.1, A_w can be easily determined as $A_w =$

$\left[2\pi\left(2R_p\right)\right](2b)$, where, in our case, $R_p = 980\ \text{nm}$ and $b = 0.34\ \text{nm}$ are the spacing of bases along a dsDNA. ΔF_p can be determined by equation (2-16):

$$\Delta F_p \approx -k_b T \ln\left[\left(1 + g_b e^{-\beta \Delta F^\circ}\right)^{N_b} - 1\right] - T\Delta S_r. \tag{2-16}$$

The rotational entropy cost ΔS_r can be determined from equation (2-18):

$$\Delta S_r = 2k_B \ln\left[1 - \left(1 - \frac{\pi\left[\left(L + \frac{l}{2}\right)^2 - \left(\frac{h}{2}\right)^2\right]}{4\pi\left(R_p + \frac{h}{2}\right)^2}\right)^{N_{tot}}\right]. \tag{2-18}$$

In our system, the length of the backbone of our dsDNA strand is $L \approx 15\ \text{nm}$. The length of sticky end is $l \approx 3.6\ \text{nm}$. Particle radius is $R_p = 980\ \text{nm}$. $N_{tot} = \chi N_t$,where $N_t = 69{,}800 \pm 4{,}800$ [see equation (2-1)]. Then, from equation (2-18), ΔS_r can well be determined for any DNA coverage χ. The values of g_b and N_b at various χ are determined from the computation described in Section 2.4.6. The computation results for our case are shown in Figure 2-23. The binding free energy of a pair of complementary DNA strands in our system $\Delta F°$ can be determined from equation (2-10):

$$\Delta F° = \Delta H° - T\left(\Delta S° + \Delta S_p\right). \tag{2-10}$$

The sequence of our sticky-end DNA can be found in Table 2-1. The contents of our buffer are $10\ \mathrm{mM}$ phosphate-buffered saline (PBS), $50\ \mathrm{mM}$ NaCl, 0.5% w/w Pluronic F127, and 0.15% w/w sodium lauryl sulfate (SDS), so the overall sodium concentration is $[\mathrm{Na}^+] = 73.4\ \mathrm{mM}$, which is $50\ \mathrm{mM}$ from NaCl, $18.2\ \mathrm{mM}$ from PBS, and $5.2\ \mathrm{mM}$ from SDS. Then, we can determine that $\Delta H° = -328{,}000\ \mathrm{J/mole}$ and $\Delta S° = -966\ \mathrm{J/mole\ K}$ [17, 62-66]. The extra configurational entropy cost ΔS_p can be determined from equation (2-17):

$$\Delta S_p = k_B \ln\left\{\frac{2\pi\sqrt{\left(L+\frac{l}{2}\right)^2-\left(\frac{h}{2}\right)^2}}{C°\left[2\pi\left(L+\frac{l}{2}\right)^2\right]^2}\right\}. \tag{2-17}$$

For our case, $L \approx 15\ \mathrm{nm}$ and $l \approx 3.6\ \mathrm{nm}$, so $\Delta S_p \approx -10k_B$. Here, we treat ΔS_p as a fitting parameter to fit the melting curve of $\chi = 1$. The fitted $\Delta S_p = -11k_B$ is pretty consistent with our calculation.

With ΔS_p being determined, we can plot equation (2-9) for $\chi = 0.025, 0.05, 0.1, 0.2, 0.3, 0.4, 0.5, 0.75, 1$ as shown in Figure 2-24 [27]. In Figure 2-24, the dots are our experimental data, and the solid curves are our model plot.

The consistency between the model and the experimental data shows that our model describes the aggregation of Watson-Crick-like DNA-coated particles well.

From Figure 2-24, we can re-plot the data and model to melting temperature T_m, defined as $f(T_m) \equiv 0.5$, vs. DNA coverage χ as shown in Figure 2-25 [27]. We still find consistency in the figure between data and our model. The dashed lines indicate the measurement error of total DNA coverage, N_t [see equation (2-1)]. Additionally, we find that our DNA-coated particles with 2.5% active DNA strands still possess well-defined melting temperatures and melting behaviors. Such result indicates that our particles can be coated with $\frac{100}{2.5} = 40$ different DNA strands and be able to recognize 40 different particles as shown in Figure 2-26 [27]. From the inset of Figure 2-25, we find that for particles with DNA coverage $\chi \approx 0.01$, the melting temperature T_m is about $0℃$ [27]. Hence, from our model, we expect that our particles may be able to recognize up to $1/0.01 = 100$ different particles at the same time at reasonable temperatures, which means $T > 0℃$.

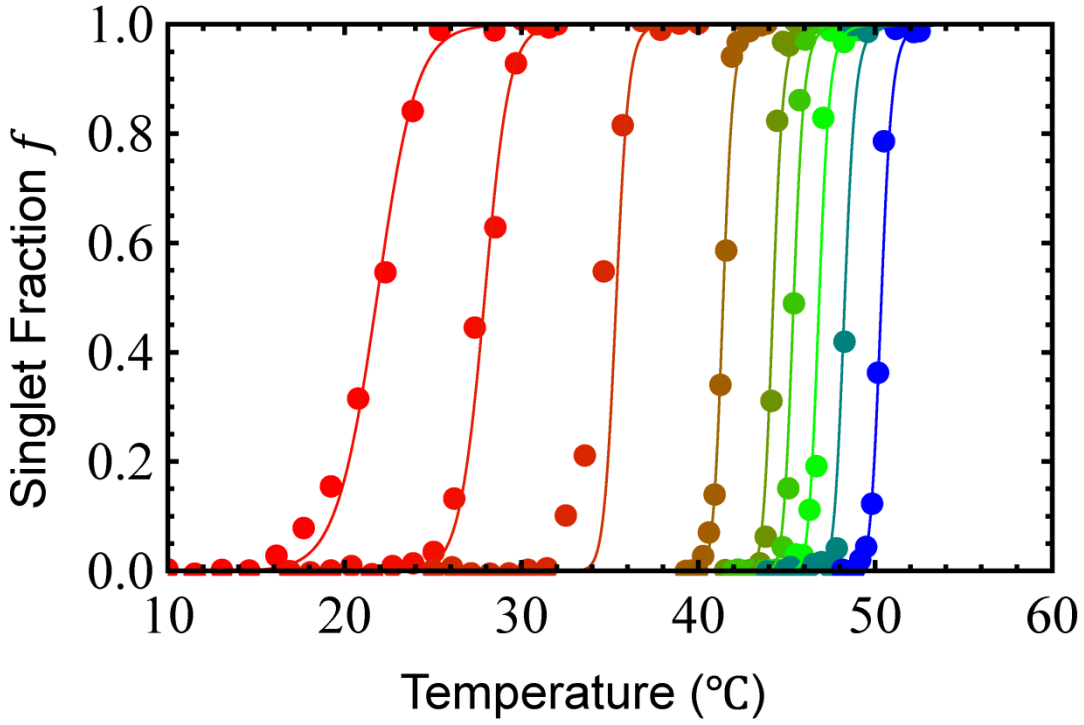

Figure 2-24: Melting curves of a Watson–Crick-like system for different coverages of χ. From left (red) to right (blue), $\chi = 0.025, 0.05, 0.1, 0.2, 0.3, 0.4, 0.5, 0.75, 1$ respectively. The solid lines are the melting curves determined from equation (2-9), whereas the dots represent the experimental data.

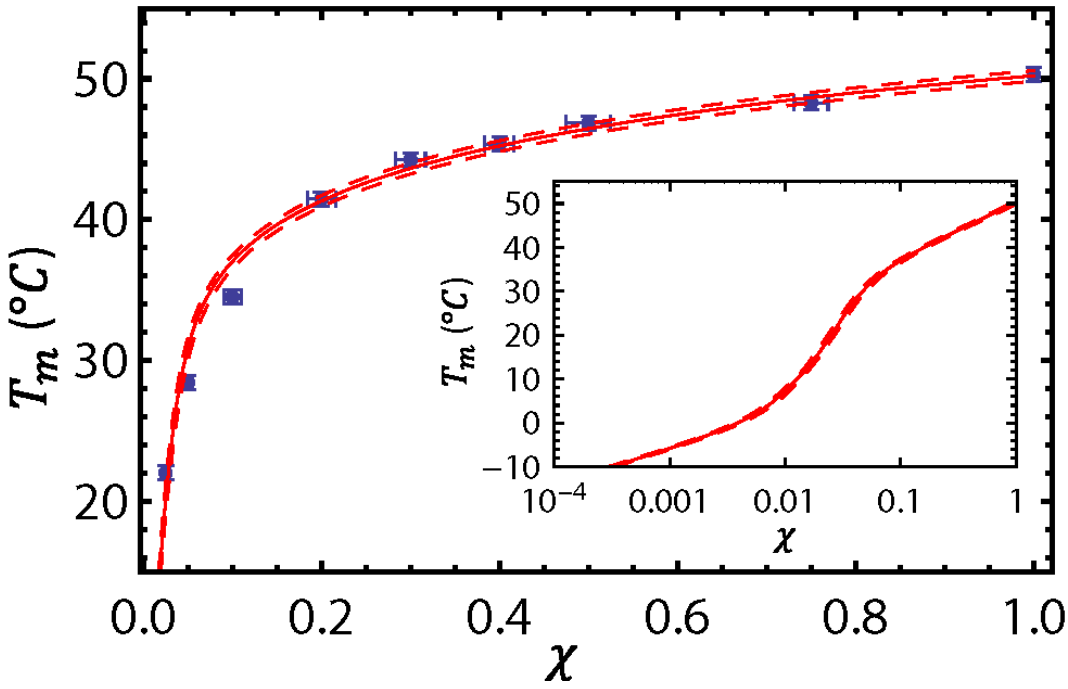

Figure 2-25: Melting temperatures as a function of the DNA sticky end coverage χ. The blue dots are the experimental data. The solid line is the melting temperature, T_m, determined from equation (2-9) by setting $f(T_m) = 0.5$. Dashed lines indicate 6.9% measurement error in the total DNA surface coverage on the particles, N_t [see equation (2-1)]. (Inset) Melting temperatures as a function of the sticky-end DNA coverage χ in a $\log(\chi)$-linear(T_m) plot.

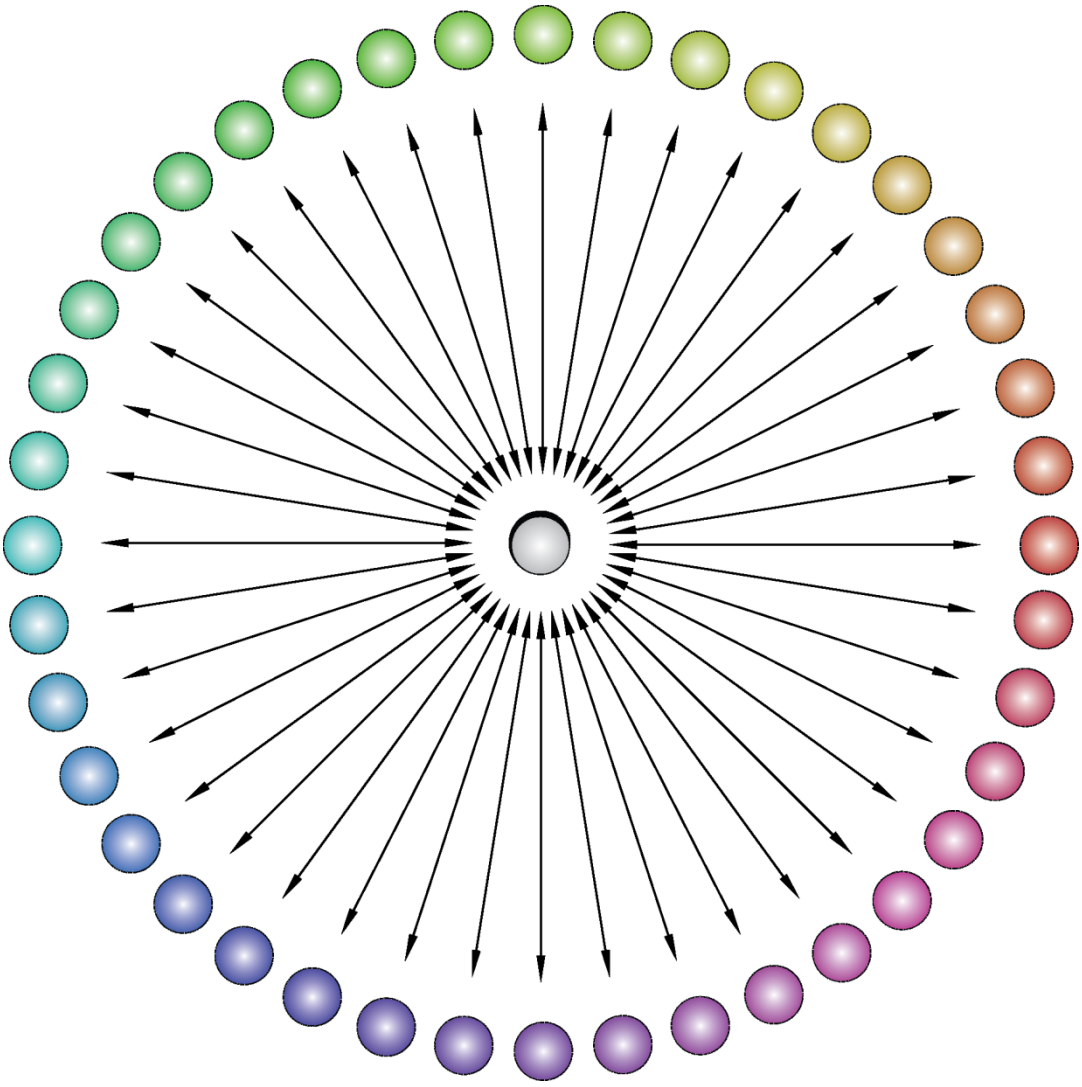

Figure 2-26: A particle coated with 40 different DNA strands can recognize 40 different particles.

2.6. ABC SYSTEM

In Section 2.5, we tested our model for the system of open structures. Here we study closed structures. We create a system with three different particles: A, B, and C as shown in Figure 2-27 [27]. In such a system, each species binds to two other species, but the particles which are the same species do not bind to each other. In such a system, A, B, and C bind together and form a triangle cluster. Therefore, the aggregation of closed structures is allowed. We now measure the melting curves of A+B, B+C, A+C, and A+B+C. Since a two-component system can only have open structures, we will compare the melting curves of A+B, B+C, and A+C with one of A+B+C and test whether or not our model can describe the aggregation behavior of the A+B+C system well.

2.6.1. DESIGN

To design ABC system, we need three pairs of complementary DNA strands as shown in Table 2-3 [27]. To avoid unwanted interaction/hybridization in our system, we check the melting temperatures of any pair of DNA sequences via UNAFold Web Server [17, 62-66]. Our buffer contains

$73.4\ \mathrm{mM}\ \mathrm{Na}^{+}$. Each of our particles carries $N_t \approx 69{,}800$ DNA strands with a particle density $C_p \approx 0.01\ \mu\mathrm{m}^{-2}$. They are placed in a capillary with a height $h_{capillary} = 0.1\ \mathrm{mm}$. The overall DNA concentration is $C_{DNA} = N_t \times \frac{C_p}{h_{capillary}} \approx 12\ \mathrm{nM}$. With $[\mathrm{Na}^{+}] = 73.4\ \mathrm{mM}$ and $C_{DNA} = 12\ \mathrm{nM}$, the solution melting temperatures of any pair of DNA sequences is shown in Table 2-4 [27]. The table shows that only the melting temperatures of complementary DNA sequences (S_1-S_1', S_2-S_2', and S_3-S_3') are above $0\ ℃$ [27]. The other melting temperatures are all significantly below $0\ ℃$. Additionally, we check the melting temperature of secondary structures (folding structures) of each DNA strand. From the data in Table 2-4, we note that the melting temperatures of secondary structures are all significantly below $0\ ℃$ too. Therefore, from Table 2-4, we are confident that at our experimental temperatures ($T > 0\ ℃$), only complementary DNA strands hybridize. The three pairs of sequences in Table 2-3 are appropriate to be three independent attraction interactions of ABC system in Figure 2-27.

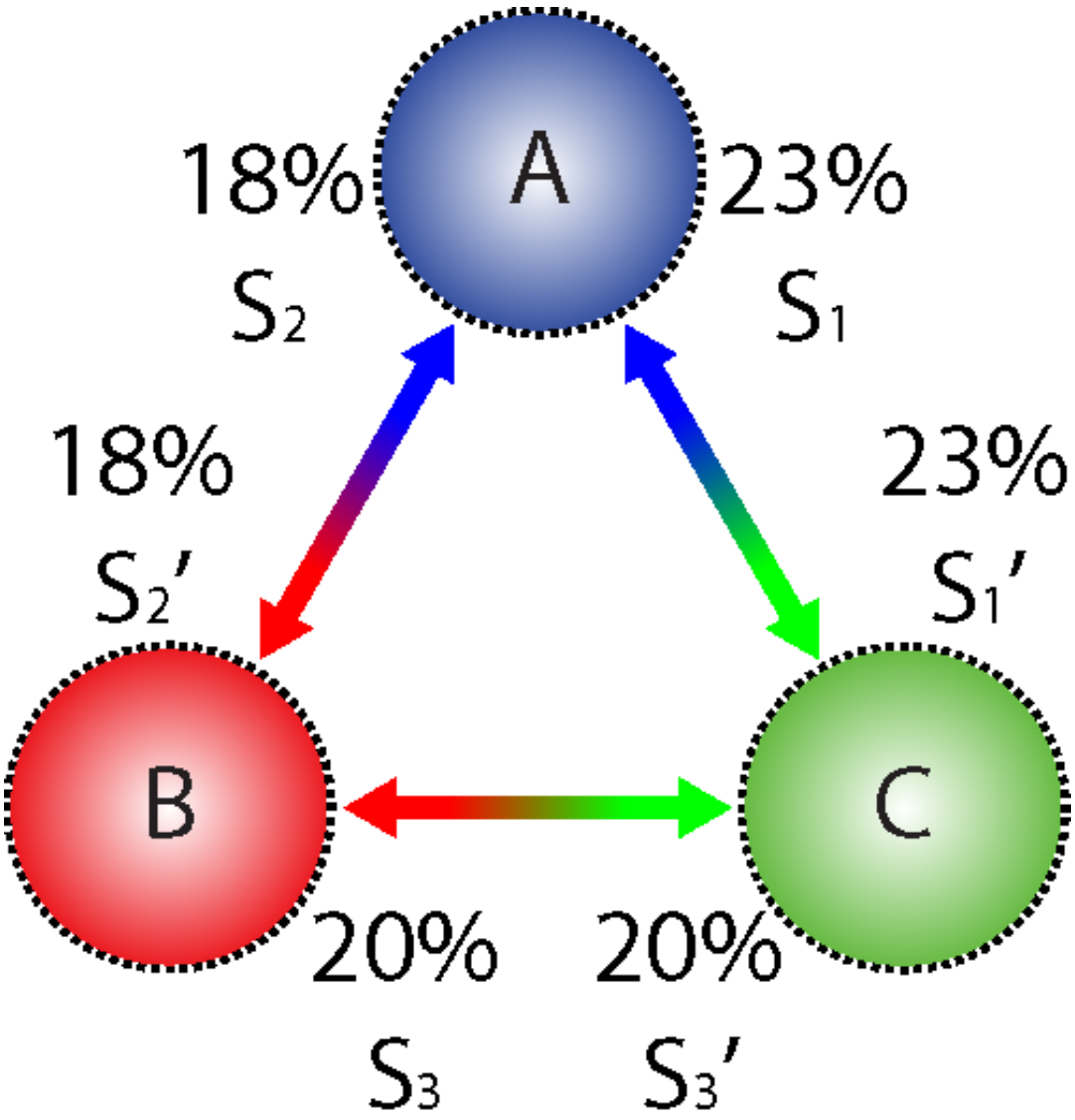

Figure 2-27: Interaction diagram of ABC system. Each particle is coated with two different kinds of DNA strands. A can bind to B and C. B can bind to A and C. C can bind to A and B.

DNA Symbols	Sequences
S_1	5’ – GTA GAA GTA GG – 3'
S_1'	5’ – CCT ACT TCT AC – 3’
S_2	5’ – GAT GGA TTA GG– 3'
S_2'	5’ – CCT AAT CCA TC – 3’
S_3	5’ – GTA TTC GAG TT – 3'
S_3'	5’ – AAC TCG AAT AC – 3’

Table 2-3: DNA sequences used in ABC system.

	S_1	S_1'	S_2	S_2'	S_3	S_3'
S_1	-214	18	-151	-68	-76	-147
S_1'	–	-214	-68	-177	-99	-69
S_2	–	–	-147	19	-138	-101
S_2'	–	–	–	N/A	-96	-102
S_3	–	–	–	–	-54	20
S_3'	–	–	–	–	–	-54
Folding	-41	-54	-175	N/A	-48	N/A

Table 2-4: Melting temperatures of DNA pair hybridization (℃) determined from the UNAFold Web Server with $73.4\ \mathrm{mM}$ sodium and $0.012\ \mu\mathrm{M}$ DNA. Data are taken from Ref. [17, 62-66]. The last row indicates the melting temperature of the secondary structure for each sticky-end DNA. N/A means that no hybridization state is found by the UNAFold Web Server.

2.6.2. EXPERIMENT

To measure the melting curves of A+B, B+C, and A+C systems, we coat Particle A with $23\%\ S_1$ and $18\%\ S_2$, Particle B with $18\%\ S_2'$ and 20% S_3, and

Particle C with $23\%\ S_1'$ and $20\%\ S_3'$. From the experiment in Section 2.3, we learn that the melting temperatures of self-assembly of DNA-coated particles can be controlled by changing the surface DNA coverage. The concentration of each DNA strands on each surface of particles is carefully adjusted, so the melting temperatures of A+B, B+C, and A+C are close. We follow the protocol used in Section 2.3.4 to measure the melting curves of A+B, B+C, and A+C. The particle concentration of A, B, or C is designed to be $\frac{C_p}{2} = 0.005\ \mu m^{-2}$. The measured melting curves are shown in Figure 2-28 [27]. The pink, yellow-green, and cyan dots are the measured melting curves for A+B, B+C, and A+C systems, respectively. Each of these systems is a two-component system like the one in Section 2.3. The aggregation structures in two-component system should only be open structures.

To study the system with closed structures, we put A's, B's, and C's together in equal amounts (the particle concentration of each species is still $\frac{C_p}{2} = 0.005\ \mu m^{-2}$) since A, B, and C can form a three-particle triangle. We measure the melting curve of A+B+C system similarly. The measured melting curve of A+B+C is the black dots in Figure 2-28 [27]. Since the melting

curves of A+B, B+C, and A+C are basically identical, naively we might expect the melting curve of A+B+C to be the same as of the other three. However, from Figure 2-28, the melting temperature of A+B+C is ~ 0.8 ℃ higher than the one of A+B, B+C, or A+C. The experimental result suggests that the melting behavior of closed structures is different from that open structures.

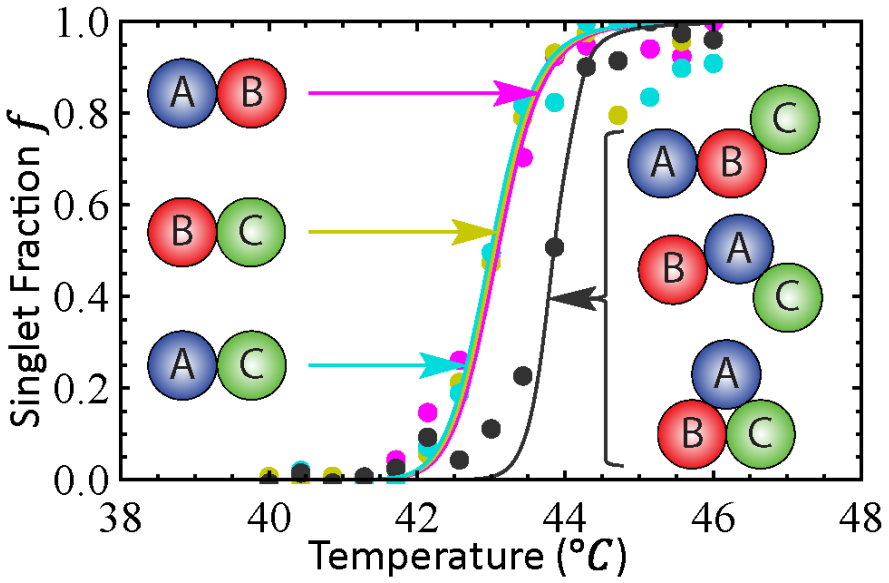

Figure 2-28: Melting curves particles that can address two different particles: AB (pink), BC (yellow-green), AC (cyan), and ABC (black). The dots are the experimental data. The solid curves are the model plots.

2.6.3. COMPARISONS BETWEEN MODEL AND DATA

To further check if our model still works in a different system, we will first compare the data of A+B, B+C, and A+C with our model to examine the system of open structures [see Section 2.4.2]. Based on the same parameters, we will predict the melting curves based on the model for closed structures [see Section 2.4.1] and compare them with the experimental data of the system with closed structures, namely, the black dots in Figure 2-28.

To plot the melting curves of A+B, B+C, and A+C, we follow a calculation similar to the one used in Section 2.5. The only parameters different from the ones in Section 2.5 are $\Delta H°$'s and $\Delta S°$'s because of the different DNA sequences used in the ABC system. The $\Delta H°$'s and $\Delta S°$'s for S_1+S_1', S_2+S_2', and S_3+S_3' are listed in Table 2-5 [17, 62-66]. Since our DNA constructs and particles are the same as the ones in Section 2.5, all the other parameters, such as $L \approx 15\ \mathrm{nm}$, $l \approx 3.6\ \mathrm{nm}$, $R_p \approx 980\ \mathrm{nm}$, and $C_p = 0.01\ \mu\mathrm{m}^{-2}$ are the same. The computed g_b's and N_b's in Figure 2-23 are also the same in this system. Since A+B, B+C, and A+C systems only aggregate open structures, we plot the melting curves of A+B, B+C, and A+C via equation (2-9) with

the corresponding parameters. The plots of the melting curves are shown in Figure 2-28 [27]. The pink, yellow-green, and cyan curves are the plots of melting curves for A+B, B+C, and A+C, respectively. The comparison between the model (solid curves) and the data (dots) in Figure 2-28 for A+B, B+C, and A+C systems show that our model describes the system with open structures pretty well.

To check whether or not our model can work for the system of closed structures, we plot the melting curve of A+B+C based on the same parameters used to plot the melting curves of A+B, B+C, and A+C. We can plot the melting curve of A+B+C via equation (2-8):

$$\frac{1}{f} = 1 - \frac{C_p f K\left[C_p f K(\Gamma + 1) - 2\right]}{\left(C_p f K - 1\right)^2 \left(C_p f K \Gamma - 1\right)^2}, \tag{2-8}$$

where $\Gamma \equiv \frac{\Omega_w}{\Omega_1} e^{-\beta \Delta F_p}$. From the geometry implied from Figure 2-16 (b), we can estimate the wiggling angle $\Omega_w \approx \arccos\left[\frac{\left(2R_p\right)^2 + \left(2R_p + 2L + l\right)^2 - R_p^2}{2\left(2R_p\right)\left(2R_p + 2L + l\right)}\right]$. However, ΔF_p is an ambiguous quantity since ABC system has three binding free energies: $\Delta F_{p,\mathrm{AB}}$, $F_{p,\mathrm{BC}}$, and $F_{p,\mathrm{AC}}$. Fortunately, the solution melting tempera-

tures of hybridization of S_1+S_1', S_2+S_2', and S_3+S_3' are similar as shown in Table 2-5 and the melting curves of A+B, B+C, and A+C are almost identical as shown in Figure 2-28, we can calculate the singlet fraction of A+B+C, f_{ABC} as

$$f_{ABC} = \frac{1}{3}(f_{\mathrm{AB}} + f_{\mathrm{BC}} + f_{\mathrm{AC}}) \tag{2-21}$$

[27], where f_{AB}, f_{BC}, and f_{AC} are determined from equation (2-8) using the same sets of parameters used in plotting the melting curves of A+B, B+C, and A+C except the total particle concentration C_p and the equilibrium constant K. The total particle concentration is changed to $\frac{3}{2}C_p = 0.015\ \mu\mathrm{m}^{-2}$ because A+B+C system has A's, B's, and C's, each of which has particle concentration $\frac{C_p}{2} = 0.005\ \mu\mathrm{m}^{-2}$. The equilibrium constant K in equation (2-8) has to be replaced by $\left(\frac{3}{2}\right)^2 K$ because in A+B+C system, each particle can bind to $2/3$ of the system while in A+B, B+C, or A+C system, each particle can only bind to $1/2$ of the system. The more fruitful binding configurations result in a larger effective equilibrium constant. A more detailed discussion of such effect can be found in Section 2.6.4. The black curve in Figure 2-28 is the plot of equation (2-21). The comparisons between our model (the

black curve) and the data (the black dots) in Figure 2-28 show that our model still describes the system of closed structures pretty well.

From the above studies, we prove that our model can describe the aggregation of DNA-coated particles with either open or closed structures. In the system of either structures, we have to determine the binding free energy of a pair of complementary particles in equation (2-16): $\Delta F_p = \Delta F_{p,DNA} - T\Delta S_r$. Rotational entropy cost ΔS_r is important for low DNA-coverage particles. Statistics of hybridization between particles is needed for consideration to determine the binding free energy contributed from DNA hybridization between particles, $\Delta F_{p,DNA}$. For DNA strands attached to surfaces of particles, the extra configurational entropic cost, ΔS_p is an important quantity to calculate their hybridization energies. After ΔF_p is determined, if the system can form closed structures, the aggregation behaviors can be determined via equation (2-8). If the system can only have clusters of open structures, equation (2-9) can be used to quantify the aggregation behaviors of such systems. The consistency between the model and data in Figure 2-28

proves that our model is applicable for describing the aggregation of both open and closed structures.

DNA Hybridization	$\Delta H°$ (J/mole)	$\Delta S°$ (J/mole K)
$S_1 + S_1'$	$-328{,}000$	-966
$S_2 + S_2'$	$-326{,}000$	-956
$S_3 + S_3'$	$-332{,}000$	-974

Table 2-5: Hybridization enthalpies and entropies of pairs of complementary DNA strands in the buffer containing $73.4\ \mathrm{mM\ Na^+}$.

2.6.4. COMPARISONS BETWEEN ABC AND AB

To get a deeper insight into the ABC system, we will discuss the reason that makes the melting curve of A+B+C different from those of A+B, B+C, or A+C. For A+B+C system, the binding configurations are more fruitful than those of A+B, B+C, and A+C systems. As a result, the melting temperature of A+B+C is higher ($\sim 0.8\ ℃$) than those of A+B, B+C, and A+C although those of A+B, B+C, and A+C are almost identical. Such extra binding con-

figurations can be attributed to two effects: 1) the $2/3$ effect, and 2) the triangle effect [27]:

1. **Two-Thirds Effect:** This effect is due to binding multiplicity in A+B+C system. In A+B, B+C, and A+C systems, the total concentration is C_p. Each particle can interact with $1/2$ of the system. In A+B system, A's and B's are in equal amounts, but each A can only bind to B's. In A+B+C system, the total particle concentration is $\frac{3}{2}C_p$. Each particle can interact with $2/3$ of the system. In A+B+C system, A's, B's, and C's are in equal amounts. Each A can bind to either B's or C's. If all concentrations and reaction rates are the same, the effect is to replace the equilibrium constant K by $\left(\frac{3}{2}\right)^2 K$. Therefore, if we use the same parameters and equations used for plotting the melting curves of A+B, B+C, and A+C systems and replace K and C_p by $\left(\frac{3}{2}\right)^2 K$ and $\frac{3}{2}C_p$, respectively, the melting curves will be shifted by ~ 0.2 ℃. Hence, the shift of the melting temperature due to the $2/3$ effect is ~ 0.2 ℃.
2. **Triangle Effect:** Sections 2.4.1 and 2.4.2 show that triangle structures are the main configuration that separates the system with

closed structures from the one with open structures. In Section 2.6.3, we plot equation (2-21) by replacing K and C_p by $\left(\frac{3}{2}\right)^2 K$ and $\frac{3}{2}C_p$, respectively, for the sake of two-thirds effect. By plotting (2-21) without the effect, the melting temperatures were lower by ~ 0.2 ℃. Therefore, the overall shift from melting temperatures, purely from triangle effect, is ~ 0.6 ℃.

To determine the melting curve of the A+B+C system, both the "$2/3$" and the "triangle" effects need to be taken into account, and combining them the melting temperature of the A+B+C system is ~ 0.8 ℃ higher than A+B, B+C, or A+C systems. Such shift of the melting temperature is ~ 0.2 ℃ from the $2/3$ effect and ~ 0.6 ℃ from the triangle effect.

2.7. CONCLUSIONS

In this chapter, we have studied how DNA-coated particles aggregate at different temperatures when the system reaches thermal equilibrium and how DNA hybridization between particles can control the melting temperatures and transitions. At the beginning, we learned that the melting temperatures and transitions of the aggregation can be controlled by the surface cover-

age of active DNA strands χ. The melting temperature increases with increasing DNA coverage while the melting transition decreases. Our experimental data show that the melting temperature increases from $22\,℃$ for $\chi = 0.025$ to $50.3\,℃$ for $\chi = 1$ while the melting transition width decreases from $5\,℃$ for $\chi = 0.025$ to $0.8\,℃$ for $\chi = 1$. Our model shows that for DNA strands attached to surfaces of particles, an extra configurational entropic cost ΔS_p must be considered for calculation of DNA hybridization free energy. Using a mean-field approximation, we can calculate the binding free energy for a pair of complementary particles contributed by DNA hybridization. If the particle surface coverage is high, the rotational entropy cost is negligible, and if low, it must be included. Finally, the aggregation behavior of a system with three-particle triangles can be quantified using equation (2-8). Our model has been carefully tested and compared with the experimental data (Figure 2-24) and the open structures are consistent with it. The model plots for the system of both open and closed structures are also consistent with the experimental data (Figure 2-28). These consistencies between the model and the data suggest that our model is reliable to describe the aggregation behavior of DNA-coated particles for the system of either closed or open structures. Further, the inset in Figure 2-25 shows that our model

implies a possibility using particles with up to ~ 100 different DNA strands to recognize up to ~ 100 different partners. With control of melting temperatures of DNA-coated particles, our thermodynamics study paves the way for complex self-assembly.

CHAPTER 3 KINETICS

DNA-functionalized colloids have got significant attention as DNA hybridization empowers them with highly selective thermo-reversible attractions [26, 52]. Rapid developments in DNA technology now allow facile synthesis of specifically designed DNA sequences easily linked to particle surfaces. Recently, FCC crystalline structures from a single component system and BCC crystals from two different colloids coated with complementary DNA sticky ends have been made [33, 34, 53]. This considerable achievement in the self-assembly field allows us to envision more complex multistage processes such as self-assembly of clusters [31] or self-replication at the colloidal scale [12]. For such multistep processes, thermodynamics controls the structure of the intermediate product at each stage, whereas kinetics controls the time it takes to form an intermediate product. Models to describe the thermodynamics of particle aggregation with varying DNA particle coverage have been successfully developed and compared to experimental data [12, 21, 22, 25-27, 34, 37, 54, 55]. However, the mechanism of particle pair formation and the kinetics of aggregation remains poorly studied. In this chapter, we discuss in the kinetics of aggregation as a function of surface

coverage and salt concentration. Additionally, we discuss how solution DNA hybridization rates control the aggregation rates of colloidal particles coated with the same DNA strands.

3.1. SYSTEM DESCRIPTION

To study how fast particles aggregate, we choose the same system used in Section 2.3. The system contains two species, which are $2\mu\mathrm{m}$ polystyrene particles coated with DNA S and DNA S' [27, 28]. The particle radius is $R_p = 980\ \mathrm{nm}$. The DNA sequences of S and S' can be found in Table 2-1. To stabilize particles, we use the same buffer containing surfactants: $10\ \mathrm{mM}$ PBS, $50\ \mathrm{mM}$ NaCl, 0.5% w/w F127, and 0.15% w/w SDS. Experiments with non-complementary particles at twice the concentration of SDS and F127 show no sign of depletion interactions. In our experiments, we measure how fast particles coated with various DNA coverages, χ's aggregate in different salt concentrations $[\mathrm{NaCl}]$'s.

To measure how fast particles coated with various DNA coverage χ's aggregate, we use the same data measured in Section 2.3.4: the time evolution of singlet fraction f. As shown in Figure 2-12, we know how singlet fraction $f(T)$ evolves over time. We can re-plot the data as singlet fraction vs. time at various temperatures (Figure 3-1) [28]. When the system reaches thermal equilibrium, f is almost independent of time. In Figure 3-1, we notice that the time to reach thermal equilibrium is almost temperature-independent. In Section 2.3.4, we measure the time evolution of the singlet fraction $f(T)$ for $\chi = 0.025,\ 0.05,\ 0.1,\ 0.2,\ 0.3,\ 0.4,\ 0.5,\ 0.75,$ and 1. Therefore, we can re-plot all the data from $f(T)$ to $f(t)$ (Figure 3-2) [28]. For each χ, the temperature is chosen to be low enough for particles to fully aggregate, i.e., $f(T, t)$ approaches zero as $t \to \infty$. Typically, we choose T to be ~ 8 ℃ below T_m. The chosen temperatures for $f(t)$ at various χ's compared to the corresponding melting temperatures are shown in Table 3-1 [27, 28]. For these measurements, the salt concentration is $[\mathrm{NaCl}] = 50\ \mathrm{mM}$. From Figure 3-2, we note that particles aggregate slower as the surface DNA coverage χ decreases.

To measure how fast particles aggregate in different salt concentrations, $[\mathrm{NaCl}]$'s, we follow the same method of measuring $f(t)$ from the measurement of time evolution of singlet fraction $f(T)$. However, instead of changing the surface DNA coverage χ, we change the salt concentration $[\mathrm{NaCl}]$. In our measurements, we choose $\chi = 0.1$ and vary the salt concentration from 0 to $200\ \mathrm{mM}$. Again, the chosen temperatures for $f(t)$ at various salt concentrations $[\mathrm{NaCl}]$'s compared to the corresponding melting temperatures are shown in Table 3-2 [28]. The measurement results for $f(t)$ at various salt concentrations are shown in Figure 3-3 [28]. From left (blue) to right (red), the salt concentrations are $[\mathrm{NaCl}] = 200, 150, 100, 50, 25,$ and $0\ \mathrm{mM}$. From Figure 3-3, we notice that particles aggregate slower at lower salt concentration $[\mathrm{NaCl}]$. As the salt concentration increases, particles aggregate faster.

From Figure 3-2 and Figure 3-3, we notice that singlet fraction decays with time in a very similar way no matter what surface DNA coverage χ or salt concentration $[\mathrm{NaCl}]$ is. Therefore, based on such observations, we are going to study: 1) the intrinsic physics that determines $f(t)$, and 2) how sur-

face DNA coverage χ and salt concentration $[\mathrm{NaCl}]$ control how fast particles aggregate.

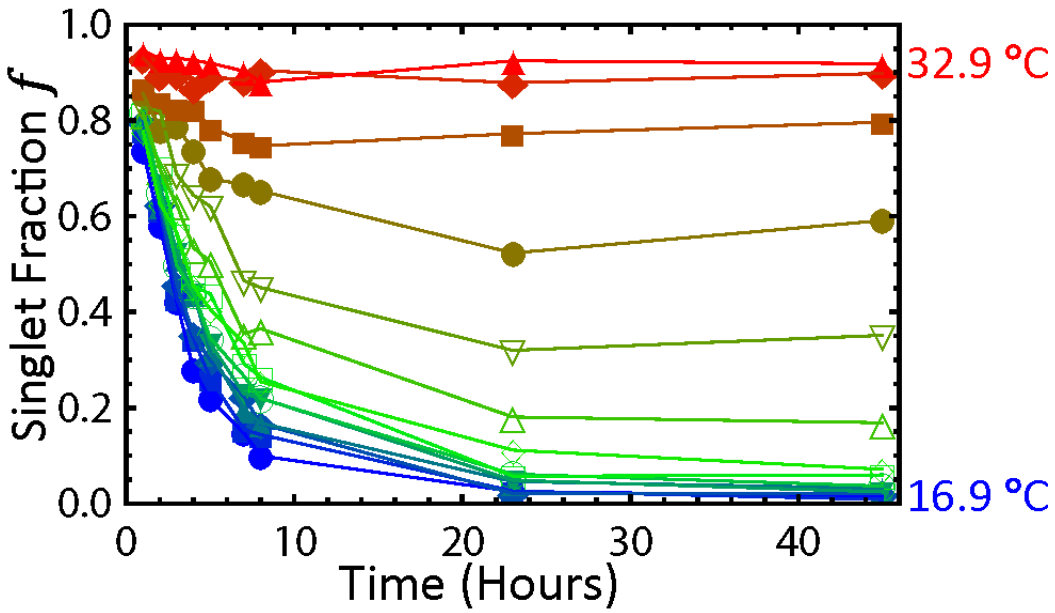

Figure 3-1: Singlet fraction f vs. time at various temperatures. This is a re-plot of Figure 2-12 from $f(T)$ at various times to $f(t)$ at various temperatures.

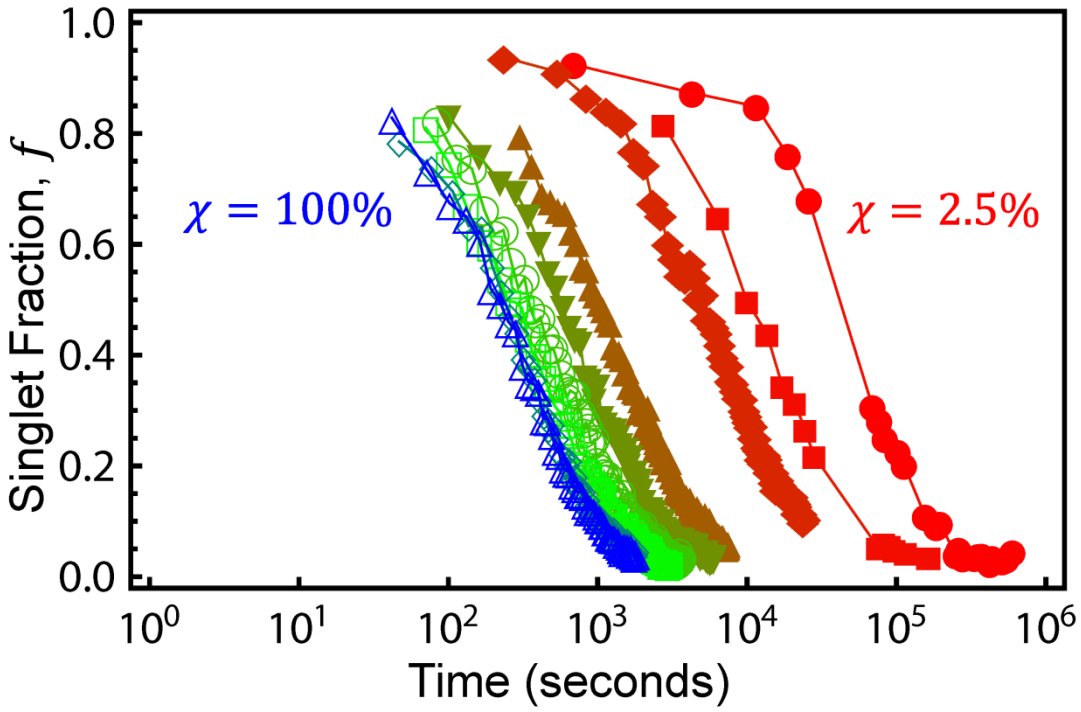

Figure 3-2: Singlet fraction vs. time at a constant salt concentration $[\mathrm{NaCl}] = 50\ \mathrm{mM}$ for each sticky-end DNA coverage ratio χ at a temperature $\sim 8\ ^{\circ}\mathrm{C}$ below each respective melting temperature. From left (blue) to right (red), $\chi = 1, 0.75, 0.5, 0.4, 0.3, 0.2, 0.1, 0.05,$ and 0.025, respectively.

χ	T (℃)	T_m (℃)
0.025	12	22
0.05	22	28.4
0.1	25	34.5
0.2	33	41.5
0.3	36	44.3
0.4	36	45.4
0.5	38	46.9
0.75	40	48.3
1	42	50.3

Table 3-1: Temperatures and melting temperatures for the measurements of $f(t)$ at various DNA coverages, χ in Figure 3-2.

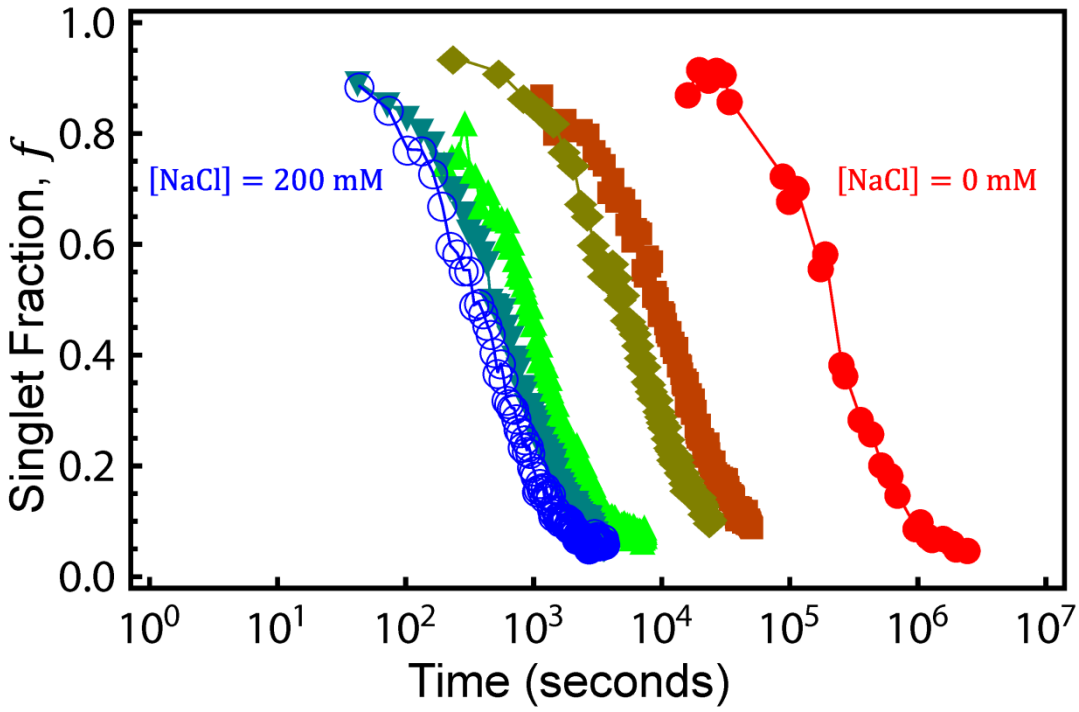

Figure 3-3: Singlet fraction vs. time at constant $\chi = 0.1$ for each salt concentration $[\mathrm{NaCl}]$ at a temperature $\sim 8\,℃$ below each respective melting temperature. From left (blue) to right (red), $[\mathrm{NaCl}] = 200, 150, 100, 50, 25,$ and 0 mM, respectively.

[NaCl] (mM)	T (℃)	T_m (℃)
0	12	16.6
25	18	28.5
50	25	34.5
100	37	43.3
150	39	47.9
200	40	50.3

Table 3-2: Temperatures and melting temperatures for the measurements of $f(t)$ at various salt concentrations, [NaCl]'s in Figure 3-3.

3.2. GENERAL COLLOIDAL AGGREGATION

To quantitatively analyze the aggregation of our system, we consider Smoluchowski's coagulation [13, 68]. First, we consider a general colloidal aggregation reaction:

$$n_i + n_j \rightleftharpoons n_k, \tag{3-1}$$

where n_i refers to the number density of clusters with i particles. Define k_{ij}^{on} as the aggregation rate for i- and j-particle clusters to group into $(i+j)$-particle clusters. Define k_{ij}^{off} as the dissociation rate as $(i+j)$-particle clusters disintegrate into i- and j-particle clusters. The chemical reaction can be decomposed into four parts (Figure 3-4); the red and blue reactions increase the number density of k-particle clusters from aggregation and dissociation, respectively, while the green and yellow reactions decrease the number density of k-particle clusters from aggregation and dissociation, respectively. Therefore, we can write down standard rate equation from the chemical equation as

$$\frac{d}{dt}n_k = \frac{1}{2}\sum_{i+j=k} k_{ij}^{on} n_i n_j - \sum_{i=1}^{\infty} k_{ik}^{on} n_i n_k - \frac{1}{2}\sum_{i+j=k} k_{ij}^{off} n_k + \sum_{i=1}^{\infty} k_{ik}^{off} n_{i+k}, \tag{3-2}$$

with initial conditions $n_k(t=0) = \delta_{k1} C_0$, where C_0 is the total particle concentration. The four terms on the right-hand side refer to the red (top-left), green (top-right), yellow (bottom-left), and blue (bottom-right) reactions in Figure 3-4. The first term (red) means that i- and j-particle clusters group into k-particle clusters. The second term (green) term means that i- and k-

particle clusters group into $(i+k)$-particle clusters. The third term (yellow) means that k-particle clusters disintegrate into i- and j-particle clusters. The fourth term (blue) means that $(i+k)$-particle clusters disintegrate into i- and k-particle clusters. To analytically solve equation (3-2), we consider the first order approximation: $k_{ij}^{on} = k^{on}$ and $k_{ij}^{off} = k^{off}$ [13, 68], which means the aggregation and dissociation rates are independent of cluster sizes. Then, equation (3-2) can be reduced to

$$\frac{d}{dt}n_k = \frac{1}{2}k^{on}\sum_{i+j=k} n_i n_j - k^{on}\sum_{i=1}^{\infty} n_i n_k \\ -\frac{1}{2}k^{off}\sum_{i+j=k} n_k + k^{off}\sum_{i=1}^{\infty} n_{i+k}. \quad (3\text{-}3)$$

To analytically solve equation (3-3), we define $S(t) \equiv \sum_{k=1}^{\infty} n_k$. Since $n_i \geq 0$ for any i, $S(t) > 0$. Since $n_1 = C_0$ and $n_{j>1} = 0$ at $t = 0$,

$$S(0) = C_0. \quad (3\text{-}4)$$

Summing up equation (3-3) from $k = 1$ to $k = \infty$ gives

$$\frac{d}{dt}\sum_{k=1}^{\infty} n_k = \frac{1}{2}k^{on}\sum_{k=1}^{\infty}\sum_{i+j=k} n_i n_j - k^{on}\sum_{k=1}^{\infty}\sum_{i=1}^{\infty} n_k n_i$$

$$-\frac{1}{2}k^{off}\sum_{k=1}^{\infty}\sum_{i+j=k} n_k + k^{off}\sum_{k=1}^{\infty}\sum_{i=1}^{\infty} n_{i+k}. \quad (3\text{-}5)$$

The term on the left-hand side is simply $\frac{d}{dt}S(t)$. Each term on the right-hand side can be expressed in terms of $S(t)$:

1. **The first term:**

   From Figure 3-5, we can visualize that

   $$\sum_{k=1}^{\infty}\sum_{i+j=k} a_{ij} = \sum_{i=1}^{\infty}\sum_{j=1}^{\infty} a_{ij}.$$

   Therefore, the first term can be written as

   $$\frac{1}{2}k^{on}\sum_{k=1}^{\infty}\sum_{i+j=k} n_i n_j = \frac{1}{2}k^{on}\sum_{i=1}^{\infty}\sum_{j=1}^{\infty} n_i n_j$$

   $$= \frac{1}{2}k^{on}\sum_{i=1}^{\infty} n_i \sum_{j=1}^{\infty} n_j$$

   $$= \frac{1}{2}k^{on}S(t)^2.$$

2. **The second term:**

The second term can be easily written in terms of $S(t)$ as

$$-k^{on}\sum_{k=1}^{\infty}\sum_{i=1}^{\infty}n_k n_i = -k^{on}\sum_{k=1}^{\infty}n_k\sum_{i=1}^{\infty}n_i = -k^{on}S(t)^2.$$

3. **The third term:**

Since we know that

$$\sum_{i+j=k} n_k = (k-1)n_k,$$

the third term can be rewritten as

$$-\frac{1}{2}k^{off}\sum_{k=1}^{\infty}\sum_{i+j=k}n_k = -\frac{1}{2}k^{off}\sum_{k=1}^{\infty}(k-1)n_k$$

$$= -\frac{1}{2}k^{off}\left(\sum_{k=1}^{\infty}kn_k - \sum_{k=1}^{\infty}n_k\right)$$

$$= -\frac{1}{2}k^{off}[C_0 - S(t)].$$

From the above derivation, we use the equivalence of $C_0 = \sum_{k=1}^{\infty}kn_k$.

4. **The fourth term:**

Similarly, we can rewrite the fourth term as

$$k^{off}\sum_{k=1}^{\infty}\sum_{i=1}^{\infty}n_{i+k} = k^{off}\sum_{k'=1}^{\infty}\sum_{i+k=k'}n_{k'}$$

$$= k^{off}\sum_{k'=1}^{\infty}(k'-1)n_{k'}$$

$$= k^{off}[C_0 - S(t)].$$

Putting the above derivations for rewriting each term in terms of $S(t)$, equation (3-5) can be rewritten as

$$\frac{d}{dt}S(t) = -\frac{1}{2}k^{on}S(t)^2 + \frac{1}{2}k^{off}[C_0 - S(t)]. \quad (3\text{-}6)$$

We will discuss equation (3-6) in two aspects: 1) thermodynamics, and 2) kinetics.

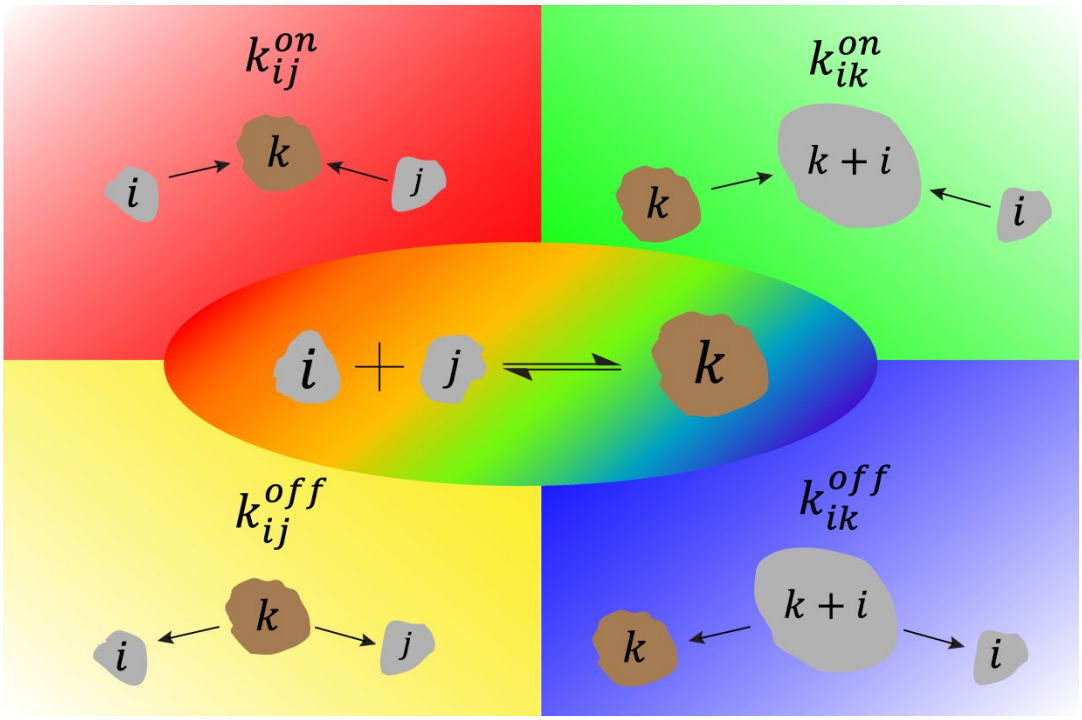

Figure 3-4: Decomposition of a colloidal chemical reaction.

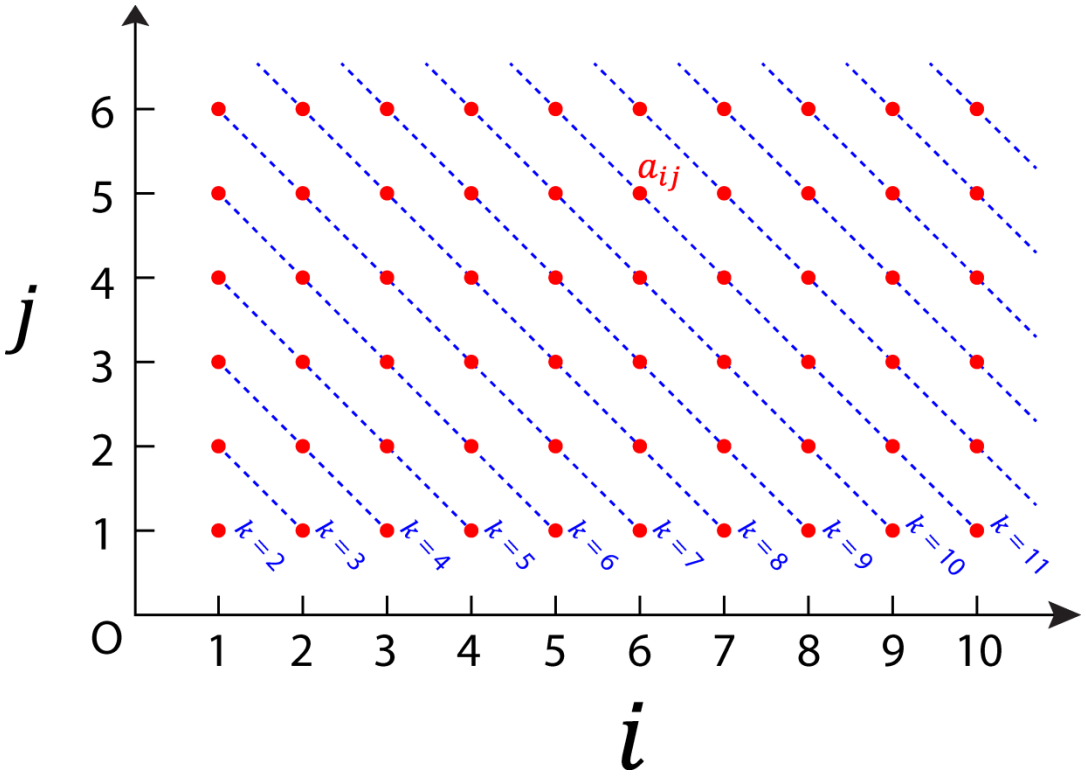

Figure 3-5: The visualization of the summation equivalence of $\sum_{k=1}^{\infty}\sum_{i+j=k} a_{ij}$ and $\sum_{i=1}^{\infty}\sum_{j=1}^{\infty} a_{ij}$.

3.2.2. THERMODYNAMICS

In thermodynamics, $\frac{d}{dt}S = 0$, equation (3-6) becomes

$$-\frac{1}{2}k^{on}S^2 + \frac{1}{2}k^{off}[C_0 - S] = 0,$$

and can be solved as

$$S = \frac{-1 + \sqrt{1 + 4KC_0}}{2K}, \tag{3-7}$$

where $K \equiv k^{on}/k^{off}$ is the equilibrium constant. In equation (3-3), if we take $k = 1$ and $\frac{d}{dt}n_1 = 0$, we get

$$Kn_1S - S + n_1 = 0 \tag{3-8}$$

or

$$n_1 = \frac{S}{KS + 1} = \frac{1 + 2KC_0 - \sqrt{1 + 4KC_0}}{2K^2C_0}.$$

Then, the singlet fraction f can be written as

$$f \equiv \frac{n_1}{C_0} = \frac{1 + 2KC_0 - \sqrt{1 + 4KC_0}}{2K^2C_0^2}, \tag{3-9}$$

which is exactly the same as equation (2-9) [21, 22, 27]. Since equation (3-2) only considers the aggregation of colloidal particles disregarding inner cluster structures, such as triangle structures discussed in Section 2.4.1, the colloidal aggregation described in equation (3-2) is the same as the system of open structures discussed in Section 2.4.2.

3.2.3. KINETICS

In kinetics, we consider the limit of full aggregation or equivalently $T \ll T_m$ since in Table 3-1 and Table 3-2, the chosen temperatures are all significantly lower than the corresponding temperatures. This limit approaches the behavior expected by setting $k^{off} = 0$ in equation (3-3) and equation (3-6), which then are reduced to

$$\frac{d}{dt} n_k = \frac{1}{2} k^{on} \sum_{i+j=k} n_i n_j - k^{on} n_k S(t), \tag{3-10}$$

and

$$\frac{d}{dt} S(t) = -\frac{1}{2} k^{on} S(t)^2 \tag{3-11}$$

respectively. From equations (3-11) and (3-4), $S(t)$ can be solved as

$$S(t) = \frac{C_0}{1 + \frac{t}{2\tau}},$$

where

$$\tau \equiv \frac{1}{k^{on} C_0} \tag{3-12}$$

is the colloidal aggregation time scale. By taking $k = 1$ in equation (3-10), we get

$$\frac{d}{dt}n_1 = -k^{on}n_1S(t) = -\frac{k^{on}C_0}{1+\frac{t}{2\tau}}n_1,$$

which gives

$$n_1 = \frac{C_0}{\left(1+\frac{t}{2\tau}\right)^2}$$

or

$$f \equiv \frac{n_1}{C_0} = \frac{1}{\left(1+\frac{t}{2\tau}\right)^2} \tag{3-13}$$

[13, 28, 68]. Here, we learn that for a colloidal system with a definite aggregation rate k^{on} between particles and a particle concentration C_0, the time-dependent singlet fraction f can be determined from equation (3-13), in which the aggregation time scale τ depends on the aggregation rate k^{on} and particle concentration C_0 [see equation (3-12)].

3.2.4. CONCLUSION

To quantitatively analyze colloidal aggregation, we consider the general colloidal reaction [see equation (3-1)] and discuss thermodynamics and kinetics of particle aggregation. For thermodynamics, every quantity in the system is time-independent in equilibrium. Then, the thermodynamic behavior can be described by equation (3-9), which is exactly the same as equation (2-9) for the system of open structures (Section 2.4.2). For kinetics, we consider the limit of full aggregation or equivalently $k^{off} = 0$. We find out that the time-dependent aggregation behaviors can be described by equation (3-13) with an aggregation time scale $\tau = \frac{1}{k^{on}C_0}$. Equation (3-13) will be mainly used since the goal of this chapter is to understand the aggregation kinetics of colloids.

3.3. TWO-DIMENSIONAL AGGREGATION RATES

In this section, we will quantify the aggregation rate k^{on} of colloids for a two-dimensional system. In equation (3-13), we know how singlet fraction decays with time. However, the decay time scale, τ, is still unclear unless

the aggregation rate k^{on} is clarified [see equation (3-12)]. Colloidal aggregation can be categorized into two types: 1) diffusion-limited aggregation (DLA), and 2) reaction-limited aggregation (RLA). In the diffusion-limited case, k^{on} is mainly controlled from particle diffusion because particles get bound immediately once they touch each other. For the reaction-limited case, k^{on} is determined by the competition between particle diffusion and particle reaction/binding rate, k_r. In the following, we will discuss and compare the aggregation rates, k^{on}'s, for both the diffusion- and the reaction-limited aggregation cases.

3.3.1. DIFFUSION-LIMITED AGGREGATION

In a diffusion-limited aggregation system, particles can diffuse freely before colliding with each other, so the free particle concentration distribution $C(\boldsymbol{r}, t)$ can be described by Fick's Law:

$$\frac{\partial}{\partial t} C(\boldsymbol{r}, t) = 2D\nabla^2 C(\boldsymbol{r}, t), \tag{3-14}$$

where $2D$ is the "relative" diffusion coefficient for a pair of particles. Consider the system is in a stationary state, $\frac{\partial}{\partial t} C(\boldsymbol{r}, t) = 0$ or $C(\boldsymbol{r}, t) = C(\boldsymbol{r})$. Then,

equation (3-14) is reduced to Poisson's equation: $\nabla^2 C(\boldsymbol{r}) = 0$. To simplify our problem, we consider that one particle is fixed at O with a radius $2R_p$, and another point-like particle freely diffuses within the disk of radius R_{disk} (Figure 3-6). The total particle concentration between $r = 2R_p$ and $r = R_{\text{disk}}$ is C_0. Then, the particle concentration can be written in terms of R_{disk} as

$$C_0 = \frac{1}{\pi(R_{disk})^2 - \pi\left(2R_p\right)^2}.$$

For a dilute particle concentration: $R_p^2 C_0 \ll 1$. Therefore, the disk radius can be written in terms of particle concentration as

$$R_{\text{disk}} = \sqrt{\frac{1 + 4\pi R_p^2 C_0}{\pi C_0}} \approx \frac{1}{\sqrt{\pi C_0}}.$$

Since our system has the azimuthal symmetry, $C(\boldsymbol{r}) = C(r)$. Equation (3-14) can be reduced to

$$\frac{1}{r}\frac{d}{dr}\left[r\frac{d}{dr}C(r)\right] = 0 \tag{3-15}$$

with a normalization condition

$$\int_{2R_p}^{R_{\text{disk}}\approx\frac{1}{\sqrt{\pi C_0}}} dr\ 2\pi r C(r) = 1. \tag{3-16}$$

In diffusion-limited aggregation system, particles bind to each other at their first collision. Equivalently, the unbound particle concentration at $r = 2R_p$ is zero:

$$C\left(2R_p\right) = 0. \tag{3-17}$$

With equation (3-17), we can solve equation (3-15) as

$$C(r) = c \ln\left(\frac{r}{2R_p}\right),$$

where c can be determined from equation (3-16) as

$$\frac{1}{c} = \frac{1}{2C_0}\left[-\ln\left(4\pi R_p^2 C_0\right) - 1 + 4\pi R_p^2 C_0\right].$$

Since the system has a dilute particle concentration: $R_p^2 C_0 \ll 1$, we can estimate c as

$$\frac{1}{c} \approx \frac{1}{2C_0}\left[-\ln\left(4\pi R_p^2 C_0\right) - 1\right] = \frac{-\ln\left(4\pi e R_p^2 C_0\right)}{2C_0}.$$

Then, $C(r)$ can be determined as

$$C(r) \approx \frac{2C_0}{-\ln\left(4\pi e R_p^2 C_0\right)} \ln\left(\frac{r}{2R_p}\right).$$

A schematic diagram of spatial distribution of particle concentration $C(r)$ in diffusion-limited system is shown in Figure 3-7 (a). For $r \gg 2R_p$, $C(r)$ is nearly r-independent. However, as r approaches $2R_p$, $C(r)$ approaches zero. Since the number of particles flowing into the inner boundary, $r = 2R_p$ is $k_{DLA}^{on} C_0$, where k_{DLA}^{on} is the aggregation rate for diffusion-limited system, we can write k_{DLA}^{on} as

$$k_{DLA}^{on} C_0 = 2\pi\left(2R_p\right)(2D)\frac{d}{dr}C\left(2R_p\right)$$

$$= 4\pi D c$$

$$\approx \frac{8\pi D C_0}{-\ln\left(4\pi e R_p^2 C_0\right)}$$

or

$$k_{DLA}^{on} \approx \frac{8\pi D}{-\ln\left(4\pi e R_p^2 C_0\right)}. \tag{3-18}$$

From equation (3-12), the aggregation time scale in diffusion-limited system can be written as

$$\tau_{DLA} = \frac{1}{k_{DLA}^{on} C_0} \approx \frac{-\ln\left(4\pi e R_p^2 C_0\right)}{8\pi D C_0} \tag{3-19}$$

[28]. This is the well-known diffusion-limited aggregation time. For a three-dimensional system, the diffusion-limited aggregation time is $\tau_{DLA}(3D) = \frac{1}{8\pi D R_p C_0}$ [13, 68].

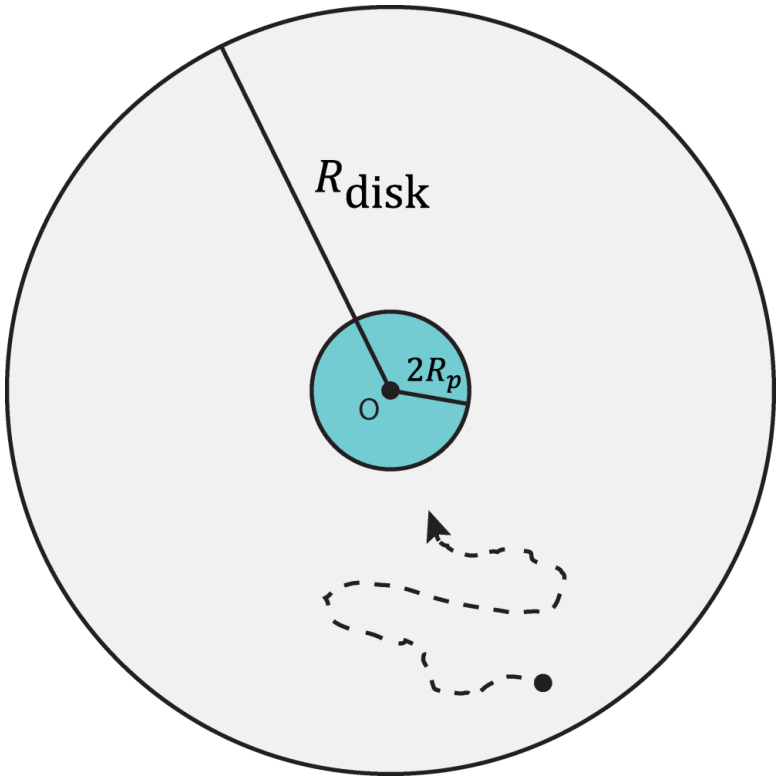

Figure 3-6: The schematic diagram of diffusion of a particle within a disk in a stationary state.

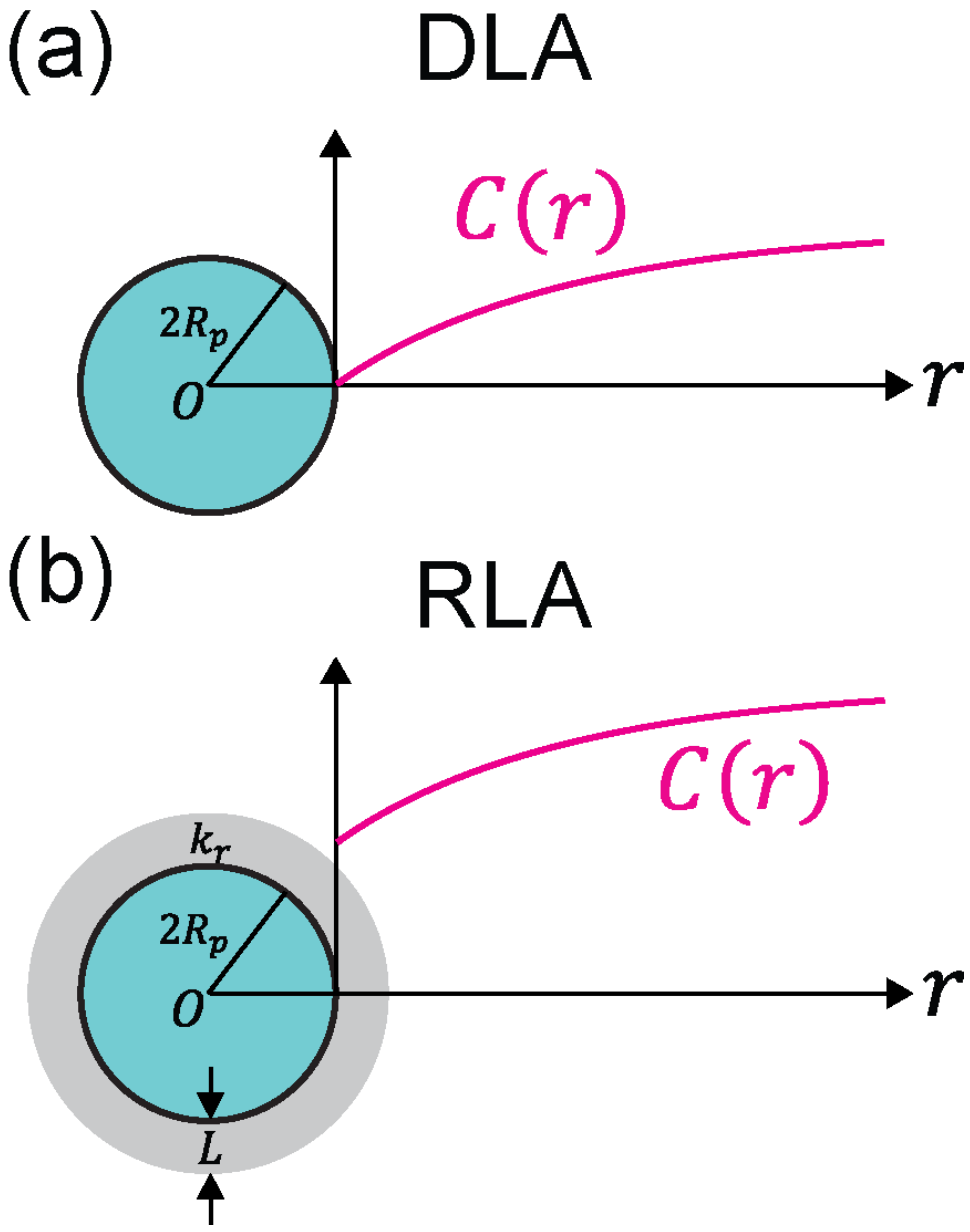

Figure 3-7: Schematic diagram of spatial distribution of free particle concentrations in (a) DLA, and (b) RLA system.

3.3.2. REACTION-LIMITED AGGREGATION

In a reaction-limited system, particles do not immediately bind together once they collide. The boundary condition for diffusion-limited system, equation (3-17), is not valid in reaction-limited system and should be modified as

$$2\pi(2R_p)(2D)\frac{d}{dr}C(2R_p) = k_r\left[L\,2\pi(2R_p)\,C(2R_p)\right] \tag{3-20}$$

[28]. The left-hand side is the number of particles flowing into the inner boundary, $r = 2R_p$, per unit time or the number of binding reaction events per unit time. The right-hand side is the number of particles in the reaction region, which has the reaction thickness L (Figure 3-7 (b)), times the binding reaction rate, k_r. Solving equation (3-15) with the boundary condition, equation (3-20) yields

$$C(r) = c'\left[\ln\left(\frac{r}{2R_p}\right) + \frac{D}{R_p k_r L}\right],$$

where c' can be determined from the normalization condition, equation (3-16) as

$$\frac{1}{c'} \approx \frac{1}{2C_0}\left\{\left[-\ln\left(4\pi e R_p^2 C_0\right)\right] + \frac{2D}{R_p k_r L}\right\}.$$

Here, we already assume the system has the dilute particle concentration: $R_p^2 C_0 \ll 1$. The distribution of particle concentration can be determined as

$$C(r) \approx \frac{2C_0}{\left[-\ln\left(4\pi e R_p^2 C_0\right)\right] + \frac{2D}{R_p k_r L}}\left[\ln\left(\frac{r}{2R_p}\right) + \frac{D}{R_p k_r L}\right].$$

The schematic diagram of spatial distribution of $C(r)$ is shown in Figure 3-7. Similarly, for $r \gg 2R_p$, $C(r)$ is nearly r-independent. However, when r approaches $2R_p$, $C(r)$ approaches a finite value instead of zero. With $C(r)$ being known, we can determine the aggregation rate for reaction-limited system, k_{RLA}^{on} as

$$\begin{aligned} k_{RLA}^{on} C_0 &= 2\pi\left(2R_p\right)(2D)\frac{d}{dr}C\left(2R_p\right) \\ &= 4\pi D c' \\ &\approx \frac{8\pi D C_0}{-\ln\left(4\pi e R_p^2 C_0\right) + \frac{2D}{R_p k_r L}} \end{aligned}$$

or

$$k_{RLA}^{on} \approx \frac{8\pi D C_0}{-\ln\left(4\pi e R_p^2 C_0\right) + \frac{2D}{R_p k_r L}}. \tag{3-21}$$

Also, the aggregation time scale for reaction-limited system from equation (3-12) can be determined as

$$\tau_{RLA} \approx \frac{-\ln\left(4\pi e R_p^2 C_0\right) + \frac{2D}{R_p k_r L}}{8\pi D C_0} \tag{3-22}$$

[28].

3.3.3. CONNECTIONS BETWEEN DLA AND RLA

From comparing equations (3-19) and (3-22), we note that the reaction-limited aggregation time, τ_{RLA}, can be written in terms of the diffusion-limited aggregation time, τ_{DLA} as

$$\tau_{RLA} \approx \tau_{DLA}\left[1 + \frac{2D}{R_p L k_r \ln\left(\frac{1}{4\pi e R_p^2 C_0}\right)}\right]$$

$$= \tau_{DLA}\left[1 + \frac{\tau_r}{\tau_c \ln\left(\frac{1}{4\pi e R_p^2 C_0}\right)}\right], \tag{3-23}$$

where $\tau_r \equiv \frac{1}{k_r}$ is the reaction time, which is the time for a pair of particles to bind if they are held in contact, and $\tau_c \equiv \frac{R_p L}{2D}$. The physical meaning of τ_c is the collision time, which is the transit time for a pair of particles to be able to react during each encounter. In our system, our particles have a radius R_p and are coated with DNA strands the length of which is L. Therefore, when a pair of particles are separated within a surface separation $2L$, the DNA strands between them can reach each other and react. However, due to strong repulsion by the unbound DNA strands on one particle encountering the surface of the complementary particle, the closest surface separation for a pair of particles to approach each other is one DNA length, L [21]. Therefore, during each encounter, the surface separation of a pair of particles stays between L and $2L$ (Figure 3-8). Also, the diffusion coefficient for a pair of particles with a surface separation L is reduced by a factor of L/R_p [13]. Therefore, we can estimate the time for this pair of particles to relatively diffuse a radial distance L, the collision time, is $\frac{L^2}{2D\ L/R_p} = \frac{R_p L}{2D}$. Then, the interpretation of equation (3-23) is: the time for a pair of particles to bind in a reaction-limited system is the diffusion time τ_{DLA}, the time to meet each other through diffusion, times the number of collisions needed to trigger the

reaction [28]. If a pair of particles can be held in contact, one reaction time τ_r is needed to trigger the reaction. Practically, particles can diffuse toward and away from each other. For each counter, particles only have one collision time τ_c to react. Therefore, the number of collisions needed to trigger the reaction is the ratio of reaction time τ_r to collision time τ_c. We also note that if the reaction time τ_r is negligible compared to collision time τ_c, which means $\tau_r \ll \tau_c$, then the reaction-limited aggregation time approaches diffusion-limited aggregation time. Therefore, we find that diffusion-limited system can be considered a reaction-limited system with zero reaction time, making the reaction instant [69, 70].

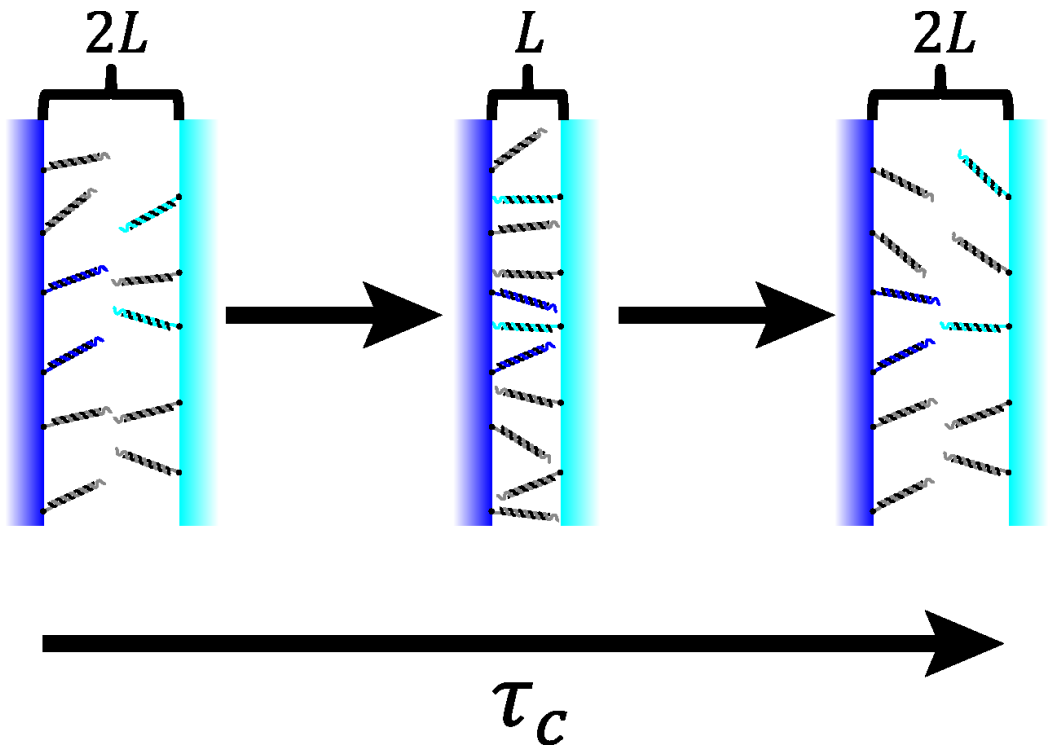

Figure 3-8: Schematic diagram of a collision process of a pair of particles. The collision starts/ends when a pair of particles approaches/ leaves each other at $2L$ surface separation. The time a collision process takes is a collision time, τ_c.

3.4. CALCULATION OF REACTION TIME, τ_r

To determine reaction-limited aggregation time from equation (3-23), we need to calculate the reaction time τ_r. In this section, we will determine the reaction time from the solution DNA hybridization time and the geometry of our DNA construct [28].

To calculate the reaction time τ_r, we must consider DNA hybridization kinetics between particles during the collision process (Figure 3-8). The reaction time is increased by slow hybridization of a pair of complementary strands and reduced by the number of possible bonding configurations N_G [28]. Here, we estimate that $N_G \approx g_b N_b$, where N_b is the number of potential bonds a pair of particles can form, and g_b, the number of DNA strands on one particle that a complementary strand on the opposing particles can reach [see Sections 2.4.3 and 2.4.6]. The reaction time can be written as

$$\tau_r = \frac{\tau_h}{N_G} \approx \frac{\tau_h}{g_b N_b}, \tag{3-24}$$

where τ_h is the hybridization time for a pair of complementary strands.

To fully determine reaction time from equation (3-24), we need to determine g_b, N_b, and τ_h. In Section 2.4.6, we learn that g_b and N_b can be determined by either calculation or computation [21, 22, 27, 28]. In the following, we use a similar logic used in Section 3.3.3 to calculate the hybridization time τ_h by determining the rotational search time τ_s, the rotational transit time τ_θ, and the intrinsic solution hybridization time τ_{DNA} for a pair of complementary strands [28].

3.4.1. ROTATIONAL SEARCH TIME FOR DNA STRANDS, τ_s

To calculate the rotational search time, we look into the dynamics of rotational diffusion of a pair of complementary strands [28]. Consider a pair of spheres each of which has a reaction patch ligand and receptor (Figure 3-9). Each sphere is allowed to rotationally diffuse freely, so the ligand and the receptor can rotate freely along the surface of the corresponding spheres. The time for a ligand and a receptor to meet each other by rotational diffusion is mostly determined by the relative capture surface, which is the ratio of the area of the ligand/receptor and the surface area of the sphere [71].

Similarly, in our case, as shown in Figure 3-10, since DNA sticky ends can only be hybridized together while both in red area, we can adapt the concept of Figure 3-9 to Figure 3-10 [28]. The time for a pair of complementary sticky ends to meet each other by the rotational diffusion of their dsDNA backbones can be estimated as

$$\tau_s = \frac{1}{D_\theta}\frac{\ln(4)}{\alpha}, \tag{3-25}$$

where $D_\theta \equiv 8\pi\eta L^3\beta$, η the solvent viscosity, is the rotational diffusion coefficient of sticky ends, $\alpha \equiv \left(2\pi d R_g\right)/(2\pi L^2)$, $2\pi d R_g$ is the red area and $2\pi L^2$ the surface area of the hemisphere (Figure 3-10), is the relative capture surface. For each pair of complementary DNA strands, d depends on the distance between them. If the distance between streptavidin-biotin binding sites of a pair of DNA strands is h, then $d = \sqrt{L^2 - (h/2)^2}$. If it is $2L$, then $d = 0$. Hence, $\sqrt{L^2 - (h/2)^2} \geq d \geq 0$. For a good estimate of the average of α, we choose

$$\bar{\alpha} \approx \left(2\pi \bar{d} R_g\right)/(2\pi L^2), \tag{3-26}$$

where $\bar{d} \equiv \frac{1}{2}\sqrt{L^2 - (h/2)^2}$. Introducing equation (3-26) into equation (3-25), we can estimate the rotational search time τ_s as

$$\tau_s \approx \frac{1}{D_\theta}\frac{\ln(4)}{\bar{\alpha}}$$

$$\approx \frac{\ln(4)}{D_\theta}\frac{2\pi L^2}{2\pi \bar{d} R_g}$$

$$= \frac{L^2 \ln(4)}{D_\theta \bar{d} R_g} \qquad \text{(3-27)}$$

[28].

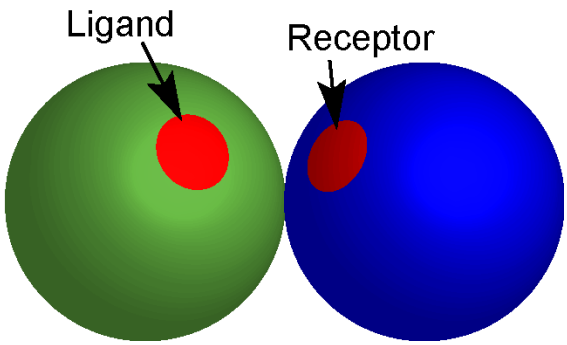

Figure 3-9: A pair of spheres with reaction patches held in contact. The red patches are a ligand for the green sphere and a receptor for the blue sphere. The two spheres are held in contact and are allowed to rotationally diffuse. The ligand–receptor reaction will be triggered when the ligand and the receptor touch each other by both having diffused to the contact point.

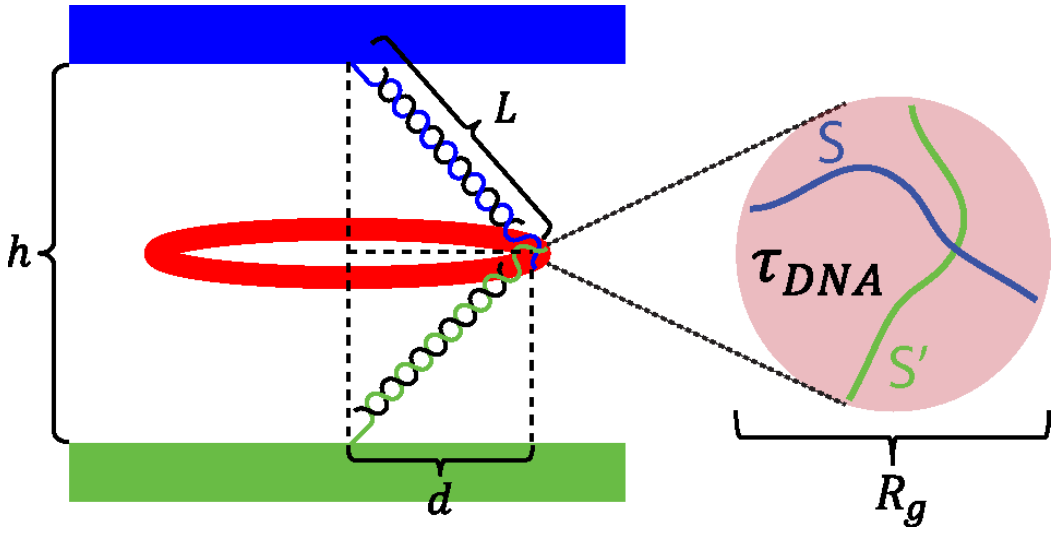

Figure 3-10: A pair of complementary DNA strands attached to colloidal surfaces. Since the backbones of the DNA strands can rotate freely, the spatial diffusion space of each sticky end is the surface of a hemisphere with a radius L. The overlapping area of the two hemispheres is the red ring. These two DNA sticky ends can only hybridize when they are both in the ring. Hence, the ring is like the reaction patch in Figure 3-9.

3.4.2. ROTATIONAL TRANSIT TIME, τ_θ

To determine the rotational transit time, we need to determine how fast a pair of DNA sticky ends rotationally diffuses their own gyration radius, R_g relatively. As shown in Figure 3-10, once a pair of DNA sticky ends encounters each other by rotational diffusion of their dsDNA backbones, they will stay within binding range ($\sim R_g$) until they diffuse apart or until hybridization occurs. Hence, the rotational transit time τ_θ is the time for the pair of DNA to relatively diffuse a solid angle $\sim \left(R_g/L\right)^2$ as shown in Figure 3-11, which gives

$$\tau_\theta \approx \frac{1}{8D_\theta}\left(\frac{R_g}{L}\right)^2 \tag{3-28}$$

[28].

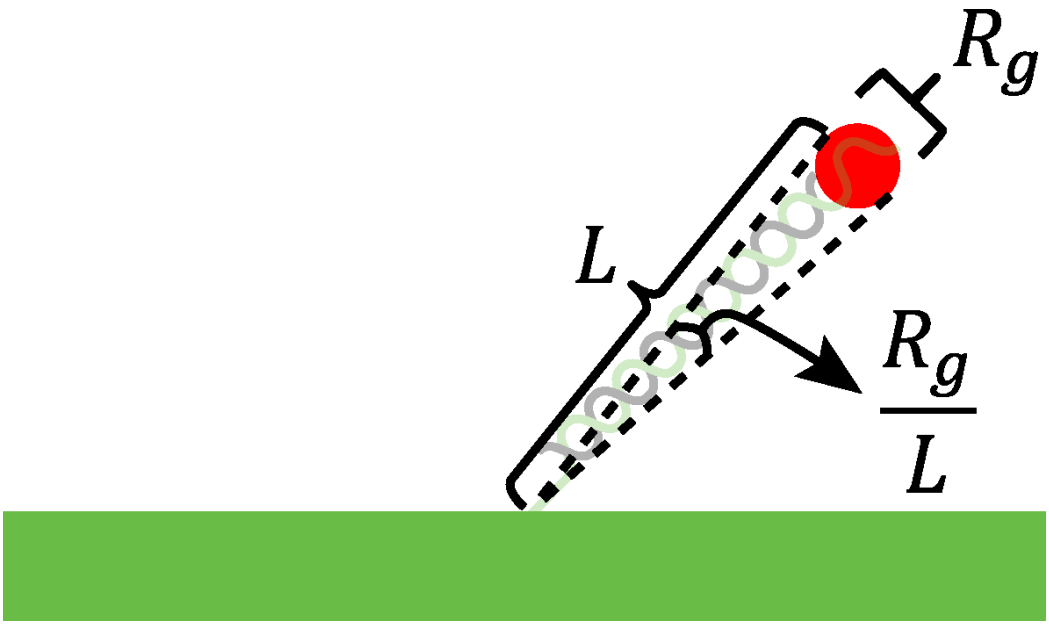

Figure 3-11: The angle for the sticky end to rotationally diffuse its own size.

3.4.3. CONNECTIONS BETWEEN τ_h AND τ_{DNA}

To calculate hybridization time τ_h from the intrinsic solution hybridization time τ_{DNA}, we follow the same logic used in Section 3.3.3. The time for a pair of complementary strands to hybridize can be calculated as the time for this pair of strands to find each other through rotational diffusion, τ_s, times the number of encounters needed to trigger the hybridization, which can be

estimated as the ratio of the intrinsic solution hybridization time τ_{DNA} to the rotational transit time τ_θ. Therefore, hybridization time can be written as

$$\tau_h = \tau_s \left(1 + \frac{\tau_{DNA}}{\tau_\theta}\right) \tag{3-29}$$

[28], where τ_s and τ_θ can be determined from equations (3-27) and (3-28), respectively. Here, the intrinsic solution hybridization time τ_{DNA} is simply the time for a pair of complementary DNA strands to hybridize if they are held within their gyration radius R_g (Figure 3-10). Therefore, τ_{DNA} does not depend on the dsDNA backbone and DNA concentration, but on the salt concentration of the buffer, the length of strands, and possibly the sequences.

Introducing equation (3-29) into equation (3-24), the reaction time can be rewritten as

$$\tau_r = \frac{1}{g_b N_b} \tau_s \left(1 + \frac{\tau_{DNA}}{\tau_\theta}\right). \tag{3-30}$$

3.5. HYBRIDIZATION ENERGY BARRIER

To determine the energy barrier for a pair of complementary strands to hybridize, we need to determine a minimum energy from electrical repulsion during the hybridization process. Since each phosphate group of the DNA strands carries negative charge [15], The strands need to overcome an electrical repulsion barrier to hybridize. Among many kinds of electrical repulsions that exist in nature, here we assume the electrical repulsion to be dominated by Coulomb repulsion [28]. Therefore, the intrinsic solution hybridization time for a pair of complementary strands can further be refined as:

$$\tau_{DNA} = \tau_{DNA}^{(0)} e^{-\beta U}, \tag{3-31}$$

where U is the minimum Coulomb repulsion barrier during the hybridization process and $\tau_{DNA}^{(0)}$, the intrinsic hybridization time if all the repulsions are well screened, namely $U = 0$ [28]. In this section, we calculate the Coulomb repulsion barrier U during the hybridization process of a pair of complementary strands.

To calculate the total Coulomb repulsion barrier, we need to know which intermediate configuration of a pair of complementary strands yields the lowest repulsion barrier. As shown in Figure 3-12, the structure of our sticky ends is an 11-mer ssDNA strand as shown in Table 2-1, so the total Coulomb repulsion between these strands can be written as

$$U = \frac{q^2}{4\pi\epsilon\epsilon_0}\sum_{i=1}^{11}\sum_{j=1}^{11}\frac{1}{r_{ij}}e^{-\frac{r_{ij}}{\lambda_D}}, \tag{3-32}$$

where q is the elementary charge, ϵ, the dielectric constant of the buffer, ϵ_0, absolute permittivity, λ_D, Debye-screening length, and r_{ij}, the distance between the i^{th} monomer in DNA S and the j^{th} monomer in DNA S' (Figure 3-12) [28]. Therefore, to determine the Coulomb repulsion barrier for hybridization of DNA S and DNA S', we need to know which configuration r_{ij} yields the lowest Coulomb repulsion U among all possible configurations during the hybridization process. However, DNA hybridization is an unresolved problem, and the configurations and trajectories of the r_{ij}'s during the process are not clear. For a pair of complementary strands to hybridize, all the base pairs do not meet each other at the same time. At the beginning of the hybridization process, the pair of complementary strands may accidentally form an "incorrect" pair (T-A or G-C) (Figure 3-13). Although the

pair is incorrect, its strands can be held together temporarily, and the rest of bases can explore other possible binding configurations. The hybridization event is triggered once a “correct” pair is formed (Figure 3-14) and is termed nucleation. Once nucleation occurs, the remaining base pairs are formed one by one instantly, and the pair of complementary strands forms a well-known duplex helix. The second process is called zippering. Nucleation and zippering are the current schematic pictures for the hybridization process [72-74]. Nevertheless, which intermediate configuration r_{ij} gives the minimum energy barrier to hybridize is still not clear. Therefore, to calculate total Coulomb repulsion barrier, we try three different configurations: 1) parallel configuration, 2) duplex helix configuration, and 3) two-point-charge model [28]. In the following, we calculate the total Coulomb repulsions based on these configurations.

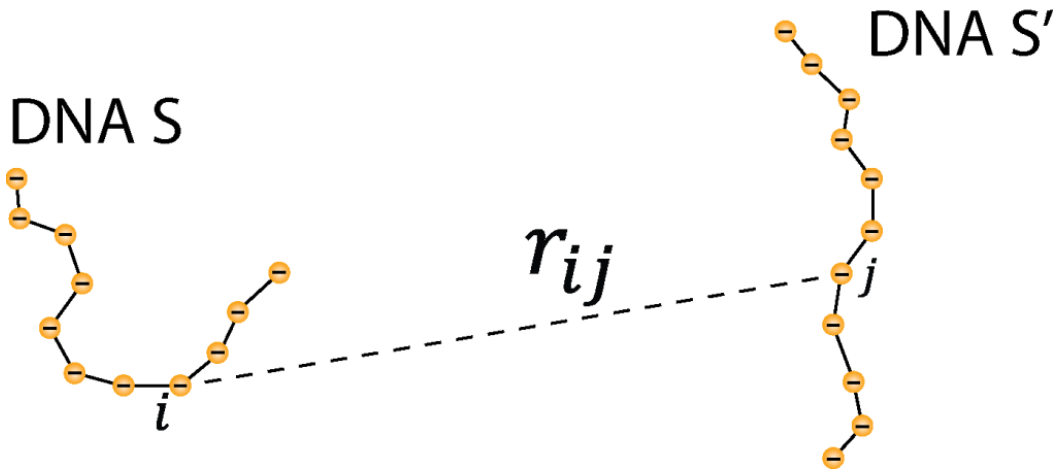

Figure 3-12: The schematic diagram of a pair of complementary DNA strands. The structure of our sticky-end DNA is 11-mer ssDNA strands as shown in Table 2-1.

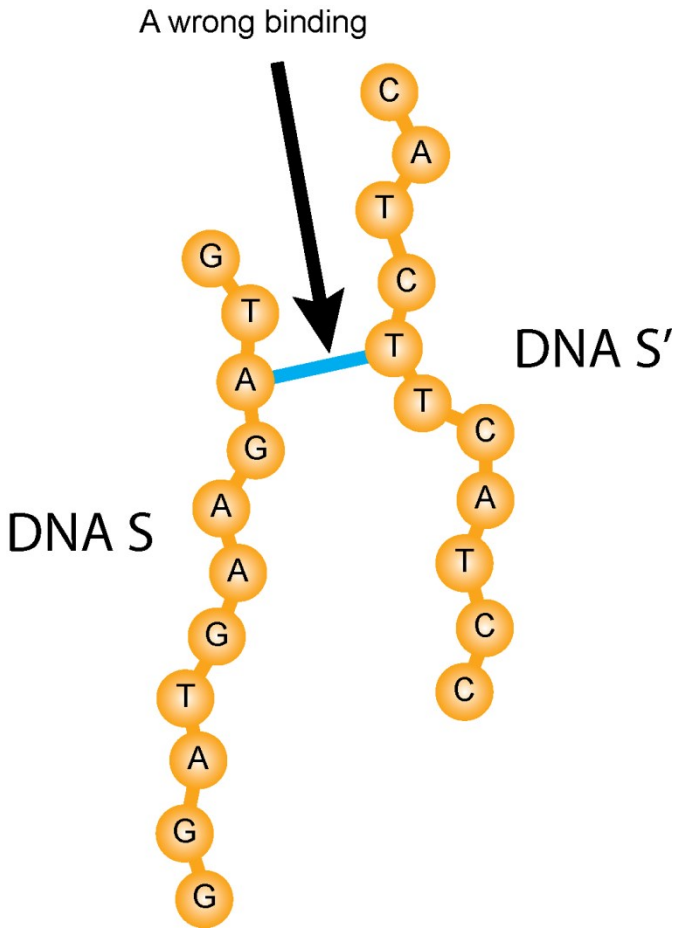

Figure 3-13: Schematic diagram of a wrong binding for a pair of complementary DNA strands.

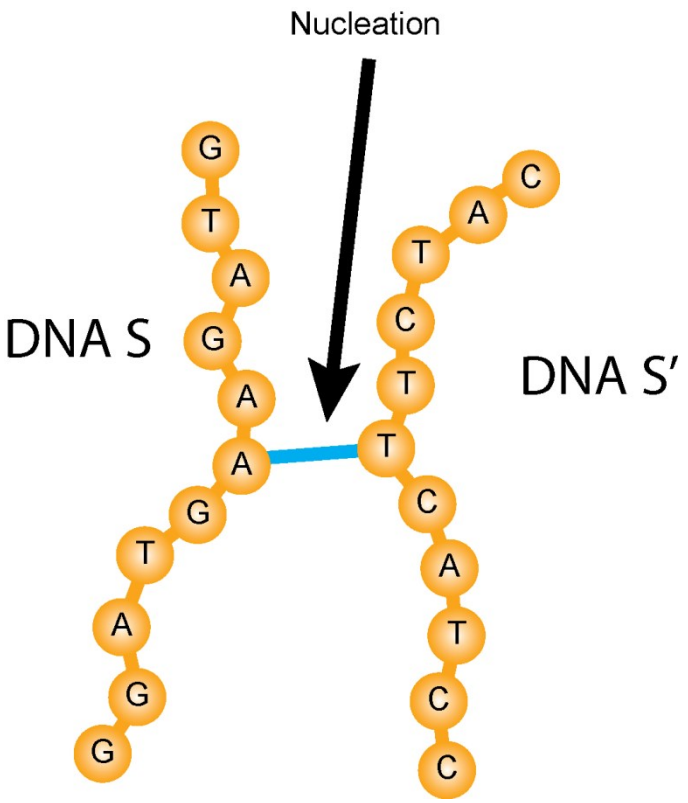

Figure 3-14: Schematic diagram of a nucleation of hybridization for a pair of complementary DNA strands.

3.5.2. PARALLEL CONFIGURATION

For parallel configuration, we consider a pair of complementary DNA strands lining up and separated by a distance a (Figure 3-15). From geometry, we can determine r_{ij} as

$$r_{ij} = \sqrt{a^2 + (i-j)^2 b^2}, \tag{3-33}$$

where $a \approx 2.3\,\mathrm{nm}$ is the separation between the two strands, and $b \approx 0.3\,\mathrm{nm}$ is the separation of each phosphate group along one DNA strand. Introducing equation (3-33) into equation (3-32), we can calculate the total Coulomb repulsion of this configuration as

$$U = \frac{q^2}{4\pi\epsilon\epsilon_0} \sum_{i=1}^{11} \sum_{j=1}^{11} \frac{1}{\sqrt{a^2 + (i-j)^2 b^2}} e^{-\frac{\sqrt{a^2+(i-j)^2 b^2}}{\lambda_D}} \tag{3-34}$$

[28].

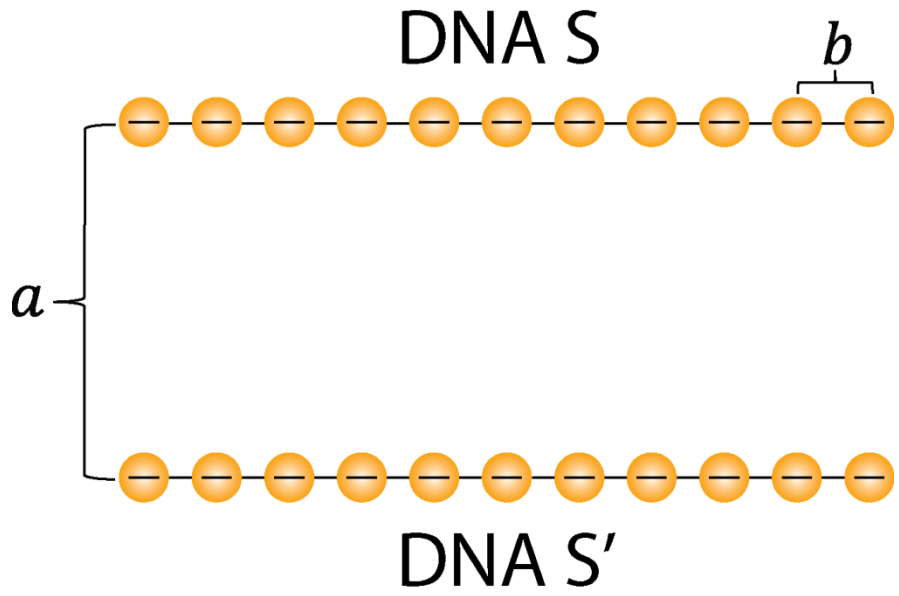

Figure 3-15: Parallel configuration. Two DNA strands are lined up and separated by a distance a.

3.5.3. DOUBLE HELIX CONFIGURATION

To calculate the total Coulomb repulsion energy for duplex helix configuration, we need to determine its r_{ij}. As shown in Figure 3-16, the two DNA strands are simplified as two helixes. The diameter of a helix is $a \approx 3.3\ \mathrm{nm}$. The phase difference between the two helixes is $\theta_p = \pi$. The height of each helix is $11b$, where $b \approx 0.3\ \mathrm{nm}$ is the separation of each phosphate group in

one DNA strand along the helix axis. Instead of considering discrete charges on the ssDNA strands as shown in Figure 3-12 and Figure 3-15, we consider each helix a curve with a uniform line charge density $\approx -$number of phosphate groups in the strand $\times\, q/$the length of the strand. The helixes can be expressed as

$$\begin{cases} r_{\mathrm{S},x} = \dfrac{a}{2}\cos\left(2\pi\dfrac{11}{n_t}t_{\mathrm{S}}\right) \\ r_{\mathrm{S},y} = \dfrac{a}{2}\sin\left(2\pi\dfrac{11}{n_t}t_{\mathrm{S}}\right) \\ r_{\mathrm{S},z} = 11bt_{\mathrm{S}} \end{cases}$$

for DNA S and

$$\begin{cases} r_{\mathrm{S'},x} = \dfrac{a}{2}\cos\left(2\pi\dfrac{11}{n_t}t_{\mathrm{S'}}\right) \\ r_{\mathrm{S'},y} = \dfrac{a}{2}\sin\left(2\pi\dfrac{11}{n_t}t_{\mathrm{S'}}\right) \\ r_{\mathrm{S'},z} = 11bt_{\mathrm{S'}} \end{cases}$$

for DNA S', where $n_t \approx 11$ is the number of base pairs per helix turn [15]. Then, as shown in Figure 3-16, $r_{SS'}$ is the distance between small segments on the helixes of DNA S and DNA S' and can be determined as

$$r_{SS'}^2 = \left(\frac{a}{2}\right)^2 \left\{\left[\cos(2\pi t_S) - \cos\left(2\pi t_{S'} + \theta_p\right)\right]^2 + \left[\sin(2\pi t_S) - \sin\left(2\pi t_{S'} + \theta_p\right)\right]^2\right\} + 11^2 b^2 (t_S - t_{S'})^2.$$

Then, the total Coulomb repulsion of this duplex helix configuration can be written as

$$U = \frac{Q^2}{4\pi\epsilon\epsilon_0} \int_0^1 dt_S \int_0^1 dt_{S'} \frac{1}{r_{SS'}} e^{-\frac{r_{SS'}}{\lambda_D}}, \tag{3-35}$$

where $Q = -11q$ is the total charge of DNA S or DNA S' since we consider that each phosphate group contributes $-q$ and DNA S and DNA S' both have 11 phosphate groups [28].

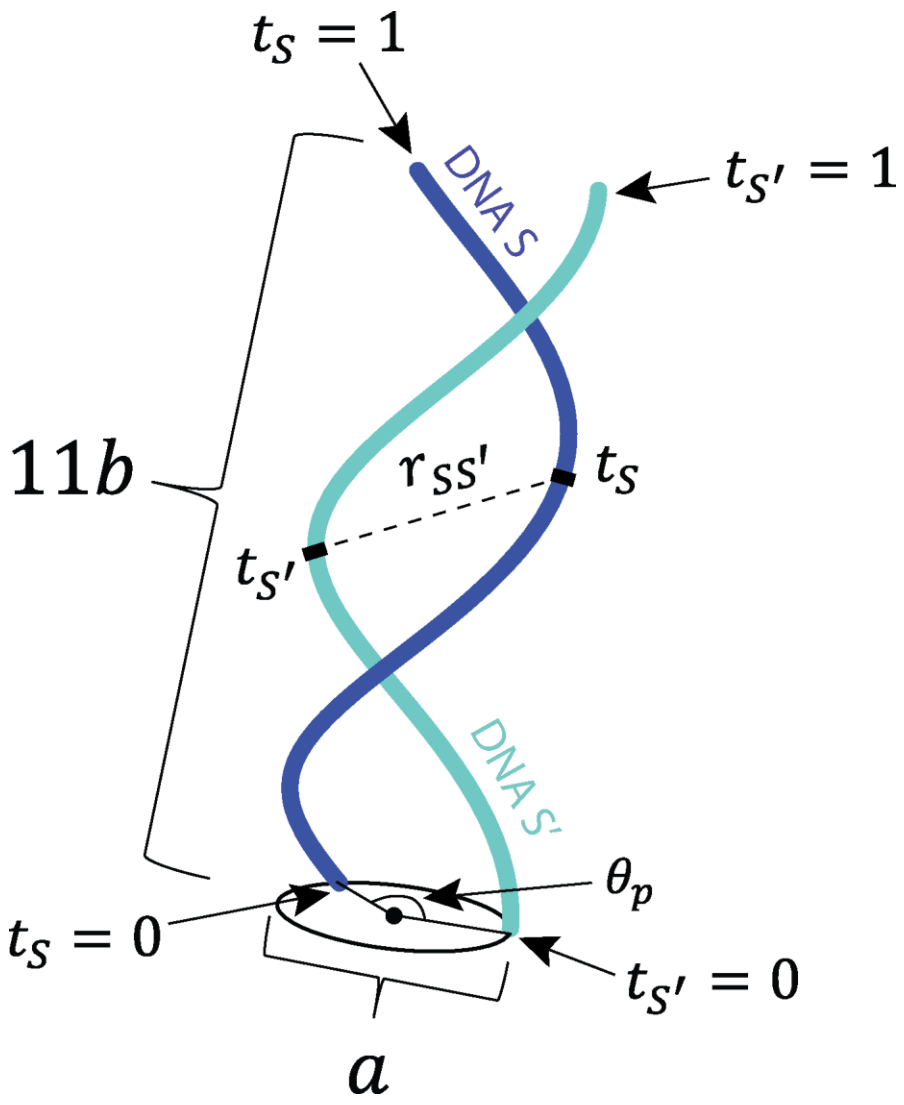

Figure 3-16: Duplex helix configuration. Two DNA strands form a duplex helix structure. θ_p is the phase difference between the two helix curves, a, the diameter of the helix, and b, the separation of each phosphate group in one DNA strand along the helix axis.

3.5.4. TWO-POINT-CHARGE MODEL

In the two-point-charge model, each DNA strand is simplified to a point charge. As shown in Figure 3-17, both DNA S and DNA S' carry an effective charge Q_{eff} and are separated by an effective distance r_{eff}. Since each phosphate group in a DNA strand carries $-q$, for our 11-mer sticky ends, $Q_{eff} = -11q$. The total Coulomb repulsion can then be straightforwardly written as

$$U = \frac{Q_{eff}}{4\pi\epsilon\epsilon_0}\frac{1}{r_{eff}}e^{-\frac{r_{eff}}{\lambda_D}}. \tag{3-36}$$

[28].

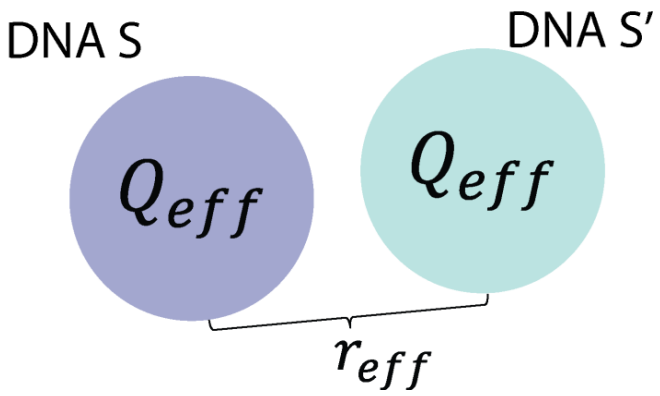

Figure 3-17: Two-point-charge model. Both the point charges carry Q_{eff} and are separated by a distance r_{eff}.

3.6. MODEL CONCLUSION

To model how fast DNA-coated particles aggregate, we include the dynamics from micron-scale particle aggregation to nano-scale DNA hybridization. In this section, we will summarize our kinetic model for self-assembly of DNA-coated particles.

From equation (3-13), we learn that the time-dependent singlet fraction f can be written as

$$f = \frac{1}{\left(1 + \frac{t}{2\tau}\right)^2}, \tag{3-13}$$

where

$$\tau = \tau_{DLA}\left[1 + \frac{\tau_r}{\tau_c \ln\left(\frac{1}{4\pi e R_p^2 C_0}\right)}\right], \tag{3-23}$$

in which τ_c is the collision time, R_p, the particle radius, and C_0, the particle concentration,

$$\tau_{DLA} = \frac{-\ln\left(4\pi e R_p^2 C_0\right)}{8\pi D C_0} \tag{3-19}$$

and

$$\tau_r = \frac{1}{g_b N_b}\tau_s\left(1 + \frac{\tau_{DNA}}{\tau_\theta}\right). \tag{3-30}$$

The physical meaning of equations (3-23) and (3-30) is that the time to trigger the binding is the diffusion search (τ_{DLA} and τ_s) times the number of encounters needed to trigger the binding (τ_r/τ_c and τ_{DNA}/τ_θ). By using similar logic twice, we can relate the micron-scale particle aggregation time τ to the nano-scale DNA solution hybridization time τ_{DNA}, which can also be written as

$$\tau_{DNA} = \tau_{DNA}^{(0)} e^{-\beta U}, \tag{3-31}$$

where U is the Coulomb repulsion barrier for a pair of complementary strands to hybridize and $\tau_{DNA}^{(0)}$ is the solution hybridization time if all the repulsion is well-screened ($U = 0$). To determine U, we have three different configurations:

1. Parallel configuration:

$$U = \frac{q^2}{4\pi\epsilon\epsilon_0}\sum_{i=1}^{11}\sum_{j=1}^{11}\frac{1}{\sqrt{a^2+(i-j)^2b^2}}e^{-\frac{\sqrt{a^2+(i-j)^2b^2}}{\lambda_{\mathrm{D}}}}, \tag{3-34}$$

where $b \approx 0.3\ \mathrm{nm}$, and $a \approx 2.3\ \mathrm{nm}$ is a fitting parameter determined from the green curve in Figure 3-21.

2. Double helix configuration

$$U = \frac{Q^2}{4\pi\epsilon\epsilon_0}\int_0^1 dt_{\mathrm{S}}\int_0^1 dt_{\mathrm{S'}}\frac{1}{r_{\mathrm{SS'}}}e^{-\frac{r_{\mathrm{SS'}}}{\lambda_D}}, \tag{3-35}$$

where $Q = -11q$ and $r_{\mathrm{SS'}}$ the distance between small segments on the helixes of DNA S and DNA S' (Figure 3-16) and can be determined as

$$r_{\mathrm{SS'}} = \left(\frac{a}{2}\right)^2\left\{\left[\cos(2\pi t_{\mathrm{S}}) - \cos\left(2\pi t_{\mathrm{S'}} + \theta_p\right)\right]^2 + \left[\sin(2\pi t_{\mathrm{S}}) - \sin\left(2\pi t_{\mathrm{S'}} + \theta_p\right)\right]^2\right\} + 11^2b^2(t_{\mathrm{S}} - t_{\mathrm{S'}})^2,$$

in which $b \approx 0.3\ \mathrm{nm}$, and $a \approx 3.3\ \mathrm{nm}$ and $\theta_p = \pi$ are fitting parameters determined from the blue curve in Figure 3-21.

3. Two-point-charge model

$$U = \frac{Q_{eff}}{4\pi\epsilon\epsilon_0}\frac{1}{r_{eff}}e^{-\frac{r_{eff}}{\lambda_D}}, \tag{3-36}$$

where $Q_{eff} = -11q$, and $r_{eff} = 2.5\,\mathrm{nm}$ is a fitting parameter determined from the red curve in Figure 3-21.

Combining equations (3-23), (3-30), and (3-31), we can rewrite particle aggregation time scale as

$$\tau = \tau_{DLA}\left[1 + \frac{1}{g_b N_b}\frac{1}{\tau_c \ln\left(\frac{1}{4\pi e R_p^2 C_0}\right)}\tau_s\left(1 + \frac{\tau_{DNA}^{(0)} e^{-\beta U}}{\tau_\theta}\right)\right] \tag{3-37}$$

From equation (3-37), we can relate the time of nano-scale DNA intrinsic solution hybridization without electrical repulsion $\tau_{DNA}^{(0)}$ to micron-scale particle aggregation time τ.

3.7. COMPARISONS BETWEEN MODEL AND DATA

To test whether our model is valid, we use equations (3-13) and (3-37) to compare our experimental data. In Section 3.1, we show two sets of experimental data: Figure 3-2 and Figure 3-3. In Figure 3-2, we measure how fast particles aggregate at different DNA coverages. In Figure 3-3, we measure how salt concentration controls particle aggregation time. In this section, we test our model in both experiments.

3.7.1. AGGREGATION TIME VS. DNA COVERAGE RATIO

To test our model, we first compare our model with the experiments in which the changing variable is DNA coverage. The singlet fraction as a function of time at various DNA coverage ratios, χ's is in Figure 3-2. We fit the experimental data by equation (3-13):

$$f = \frac{1}{\left(1+\frac{t}{2\tau}\right)^2}. \tag{3-13}$$

The fit results are shown in Figure 3-18 [28]. We note from the figure that the fitted curves from equation (3-13) are consistent with the experimental data, and the equation well describes colloidal aggregation.

To further test our model for describing the colloidal aggregation time, we re-plot Figure 3-18 to aggregation time vs. DNA coverage ratio χ. By fitting each experimental data with a specific χ in Figure 3-18 to equation (3-13), we get the corresponding aggregation time τ. From equation (3-13), we learn that τ can be obtained from $f(t = \tau) = \frac{4}{9}$. In Figure 3-18, the aggregation times for experiments with various DNA coverage ratios χ's can be

found as the intersections of the dashed line and the solid curves. However, the aggregation times are measured at various temperatures as shown in Table 3-1, and particle diffusion coefficient is temperature-dependent. Therefore, we normalize all times by setting the diffusion coefficient at $27\ ℃$, namely $D \equiv D_{27\ ℃}$ [28]. For example, the fitted aggregation time for the experiments of $\chi = 1$ is $242\ \mathrm{s}$. Since the experiment is done at $T = 42\ ℃$ as shown in Table 3-1, the aggregation time is normalized to $242\ \mathrm{s} \times D_{42\ ℃}/D_{27\ ℃} = 343\ \mathrm{s}$. Also, since in our model, τ is written in terms of bonding arrangement $N_G \approx g_b N_b$ [see equation (3-37)], we replace χ with $N_G \approx g_b N_b$ using the computation results in Figure 2-23. Then, we can replot the data in Figure 3-18 as aggregation time vs. bonding configuration N_G as shown in Figure 3-19 [28]. With the experimental data in Figure 3-19, we are now ready to test equation (3-37):

$$\tau = \tau_{DLA}\left[1 + \frac{1}{g_b N_b}\frac{1}{\tau_c \ln\left(\frac{1}{4\pi e R_p^2 C_0}\right)}\tau_s\left(1 + \frac{\tau_{DNA}^{(0)} e^{-\beta U}}{\tau_\theta}\right)\right]. \tag{3-37}$$

Here, τ_{DLA} and $\tau_{DNA} = \tau_{DNA}^{(0)} e^{-\beta U}$ are treated as fitting parameters, and $C_0 = C_p/2 = 0.005\ \mu\mathrm{m}^{-2}$ is chosen to be the concentration of particles coat-

ed with either DNA S or DNA S' since our experimental system has two populations. The fitted results are

$$\begin{cases} \tau_{DLA} = (313 \pm 27)\ \mathrm{s} \\ \\ \tau_{DNA} = (4.5 \pm 0.8)\ \mathrm{ms} \end{cases} \tag{3-38}$$

The plot of equation (3-37) with the fitted τ_{DLA} and τ_{DNA} is shown as the red curve in Figure 3-19. The comparison between the model and the experimental data shows that our model describes the aggregation time of DNA-coated colloidal particles well by varying the surface DNA coverage ratio χ.

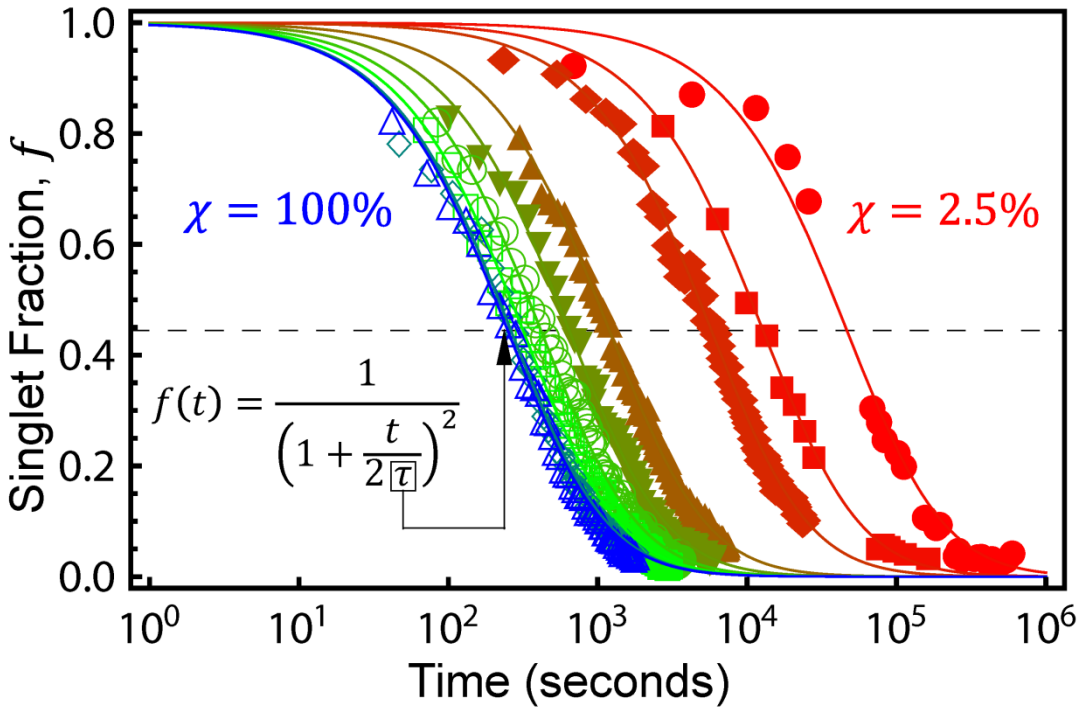

Figure 3-18: The fitting of experimental data in Figure 3-2 by equation (3-13). From left (blue) to right (red), $\chi = 1, 0.75, 0.5, 0.4, 0.3, 0.2, 0.1, 0.05$, and 0.025, respectively. The intersection of the dashed line and the solid curve indicate the aggregation time τ.

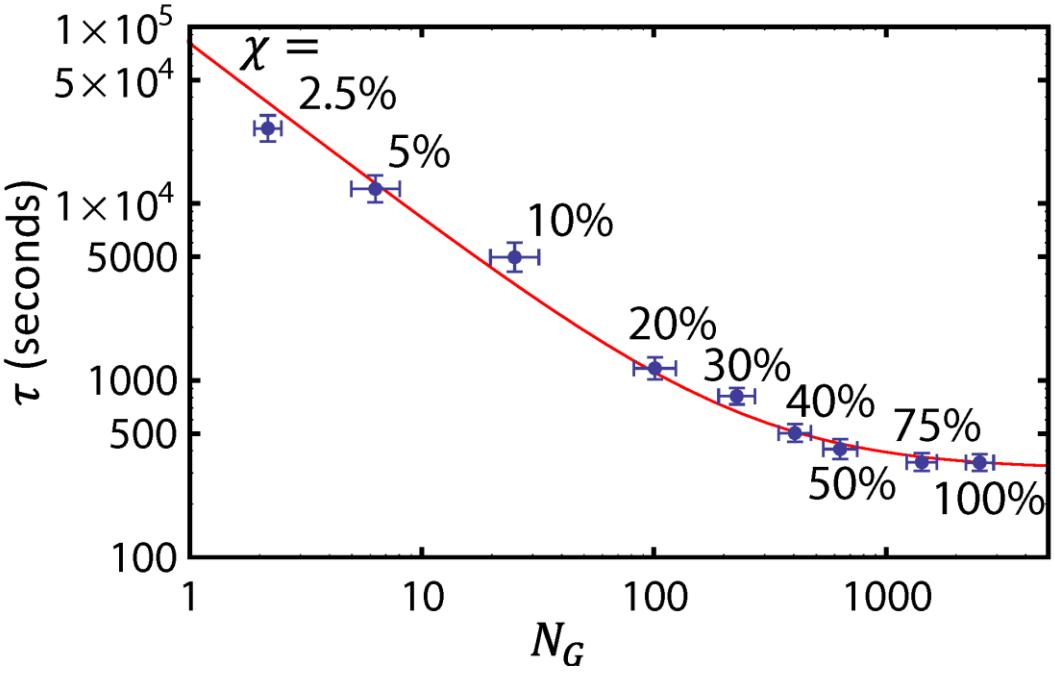

Figure 3-19: The aggregation time τ vs. possible bonding configuration N_G. The blue dots are the fitting results from Figure 3-18, and the red curve is determined by equation (3-37) with $\lambda_D = 1$ nm, $\tau_{DLA} = 313$ s, and $\tau_{DNA}^{(0)} e^{-\beta U} = 4.5$ ms.

3.7.2. AGGREGATION TIME VS. SALT CONCENTRATION

To test our model with the experimental data in which the changing variable is salt concentration $[\mathrm{NaCl}]$, we follow the analysis similar to the one in Section 3.7.1. We use equation (3-13):

$$f = \frac{1}{\left(1 + \frac{t}{2\tau}\right)^2} \tag{3-13}$$

to fit the experimental data in Figure 3-3 [see Figure 3-20]. Again, we find that equation (3-13) describes the aggregation of colloidal particles pretty well. Also, the aggregation time τ in our model is written in terms of energy barrier U, which is a function of Debye screening length λ_D. We replace the salt concentration $[\mathrm{NaCl}]$ with Debye screening length by

$$\lambda_D = \sqrt{\frac{2q^2}{\epsilon\epsilon_0 k_B T}\{[\mathrm{NaCl}] + I_0\}},$$

where $I_0 = 35.2\ \mathrm{mM}$ is the ion contribution from PBS and SDS in our buffer, which contains $10\ \mathrm{mM}$ PBS and 0.15% w/w SDS [13, 20]. Then, we can replot the experimental data in Figure 3-20 as aggregation time τ vs. Debye screening length λ_D (Figure 3-21) [28]. In Section 3.7.1, we measure τ_{DLA}

[see equation (3-38)]. Equation (3-19) shows that τ_{DLA} depends on particle concentration, particle radius, and particle diffusion coefficient. These parameters in τ vs. $[\mathrm{NaCl}]$ are the same as the ones in τ vs. χ, so we expect τ_{DLA} to be the same in both experiments. However, to use our model to plot τ as a function of λ_D in equation (3-37):

$$\tau = \tau_{DLA}\left[1 + \frac{1}{g_b N_b}\frac{1}{\tau_c \ln\left(\frac{1}{4\pi e R_p^2 C_0}\right)}\tau_s\left(1 + \frac{\tau_{DNA}^{(0)} e^{-\beta U}}{\tau_\theta}\right)\right], \tag{3-37}$$

we must calculate the Coulomb barrier U as a function of λ_D. In Section 3.5, we calculate U based on several configurations: 1) parallel configuration, 2) duplex helix configuration, and 3) two-point-charge model. We plot τ as a function of λ_D using equation (3-37) as shown in Figure 3-21. Green, blue, and red curves are plots based on parallel configuration, duplex helix configuration, and two-point-charge model, respectively. Surprisingly, all of the three curves are pretty consistent with the experimental data. Such consistency shows that the Coulomb barrier really dominates the electrical repulsion barrier of DNA hybridization process. As long as we include Coulomb repulsion barrier in our model, we can well describe how fast DNA-coated particles aggregate at various salt concentrations. For the sake of

simplicity, we choose the two-point-charge model to calculate the Coulomb barrier in the following. Using this two-point-charge model, we can calculate $\tau_{DNA}^{(0)}$ from equations (3-31) and (3-38) as

$$\tau_{DNA}^{(0)} = (230 \pm 50)\ \mu s. \tag{3-39}$$

Although this model is the most crude and simplest, it contains the essential elements for estimating the Coulomb repulsion barrier for a pair of complementary DNA strands to hybridize.

To check for Manning condensation effects in the DNA hybridization process, we use our two-point charge model and vary the effective charge Q_{eff}. ssDNA does not have Manning condensation but dsDNA has 75% charge reduction [75], and we expect Manning condensation to go from 0% to 75% during the hybridization process. Here, we try 25% Manning condensation and set $Q_{eff} = 0.75 \times (-11q)$ in our two-point charge model [see equation (3-36)]. Then, we treat r_{eff} as a fitting parameter to fit our experimental data in Figure 3-21. With the fitted $r_{eff} = 2\ \mathrm{nm}$, we plot τ as a function of λ_D, which is the purple curve in Figure 3-21. Even though we assume 25% Manning condensation, our model still describes particle aggregation at var-

ious salt concentrations pretty well when we adjust r_{eff}. Since what matters the most during hybridization process is the electrical repulsion "barrier," the most reasonable Q_{eff} is "without" Manning condensation, namely, $Q_{eff} = -11q$ in our case [28].

3.7.3. CONCLUSIONS

In this section, we test our kinetic model with two experiments. The first is aggregation time vs. DNA coverage ratio, and the second aggregation time vs. salt concentration. In Figure 3-19 and Figure 3-21, we find that our model: equation (3-37) describes the aggregation time of colloidal particles well. Further, from our model plot based on various intermediate configurations (Figure 3-21), we note that the electrical repulsion of DNA hybridization is dominated by Coulomb repulsion no matter what intermediate state a pair of complementary strands is in. Therefore, the Coulomb repulsion barrier can be estimated crudely as two-point charges (Figure 3-17). We also note that Manning condensation does not play an important role in DNA hybridization although dsDNA has a serious Manning condensation effect. Considering the above, we can estimate the intrinsic solution hybridization

time of our sticky ends in the absence of Coulomb repulsion [see equation (3-39)]. This hybridization time is independent of DNA concentration, backbone structures, and salt concentration and only depends on free diffusion, strand length, and possibly sequence of a pair of complementary strands. As long as we know this fundamental hybridization time $\tau_{DNA}^{(0)}$, we can control the speed of aggregation of our DNA-coated particles.

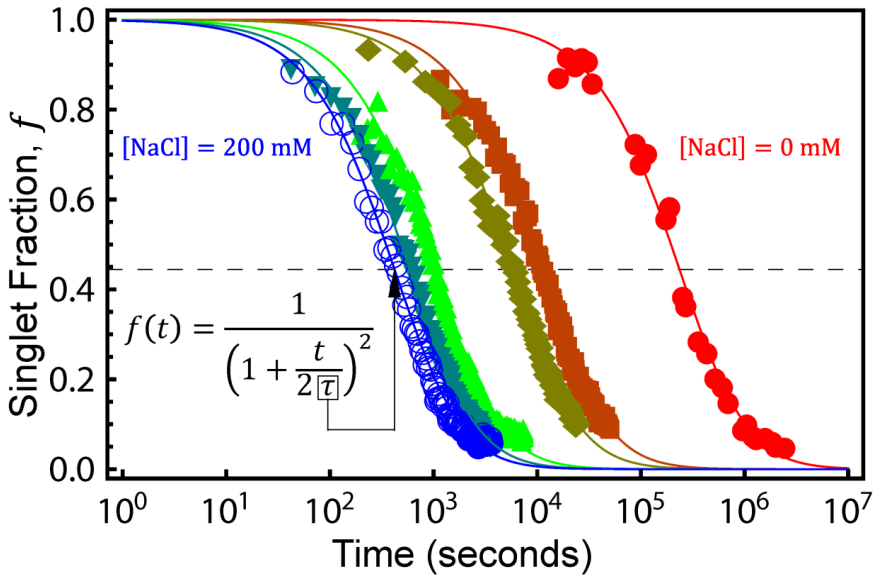

Figure 3-20: The fitting of experimental data in Figure 3-3 by equation (3-13). From left (blue) to right (red), $[\mathrm{NaCl}] = 200, 150, 100, 50, 25$, and 0 mM, respectively. The intersection of the dashed line and the solid curve indicate the aggregation time τ.

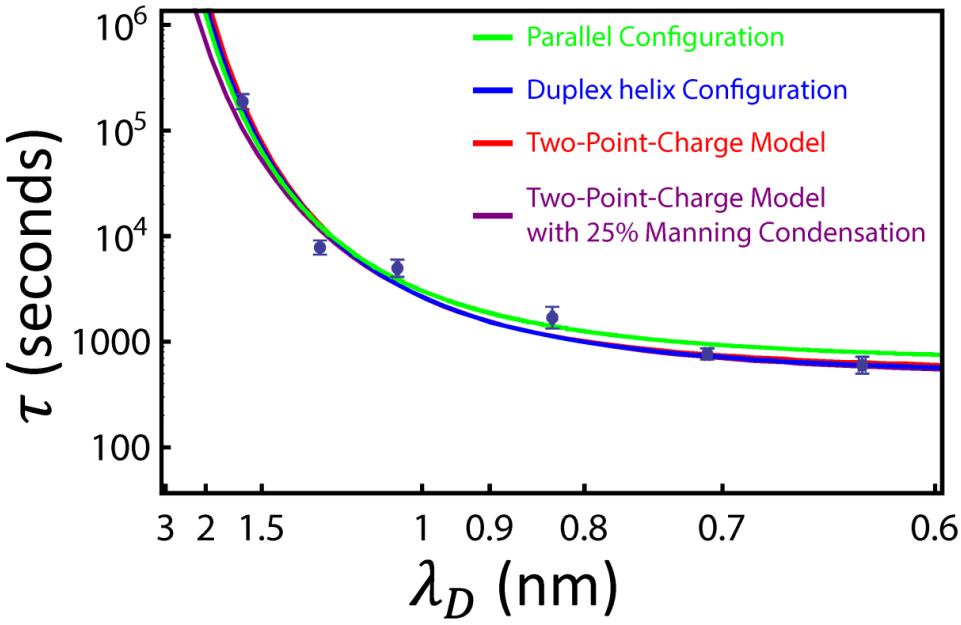

Figure 3-21: Aggregation time τ vs. Debye screening length λ_D. The blue dots are the fitting results from Figure 3-20. The solid curves are determined by equation (3-37) with $\chi = 0.1$ and $\tau_{DLA} = 313\ s$ based on four different configurations.

3.8. COMPARISONS OF INTRINSIC SOLUTION HYBRIDIZATION TIME WITH EXISTING WORK

To further test whether or not the intrinsic solution hybridization time measured through our model [see equation (3-39)] is reliable, we compare it with

other previous measurements. From Ref. [76], we learn that the solution hybridization rate can be written as

$$k_{DNA}^{on} = 4\pi(2D_{DNA})(2r_{hp})W_h e^{-\beta U}, \tag{3-40}$$

where D_{DNA} is the diffusion coefficient of a ssDNA strand, $r_{hp} \approx 1\,\mathrm{nm}$, the distance between a hydrogen bond and the corresponding phosphate group in a dsDNA strand, U, the energy barrier discussed in Section 3.5, and W_h, a dimensionless quantity and a function of the width of hydrogen bond. From Ref. [77], we know that the solution hybridization rate for a pair of 10-mer complementary DNA strand in $100\,\mathrm{mM\,[NaCl]}$ at $20\,℃$ is $8 \times 10^4\ \mathrm{M^{-1}s^{-1}}$. Additionally, from Ref. [78], we learn that the diffusion coefficient of a ssDNA can be estimated as

$$D_{DNA} \approx (8.1 \times 10^{-6})M^{-0.68}\ \mathrm{cm^2/s}, \tag{3-41}$$

where M is the number of bases of a ssDNA. For 10-mer DNA, the diffusion coefficient is $1.7 \times 10^{-6}\ \mathrm{cm^2/s}$. If we choose the two-point charge model to calculate U [see equation (3-36)], we find

$$W_h = 1.6 \times 10^{-4}.$$

Then, we are able to use equations (3-40) and (3-41) to calculate the solution hybridization rate for our 11-mer ssDNA. Using equation (3-41), we can

estimate the diffusion coefficient of our 11-mer ssDNA at $27\ ℃$ at about $1.6 \times 10^{-6}\ \mathrm{cm}^2/\mathrm{s}$. From equation (3-40), we can determine that the solution hybridization rate for our sticky ends without Coulomb repulsion barrier, namely, $U = 0$, is

$$k_{DNA}^{on}(U = 0) \approx 7.7 \times 10^5\ \mathrm{M}^{-1}\mathrm{s}^{-1}.$$

Then, we can estimate the solution hybridization time without Coulomb repulsion barrier as

$$\tau_{DNA}^{(0)} \approx \frac{\frac{4}{3}\pi R_g^3}{k_{DNA}^{on}(U = 0)} \approx 150\ \mu\mathrm{s}, \tag{3-42}$$

where $R_g \approx 3.6\ \mathrm{nm}$ is the gyration radius of our DNA strand. Comparing the estimated $\tau_{DNA}^{(0)} = 150\ \mu\mathrm{s}$ from other measurements [see equation (3-42)] with our measured $\tau_{DNA}^{(0)} = (230 \pm 50)\ \mu\mathrm{s}$ [see equation (3-39)], we note that our measured $\tau_{DNA}^{(0)}$ is roughly consistent with our previous measurements. Such consistency suggests that we can describe particle aggregation rates to within a factor of 2.

3.9. CONCLUSIONS

In this chapter, we study the kinetics of aggregation of DNA-coated particles. We learn that the DNA-mediated aggregation rate is reduced from the conventional diffusion-limited result by a kinetic factor of $\frac{\tau_c}{\tau_h/N_G}$. This factor represents the number of collisions needed to trigger the binding. A particle diffuses into and out of a reaction zone in time τ_c and must make many additional attempts if the reaction time $\tau_h/N_G > \tau_c$. This represents a well-known crossover from diffusion-limited aggregation to a reaction-limited aggregation [69, 70]. Similarly, the hybridization time τ_h also deviates from the solution hybridization time by a kinetic factor of $\frac{\tau_{DNA}}{\tau_\theta}$. Solution hybridization is also retarded by a Coulomb repulsion barrier. A simple model appropriate for DNA-functionalized particles quantitatively describes the aggregation kinetics well based on the kinetics of solution DNA hybridization. More surprisingly, our measured solution hybridization time is consistent with measurements from other experiments. Our model is useful in designing and optimizing more complex self-assembly processes involving many steps of reversible and irreversible binding. Our model can also be used to study the kinetics of DNA hybridization and the binding of proteins and other molecu-

lar and nano-scale constructs. Typically, these reactions occur on a $10^{-6} - 10^{-3}\ s$ time scale. Using our model, particles coated with these ligands substituted for DNA can conveniently be studied on a minutes-to-hours time scale with simple microscopic observation or by dynamic light scattering.

CHAPTER 4 POLYGAMOUS PARTICLES

DNA is increasingly used as an important tool in programming the self-assembly of micro- and nanometer-scale particles. This is largely due to the highly specific thermo-reversible interaction of complementary DNA strands, which, when placed on different particles, have been used to bind precise pairs in aggregates and crystals [21, 22, 26, 27, 32, 34-37, 53]. However, DNA functionalized particles will only reach their true potential for particle assembly when each particle can address and bind to many different kinds of particles. Although nano-scale particles are typically coated with tens to hundreds of DNA molecules, micrometer-scale colloids can be coated with $10^4 - 10^5$ DNA strands. There has been little work on coating particles with more than one or two types of DNA sequence on the same particle. Allowing these particles to be multifunctional or "polygamous," to specifically bind to a set of other particles, enables not only the fabrication of more complex crystals but the design of more general programmed structures. For rigid structures, specifying each inter-particle bond specifically is sufficient to define the structure of an object [40, 41]. Therefore, the construction can be set by coating each particle with the DNA strands that only link to other

specific particles. In this chapter, we will outline the design rules by which polygamous particles can be made and demonstrate, in the case of four different coatings, that one particle can bind to four different particles without mutual interference. Then, we will address the limitations of polygamous particle: setting an upper limit to many different strands we can have on each particle while maintaining its ability to attract and mate with other particles. One might suppose that if a particle can accommodate 10^5 different strands, it can be coated with 10^5 different sequences to bind to 10^5 different particles, not all at the same time, of course, but a total of 10^5 potential mates. However, even if a DNA strand can bind to its complementary strand when suspended in solution, two DNA strands attached to the surface of two different spheres can only bind when the spheres are in particular configurations [see Section 2.4.5]. The result is a substantial entropy cost which has to be taken into account in the binding energy of the DNA-coated particles. By contrast, when many identical DNA strands coat the particles uniformly, bonds can form in any orientation. Diluting the surface coverage of each sequence restricts the configurations and increases the entropy cost. Also, we require that subsequences do not pair with subsequences on wrong chains or form hairpins. Avoiding mutual interference of

subsequences greatly limits the number of available partners. For example, the longer is the length of sticky-end DNA, fewer are sequences that avoid five-base interferences that would hybridize above $0\,℃$. As a result, there is a practical limit of ~ 100 different partners for our $2\text{-}\mu\mathrm{m}$ particles. We will show how to calculate the number of distinct pairs of sequences of N bases avoiding M overlaps. Finally, we demonstrate how we can use such polygamous particles to synthesize an elementary system with properties that cannot be achieved by traditional monogamous particles: a system that gels when it is quenched and forms isolated clusters when it is cooled slowly.

4.1. DESIGN RULES

To manufacture polygamous particles, special attention needs to be paid to the design of complementary pairs of DNA. The hybridization of DNA strands involves competition between an enthalpic contribution, which includes hydrogen bonding and hydrophobic interactions and therefore depends directly on DNA sequences, and an entropic contribution, which includes the loss of configurational entropy when two flexible single strands make one more rigid double strand. Hence, the free energy and melting

temperature of hybridization depend on the DNA sequences. Two rules emerge for designing the sequences of DNA on polygamous particles [27, 48, 49]. They are:

1. Over the temperature range of the experiments, only complementary pairs of DNA should hybridize. The melting temperatures of non-complementary pairs of DNA should be set below the working range, namely, below $0\ ^{\circ}\mathrm{C}$. This step is to ensure that each DNA flavor of a polygamous particle is specific and that no non-specific DNA links are allowed between particles.
2. Folding structures for all the DNA sticky ends must be minimized. Secondary structures, such as loops and hairpins, reduce the number of active ends, and hence, the binding free energy and melting temperature [25, 79-82]. Loops and hairpins can also lead to unwanted nonspecific binding of particles through entanglements [24].

By following our design rules, we can avoid unwanted hybridization in the system and make each interaction highly specific.

4.2. UPPER LIMIT OF POLYGAMOUS PARTICLES

We would like to design DNA sequences that bind only to their complementary sequences using the complete N bases. We want to avoid any hairpins or improper binding of sequences above a minimum temperature considerably below our characteristic melting curves [27]. As the melting temperatures for 5-bp dsDNA is about $0\ ℃$, we woud like to avoid any inadvertent 5-bp sequence overlaps in our 11-bp sticky ends. First, we treat the general problem of avoiding M-bp sequences in N-bp strings. The number of M-bp sequences is 4^M. By following Rule No. 2, we wish to avoid any palindromes because they can lead to strands sticking to themselves or forming hairpins. The number of palindromes is $4^{M/2}$ if M is even. There are no DNA palindromes if M is odd. A DNA sequence is palindromic if the sequence read from left to right is complementary to that read from right to left. For example, GATC is a palindromic sequence as it is complementary to CTAG. However, GAXTC cannot be a palindromic sequence since it is not complementary to CTXAG as no base can be its own complementary. The number of M-bp words in an N-bp sequences is $(N - M + 1)$. By following Rule No. 1, we require all these M-bp words to be different. We also require

that the complementary strand be read in the same $5' \rightarrow 3'$ direction as the original strand to have different M-letter words. Thus, each distinct pair of sequences deplete $2 \times (N - M + 1)$ sequences or words of M bp from the total number of $4^M - 4^{M/2}$ for even M or 4^M for odd M. The number, $P_{\max}$ of distinct pairs of sequences, is then

$$P_{\max} = \begin{cases} \left\lfloor \dfrac{4^M - 4^{M/2}}{2 \times (N - M + 1)} \right\rfloor & \text{for even } M \\ \\ \left\lfloor \dfrac{4^M}{2 \times (N - M + 1)} \right\rfloor & \text{for odd } M \end{cases}, \tag{4-1}$$

where $\lfloor \cdots \rfloor$ is the integer part function. $P_{\max}$ in equation (4-1) is the upper limit. It is not evident that $P_{\max}$ distinct pairs of sequences can be found. To verify equation (4-1), we perform a computation to directly enumerate all the distinct pairs of sequences that follow our design rules. The algorithm of enumerating all the complementary pairs of N-bp DNA sequences which avoid M-bp overlaps is as follows:

1. List all the possible DNA sequences with the specific length N. This will allow 4^N different DNA sequences.
2. If the chosen M is even, eliminate palindromic sequences.

3. Eliminate the sequences that have M-bp overlap to themselves.
4. Eliminate the sequence pairs that contain M-bp overlap.

Step 2 is to enforce Rule No. 2. Steps 3 and 4 are to enforce Rule No. 1. The number of distinct pairs of sequences through computation with various sequence lengths along with a comparison with equation (4-1) is shown in Table 4-1. From the table, we find out that the number of distinct pairs of sequences found through computation is equal or less than the calculation from equation (4-1). Therefore, equation (4-1) provides an upper limit for the number of distinct pairs of sequences that can be used for synthesizing polygamous particles. Additionally, we note that the number of distinct pairs of sequences decreases with increasing DNA length (Figure 4-1). This is a surprising result. Intuitively, we expect that the number of distinct pairs of sequences increases with increasing DNA length since the total number of different sequences increases exponentially, namely 4^N. However, from our design rules, especially Rule No. 1, more DNA sequences need to be eliminated as the length of DNA sequences increases. The result is a decreasing number of distinct pairs of sequences as the length of DNA increases. For our experimental condition, $N = 11$ and $M = 5$. The upper limit is $P_{\max} = 73$. Additionally, the actual number of distinct pairs should be deter-

mined with the actual melting temperatures of sequence pairs. Therefore, in our experimental system, a practical limit of ~ 100 different partners for a polygamous particle is reasonable [27].

DNA Length	# of Distinct Pairs from Computation		$P_{\max}$
5	512	$=$	512
6	219	$<$	256
7	114	$<$	170
8	106	$<$	128
9	102	$=$	102
10	76	$<$	85
11	63	$<$	73

Table 4-1: Comparisons of the numbers of distinct pairs from computation with $P_{\max}$ from equation (4-1).

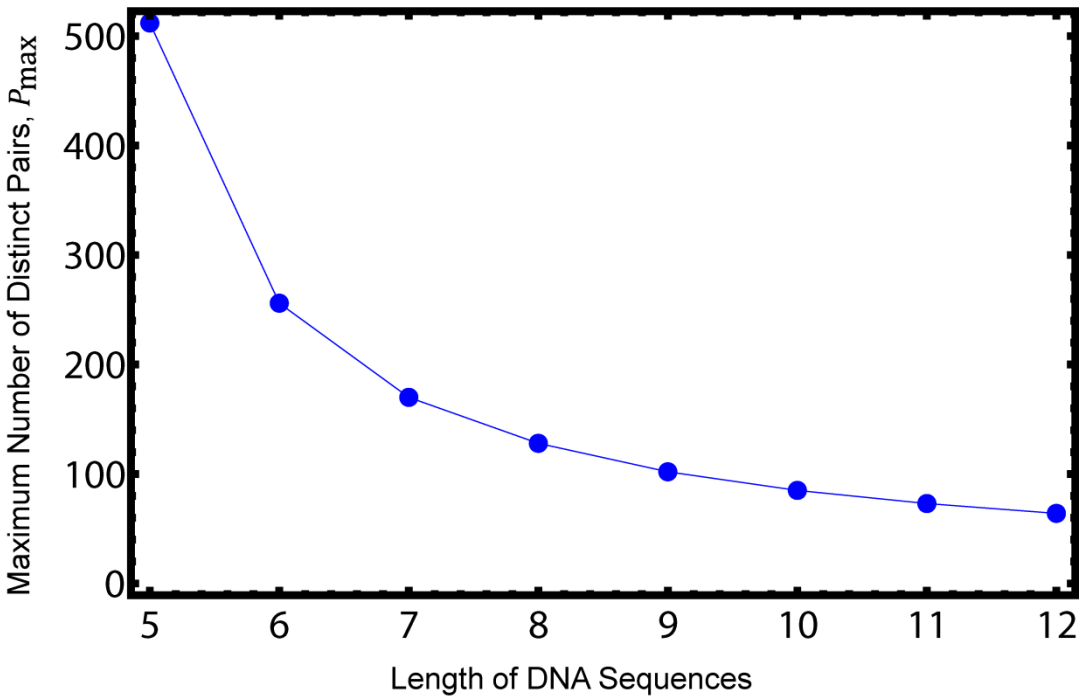

Figure 4-1: Maximum number of distinct pairs, $P_{\max}$ vs. length of DNA sequences. 5-bp sequences are avoided ($M = 5$). As the length of DNA sequences increases, the maximum number of distinct pairs decreases.

4.3. ONE WIFE AND FOUR HUSBANDS

In this section, we synthesize a polygamous particle that can recognize four different particles [27]. To manufacture such polygamous particles, we need

four different pairs of strands. Therefore, four sequences and their complements need to be designed with regard to our design rules expressed in Section 4.1. The sequences we generate and use are shown in Table 4-2 [27]. The first three pairs of sequences: S_1, S_1', S_2, S_2', S_3, and S_3' are the same as the sequences used in Section 2.6. Similarly, we use an internet-based application, the UNAFold Web Server to predict the melting temperatures of DNA to give a check of the sequences [17, 62-66]. Since the experimental condition remains the same, sodium concentration is still chosen to be $[Na^+] = 73.4\ mM$, and DNA concentration is still $0.012\ \mu M$. The melting temperatures for all possible pairs of DNA sequences are shown in Table 4-3 [27]. Still, there are no unwanted associations above $0\ ℃$. The melting temperatures of the secondary structures of all DNA sequences are also listed at the bottom of Table 4-3. We find that hairpins are also suppressed above $0\ ℃$. Similarly, the enthalpies and entropies of hybridization of DNA pairs in Table 4-2 can be determined and shown in Table 4-4 [17, 62-66]. Table 4-3 shows that we can easily find DNA sequences obeying the design rules when the number of distinct pairs of sequences needed is significantly lower than $P_{\max}$.

From Table 4-3, we have four distinct pairs of sequences, so we are ready to synthesize four-partner polygamous particles. We synthesize these particles by coating them with $25\%\ S_1$, $25\%\ S_2$, $25\%\ S_3$, and $25\%\ S_4$ (Figure 4-2) [27]. The four partners of the polygamous particles are only coated with one kind of DNA. E is coated with S_4', F with S_2',G with S_3',and H with S_1'. As particles are optically identical, we can not show directly that one particle has paired specifically with a number of different particles. For this demonstration of four-partner polygamous particles, we need labeled particles. E is a 0.9-μm fluorescent polystyrene particle, F, a 1-μm fluorescent polystyrene particle, G, a 1-μm fluorescent polystyrene particle, and H, a 2-μm fluorescent polystyrene particle. The excitation and emission peaks are shown in Table 4-5. Therefore, E, F, G, and H can be distinguished by either fluorescence or size. However, D is a non-fluorescent 2-μm polystyrene particle. Therefore, we dye the buffer with fluorescein, the excitation and emission peak of which are shown in Table 4-5, so our non-fluorescent polygamous particle D can be identified as the black object in the fluorescent environment [27].

To check whether or not D can recognize four different particles E, F, G, and H at the same time, we perform two control experiments and one polygamous experiment. In Figure 4-3, we put E, F, G, and H separately with D [27]. The four confocal images show that D can bind to E, F, G, and H separately. Then, we compare the aggregation of a mixture of all five particles and the four monogamous spouses without the polygamous one. In Figure 4-4, clusters form in the presence of the polygamous D, but there are only unbound particles when E, F, G, and H are suspended in solution without D [27]. Aggregates form when there are a sufficient amount of polygamous particles to bridge clusters (or to share partners.) If we reduce the number of polygamous D particles relative to the number of other species, only single clusters form with D surrounded by its partners. An example is shown in Figure 4-5: a cluster of E, G, H, and 2 F's is bound to a polygamous D [27]. Figure 4-5 is also direct evidence of successfully synthesizing polygamous particles.

DNA Symbols	Sequences
S_1	5’ – GTA GAA GTA GG – 3'
S_1'	5’ – CCT ACT TCT AC – 3’
S_2	5’ – GAT GGA TTA GG– 3'
S_2'	5’ – CCT AAT CCA TC – 3’
S_3	5’ – GTA TTC GAG TT – 3'
S_3'	5’ – AAC TCG AAT AC – 3’
S_4	5’ – ATA GAT TCC GA – 3’
S_4'	5’ – TCG GAA TCT AT – 3’

Table 4-2: DNA sequences used for synthesizing four-partner polygamous particles. This table is similar to Table 2-3 except that a fourth pair, S_4 and S_4', is introduced for creating the fourth partner of four-partner polygamous particles.

	S_1	S_1'	S_2	S_2'	S_3	S_3'	S_4	S_4'
S_1	-214	18	-151	-68	-76	-147	-66	-66
S_1'	–	-214	-68	-177	-99	-69	-80	-78
S_2	–	–	-147	19	-138	-101	-77	-39
S_2'	–	–	–	N/A	-96	-102	-45	-50
S_3	–	–	–	–	-54	20	-56	-55
S_3'	–	–	–	–	–	-54	-56	-55
S_4	–	–	–	–	–	–	-52	19
S_4'	–	–	–	–	–	–	–	-51
Folding	-41	-54	-175	N/A	-48	N/A	N/A	-81

Table 4-3: Melting temperatures for DNA pair hybridization (℃) determined from the UNAFold Web Server with $73.4\ \mathrm{mM}$ sodium and $0.012\ \mu\mathrm{M}$ DNA. Data are taken from Ref. [17, 62-66]. The last row indicates the melting temperature of the secondary structure for each sticky-end DNA. N/A means that no hybridization state is found by the UNAFold Web Server. This table is similar to Table 2-4 except that a fourth pair, S_4 and S_4', is included for comparison.

DNA Hybridization	$\Delta H°$ (J/mole)	$\Delta S°$ (J/mole K)
$S_1 + S_1'$	$-328{,}000$	-966
$S_2 + S_2'$	$-326{,}000$	-956
$S_3 + S_3'$	$-332{,}000$	-974
$S_4 + S_4'$	-318,000	-926

Table 4-4: Hybridization enthalpies and entropies of pairs of complementary DNA strands in Table 4-2 in the buffer containing 73.4 mM Na^+.

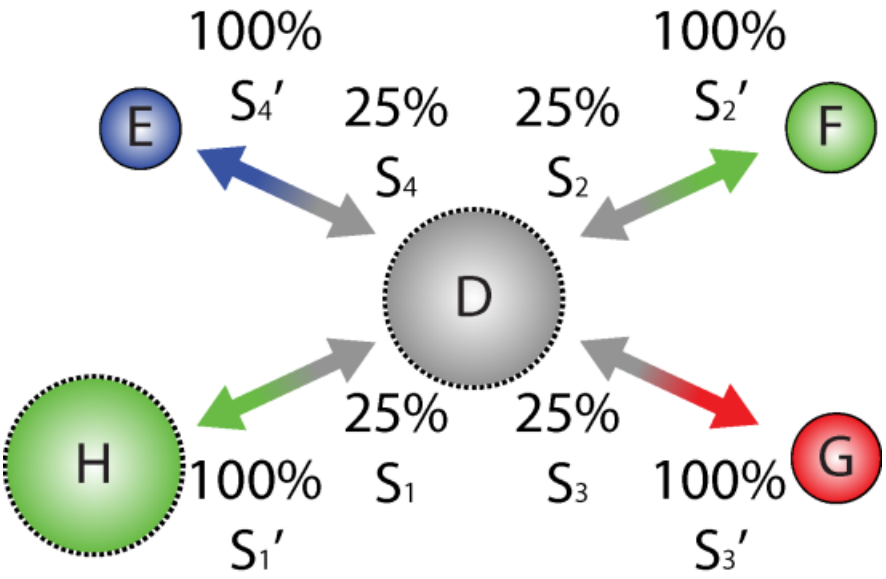

Figure 4-2: Particles coated with four different kinds of DNA being able to address four different kinds of particles.

Particles or Dye	Excitation Peak (nm)	Emission Peak (nm)
E	670	700
F	505	515
G	580	605
H	441	486
Fluorescein	494	521

Table 4-5: Excitation and emission peaks of our particles and fluorescein.

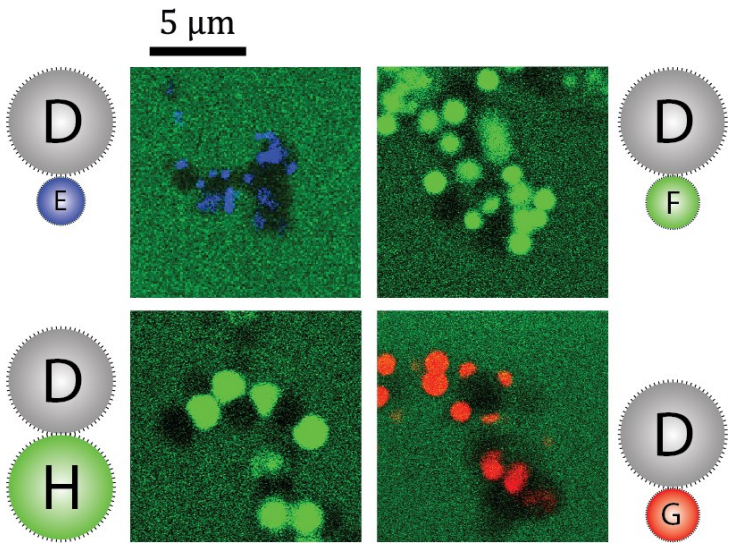

Figure 4-3: First control experiment. D can bind to each of E, F, G, and H separately.

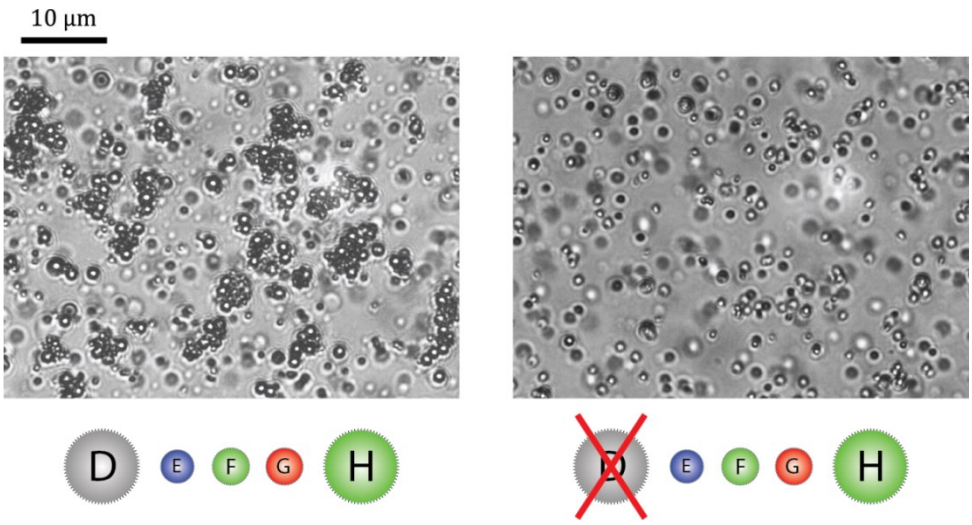

Figure 4-4: Second control experiment: E, F, G, and H can not form any aggregation without D.

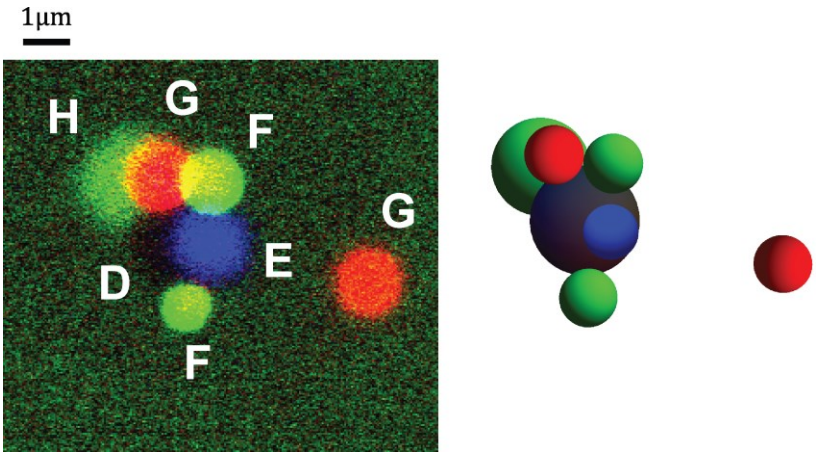

Figure 4-5: D Attached to four different particles E, F, G, and H simultaneously.

4.4. DUAL-PHASE MATERIALS

To demonstrate the utility of polygamous particles, we synthesize dual-phase materials [27]. As shown in Figure 4-6, Y is the polygamous particle that can address X and Z at the same time [27]. Particles used here are $1\text{-}\mu\text{m}$ polystyrene Dynabeads (MyOne Streptavidin C1, Molecular Probes, 3% polydispersity) [21, 22]. To form a two-shell-like clusters as shown in Figure 4-6, the melting temperature of X-Y, T_{XY}, must be higher than the melting temperature of Y-Z, T_{YZ}. Hence, based on the thermodynamic model we developed in Chapter 2, we control the melting temperatures of T_{XY} and T_{YZ} by adjusting the coverage ratios of S_1, S_1', S_3, and S_3' on X, Y, and Z. X is coated with $100\%\ \text{S}_3$, Y with $75\%\ \text{S}_3'$ and $10\%\ \text{S}_1$, and Z with $50\%\ \text{S}_1'$. Particle concentration is also the key to synthesize two-shell-like clusters. Particle concentrations of X, Y, and Z are controlled to be $n_{\text{X}} = 0.006\ \mu\text{m}^{-2}$, $n_{\text{Y}} = 0.03\ \mu\text{m}^{-2}$, and $n_{\text{Z}} = 0.06\ \mu\text{m}^{-2}$, respectively.

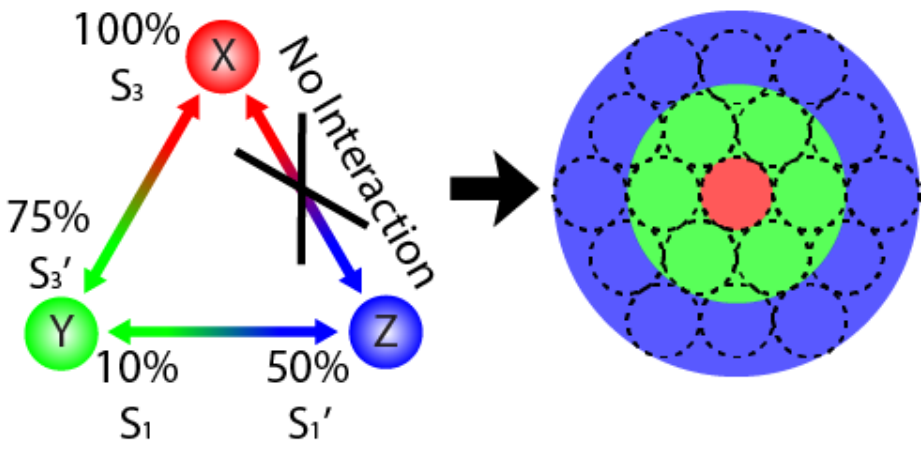

Figure 4-6: Two-shell system. An X is first surrounded by Y's to form a complete shell (green), and the green shell is then surrounded by Z's (blue shell) to form, finally, a two-shell cluster.

4.4.1. THE MELTING CURVE

To quantitatively control the thermodynamics of X-Y-Z system, we measure the melting curve and compare it with our thermodynamic model expressed in Chapter 2. We first place the sample on the temperature gradient and measure the melting curve through the same method in Section 2.3. The singlet fraction with respect to temperature in thermal equilibrium is shown in Figure 4-7 [28]. From our experimental data, we note that the melting curve is unlike the traditional melting curves, such as the ones in Figure

2-24, and has two melting transitions. The first transition represents the Y-Z melting, and the second the X-Y melting. The melting temperatures of X-Y and Y-Z are $T_{\mathrm{XY}} \approx 41\ ℃$ and $T_{\mathrm{YZ}} \approx 47\ ℃$, respectively. By measuring the melting curve of X-Y-Z system, we can easily tune the attraction of X-Y and Y-Z by controlling temperatures.

To further demonstrate that our thermodynamic model developed in Chapter 2 provides a guide for designing systems with polygamous particles, we use our model to predict the melting curve in Figure 4-7. We use the same set of parameters as in Chapter 2 except that the particle radius R_p is changed to $R_p \approx 500\ \mathrm{nm}$ and the total DNA coverage N_t is changed to $N_t = 22{,}000 \pm 2200$ [21, 22]. The rotational entropy discussed in Section 2.4.5 is modified to

$$\Delta S_r(\chi_1, \chi_2) = k_B \ln\left[1 - \left(1 - \frac{A_{DNA}}{A_{surface}}\right)\right]^{N_t\chi_1} + k_B \ln\left[1 - \left(1 - \frac{A_{DNA}}{A_{surface}}\right)\right]^{N_t\chi_2}$$

for a pair of complementary particles with active DNA coverage ratios χ_1 and χ_2, respectively, since the DNA coverage ratios of a pair of complementary particles are different [27]. We also need to re-compute g_b's and

N_b's for the binding of X-Y and Y-Z. Table 4-6 shows the g_b's and N_b's for X-Y and Y-Z by following the same algorithm in Section 2.4.6. The enthalpies and entropies of S_1-S_1' and S_2-S_2' are known from Table 4-4. Also, X-Y-Z system is unlike the ABC system discussed in Section 2.6 since X and Z do not have attraction, and X-Y-Z system does not form any triangle clusters. Hence, X-Y-Z system only has clusters of open structures. After collecting all the parameters, the melting curves of X-Y, f_{XY}, and Y-Z, f_{YZ}, can be determined from equation (2-9). Then, the total melting curve, f_{XYZ} can be written as

$$f_{XYZ} = \frac{n_X + n_Y}{n_X + n_Y + n_Z} f_{XY} + \frac{n_Z}{n_X + n_Y + n_Z} f_{YZ} \tag{4-2}$$

[27]. The plot of equation (4-2) is shown in Figure 4-7. Comparing our model plot and the experimental data, we find that our model successfully predicts the melting behaviors of X-Y-Z system. The good agreement shows that our simple mean field model developed in Chapter 2 is sufficient to predict the melting behaviors of more complex systems in a semi-quantitative manner. We can use the model developed in Chapter 2 to guide the design of the system of polygamous particles.

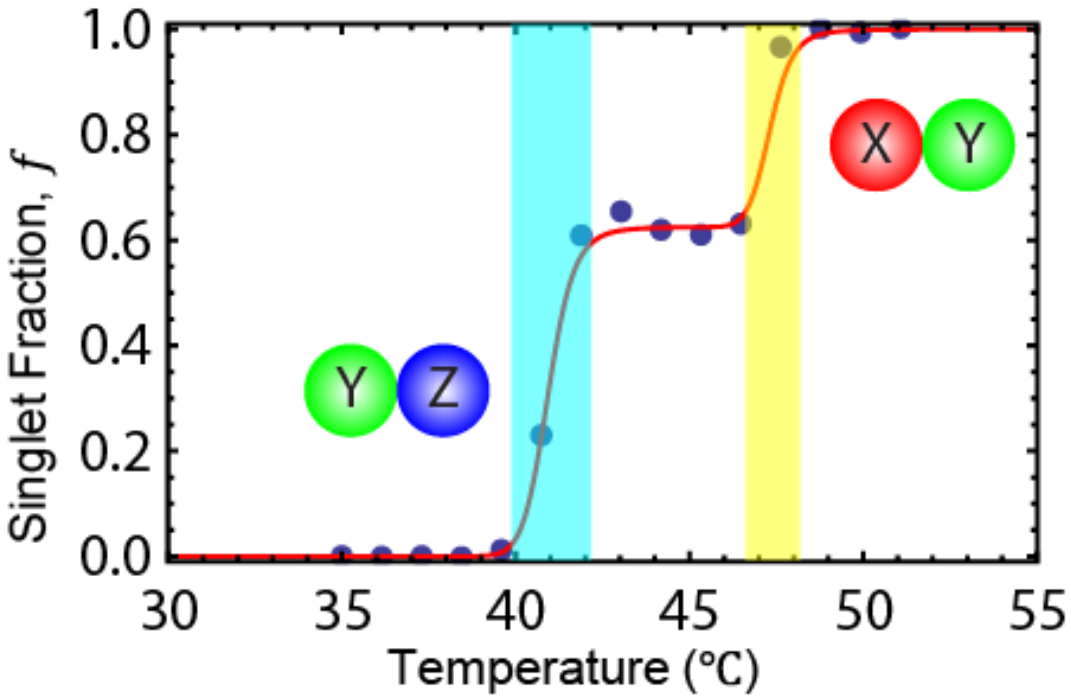

Figure 4-7: Melting curve of an X-Y-Z system. The blue dots are data. The red curve is the model plot.

Particle Interaction	g_b	N_b
X-Y	7	163
Y-Z	6	22

Table 4-6: Computed g_b's and N_b's of a pair of complementary particles based on the algorithm used in Section 2.4.6.

4.4.2. HISTORY-DEPENDENT PHASE

To demonstrate the uniqueness of our X-Y-Z system, we cool the system in two different manners. As shown in Figure 4-8 (a) [27], we first heat the sample to $52\,℃$, where all clusters are melted, for $5\,\text{minutes}$. Then, we quench the sample to $23\,℃$, at which X binds to Y, and Y to Z, for $160\,\text{minutes}$. The system is similar to a usual binary system. Particles aggregate and form a branched percolating network as shown in Figure 4-8 (a). Since all the clusters are immobile and not diffusive, the system is a gel. In contrast, as shown in Figure 4-8 (b) [27], if we cool the system to $43\,℃$, which is between T_{XY} and T_{YZ}, for $120\,\text{minutes}$, X will absorb all the Y's in solution and form a cluster with X as a core and Y's as the shell. Then, we cool the system to $23\,℃$, which is below both T_{XY} and T_{YZ}, for $160\,\text{minutes}$. At this stage, Z's will stick to the one-shell cluster, saturate the periphery of the cluster, and form the second shell as shown in Figure 4-6. The one-shell clusters diffuse too slowly to aggregate before being coated by the Z's. After that, the system will only have several two-shell clusters and some excess individual Z particles. Although some cluster–cluster bridging is unavoidable, this aggregation is too little to percolate as shown in Figure 4-8

(b). Such system has many mobile clusters and single particles, which are inert to each other and diffusive, so the system behaves like a fluid. Therefore, we find that by using polygamous particles, we can make a dual-phase system whose connectivity or rheology is history/protocol-dependent. The system is designed so that its structural and physical properties depend on the cooling process. Basically, a few X particles sequester enough Y particles to inhibit percolation of the Y-Z system. Slow or two-step cooling yields a fluid phase with disconnected clusters. A quench yields a percolating rigid gel. By adopting polygamous particles, we are able to perform self-assembly that monogamous system can not achieve.

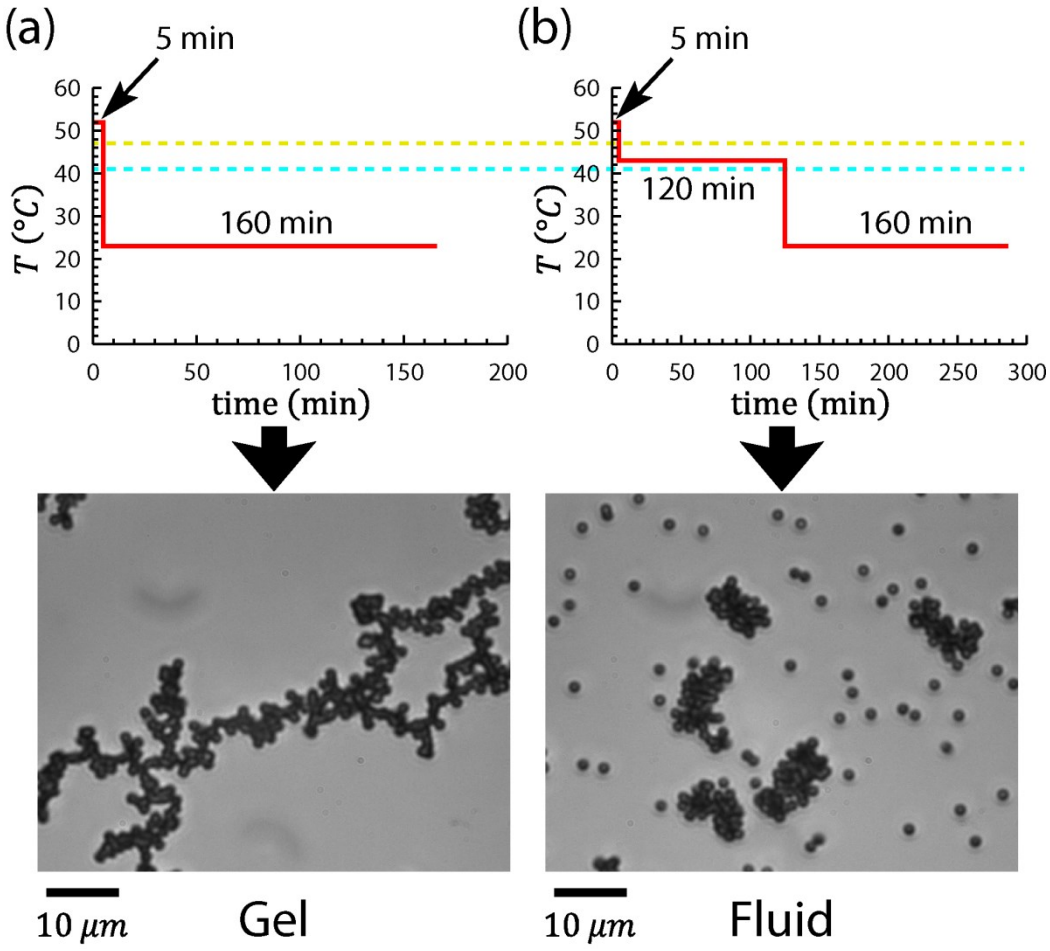

Figure 4-8: Demonstration of dual-phase materials. (a) Gel synthesized by one-step quenching. The yellow and cyan dashed lines are the melting temperature of X-Y and Y-Z, respectively. (b) Fluid synthesized by two-step cooling.

4.5. CONCLUSIONS

In this chapter, we have shown that particles can address many different particles by coating many carefully designed, independent pairs of DNA strands. We outline the design rules of the DNA sequences for synthesizing polygamous particles. We demonstrate the use of our design rules by synthesizing four-partner particles. Then, we illustrate how to use polygamous particles to perform the self-assembly that monogamous systems can not achieve by synthesizing dual-phase materials which can be either a gel or a fluid at the same temperature. The phase of the dual-phase materials is protocol dependent. We also prove that our thermodynamic model developed in Chapter 2 provides the guide to design a complicated polygamous system. Then, we find out that the number of partners of a polygamous particle is strongly limited by the intrinsic properties of DNA hybridization and sequence combination. In our system with 11-mer sticky end, the practical limit is ~ 100. Of course, for particles of the same size in direct contact, the maximum number of partners a particle can have is 12, but a set of particles with particular properties (e.g., color, dielectric constant, and conductivity) could be programmed to associate with up to ~ 100 different particles or

~ 100 different sites in a structure. For particles of different sizes, there is no limit to the number of, for example, small partners a large particle can have. For immunology or other bulk assays, such polygamous particles could quickly separate a host of other particles from suspension. For colloidal architecture, many repeating motifs could be bound to different places on the structure. Therefore, the technique of synthesizing polygamous particles paves the path to optimizing or simplifying synthesis process and opens the door to many new fields of self-assembly.

CHAPTER 5 MOBILE BONDS

From Figure 4-8 (b), we learn that the particles in X-Y-Z system can form two-shell clusters in Figure 4-6. However, the two-shell clusters in Figure 4-8 (b) are not as compact as the one in Figure 4-6. The reason for such a difference is the lack of mobile bonds in our experimental system. As shown in Figure 5-1 (a), the blue particles attract each other. If the system allows mobile bonds, three particles form a triangle structures since a triangle cluster contains three bonds and is the configuration of the lowest energy state. However, if the system does not allow mobile bonds, three particles will mostly form a linear structure as shown in Figure 5-1 (b). That is because a particle can not roll along the surface of the other particle while they are bound together. Therefore, if bonds are not mobile, the structure of the three particles depends on how the first bond between a pair of particles is formed. Once a bond between a pair of particles is formed, the relative orientation between these two particles is fixed. Since our experimental system does not have mobile bonds to utilize DNA-coated particles for synthesizing a designed structure such as the one in Figure 4-6, developing a technique to allow particles to form mobile bonds is necessary. In this chap-

ter, we show how to introduce weak depletion to make particles roll along the surface of each other and how to assemble simple structures by using such a technique.

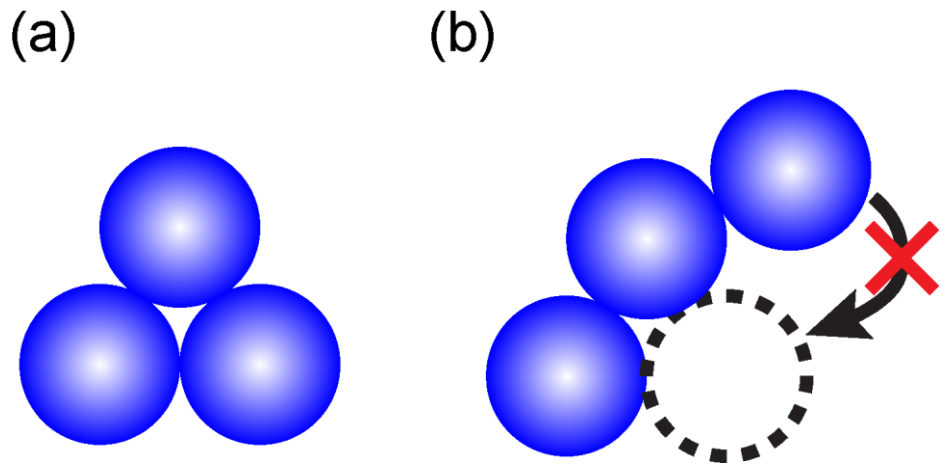

Figure 5-1: Comparisons between systems with and without mobile bonds.

5.1. TEMPERATURE-DEPENDENT DEPLTION

To introduce depletion to our system, we have to understand how depletion works in the system with our DNA-coated particles. In this section, we will

introduce an unusual depletion interaction between our particles. Normally, depletion is temperature-independent. However, due to the temperature-dependent surface adsorption of depletants, the depletion interaction between our particles is temperature-dependent.

5.1.1. SYSTEM DESCRIPTION

In this chapter, we use 1-μm neutravidin-coated polystyrene particles since the shape of particles is more uniform and spherical (Figure 5-2) than our usual 2-μm polystyrene particles (Figure 2-1). Also, our 1-μm polystyrene particles in Figure 5-2 form crystals. Such result suggests that the surfaces of our 1-μm particles are smooth enough to form mobile bonds. Since neutravidin, like streptavidin, can bind irreversibly to biotin in our temperature regime, the way we coat the 1-μm neutravidin-coated particles with biotinylated DNA strands is similar to that of 2-μm streptavidin-coated particles with biotinylated DNA strands in Section 2.1. Therefore, we will use 1-μm DNA-coated polystyrene particles to perform the experiments.

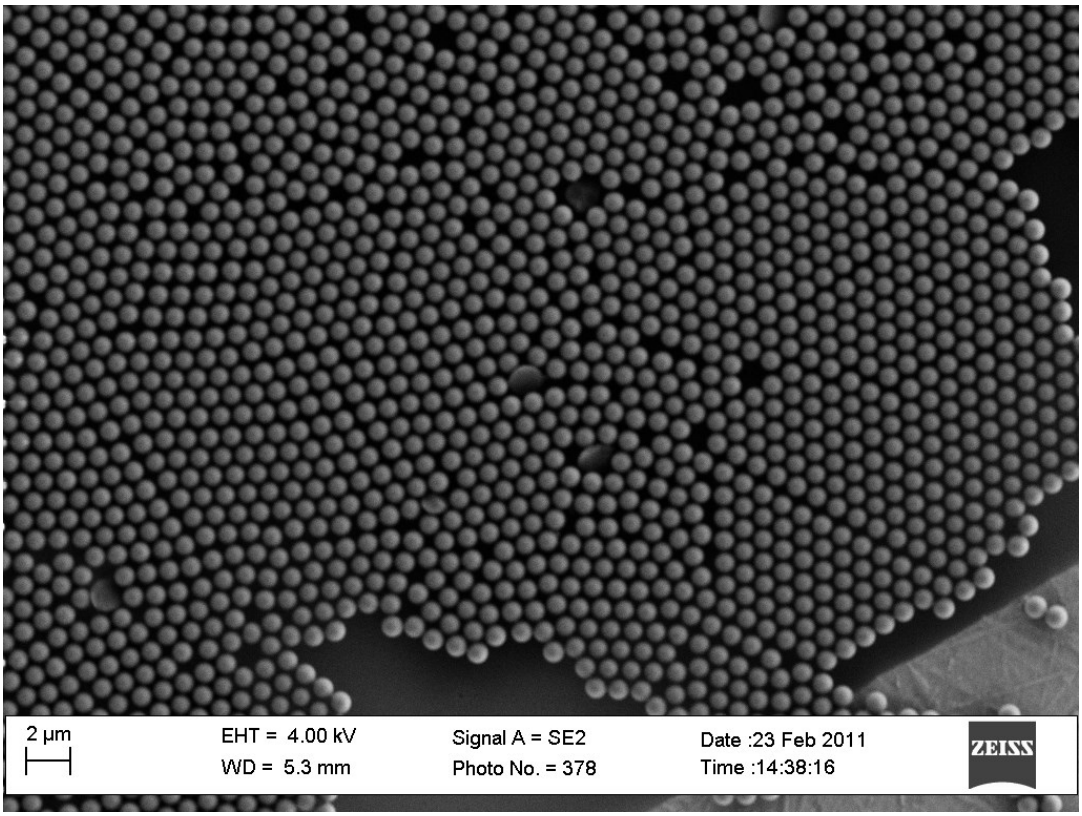

Figure 5-2: Electron microscopy of 1-μm polystyrene microspheres.

5.1.2. NORMALIZED CHANGED PIXELS

To quantify the aggregation behaviors of 1-μm polystyrene particles, we measure normalized changed pixels instead of fraction of single particles (see the definition and explanation below). Since the gravitational height of

1-μm polystyrene particles is $\sim 16\ \mu m$, the particles float, and the system is generally a three-dimensional one (Figure 5-3). Therefore, measuring the fraction of single particles in a three-dimensional system is not an efficient way to quantify particle aggregation. Therefore, we will measure normalized changed pixels to quantify/characterize the aggregation of 1-μm polystyrene particles.

To measure the normalized changed pixels, we take a three-second long movie and compare the pixels changed in three seconds. Since the diffusion coefficient of 1-μm particles is $\sim 1\ \mu m^2/s$, a single particle diffuses $\sim 2\ \mu m$ after three seconds. However, a cluster with more than two particles moves $\leq \frac{1}{2}$ as fast and does not diffuse significantly in three seconds. An example of two images taken at times differed by three seconds is shown in Figure 5-5. We quantify the aggregation behavior of such an image by counting the pixels changed from Figure 5-5 (a) to Figure 5-5 (b). In case of big clusters, they are basically static in three seconds, so the pixels of the clusters do not change. However, as single particles diffuse significantly in three seconds, their pixels are changed. Therefore, for the system with no

single particles, the number of changed pixels is ~ 0. For the system with only single particles, the number of changed pixels is about twice the number of pixels of total single particles. Since the number of pixels depends on particle concentrations, we normalize the number of changed pixels by the following equation:

$$\text{Normalized Changed Pixels} \equiv \frac{\#\text{ of changed pixels} - N_0}{N_1 - N_0},$$

where N_0 is the average number of changed pixels for fully aggregated system, and N_1, the average number of changed pixels for non-aggregated system. Therefore, measuring normalized changed pixels is similar to measuring fraction of single particles. For fully aggregated system, the normalized changed pixels is ~ 0. For non-aggregated system, the normalized changed pixels is ~ 1. By measuring the normalized changed pixels, we can quantify the aggregation behaviors of either three- or two-dimensional systems.

To check whether or not measuring normalized changed pixels is a reliable and accurate measurement to quantify particle aggregation, we compare

with each other the melting curves of a two-dimensional system, in which measuring singlet fraction is straightforward (see Section 2.3.3), in terms of normalized changed pixels and singlet fraction. The system contains two species of particles. The one is coated with S_3 while the other is coated with S_3'. The sequences of S_3 and S_3' are shown in Table 4-2. The two species are mixed homogeneously in equal amounts. The sample is placed on a temperature gradient stage, and after 5-hour equilibration time, the singlet fraction vs. temperature (red curve in Figure 5-4) and normalized changed pixels vs. temperature (blue curve in Figure 5-4) are both measured. From Figure 5-4, we read that the melting temperature and melting transition width from the measurement of singlet fraction are $43.0\,℃$ and $2.0\,℃$, respectively, and from the measurement of normalized changed pixels are $42.3\,℃$ and $2.8\,℃$, respectively. Comparisons of melting temperatures and melting transition widths between these two measurements show that they both provide similar (although not identical) results for quantifying particle aggregation in the same system. Therefore, while the system is three-dimensional and singlet fraction is hard to be measured, measuring normalized changed pixels is a good alternative to quantify particle aggregation.

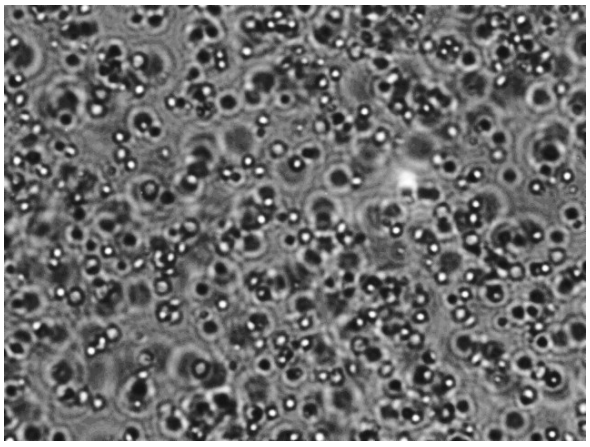

Figure 5-3: An Image of 1-μm polystyrene particles. Since 1-μm polystyrene particles float, the system is three-dimensional.

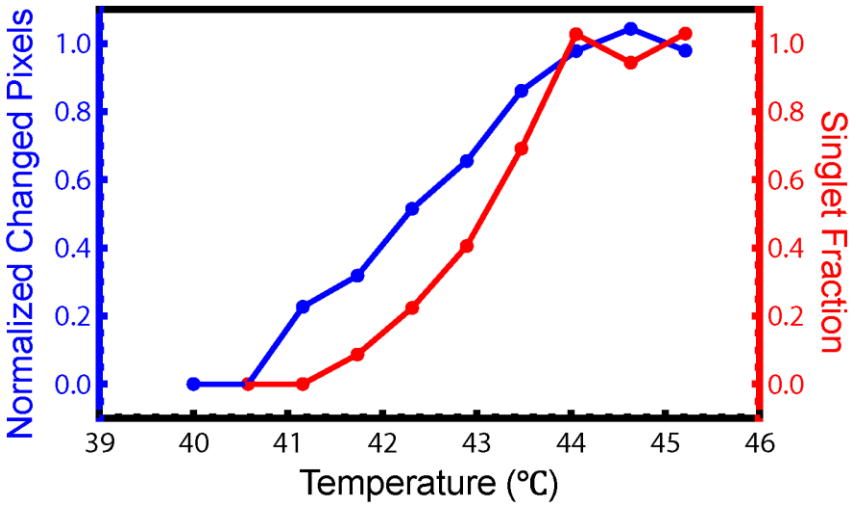

Figure 5-4: Comparison of measurements of melting curves in terms of normalized changed pixels (blue) and singlet fraction (red).

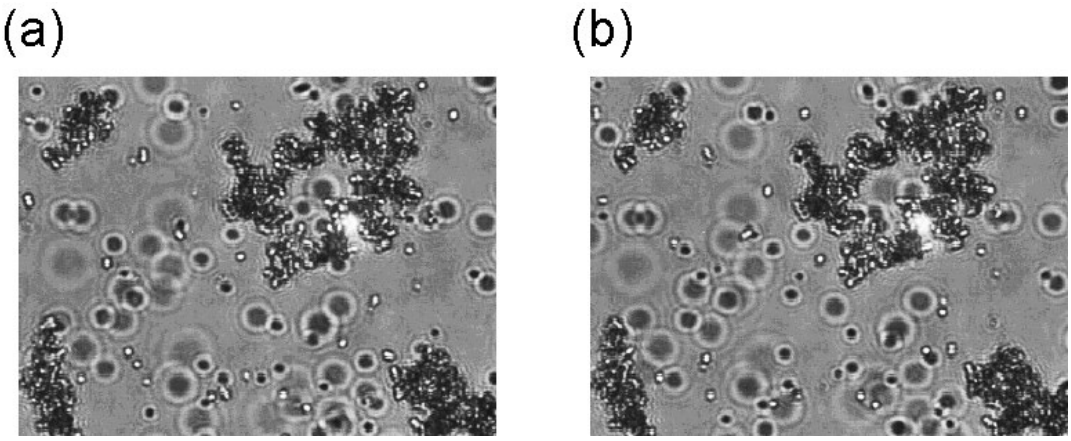

Figure 5-5: Comparison of images taken at different times. (b) Image captured three seconds after (a).

5.1.3. MEASUREMENT OF MELTING CURVES

To measure the melting curve of $1\text{-}\mu\text{m}$ DNA-coated particles in the buffer containing depletants, we place our sample on the temperature gradient and measure the normalized changed pixels with respect to temperature when the system reaches thermal equilibrium. Particles are coated with DNA S, the sequence of which is shown in Table 2-1. Since S does not hybridize to itself, particles coated with S should not aggregate through the DNA interaction. However, since particles adsorb depletant differently at different temperatures, the depletion interaction is temperature-dependent.

The particle aggregation behavior is temperature-dependent. In Figure 5-6 (a), particles do not adsorb depletants at $19.7\,℃$, so particles form crystals by depletion interaction. In Figure 5-6 (b), particles adsorb depletants at $30.0\,℃$, so depletion force is weakened. As a result, particles do not aggregate or form any crystals. Our particles are contained in a capillary. Since the particles can also be attracted to the capillary surface through depletion interaction, the system is two-dimensional. Comparisons between Figure 5-6 (a) and Figure 5-6 (b) show that the depletion interaction in our system is temperature-dependent. The measured melting curve is shown in Figure 5-7. The melting temperature is $22.8\,℃$. The melting transition width is $1.1\,℃$. From the measurement of the melting curve, we can tune the depletion interaction by controlling temperatures.

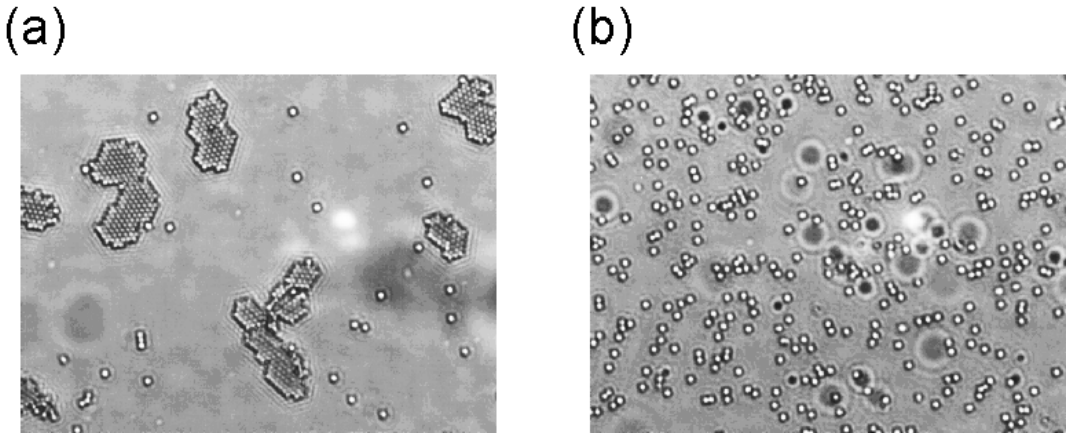

Figure 5-6: Temperature-dependent depletion interaction. Particles (a) form crystals at 19.7 ℃, and (b) do not aggregate at 30.0 ℃.

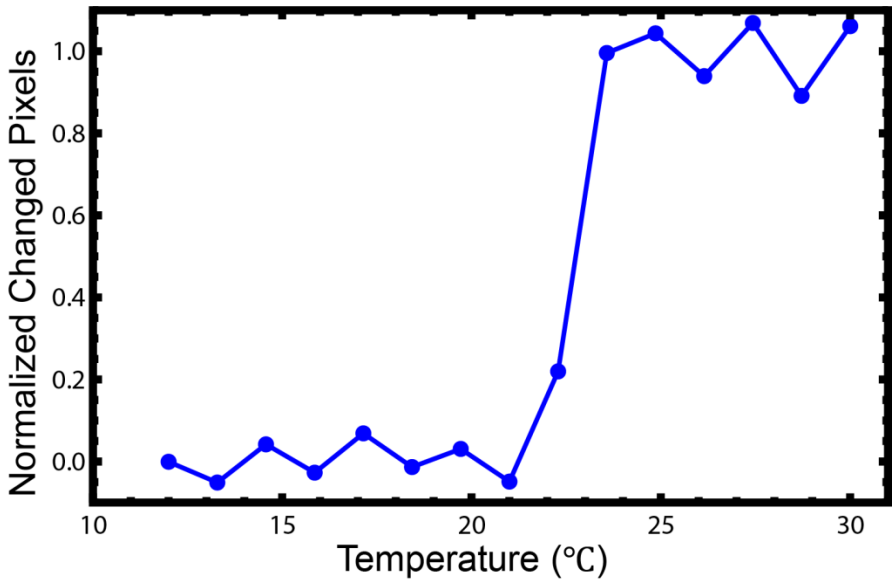

Figure 5-7: Normalized changed pixels vs. temperatures.

5.2. WHEN DNA MEETS DEPLETION

To create mobile bonds and allow particles to roll along the surface of each other, we introduce weak depletion into the system. In this section, we propose a hypothesis for a potential solution of creating mobile bonds.

As shown in Figure 5-8, the blue curve is the schematic melting curve of depletion interaction of DNA-coated particles. Without introducing depletants into the system, the schematic melting curve of DNA interaction is the pink curve. In our usual DNA-mediated system, particles bind together but do not roll on each other when the temperature is below the melting transition (Point A in Figure 5-8), and they do not aggregate if beyond melting transition (Point B in Figure 5-8) but can roll along the surface of each other. Therefore, schematically, the melting curve of DNA interaction, the pink curve in Figure 5-8, represents the mobility of DNA bonds. At the bottom of the melting curve (Point A in Figure 5-8) DNA bonds are immobile, and at its top (Point B in Figure 5-8) mobile. In such a system, if we introduce depletion interaction (melting curve is the blue curve in Figure 5-8), the overall melting curve (DNA plus depletion) should shift to higher tem-

perature since particles gain extra attraction energy from depletion and need a higher thermal energy to melt. The schematic melting curve of DNA plus depletion is the red curve in Figure 5-8. At the same time, the pink curve, which is the melting curve for the DNA interaction, remains unchanged since it depends on the properties of DNA and is independent of the depletion interaction. Our hypothesis is that under such conditions, there will be a temperature range at which particles can bind well to each other and roll along each other's surface. For example, particles at Point C in Figure 5-8 can bind to each other since it is at the bottom of the melting curve of DNA plus depletion (the red curve in Figure 5-8). At the same time, Point C is also at the top of the melting curve of DNA interaction (the pink curve in Figure 5-8). This means that DNA bonds holding particles together are mobile. The particles at Point C may be able to bind to each other, and the DNA bonds between them may also be mobile. Therefore, combing DNA and weak depletion, we may be able to create mobile bonds, so particles can roll along the surface of each other while they are bound.

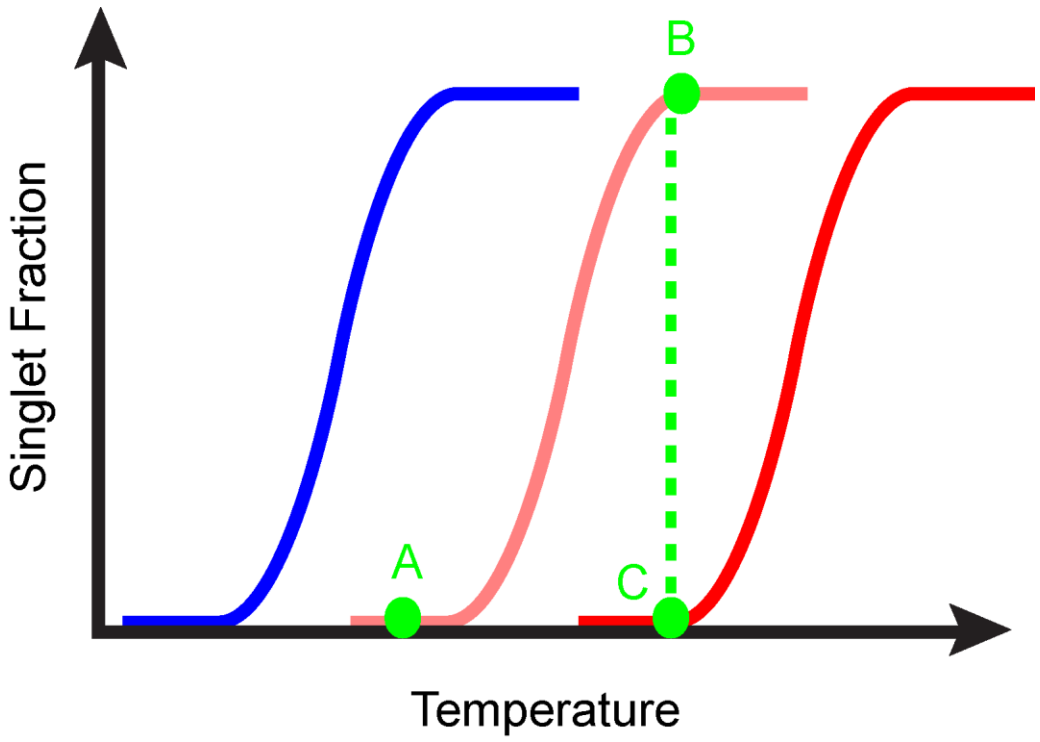

Figure 5-8: Schematic diagram of melting curves of depletion (blue), DNA (pink), and DNA plus depletion (red).

5.3. EXPERIMENTAL VERIFICATION

To check whether or not our hypothesis of using DNA plus depletion to create mobile bonds is real, we perform experiments to test it. As shown in Figure 5-9, we choose a Watson-Crick-like binary system. Blue particles (V)

are coated with DNA S. Cyan particles (W) are coated with DNA S′. The sequences of S and S′ are shown in Table 2-1. First, we measure the melting curves of depletion interaction between V's and W's separately. We make two samples—one with only V's and the other with only W's. We choose polyethylene oxide (PEO) with a concentration of $1.1\ \mathrm{g/L}$ and an average molecular weight of $600{,}000\ \mathrm{u}$ as the depletant. Measured depletion melting curves of the two samples are shown in Figure 5-10. The blue and cyan curves represent the melting curves of the samples containing V's and W's, respectively. The melting transition widths are $1.1\ ℃$ and $3.1\ ℃$, respectively. We also measure the melting curve of V+W without depletants. The measured melting curve is the pink one in Figure 5-10, its melting temperature $28.4\ ℃$, and the melting transition width $3.6\ ℃$. Finally, we wish to measure the melting curve of V+W in the buffer containing $1.1\ \mathrm{g/L}$ PEO. The measured melting curve is the red one in Figure 5-10, its melting temperature $33.9\ ℃$ and melting transition width $2.8\ ℃$. As expected, the melting curve of V+W without depletants (the pink curve) is shifted to higher temperature direction once depletants are added to the system. Additionally, the melting transition after the shift is about the same. This implies that the red curve is the melting behavior of both DNA and depletion interactions. Further, the

particle images of Points D and F in Figure 5-10 are shown in Figure 5-11 (a) and Figure 5-11 (b), respectively. Figure 5-11 (a) shows the particles form fractal structures as strong DNA bonds prohibit particles from rolling. Figure 5-11 (b) shows that particles do not aggregate at all as attractions from DNA and depletion are too weak to hold a pair of particles together. However, Figure 5-12 (a), which is the particle image of Point E in Figure 5-10, shows that particles form crystals. The reason for forming of such crystals could be that DNA bonds are weak enough to allow rolling. At the same time, depletion interaction complements the attraction needed to hold particles together. As a result, particles can roll due to the weak DNA interaction while bound due to the cooperation of DNA and depletion interactions. To be more careful about the result of crystals in Figure 5-12 (a), we take the images of the samples only with V's and only with W's, respectively, at the same temperature and PEO concentration as shown in Figure 5-12 (b) and Figure 5-12 (c), respectively. We find that at the same depletion condition, the system containing either only V's or only W's does not form any stable aggregates since depletion attraction alone is too weak to hold a pair of particles together. However, as shown in Figure 5-12 (a), if the system contains both V's and W's, the system contains both DNA and deple-

tion attractions. V's and W's have enough attraction energy to form stable crystals. This shows that particles can roll along the surface of each other while they are bound enabling them to find the lowest energy state, i.e., crystals.

To verify the composition of crystals, we use fluorescently labeled particles. As shown in Figure 5-13 (a), V_G and W_R are fluorescent particles and can be distinguished by their fluorescent emissions. The fluorescent excitation and emission wavelengths of V_G and W_R are shown in Table 5-1. We put V_G's and W_R's together in equal amounts in a buffer containing $1.1\ \mathrm{g/L}$ PEO. At $45\ ^{\circ}\mathrm{C}$, we again find several crystals as shown in Figure 5-13 (b). The green and red particles are V_G's and W_R's, respectively. Figure 5-13 (b) shows the correlation between V_G's and W_R's in the crystals. We find out that the crystals are formed by the cooperation of DNA and depletion interactions. The sample containing only depletion can not form crystals with such correlation between two species of particles. Therefore, by using labeled particles, we confirm that the crystals in Figure 5-12 (a) and Figure 5-13 (b) are the results of cooperation of DNA and depletion. The crystals

contain both species with correlation due to DNA interaction among different species.

To sum up, in this section, we have shown that combining DNA and depletion, we are able to create mobile bonds, so particles can explore lots of binding configurations and find the lowest energy state. Additionally, although depletion does not have specificity, the interaction of DNA plus depletion is specific since DNA interaction is highly specific. By using DNA plus depletion, we are able to create the binding between particles which is both mobile and specific.

Figure 5-9: DNA interaction diagram. V and W attract each other through DNA strands coated on their surfaces. V is coated with DNA S and W with DNA S'. The sequences of S and S' are shown in Table 2-1.

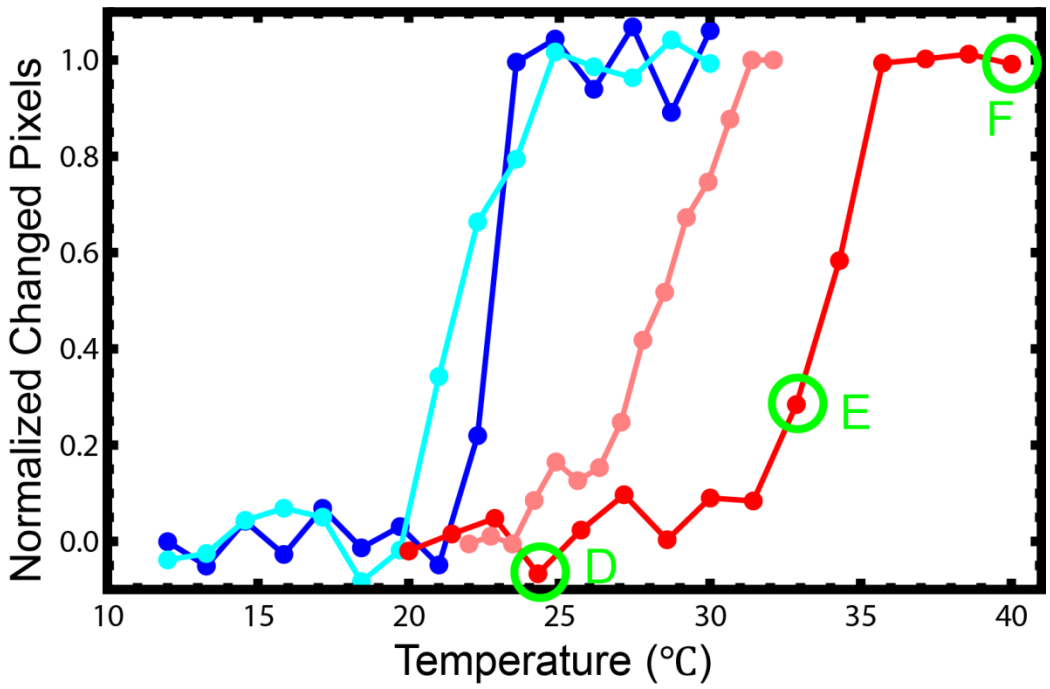

Figure 5-10: Melting curves of systems with V's or W's with or without depletion. The blue and cyan curves are the melting curve of V's and W's in $1.1\ \mathrm{g/L}$ PEO, respectively. The pink and red curves are the melting curves of V+W without depletion and with $1.1\ \mathrm{g/L}$ PEO, respectively.

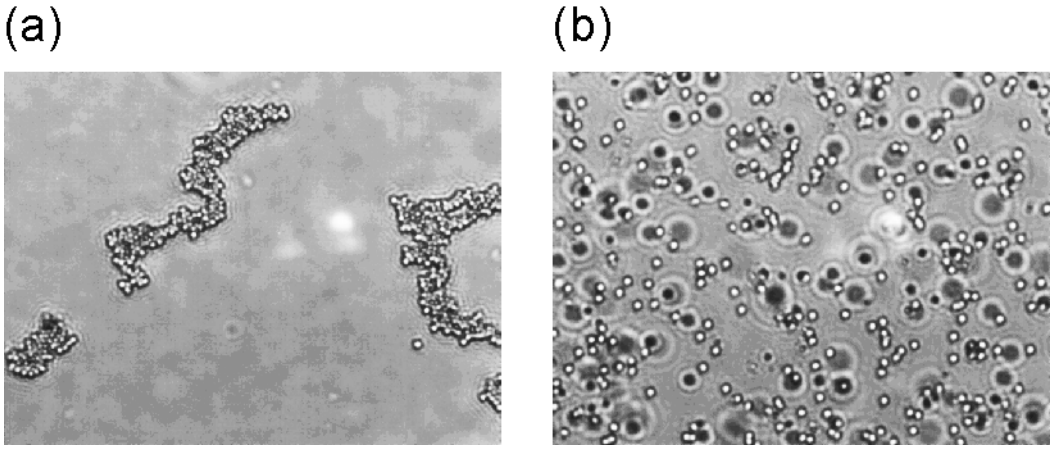

Figure 5-11: Images of V+W in the buffer containing 1.1 g/L PEO at different temperatures. The image of (a) Point D at 24.3 ℃, and (b) Point F in Figure 5-10 at 40.0 ℃.

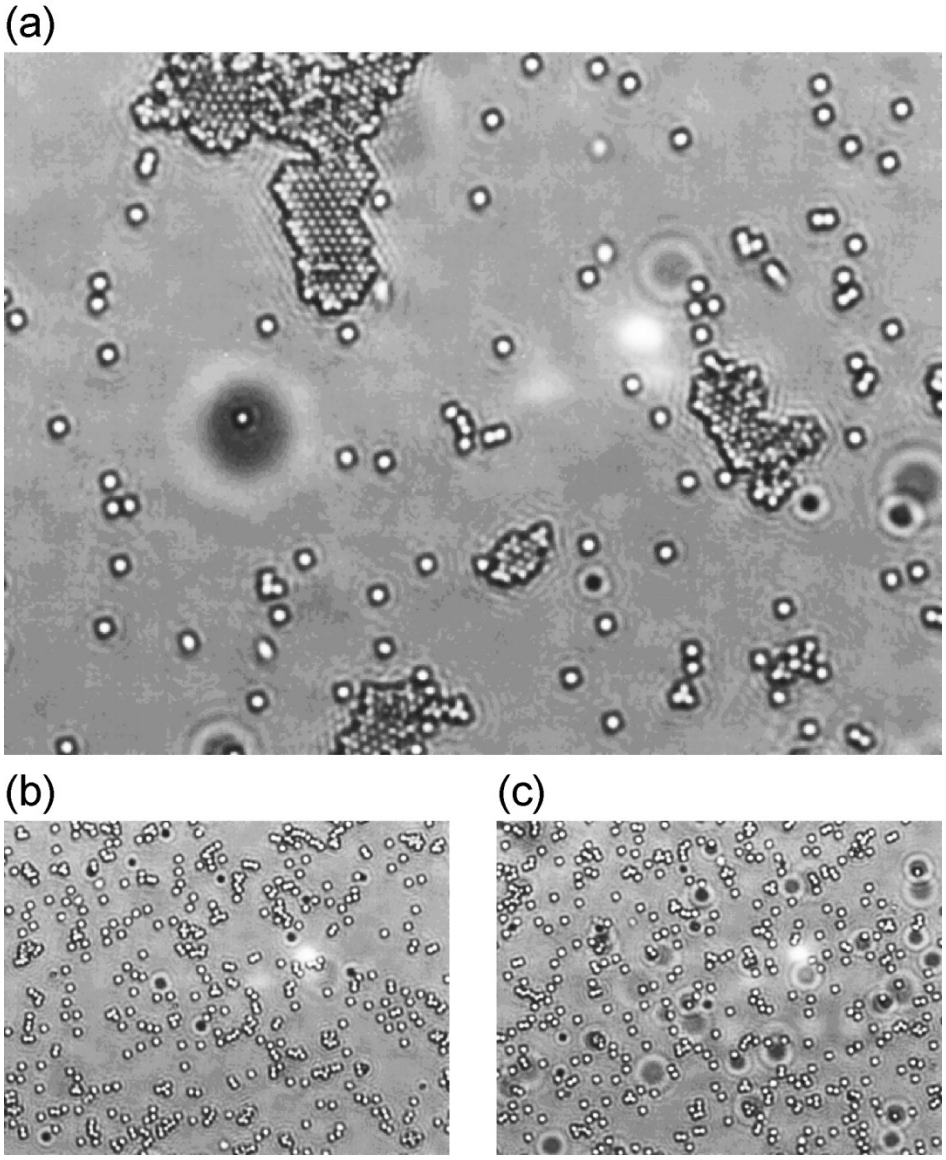

Figure 5-12: Images of V+W, V, and W in the buffer containing $1.1\ \mathrm{g/L}$ PEO at $32.9\ ^{\circ}\mathrm{C}$. The system contains (a) equal amounts of V's and W's. (b) only V's, and (c) only W's.

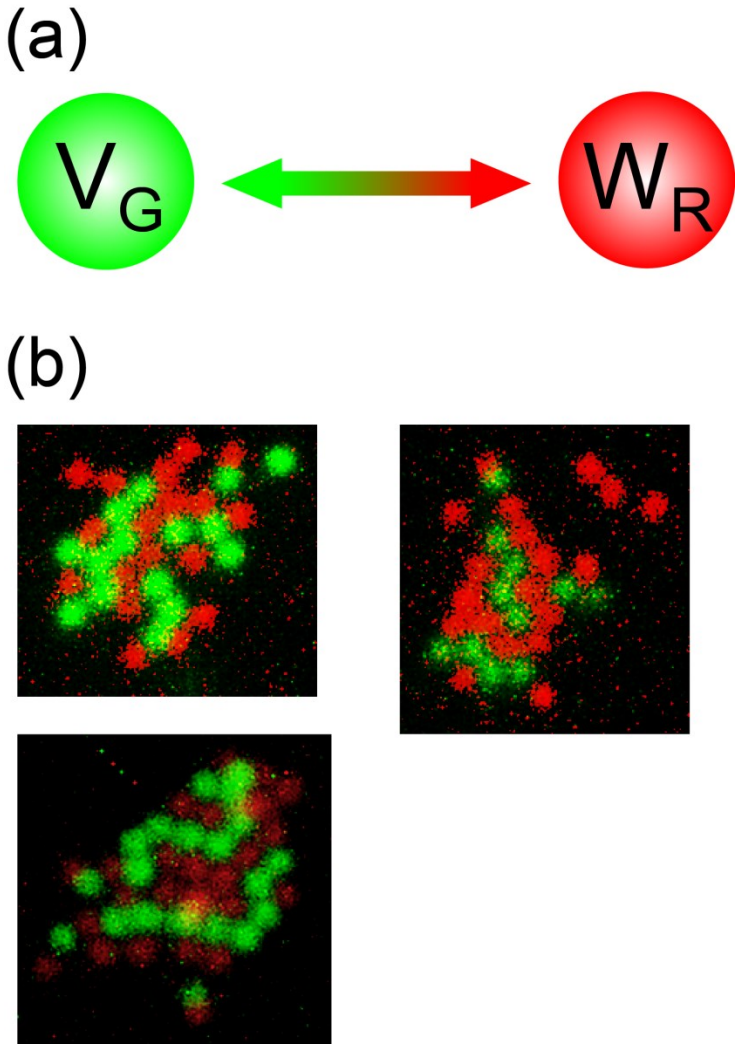

Figure 5-13: System containing fluorescently labeled particles. The PEO concentration is $1.1\,\mathrm{g/L}$. (a) Complementary particles V_G and W_R are both fluorescent and are coated with DNA S and DNA S', respectively. (b) The images of crystals with labeled particles at $45\,^{\circ}\mathrm{C}$. Note

that only few bonds are V_R-V_R or V_G-V_G. Rather the clusters are held together by V_G-V_R bonds and are correlated with most neighbors of the opposite color.

Particles	Excitation Peak (nm)	Emission Peak (nm)
V_G	505	515
W_R	580	605

Table 5-1: Excitation and emission peaks of particles V_G and W_R.

5.4. SIMPLE COLLOIDAL ARCHITECTURE

To demonstrate the use of specific mobile bonds studied in this chapter, we synthesize hexagon clusters using a specifically designed system. As shown in Figure 5-14 (a), we still use Particles V and W from Figure 5-9. However, instead of using equal amounts of V's and W's in Section 5.3, the ratio of V's and W's is designed to be about $1:100$. Since the system is two-dimensional, we can expect the lowest-energy cluster to be a hexagon cluster as shown in Figure 5-14 (a). We made a sample like the one in Section

5.3 except the ratio of V's and W's was about $1:100$. The concentration of PEO is also $1.1\ \mathrm{g/L}$. At $31.6\ ℃$, we find out that the system contains several hexagon clusters as shown in Figure 5-14 (b). These results demonstrate that we can make a simple colloidal architecture by designing the interactions of DNA and adding depletion between particles to facilitate bound particle relative motion. It also shows that the interaction of DNA plus depletion is a specific interaction. By carefully designing interactions of DNA and adding depletants to a system with many different species, we expect that synthesizing more sophisticated colloidal architecture is doable.

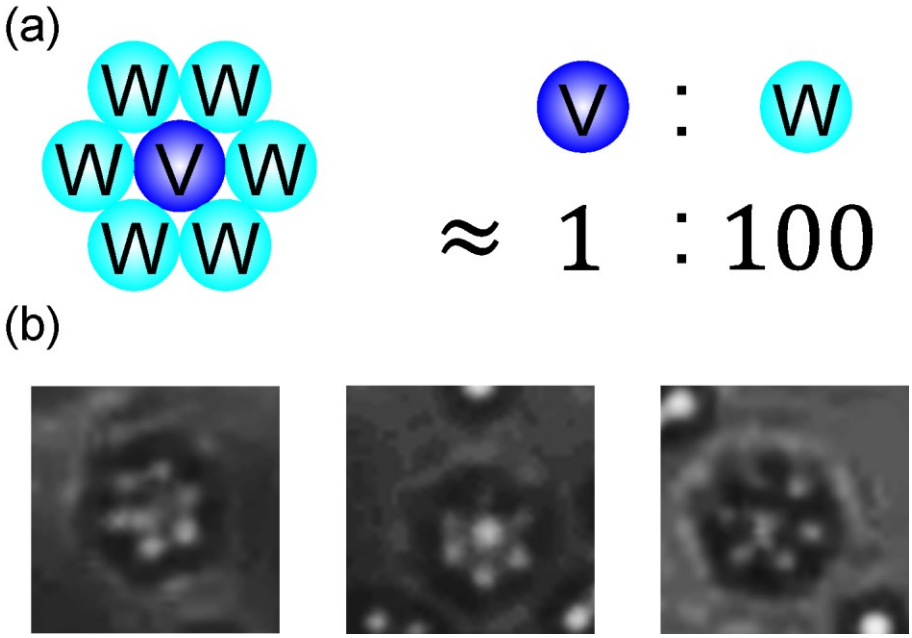

Figure 5-14: Demonstration of simple colloidal architecture. (a) Design of synthesizing a hexagon cluster. The ratio of the numbers of V's and W's is about $1:100$. (b) Images of hexagon clusters synthesized through the design in (a). The temperature of the images is 31.6 ℃.

5.5. CONCLUSIONS

In this section, we found that we can create specific mobile bonds through a combination of DNA and depletion interactions. If we use only DNA, the bonds between particles are so immobile that the structures of clusters are

essentially stuck in the initial contact configuration. Although DNA interactions are highly specific, the frozen kinetics of cluster limits the potential use of DNA-coated particles for synthesizing designed structures. For depletion interaction, the binding between particles is flexible/mobile. Particles can form crystals without undergoing any frozen kinetics. However, the depletion interaction is not specific. In this chapter, we find out that by carefully mixing and controlling DNA and depletion interactions between particles, we can create an interaction that allows binding to be both specific and mobile. This should enable the door to the synthesis of complicated, DNA-directed, designed structures.

CHAPTER 6 PHOTO-CROSSLINKING

The advantage of using DNA molecules for self-assembly is to create high specific and thermo-reversible binding and therefore to synthesize designed structures [12, 21, 22, 25-27, 30, 32-34, 37, 43, 50, 52, 83]. For many years, DNA has been used to fabricate various functional systems, such as crystals, replicators, motors, robots, computers, and machines [12, 33, 46, 47, 50, 84-90]. However, to synthesize higher-order constructs or to provide structural information on biomacromolecules when standard techniques were not applicable, irreversible/permanent crosslinking is necessary [91]. Several crosslinking methods have been studied. The most commonly used method is to use psoralen that forms covalent links to thymines on exposure to ultraviolet light [92]. However, using psoralen as the crosslinking agent requires the attachment of the psoralen group at the 5'-TpA site (T-A sequence) of a DNA sticky end [93]. This requirement not only limits the design of DNA sequences with a crosslinking agent but also reduces the crosslinking specificity since unwanted TA pairs could be inadvertently crosslinked. In this chapter, we introduce cinnamate as a crosslinking agent. Two cinnamate molecules form covalent bonds once exposed to $360-$

$390\ \mathrm{nm}$ ultraviolet light. By using a pair of complimentary cinnamate-modified strands, we show that the crosslinking is highly specific. To show the potential of using cinnamate-modified DNA strands, we developed a new photolithography in which we make micrometer-scale DNA-functionalized patterns on a gold surface through patterned ultraviolet light. We can then reversibly attach DNA strands and DNA-coated colloids complementary to our photo-patterned region.

6.1. CINNAMATE AND DNA

To perform a specific photo-crosslinking for a pair of complementary DNA strands, we choose cinnamate as the crosslinking agent. As shown in Figure 6-1 [94], cinnamate can be formed as an artificial nucleoside and incorporated in a DNA strand. For a pair of cinnamate groups in contact as shown in Figure 6-2 [94], the configuration of their encounter can be either head-to-head [see Figure 6-2 (a)] or head-to-tail [see Figure 6-2 (b)]. The cycloaddition product can occur on exposure of a pair of cinnamate groups to $360 - 390\ \mathrm{nm}$ ultraviolet light, after which the cinnamate groups are covalently bound together. Therefore, we use here cinnamate-modified DNA

strands. When a pair of cinnamate-modified complementary strands hybridizes, the cinnamate groups between DNA strands are brought together. Then, it does not matter if the two cinnamate groups are in head-to-head or head-to-tail configuration. After exposure to $360\ \mathrm{nm}$ ultraviolet light, these two cinnamate groups are held together covalently, and the complementary DNA strands are held together covalently too. By intercalating cinnamate group into DNA strands, we are able to perform specific photo-crosslinking.

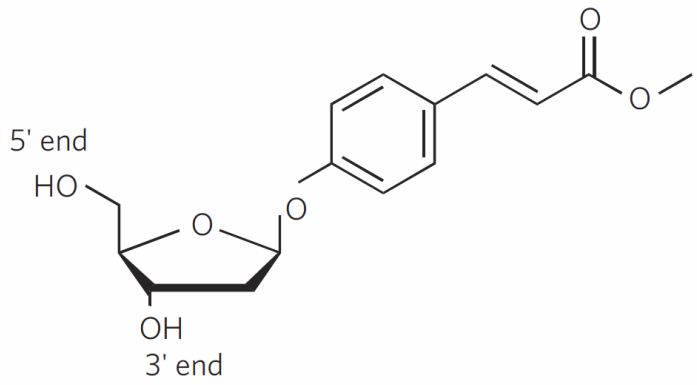

Figure 6-1: Schematic representation of cinnamate-containing nucleoside.

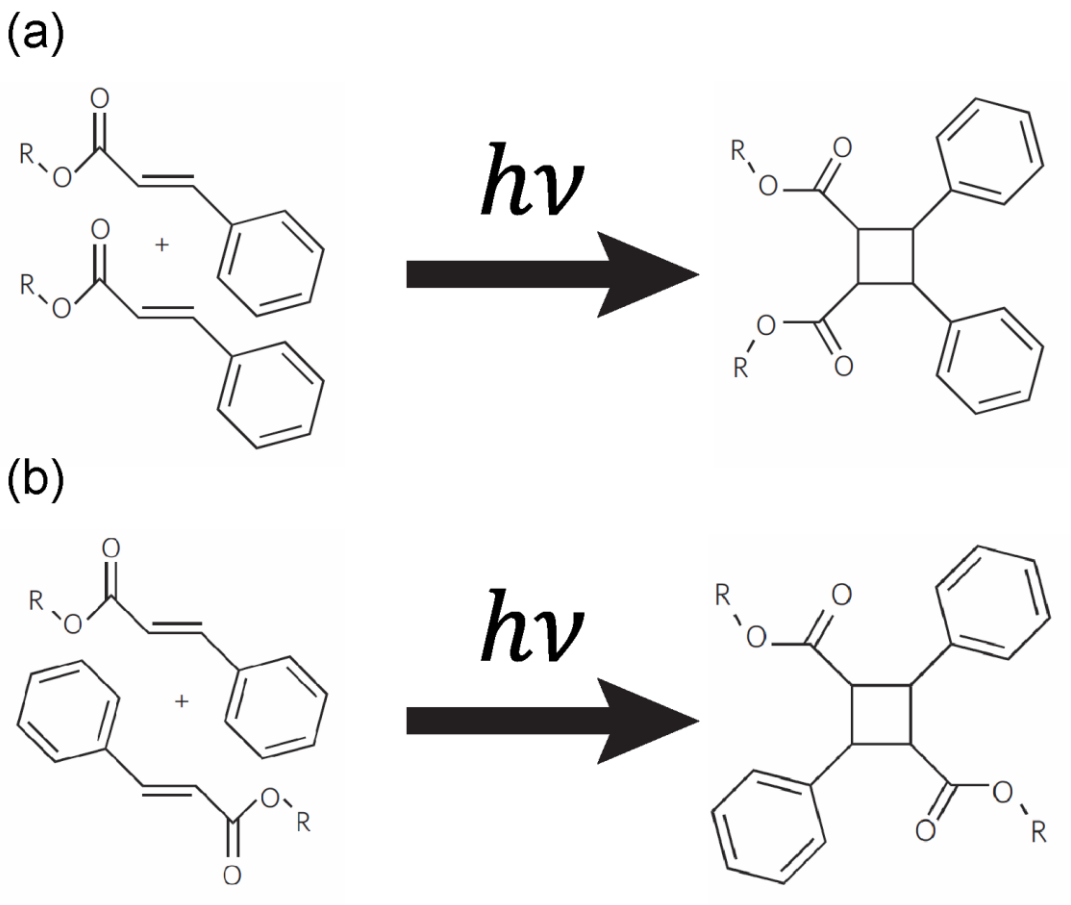

Figure 6-2: Schematic representation of the cycloaddition between two cinnamate groups. (a): Head-to-head, and (b): Head-to-tail cyclo-addition.

6.2. TEST OF SPECIFIC PHOTO-CROSSLINKING

To verify that we can really perform photo-crosslinking by using cinnamate groups, we did an experiment with particles coated with cinnamate-modified DNA strands. As shown in Figure 6-3 [94], we use the method of Section 2.1 to coat our streptavidin particles. However, we choose $1\text{-}\mu\text{m}$ polystyrene particles and the sequences of the sticky ends are replaced by cinnamate-modified DNA strands. As shown in Figure 6-3, the blue particles are coated with S_5, and the cyan particles with S_5'. The DNA sequences of S_5 and S_5' are shown in Table 6-1. X represents a cinnamate group. At $30\ ^\circ\text{C}$, we note that all particles aggregate (Figure 6-3). The complementary sticky ends are hybridized, and the corresponding pair of cinnamate groups is held in contact as shown in Figure 6-3. Then, particles are exposed to $\sim 360\ \text{nm}$ ultraviolet light for 15 seconds. During the exposure, pairs of cinnamate groups are brought together due to hybridization of complementary DNA strands and form covalent bonds. After that, the temperature of the system is increased to $55\ ^\circ\text{C}$. Although DNA strands between particles should dehybridize at such temperature, particles are still held together and do not dissociate as shown in Figure 6-3. This is because the covalent bonds

formed between two cinnamate groups hold DNA strands covalently and therefore particles are held together by these bonds.

To further verify that DNA hybridization is necessary to trigger photo-crosslinking during UV exposure, we perform another experiment with particles coated with non-complementary and palindromic strands. As shown in Figure 6-4 [94], the green particles are coated with both S_5 (green) and S_6 (black). The sequences of S_5 and S_6 are shown in Table 6-1. S_5 is a cinnamate-modified strand and is not complementary to itself. S_6 is a palindromic sequence and self-complementary. Therefore, at $30\ ℃$, particles still aggregate together due to hybridization of S_6 (Figure 6-4). Since S_5 is not complementary to itself, no DNA bridge is formed by S_5. We apply $\sim 360\ \mathrm{nm}$ ultraviolet light for 15 seconds. Since S_5's do not hybridize, the cinnamates are not close enough to form covalently link under UV exposure. We then increase the temperature to $55\ ℃$. Since no covalent bonds are formed to hold particles together, particles dissociate due to dehybridization of S_6 (Figure 6-4). DNA hybridization is necessary to trigger the photo-

crosslinking during UV exposure since a pair of cinnamate groups needs to be held together in contact to form covalent bonds.

To quantify the use of UV exposure, we vary the exposure time of the experiments in Figure 6-3 and Figure 6-4 and measure the final singlet fraction at $55\ ^{\circ}\mathrm{C}$. Figure 6-5 shows the final singlet fraction at $55\ ^{\circ}\mathrm{C}$ vs. the exposure time of $\sim 360\ \mathrm{nm}$ ultraviolet lights [94]. The red and black dots are the experimental data for the system in Figure 6-3 and Figure 6-4, respectively. We note that the singlet fraction of the system in Figure 6-3 decays from ~ 1 to ~ 0 as the exposure time increases from 0 to 15 seconds. We find that the singlet fraction is about zero if the exposure time is longer than 15 seconds. Hence, applying the ultraviolet light for 15 seconds is sufficient to crosslink most of the cinnamate groups if they are held together in contact due to hybridization of complementary strands. Additionally, we find that the singlet fraction of the system in Figure 6-4 remains ~ 1 even after we apply the ultraviolet lights over one minute. This is additional evidence that our photo-crosslinking is not triggered unless cinnamate groups are held together in contact by complementary strands.

Putting together the experimental results of Figure 6-3, Figure 6-4, and Figure 6-5, we claim that by using cinnamate-modified DNA strands, we can perform the photo-crosslinking with high specificity. Such highly specific photo-crosslinking enables the processing of more complex processes and more permanent structures.

DNA Symbols	Sequences
S_5	5' – CCA AGT X TAT GA – 3'
S_5'	5' – TCA TA X ACT TGG – 3'
S_6	5' – AAT CAT GAT T – 3'

Table 6-1: Cinnamate-modified DNA sequences and a palindromic DNA sequence. X represents a cinnamate group. S_6 is a palindromic sequence and is complementary to itself.

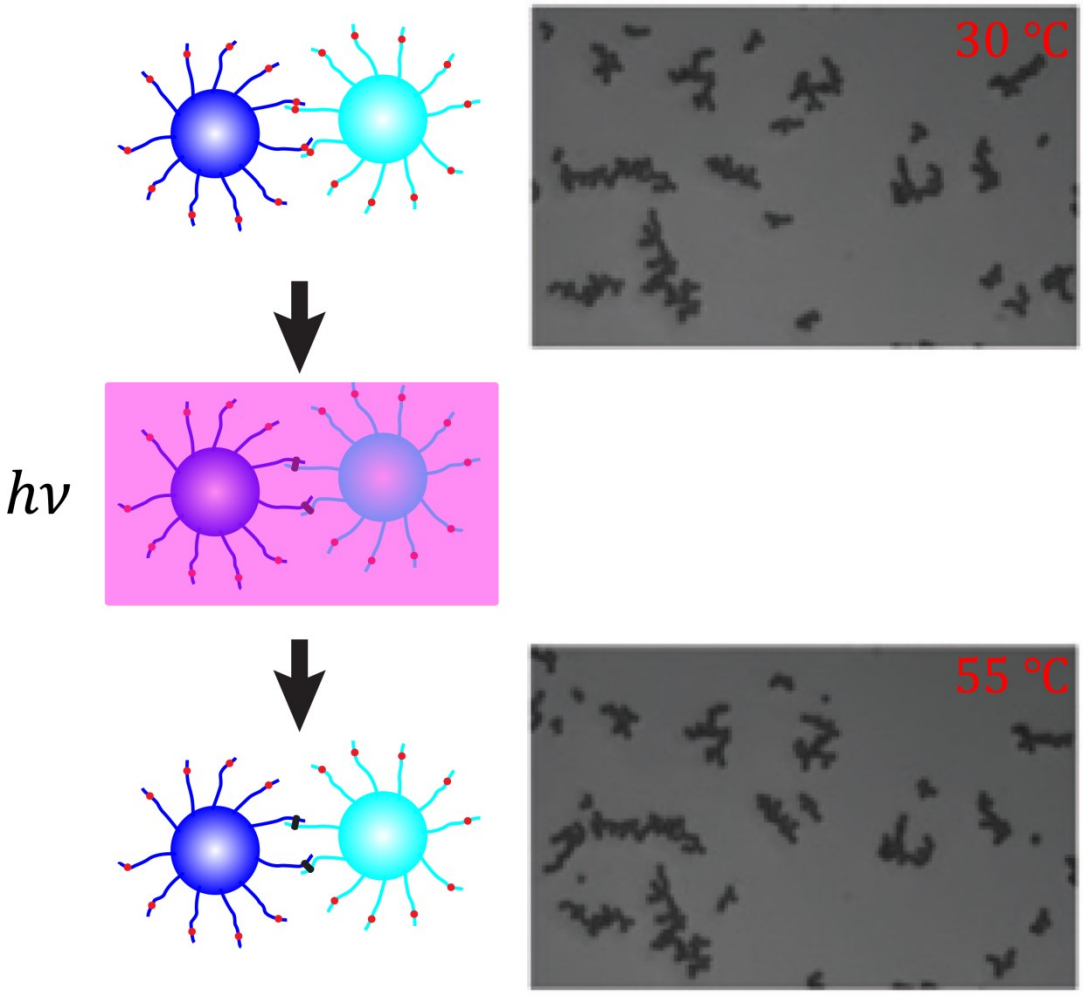

Figure 6-3: A demonstration of crosslinking particles. Particles coated with complementary sticky ends with crosslinkers are covalently bound at 30 ℃ once exposed to ultraviolet light and do not dissociate due to de-hybridization of DNA strands between particles at 55 ℃. The red dots represent cinnamate groups.

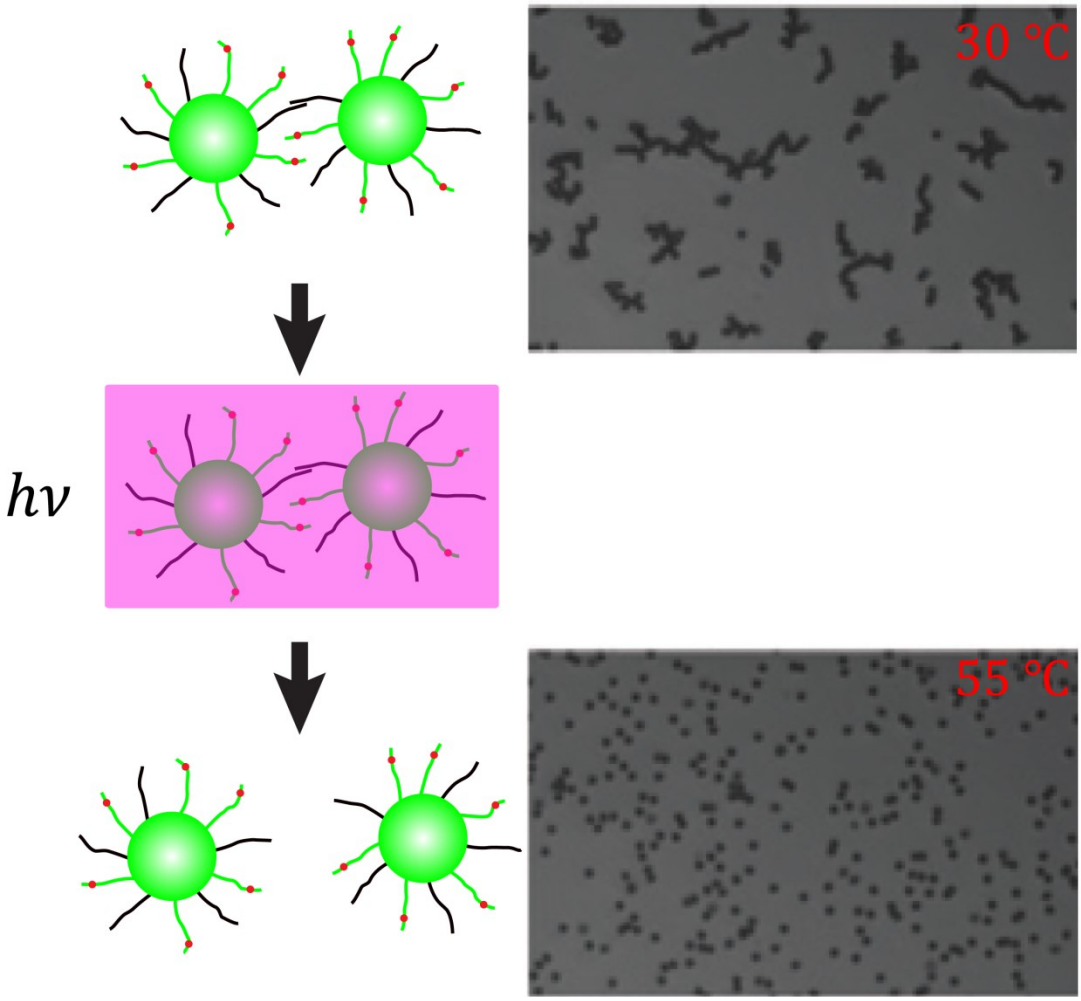

Figure 6-4: A demonstration of specific photo-crosslinking of cinnamate-modified DNA strands. Particles coated with cinnamate-modified non-complementary strands (green strands) and palindromic strands (black strands) are not crosslinked at 30 ℃ after exposure to

ultraviolet lights. At 55 ℃, particles dissociate due to de-hybridization of non-crosslinked DNA strands. The red dots are cinnamate groups.

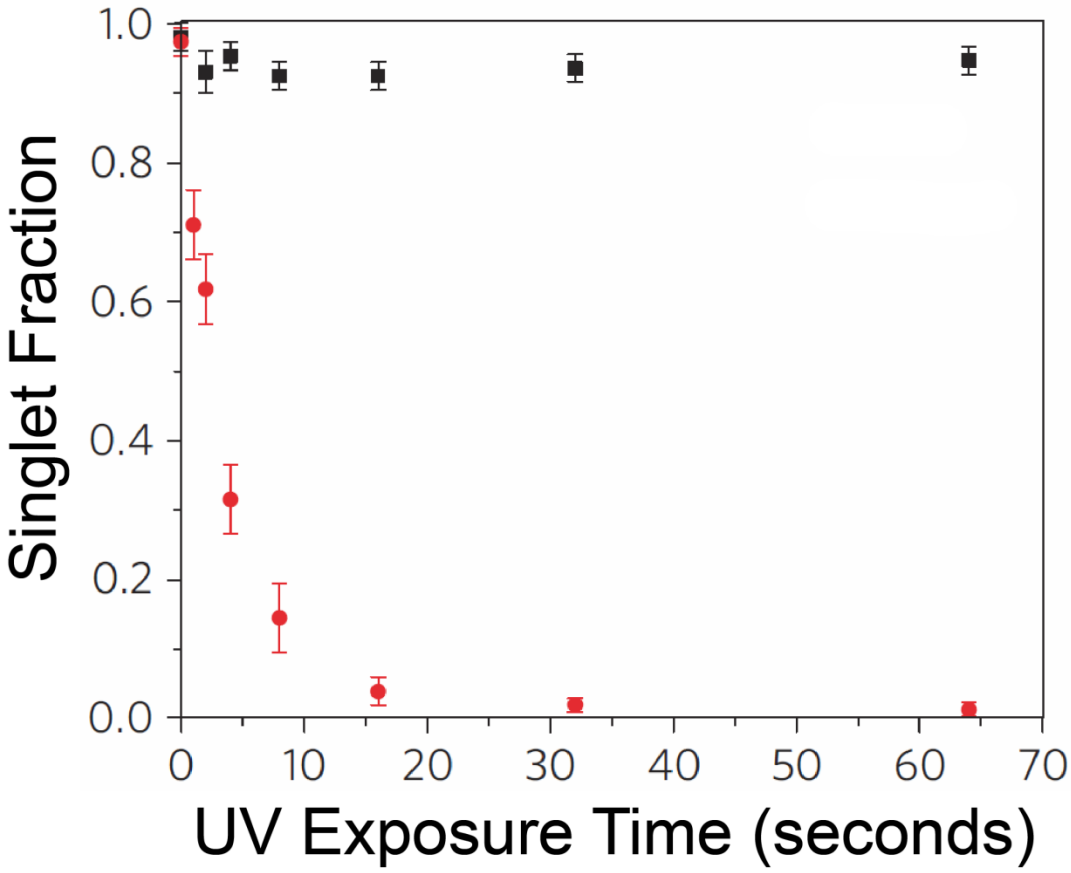

Figure 6-5: Singlet fraction vs. UV exposure time for particles in Figure 6-3 (red) and Figure 6-4 (black).

6.3. PHOTOLITHOGRAPHY

To show the use of specific photo-crosslinking of cinnamate-modified complementary strands, we developed DNA photolithography. In this section, we show how to use patterned ultraviolet light to functionalize a surface which can bind either to conjugated DNA-coated particles or fluorescent DNA strands. Furthermore, we demonstrate how we can make multi-functionalized surface, where fluorescent DNA and fluorescent streptavidin can bind to their conjugated areas respectively without mutual interference. From this section, we believe that we can utilize the high specific crosslinking of cinnamate-modified DNA strands to functionalize surface for various downstream applications, such as genetic detection [95] and DNA microarrays [96].

6.3.1. FUNCTIONALIZED SURFACE

To functionalize the surface, we coat a gold substrate with thiolated DNA strands containing cinnamate. We then attach linker strand half of which is complementary to the surface strand and also contains cinnamate and the

other half is then available for joining to other DNA strands. The protocol of making the functionalized surface with a specific pattern is the following:

1. Prepare a gold surface.
2. Grow cinnamate-modified DNA strands, which are the strands with dark blue and black in Figure 6-6 (a), on the gold surface. The red dots represent a cinnamate group.
3. As shown in Figure 6-6 (a), flow in the strands with light blue and light pink in solution. The sequences of light and dark blue sticky ends are complementary to each other.
4. As shown in Figure 6-6 (b), lower the temperature below the melting temperature of light and dark blue sticky ends. At this stage, the DNA strands in solution (the light pink-light blue strands) hybridize to those on the surface (the dark blue-black strands).
5. Apply $\sim 360\ \mathrm{nm}$ of ultraviolet light with a specific pattern to the surface for 15 seconds as shown in Figure 6-6 (c). At this stage, a pair of contacting cinnamate groups exposed to ultraviolet light crosslinks and forms covalent bonds.
6. Increase the temperature to de-hybridize non-crosslinked dark and light blue sticky ends in Figure 6-6 (c).

7. Wash out all the DNA strands in solution, and we get a surface functionalized at a specific area by the light pink sticky end as shown in Figure 6-6 (d).

As shown in Figure 6-6 (d), since the surface is functionalized by light pink sticky ends, the DNA strands complementary to them e.g., the dark pink sticky ends in Figure 6-7 (b) and Figure 6-7 (c), hybridize to the specific area, and its pattern is determined by ultraviolet light.

To prove that the above protocol works, we use the ultraviolet light with a signature “NYU” to pattern the surface. A micrograph of the patterned ultraviolet light is shown in Figure 6-7 (a) [94]. The DNA sequences of sticky ends of dark and light blue, and light pink used in Figure 6-6 are shown in Table 6-2. The experiment is done in the buffer with $10\ \mathrm{mM\ PBS}$, $50\ \mathrm{mM\ NaCl}$, $1\%\ \mathrm{w/w\ F127}$. The melting temperature of the sticky ends of dark and light blue with $0.1\ \mu\mathrm{M}$ strand concentration is measured to be $\sim 45\ ^{\circ}\mathrm{C}$ in the buffer. After following the above protocol to make the functionalized surface in Figure 6-6 (d), we synthesize $1\text{-}\mu\mathrm{m}$ polystyrene particles coated with dark pink sticky end as shown in Figure 6-7 (b). The se-

quence of the dark pink sticky end is shown in Table 6-2. Since the dark and light pink sticky ends are complementary to each other, the particles are adsorbed to the functionalized surface (the area with light pink sticky ends) and constitute a colloidal NYU pattern as shown in Figure 6-7 (b) [94]. Similarly, if we flow in the dark pink strands, they hybridize to functionalized surface (the area with light pink sticky ends) and constitute a fluorescent NYU pattern as shown in Figure 6-7 (c) [94]. The reason the dark pink strand can be identified by fluorescence is because we functionalize the dark pink strand by a biotin molecule and label the dark pink strand by fluorescent streptavidin with Alexa Fluor 488, the excitation and emission peaks of which are shown in Table 6-3.

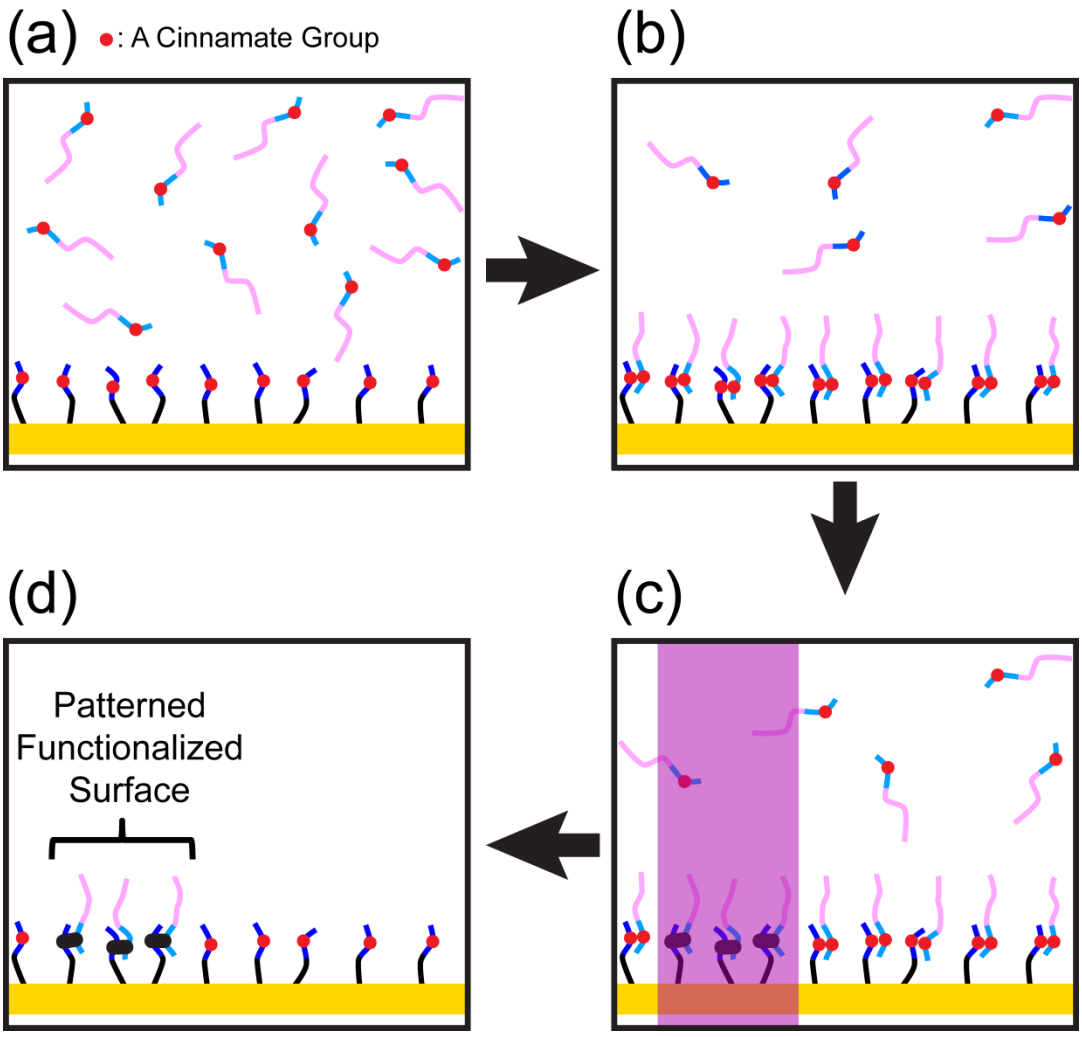

Figure 6-6: Schematic protocol for DNA photolithography with cinnamte-modified DNA strands. By following the protocol, only the area exposed to ultraviolet light is functionalized. (a) A gold surface is coated with thiolated cinnamate-modified strands (dark blue and

black). The solution is filled with linker strands (light pink and light blue). The light and dark blue are complementary. (b) The light and dark blue strands hybridize at the temperature below their melting temperature. (c) A pair of contacting cinnamate groups crosslinks and forms covalent bonds after exposed to a patterned ultraviolet light. (d) Increase temperature to de-hybridize non-crosslinked strands, and wash out all the strands in solution. The region exposed to the ultra-violet light is functionalized with pink sticky ends.

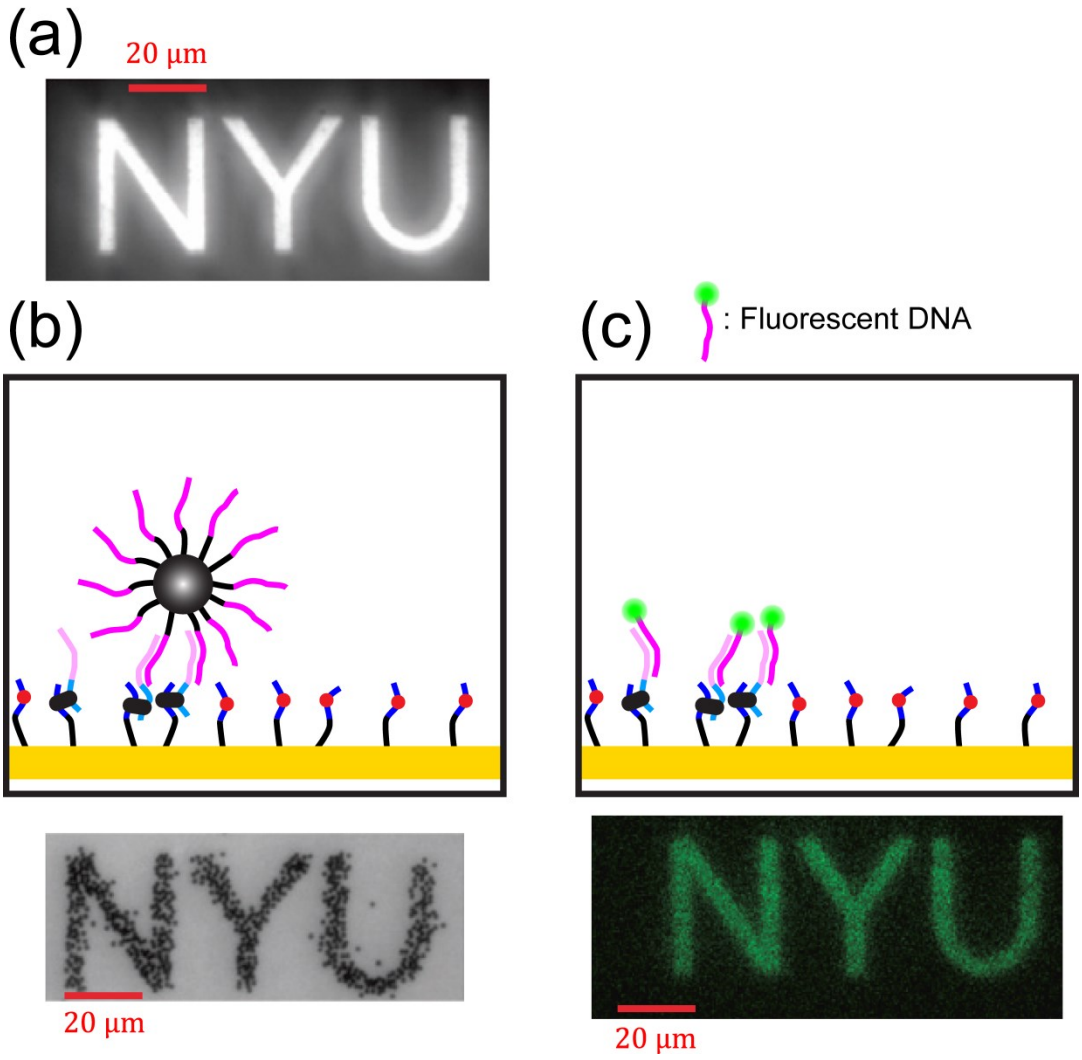

Figure 6-7: Experimental results of photolithography by following the protocol in Figure 6-6. (a) NYU pattern of ultraviolet light. (b) Colloidal particles adsorbed to functionalized surface. (c) Fluorescent DNA adsorbed to functionalized surface.

DNA	DNA Sequences
Dark Blue	5’ – TTG AGA AAT GC X CGT AAA GAG TT – 3’
Light Blue	5’ – AAC TCT TTA CG X GCA TTT CTC AA – 3’
Light Pink	5’ – CAT CTT CAT CC – 3’
Dark Pink	5’ – GGA TGA AGA TG – 3’

Table 6-2: DNA sequences used in Figure 6-6, Figure 6-7, Figure 6-8, and Figure 6-9. X represents a cinnamate group.

Fluorescent Streptavidin	Excitation Peak (nm)	Emission Peak (nm)
Stretavidin with Alexa Fluor 488	495	519
Streptavidin with Alexa Fluor 633	632	647

Table 6-3: Excitation and emission peaks of fluorescent streptavidin.

6.3.2. MULTI-FUNCTIONALIZED SURFACE

To demonstrate the versatility of our method, we made a spatially dependent multi-functionalized surface. We follow Steps 1–7 in Section 6.3.1 to functionalize a region of the surface as shown in Figure 6-6 (d) except that "materials" is chosen to be the pattern of ultraviolet light. Then, we follow the protocol in Section 6.3.1 again. However, the light blue-light pink strand is replaced by a light blue strand functionalized by a biotin molecule at the 5' end as shown in Figure 6-8 (a). Also, the ultraviolet light with a pattern "nature" is used to expose the different areas on the surface. By following our protocol in 6.3.1 twice, with two different linker strands, we can make the surface dual-functional as shown in Figure 6-8 (b). One region is functionalized by light pink sticky ends while the other is functionalized by biotin molecules. Then, as shown in Figure 6-9 (a) [94], to visualize the functionalized areas, we flow in both fluorescently labeled DNA strands (the dark pink strands fluorescently labeled by Alexa Fluor 488) and fluorescent streptavidin with Alexa Fluor 633. The excitation and emission peaks of Alexa Fluor 488 and Alexa Fluor 633 are shown in Table 6-3. In Figure 6-9 (b) [94], we note that the red streptavidin and the green fluorescent DNA constitute red

“nature” and green “materials” separately. From Figure 6-9 (b), we confirm that by following our protocol in Section 6.3.1, we can make the surface multi-functional and each functionalized area is independent of each other without mutual interference.

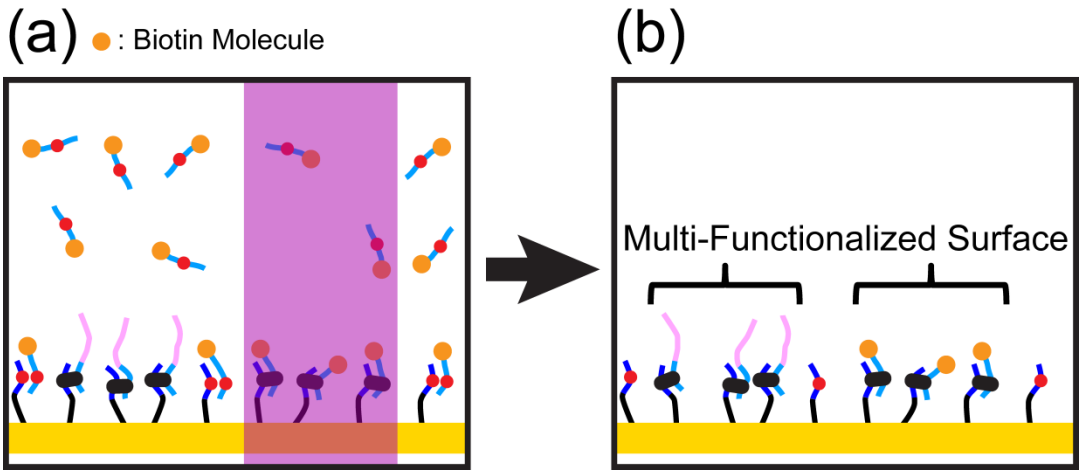

Figure 6-8: Schematic protocol of multi-functionalizing the surface. Step (a) is followed after Step (d) in Figure 6-6. (b) The surface is dual-functionalized after following the protocol in Figure 6-6 twice.

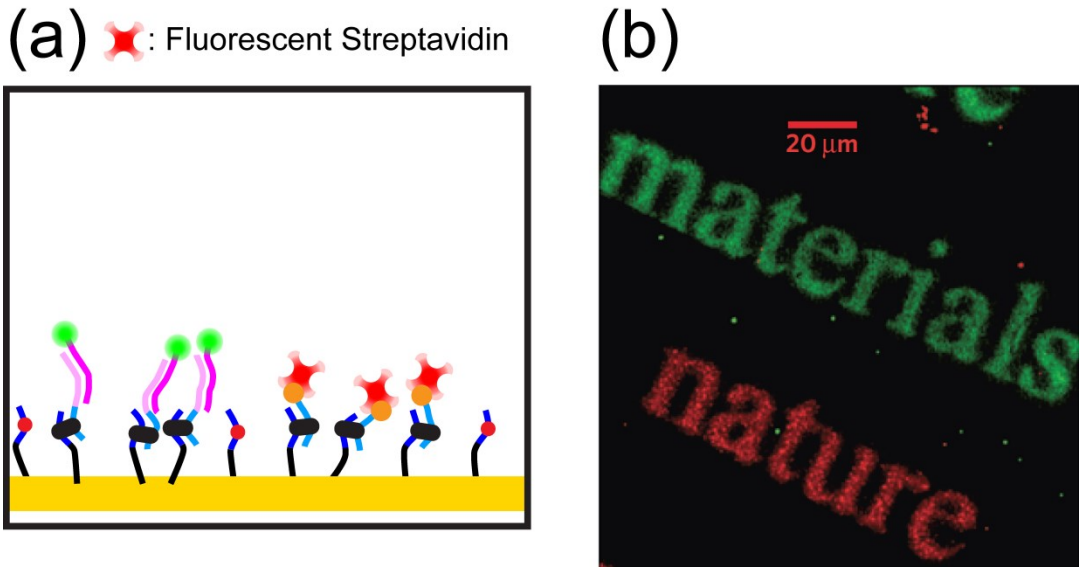

Figure 6-9: Dual-functionalized surface. (a) Fluorescent DNA is adsorbed to the DNA-functionalized surface (left). Fluorescent streptavidin is adsorbed to biotin-functionalized surface (right). (b) Fluorescent DNA is adsorbed to DNA-functionalized surface with the "materials" pattern. Fluorescent streptavidin is adsorbed to biotin-functionalized surface with the "nature" pattern.

6.4. CONCLUSIONS

In this chapter, we show that a pair of cinnamate groups adjacently placed in complementary DNA pairs provides an efficient, addressable, ultraviolet

light-based method to bond complementary DNA strands covalently. Since DNA hybridization is highly specific, by using cinnamate-modified DNA strands, we successfully photo-crosslinked particles with a high specificity. Further, we demonstrate the use of cinnamate-modified DNA strands for photolithography. By using patterned ultraviolet light to crosslink and functionalize surface with a specific pattern, the conjugated particles or DNA strands are adsorbed to the functionalized surface and constitute the original pattern of ultraviolet light. Furthermore, the surface can be made multifunctional. The conjugated DNA strands and streptavidin bind to the corresponding areas without mutual interference. Our photolithographic technique opens the door not only to printing different patches on micrometer-sized colloidal particles for various medical and soft-matter researches [97, 98] but also to making multi-functionalized DNA surfaces for genetic detection [95], DNA microarray [96], or DNA computing [99].

CHAPTER 7 CONCLUSIONS

In this dissertation, we have built the foundation for self-assembly and self-replication of colloidal particles. To realize self-replication of DNA-coated particles, we have to understand their thermodynamics and kinetics of self-assembly. Also, particles need to be bound reversibly or irreversibly, and the particle binding should be flexible enough to enable particles to self-assemble into the lowest energy state, which is the designed structure. In this dissertation, we make contributions to solving these problems, develop the needed techniques, and pave the path to colloidal self-replication. Such a technique, if implemented, helps us to understand the origin of life and more importantly natural evolution. For example, given the fact that seeds might not perfectly self-replicate in each cycle, mutation is unavoidable and competes with the original seeds [100]. As the mechanism of colloidal self-replication is easy to visualize through a conventional microscope, a new picture of evolution could be discovered. In addition to evolution, self-assembly of replicated building blocks into larger-scale functional structures can be done [12]. One can use light tweezers to build one building block and allow it to self-replicate and then self-assemble into a bigger designed

structure. Given the fact that the amount of seeds is doubled in each cycle of self-replication, the fabrication of microscopic building blocks can be produced exponentially rather than linearly. In large-scale production, self-replication provides a more efficient way to synthesize a large amount of nano-components in a relatively short period of time.

APPENDIX A DNA PURITY CHECK

Our DNA strands were bought from Integrated DNA Technologies (IDT), Coralville, IA. Before use, we wanted to be sure of their purity for quantitative measurements, and hence ran polyacrylamide gel electrophoresis (PAGE) check (details in APPENDIX D). The experimental protocol followed in the case of our 61-mer ssDNA is listed here.

1. Wash 2 gel glass plates, 3 spacers, and 1 cone.
2. Use acetone to clean the glass plates again.
3. Put two spacers at two ends of a glass plate.
4. Flip the other glass plate and put it on top of the first one, and the glass plates are separated by two spacers.
5. Clamp the two glass plates on both sides ensuring that they are aligned to prevent buffer-leakage.
6. Use vacuum grease to seal any possible buffer leak.
7. Put the glass plates at stand and use two screws to tie the glass plates to the gel glass stand.
8. Preparing 15% denaturing solution:

a. Mix 5 mL 0% Denaturing Solution, 15 mL 20% Denaturing Solution, and 200 μL 10% APS.
b. Stir the solution.
c. Add 20 μL Tetramethylethylenediamine 99%, and stir the solution. Note: Complete Step 9 as soon as possible as otherwise the solution will be polarized.

9. Add the denaturing solution into the gap between the glass plates.
10. If any bubbles form between glass plates, shake the plates to remove them.
11. Insert the cone on top of the gap to make channels. Note: 1-cm depth is enough.
12. Remove the cone when the denaturing solution is completely polarized and becomes a gel. Carefully swing the glass plates to remove any possible non-polarized denaturing solution between the plates.
13. Mix 25 μL DNA solution and 75 μL Denaturing Dye (90% Formamide, 10 mM Sodium Hydroxide Xylene Cyanole FF, Harmful) in a tube.
14. Make 500 mL of 1X TBE buffer. Note: 500 mL of 1X TBE buffer is made by mixing 50 mL of 10X TBE with 450 mL of double-distilled water.

15. Fill the channels by $1X$ TBE buffer.
16. Add 10 μL of denaturing-dyed DNA solution to each channel.
17. Load a buffer container on top of the gel glass plates.
18. Pour 500 mL of $1X$ TBE buffer into the buffer container.
19. Put the gel glass plates along with the buffer container into a gel box.
20. Apply 600-volt D.C. between the top and the bottom of the gel.
21. Wait until the blue dyes goes down to $\sim 50\%$. Note: The actual position of the DNA is below the blue line.
22. Turn off D.C. power.
23. Remove the buffer in the buffer container.
24. Unload the buffer container.
25. Take out the gel.
26. Put the gel into the solution of Stains All until the main bands in the gel can be seen clearly. Note: While the gel immerges in the solution of Stains All, the whole solution needs to be covered under the foil to avoid any exposure to light.
27. Take the gel into the tray containing pure water.
28. Expose the gel under the strong white light until the extra Stains All in the gel disappears and only DNA bands remain.

29. Check if there are any sub-bands besides the main band.

An example of our DNA purity check is shown in Figure A-1. The DNA sequences used are shown in Table A-1. The length of RCS, RCN, RDN, and RT are 49, 61, 61, and 61, respectively. Therefore, the main band of RCN, RDN, RDN, and RT are at the similar $\mathrm{y\text{-}axis}$. The y position of the main band of RCS is larger than RCN, RDN, and RT. Also, below each main band, we can clearly see several sub-bands for RCS, RCN, RDN, and RT. From Figure A-1, we claim that the DNA purity of IDT is $\sim 50\%$. Therefore, if we want to quantitatively control the use of DNA strands. We have to purify our DNA strands.

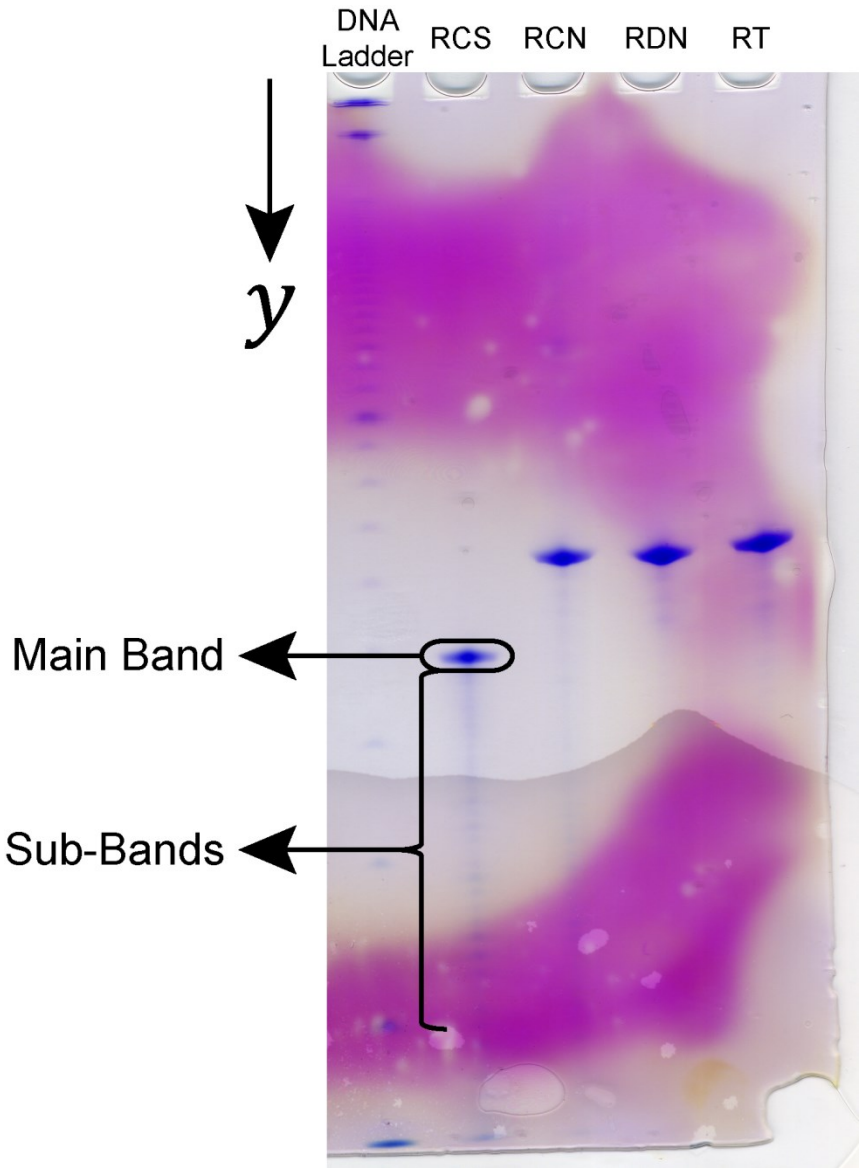

Figure A-1: An Image of 15% denaturing gel. DNA strands from IDT are run through a denaturing gel and shows a main band and several sub-bands. The result proves that the purity of DNA strands is low.

DNA Symbols	Sequences
RCS	5’ – TAG CGA TGG GAA GCG TGT CAG TTA GGT CTC TCG GGA CGG AAA GTA ATG C – 3'
RCN	5’ – GGA TGA AGA TGA ATC GCT ACC CTT CGC ACA GTC AAT CCA GAG AGC CCT GCC TTT CAT TAC G – PEG – BIOTIN – 3’
RDN	5’ – CAT CTT CAT CCA ATC GCT ACC CTT CGC ACA GTC AAT CCA GAG AGC CCT GCC TTT CAT TAC G – PEG – BIOTIN – 3’
RT	5’ – TTT TTT TTT TTA ATC GCT ACC CTT CGC ACA GTC AAT CCA GAG AGC CCT GCC TTT CAT TAC G – PEG – BIOTIN – 3’

Table A-1: DNA sequences used in Figure A-1 and Figure B-1.

APPENDIX B DNA PURIFICATION

APPENDIX A shows that the DNA purity from IDT is low. To quantitatively control the use of DNA strands, we have to purify DNA strands ourselves. We use PAGE to purify our DNA strands. Our protocol of purifying DNA strands is the following.

1. Do Step 1 to Step 25 in APPENDIX A to get the gel containing DNA strands.
2. Put the gel in $600\ \mu\mathrm{L}$ of Ethidium Bromide (EB).
3. Shine UV from the bottom of the gel in the cold room, $\sim 4\ ^{\circ}\mathrm{C}$.
4. Cut out the shining main bands in the gel.
5. Put the bands into a tube.
6. Take $600\ \mu\mathrm{L}$ of elution buffer ($500\ \mathrm{mM}$ Ammonium Acetate, $10\ \mathrm{mM}$ Magnesium Acetate, and $2\ \mathrm{mM}$ EDTA, TOXIC) into the tube.
7. Vortex the tube.
8. Put the tube on the shaker in the cold room overnight.
9. Pipette out the solution containing DNA strands in the tube into another tube.

10. Use n-Butanol to decrease the volume of DNA solution to $1/3$ of the original volume.
    a. Add $1\ \mathrm{mL}$ n-Butanol into the tube.
    b. Vortex the tube.
    c. Centrifuge the tube.
    d. Take out the supernatant in the tube.
    e. Repeat Step a-d until the volume decreases less than $1/3$ of the original volume.
11. Add $1\ \mathrm{mL}$ of 100% ethanol into the tube.
12. Vortex the tube.
13. Put the tube in the dry ice for 45 minutes.
14. Centrifuge the tube at the maximum speed of the centrifugal machine for $30\ \mathrm{minutes}$.
15. Dump the solution. Note: At this step, DNA strands form a sediment at the bottom of the tube, so dumping the solution will not result in any loss of DNA.
16. Add $1\ \mathrm{mL}$ of 70% Ethanol, and DO NOT VORTEX the tube.
17. Centrifuge the tube for 7 minutes.
18. Dump the solution again.

19. Dry the tube.

An example of purifying DNA strands by our protocol along with the comparison with the DNA strands without purification is shown in Figure B-1. The sequences of RCN, RDN, and RT are shown in Table A-1. From Figure B-1, we find out that RCN, RDN, and RT all have sub-bands before DNA purification. After we purify them, the sub-bands of each DNA strands disappear. From Figure B-1, we learn that our purification protocol can greatly increase the purity of DNA strand, and we purify all of our DNA strands before using them to coat our particles.

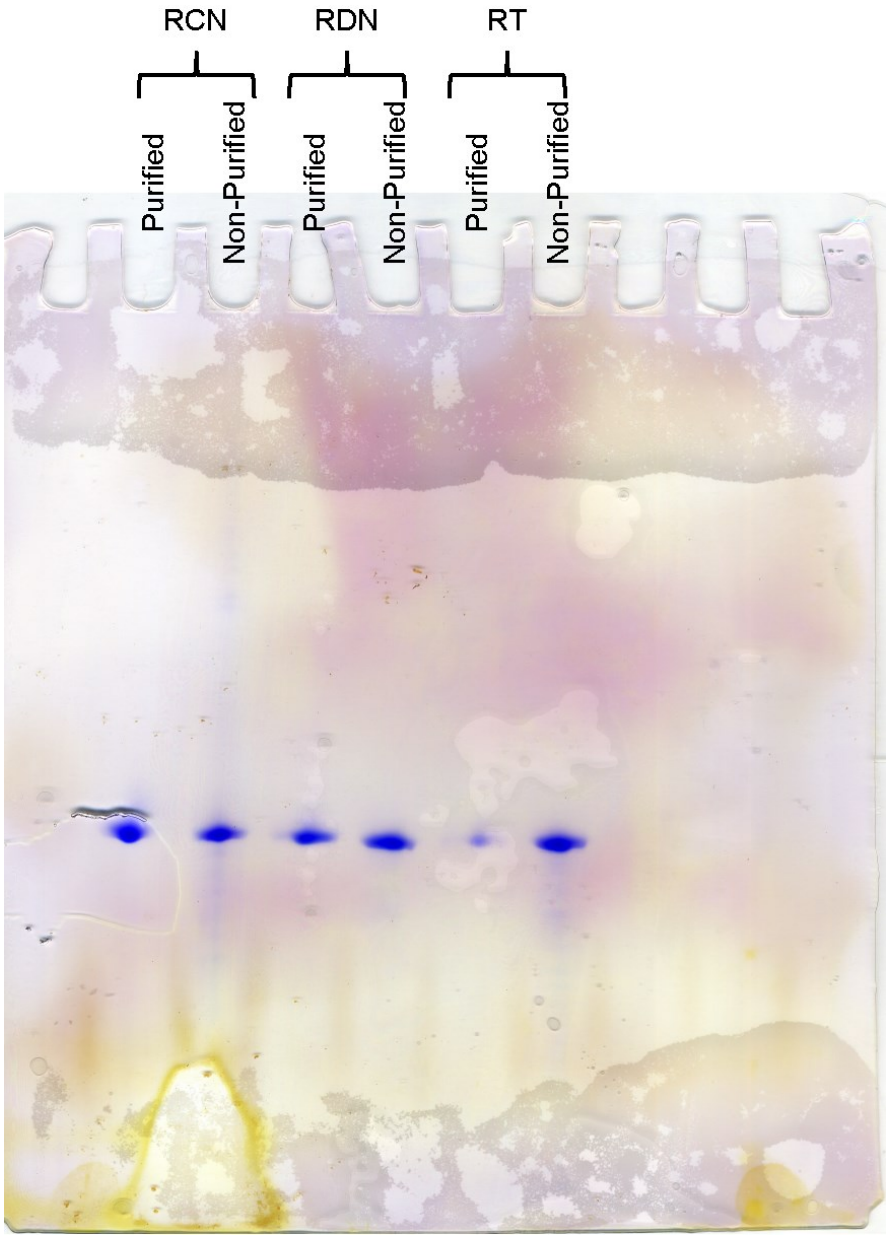

Figure B-1: Comparisons between Purified and Non-Purified DNA Strands.

APPENDIX C LABELING DNA

To measure the number of DNA strands per particle, we need to radioactively label the strands. By measuring the strength of radioactive signals, we can determine the number of DNA strands on our particles. We use radioactive isotope of phosphorus 32, which decays into sulfur 32 and emits an electron. Note that since radioactive materials might cause potential harm to human bodies, all the processes relating to radioactive materials should be done behind a shield. Anything that might be contaminated by the radioactive material, such as pipette tips, tubes, and butanol waste, should be dumped into the shielded trash can. Our protocol of synthesizing phosphorus 32-labeled DNA strands is the following.

1. Make $1\ \mu M$ of DNA strands that are needed to be labeled.
2. Put $2\ \mu L$ of $1\ \mu M$ DNA, $1\ \mu L$ of $10X$ T4 PNK Reaction Buffer, and $4\ \mu L$ of double-distilled water together into a tube.
3. Vortex the tube.
4. Add $1\ \mu L$ of $1X$ T4 PNK into the tube. The preparation of $1X$ T4 PNK is as follows:

a. Use a STYLIZED tip to take $1\ \mu L$ of $10X$ T4 PNK.

b. Mix $1\ \mu L$ of $10X$ T4 PNK and $9\ \mu L$ of double-distilled water.

c. Stir the tube with tips. Do NOT vortex.

5. Stir the tube by a pipette tip. Do NOT vortex.
6. Check if the tube radiates using the radiation counter. Note: At this step, no radiation should be found.
7. Add $2\ \mu L$ of ATP into the tube. Note: The concentration of ATP is $\sim 2.2\ \mu M$.
8. Write down the record of using ATP: Time, Balance, Sued, Activity, and Type.
9. Stir the tube by a pipette tip. Do NOT vortex.
10. Incubate the tube at $37\ ^{\circ}C$ overnight. This process is to grow phosphorus 32 to 5' end of DNA strands.
11. Filter the extra ATP that is not attached to DNA strands in the tube by G25 column.

    a. Take a G25.

    b. Break the blocker at the bottom.

    c. Vortex the G25, which filters smaller molecules.

    d. Slightly open the lid of the G25, and spin it for $1\ \text{minute}$.

e. Put the tube in Step 10, called DNA-ATP tube, as described below, at 90 ℃ for 15 minutes to prevent growth of phosphorus 32 on DNA.

f. Centrifuge the DNA-ATP tube.

g. Add 50 μL of double-distilled water into the DNA-ATP tube.

h. Vortex the DNA-ATP tube.

i. Mount the G25 onto another clean tube.

j. Open the lid of G25, and put all the solution in DNA-ATP tube into it.

k. Slightly close the lid of G25, and do not seal it. The aim is to allow the air to be able to flow into/out of G25.

l. Spin the tube for 1 minute.

m. Take out G25, and check with radiation counter if it has any radiation. Note: At this step, G25 should contain some ATP; G25 is radioactive.

n. Check with radiation counter if the tube has radiation. Note: If the solution has radiation, that probably means that phosphorus 32 is attached to DNA at the 5'-end.

12. Do Step 1 to Step 24 in APPENDIX A to run the radioactive DNA strands through a denaturing gel. However, since the gel is radioactive, follow the following steps to locate DNA strands in the gel instead of using EB.
13. Get rid of the upper glass plate.
14. Wrap the bottom glass plate and the gel together with a transparent plastic wrap.
15. Turn the glass plate and the gel upside down. Note: The gel part should face down to block radiation.
16. Bring glass plate and gel to the cold room.
17. Turn off light in the cold room.
18. Take a film and put it on a paper tower.
19. Keep the glass plate on the film. Note that the gel side should directly face the film, so radiation from the gel can be detected by the film.
20. Use a pencil to mark the position of the glass plate on the film since we will use radiation-exposed film to locate the position of radioactive DNA strands in the gel.
21. Expose the film to radioactive gel for $3\ \text{minutes}$. Note: The exposure time depends on the strength of radiation.

22. Keep the film in the developer solution until the bands, which should be black, are shown on the film. Note: Usually, this step would take 1 minute.
23. Wash the film with water.
24. Wash the film with the fixer solution for a few seconds.
25. Wash the film with water again.
26. Turn on the light in the cold room.
27. Use paper tower to dry the film.
28. Remove the plastic wrap.
29. Flip the glass plate, so now the gel side faces up.
30. Use the mark marked in Step 20 to align the glass plate and the film. Then, locate the position of the radioactive DNA in the gel with the black band of the film.
31. Cut gel piece containing the radioactive DNA.
32. Take gel containing the radioactive DNA into a tube.
33. Check with the radiation counter if the tube has any radiation. Note: This step is to make sure that the radioactive DNA strands are correctly cut from the gel in Step 31.

34. Do Step 6-19 in APPENDIX B to have the dried radioactive DNA strands in the tube.

After following the above protocol, we can successfully label our DNA strands with radioactive phosphorus 32. Then, by measuring the radioactive strength of particles coated with these radioactive DNA strands, we can determine how many DNA strands are coated on one particle [see Section 2.2].

APPENDIX D POLYACRYLAMIDE GEL ELECTRO-PHORESIS

To check DNA purity [see APPENDIX A] or purify DNA strands [see APPENDIX B], using polyacrylamide gel electrophoresis is unavoidable (Figure D-1). Normally, the mesh size of polyacrylamide gel we used in our experiment is $\sim 11\ \mathrm{nm}$. Since the phosphate group of DNA carries negative charges, if we apply electrical potential across the gel as shown in Figure D-1, DNA strands will be driven to move from top to bottom. Additionally, the strand with a large molecular weight or equivalently a longer strand migrates slower than the one with smaller molecular weight or equivalently a shorter strand. As a result, if a DNA sample contains the DNA strands with various lengths, the spacial distribution of DNA strands after running the electrophoresis will be spread out like the right channel of Figure D-1 compared to the ones in the left and middle channels of Figure D-1, the molecular distributions of which are both sharp. Therefore, by using polyacrylamide gel electrophoresis, we can not only know the size of DNA molecules but also detect the purity or mass distribution of DNA samples.

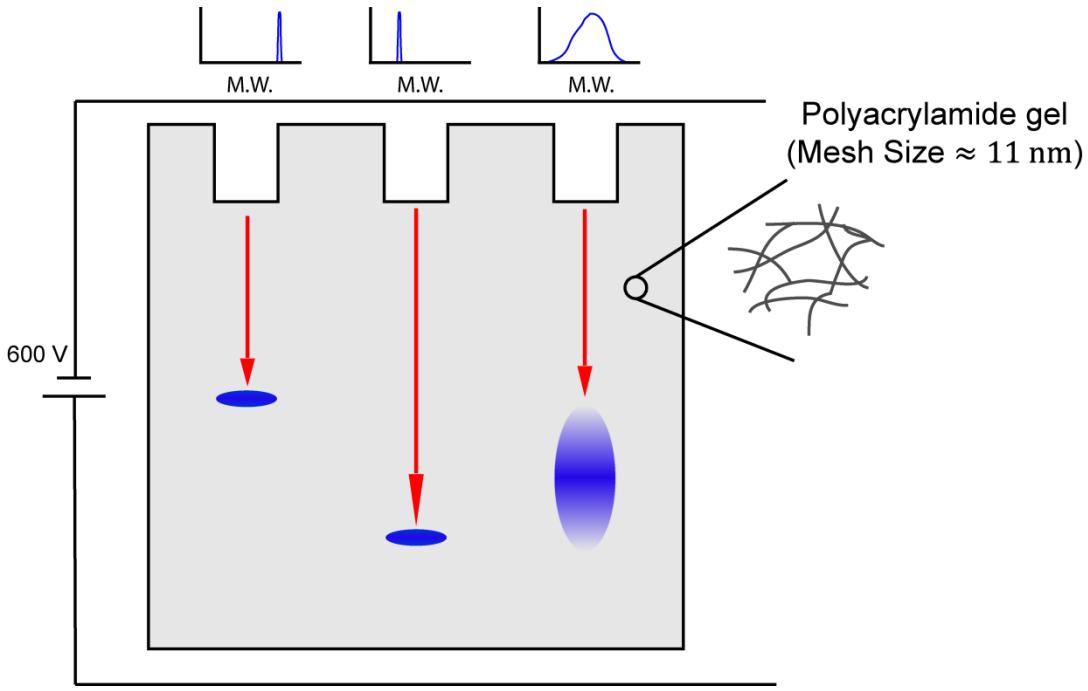

Figure D-1: Schematic diagram of polyacrylamide gel electrophoresis.

BIBLIOGRAPHY

1. Schulze-Makuch, D., et al., *Venus, Mars, and the ices on Mercury and the Moon: Astrobiological implications and proposed mission designs.* Astrobiology, 2005. **5**(6): p. 778-795.

2. Schulze-Makuch, D. and L.N. Irwin, *Alternative energy sources could support life on Europa.* Eos, Transactions American Geophysical Union, 2001. **82**(13): p. 150-150.

3. Sobron, P., A. Wang, and F. Sobron, *Extraction of compositional and hydration information of sulfates from laser-induced plasma spectra recorded under Mars atmospheric conditions — Implications for ChemCam investigations on Curiosity rover.* Spectrochimica Acta Part B: Atomic Spectroscopy, 2012. **68**(0): p. 1-16.

4. Wacey, D., et al., *Microfossils of sulphur-metabolizing cells in 3.4-billion-year-old rocks of Western Australia.* Nature Geosci, 2011. **4**(10): p. 698-702.

5. Hawking, S., *A brief history of time : from the big bang to black holes*. 1988, Toronto ; New York: Bantam Books. x, 198 p.

6. Zalta, E.N. and Center for the Study of Language and Information (U.S.). Metaphysics Research Lab., *Stanford encyclopedia of philosophy*, Metaphysics Research Lab, Center for the Study of Language and Information, Stanford University: Stanford, Calif.

7. MAUTNER, M.N., *DIRECTED PANSPERMIA. 3. STRATEGIES AND MOTIVATION FOR SEEDING STAR-FORMING CLOUDS.* Journal of The British Interplanetary Society, 1997. **50**: p. 93-102.

8. Nealson, K.H. and P.G. Conrad, *Life: past, present and future.* Philosophical Transactions of the Royal Society of London. Series B: Biological Sciences, 1999. **354**(1392): p. 1923-1939.

9. McKay, C.P., *What is life - and how do we search for it in other worlds?* Plos Biology, 2004. **2**(9): p. 1260-1263.

10. Mautner, M.N., *LIFE-CENTERED ETHICS, AND THE HUMAN FUTURE IN SPACE.* Bioethics, 2009. **23**(8): p. 433-440.

11. Palacci, J., et al., *Living Crystals of Light-Activated Colloidal Surfers.* Science, 2013. **339**(6122): p. 936-940.

12. Leunissen, M.E., et al., *Towards self-replicating materials of DNA-functionalized colloids.* Soft Matter, 2009. **5**(12): p. 2422-2430.

13. Russel, W.B., D.A. Saville, and W.R. Schowalter, *Colloidal dispersions*. Cambridge monographs on mechanics and applied mathematics. 1989, Cambridge ; New York: Cambridge University Press. xvii, 525 p., 1 leaf of plates.

14. Watson, J.D. and F.H.C. Crick, *Molecular Structure of Nucleic Acids - a Structure for Deoxyribose Nucleic Acid.* Nature, 1953. **171**(4356): p. 737-738.

15. Bates, A.D. and A. Maxwell, *DNA topology*. 2nd ed. 2005, Oxford ; New York: Oxford University Press. xviii, 198 p.

16. Hagerman, P.J., *Flexibility of DNA.* Annual Review of Biophysics and Biophysical Chemistry, 1988. **17**: p. 265-286.

17. SantaLucia, J., *A unified view of polymer, dumbbell, and oligonucleotide DNA nearest-neighbor thermodynamics.* Proceedings of the National Academy of Sciences of the United States of America, 1998. **95**(4): p. 1460-1465.

18. Mergny, J.L. and L. Lacroix, *Analysis of thermal melting curves.* Oligonucleotides, 2003. **13**(6): p. 515-537.

19. Rothemund, P.W.K., *Folding DNA to create nanoscale shapes and patterns.* Nature, 2006. **440**(7082): p. 297-302.

20. Chaikin, P.M. and T.C. Lubensky, *Principles of condensed matter physics*. 1995, Cambridge ; New York, NY, USA: Cambridge University Press. xx, 699 p.

21. Dreyfus, R., et al., *Aggregation-disaggregation transition of DNA-coated colloids: Experiments and theory.* Physical Review E, 2010. **81**(4).

22. Dreyfus, R., et al., *Simple Quantitative Model for the Reversible Association of DNA Coated Colloids.* Physical Review Letters, 2009. **102**(4): p. 048301.

23. Feng, L., et al., *DNA Patchy Particles.* Advanced Materials, 2013. **25**(20): p. 2779-2783.

24. Feng, L., et al., *Topological Interaction by Entangled DNA Loops.* Physical Review Letters, 2012. **109**(18): p. 188301.

25. Leunissen, M.E., et al., *Switchable self-protected attractions in DNA-functionalized colloids.* Nature Materials, 2009. **8**(7): p. 590-595.

26. Valignat, M.P., et al., *Reversible self-assembly and directed assembly of DNA-linked micrometer-sized colloids.* Proceedings of

the National Academy of Sciences of the United States of America, 2005. **102**(12): p. 4225-4229.

27. Wu, K.-T., et al., *Polygamous particles.* Proceedings of the National Academy of Sciences, 2012. **109**(46): p. 18731-18736.

28. Wu, K.-T., et al., *Kinetics of DNA-coated sticky particles.* Physical Review E, 2013. **88**(2): p. 022304.

29. Xu, Q., et al., *Subdiffusion of a Sticky Particle on a Surface.* Physical Review Letters, 2011. **106**(22): p. 228102.

30. Alivisatos, A.P., et al., *Organization of 'nanocrystal molecules' using DNA.* Nature, 1996. **382**(6592): p. 609-611.

31. Maye, M.M., et al., *Stepwise surface encoding for high-throughput assembly of nanoclusters.* Nat Mater, 2009. **8**(5): p. 388-391.

32. Maye, M.M., et al., *DNA-Regulated micro- and nanoparticle assembly.* Small, 2007. **3**(10): p. 1678-1682.

33. Nykypanchuk, D., et al., *DNA-guided crystallization of colloidal nanoparticles.* Nature, 2008. **451**(7178): p. 549-552.

34. Biancaniello, P.L., A.J. Kim, and J.C. Crocker, *Colloidal Interactions and Self-Assembly Using DNA Hybridization.* Physical Review Letters, 2005. **94**(5): p. 058302.

35. Crocker, J.C., *Nanomaterials: Golden handshake.* Nature, 2008. **451**(7178): p. 528-529.

36. Milam, V.T., et al., *DNA-driven assembly of bidisperse, micron-sized colloids.* Langmuir, 2003. **19**(24): p. 10317-10323.

37. Rogers, W.B. and J.C. Crocker, *Direct measurements of DNA-mediated colloidal interactions and their quantitative modeling.* Proceedings of the National Academy of Sciences of the United States of America, 2011. **108**(38): p. 15687-15692.

38. Jones, M.R., et al., *DNA-nanoparticle superlattices formed from anisotropic building blocks.* Nat Mater, 2010. **9**(11): p. 913-917.

39. Wang, Y., et al., *Colloids with valence and specific directional bonding.* Nature, 2012. **491**(7422): p. 51-55.

40. Arkus, N., V.N. Manoharan, and M.P. Brenner, *Minimal Energy Clusters of Hard Spheres with Short Range Attractions.* Physical Review Letters, 2009. **103**(11).

41. Arkus, N., V.N. Manoharan, and M.P. Brenner, *Deriving Finite Sphere Packings.* Siam Journal on Discrete Mathematics, 2011. **25**(4): p. 1860-1901.

42. Halverson, J.D. and A.V. Tkachenko, *DNA-programmed mesoscopic architecture.* Physical Review E, 2013. **87**(6): p. 062310.

43. Seeman, N.C., *DNA in a material world.* Nature, 2003. **421**(6921): p. 427-431.

44. Aldaye, F.A., A.L. Palmer, and H.F. Sleiman, *Assembling materials with DNA as the guide.* Science, 2008. **321**(5897): p. 1795-1799.

45. Yan, H., et al., *A robust DNA mechanical device controlled by hybridization topology.* Nature, 2002. **415**(6867): p. 62-65.

46. Winfree, E., et al., *Design and self-assembly of two-dimensional DNA crystals.* Nature, 1998. **394**(6693): p. 539-544.

47. Yurke, B., et al., *A DNA-fuelled molecular machine made of DNA.* Nature, 2000. **406**(6796): p. 605-608.

48. Seeman, N.C., *Nucleic-Acid Junctions and Lattices.* Journal of Theoretical Biology, 1982. **99**(2): p. 237-247.

49. Nilsen, T.W., J. Grayzel, and W. Prensky, *Dendritic nucleic acid structures.* Journal of Theoretical Biology, 1997. **187**(2): p. 273-284.

50. Wang, T., et al., *Self-replication of information-bearing nanoscale patterns.* Nature, 2011. **478**(7368): p. 225-228.

51. Tkachenko, A.V., *Morphological diversity of DNA-colloidal self-assembly.* Physical Review Letters, 2002. **89**(14).

52. Mirkin, C.A., et al., *A DNA-based method for rationally assembling nanoparticles into macroscopic materials.* Nature, 1996. **382**(6592): p. 607-609.

53. Park, S.Y., et al., *DNA-programmable nanoparticle crystallization.* Nature, 2008. **451**(7178): p. 553-556.

54. Mognetti, B.M., M.E. Leunissen, and D. Frenkel, *Controlling the temperature sensitivity of DNA-mediated colloidal interactions through competing linkages.* Soft Matter, 2012. **8**(7): p. 2213-2221.

55. Mognetti, B.M., et al., *Predicting DNA-mediated colloidal pair interactions.* Proceedings of the National Academy of Sciences of the United States of America, 2012. **109**(7): p. E378-E379.

56. Gonzalez, M., et al., *Interaction of biotin with streptavidin - Thermostability and conformational changes upon binding.* Journal of Biological Chemistry, 1997. **272**(17): p. 11288-11294.

57. Wylie, R.G., et al., *Spatially controlled simultaneous patterning of multiple growth factors in three-dimensional hydrogels.* Nature Materials, 2011. **10**(10): p. 799-806.

58. Bennett, S., *Nicholas Minorsky and the automatic steering of ships.* Control Systems Magazine, IEEE, 1984. **4**(4): p. 10-15.

59. Bennett, S., *Development of the PID controller.* Control Systems, IEEE, 1993. **13**(6): p. 58-62.

60. Tang, K.S., K.F. Man, and G. Chen. *Solar plant control using genetic fuzzy PID controller*. in *Industrial Electronics Society, 2000. IECON 2000. 26th Annual Confjerence of the IEEE*. 2000.

61. Reif, F., *Fundamentals of statistical and thermal physics*. McGraw-Hill series in fundamentals of physics. 1965, New York,: McGraw-Hill. x, 651 p.

62. Markham, N.R. and M. Zuker, *DINAMelt web server for nucleic acid melting prediction.* Nucleic Acids Research, 2005. **33**(suppl 2): p. W577-W581.

63. Markham, N.R. and M. Zuker, *UNAFold*. 2008. p. 3-31.

64. Dimitrov, R.A. and M. Zuker, *Prediction of Hybridization and Melting for Double-Stranded Nucleic Acids.* Biophysical journal, 2004. **87**(1): p. 215-226.

65. Walter, A.E., et al., *Coaxial stacking of helixes enhances binding of oligoribonucleotides and improves predictions of RNA folding.* Proceedings of the National Academy of Sciences, 1994. **91**(20): p. 9218-9222.

66. Mathews, D.H., et al., *Expanded sequence dependence of thermodynamic parameters improves prediction of RNA secondary structure.* Journal of Molecular Biology, 1999. **288**(5): p. 911-940.

67. Press, W.H., *Numerical recipes : the art of scientific computing*. 3rd ed. 2007, Cambridge, UK ; New York: Cambridge University Press. xxi, 1235 p.

68. Von Smoluchowski, M., *Versuch einer mathematischen Theorie der Koagulationskinetik kolloidaler Lösungen.* Zeitschrift für physikalische Chemie, 1917. **92**(2): p. 129-168.

69. Ball, R.C., et al., *Universal kinetics in reaction-limited aggregation.* Physical Review Letters, 1987. **58**(3): p. 274-277.

70. Weitz, D.A., et al., *Limits of the Fractal Dimension for Irreversible Kinetic Aggregation of Gold Colloids.* Physical Review Letters, 1985. **54**(13): p. 1416-1419.

71. Lee, N.-K., et al., *Ligand−Receptor Interactions in Chains of Colloids: When Reactions Are Limited by Rotational Diffusion†.* Langmuir, 2007. **24**(4): p. 1296-1307.

72. Craig, M.E., D.M. Crothers, and P. Doty, *Relaxation Kinetics of Dimer Formation by Self Complementary Oligonucleotides.* Journal of Molecular Biology, 1971. **62**(2): p. 383-&.

73. Peterson, A.W., L.K. Wolf, and R.M. Georgiadis, *Hybridization of Mismatched or Partially Matched DNA at Surfaces.* Journal of the American Chemical Society, 2002. **124**(49): p. 14601-14607.

74. Deng, P.G., Y.K. Lee, and P. Cheng, *Two-dimensional micro-bubble actuator array to enhance the efficiency of molecular beacon based DNA micro-biosensors.* Biosensors & Bioelectronics, 2006. **21**(8): p. 1443-1450.

75. Bloomfield, V.A., D.M. Crothers, and I. Tinoco, *Nucleic acids : structures, properties, and functions*. 2000, Sausalito, Calif.: University Science Books. x, 794 p.

76. Zhou, H.X., *Brownian dynamics study of the influences of electrostatic interaction and diffusion on protein-protein association kinetics.* Biophysical Journal, 1993. **64**(6): p. 1711-1726.

77. Okahata, Y., et al., *Kinetic Measurements of DNA Hybridization on an Oligonucleotide-Immobilized 27-MHz Quartz Crystal Microbalance.* Analytical Chemistry, 1998. **70**(7): p. 1288-1296.

78. Nkodo, A.E., et al., *Diffusion coefficient of DNA molecules during free solution electrophoresis.* ELECTROPHORESIS, 2001. **22**(12): p. 2424-2432.

79. Bonnet, G., O. Krichevsky, and A. Libchaber, *Kinetics of conformational fluctuations in DNA hairpin-loops.* Proceedings of the National Academy of Sciences of the United States of America, 1998. **95**(15): p. 8602-8606.

80. Wallace, M.I., et al., *FRET fluctuation spectroscopy: Exploring the conformational dynamics of a DNA hairpin loop.* Journal of Physical Chemistry B, 2000. **104**(48): p. 11551-11555.

81. Antao, V.P. and I. Tinoco, *Thermodynamic Parameters for Loop Formation in Rna and DNA Hairpin Tetraloops.* Nucleic Acids Research, 1992. **20**(4): p. 819-824.

82. Ying, L.M., M.I. Wallace, and D. Klenerman, *Two-state model of conformational fluctuation in a DNA hairpin-loop.* Chemical Physics Letters, 2001. **334**(1-3): p. 145-150.

83. Rogers, P.H., et al., *Selective, Controllable, and Reversible Aggregation of Polystyrene Latex Microspheres via DNA Hybridization.* Langmuir, 2005. **21**(12): p. 5562-5569.

84. Zheng, J., et al., *From molecular to macroscopic via the rational design of a self-assembled 3D DNA crystal.* Nature, 2009. **461**(7260): p. 74-77.

85. Macfarlane, R.J., et al., *Nanoparticle Superlattice Engineering with DNA.* Science, 2011. **334**(6053): p. 204-208.

86. Sherman, W.B. and N.C. Seeman, *A Precisely Controlled DNA Biped Walking Device.* Nano Letters, 2004. **4**(7): p. 1203-1207.

87. Lewin, D.I., *DNA computing.* Computing in Science & Engineering, 2002. **4**(3): p. 5-8.

88. Qian, L. and E. Winfree, *Scaling Up Digital Circuit Computation with DNA Strand Displacement Cascades.* Science, 2011. **332**(6034): p. 1196-1201.

89. Schulman, R. and E. Winfree, *Synthesis of crystals with a programmable kinetic barrier to nucleation.* Proceedings of the National Academy of Sciences, 2007. **104**(39): p. 15236-15241.

90. Gu, H., et al., *A proximity-based programmable DNA nanoscale assembly line.* Nature, 2010. **465**(7295): p. 202-205.

91. Wassarman, D. and J. Steitz, *Interactions of small nuclear RNA's with precursor messenger RNA during in vitro splicing.* Science, 1992. **257**(5078): p. 1918-1925.

92. Takasugi, M., et al., *Sequence-specific photo-induced cross-linking of the two strands of double-helical DNA by a psoralen covalently linked to a triple helix-forming oligonucleotide.* Proceedings of the National Academy of Sciences, 1991. **88**(13): p. 5602-5606.

93. Wu, Q., et al., *Mismatch repair participates in error-free processing of DNA interstrand crosslinks in human cells.* EMBO Rep, 2005. **6**(6): p. 551-557.

94. Feng, L., et al., *Cinnamate-based DNA photolithography.* Nat Mater, 2013. **12**(8): p. 747-753.

95. Chee, M., et al., *Accessing Genetic Information with High-Density DNA Arrays.* Science, 1996. **274**(5287): p. 610-614.

96. Xia, D., J. Yan, and S. Hou, *Fabrication of Nanofluidic Biochips with Nanochannels for Applications in DNA Analysis.* Small, 2012. **8**(18): p. 2787-2801.

97. Pregibon, D.C., M. Toner, and P.S. Doyle, *Multifunctional Encoded Particles for High-Throughput Biomolecule Analysis.* Science, 2007. **315**(5817): p. 1393-1396.

98. Jiang, S., et al., *Janus Particle Synthesis and Assembly.* Advanced Materials, 2010. **22**(10): p. 1060-1071.

99. Liu, Q., et al., *DNA computing on surfaces.* Nature, 2000. **403**(6766): p. 175-179.

100. Benner, S.A., *Defining life.* Astrobiology, 2010. **10**(10): p. 1021-30.